Jesper Jung

Plasmonic Waveguides, Resonators, and Superlenses

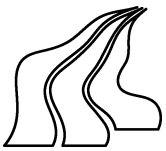

Department of Physics and Nanotechnology,
Aalborg University, Denmark

Plasmonic Waveguides, Resonators, and Superlenses

Plasmon Optiske Bølgeledere, Resonatorer og Superlinser

Published and distributed by
Department of Physics and Nanotechnology, Aalborg University
Skjernvej 4A, DK–9220 Aalborg Øst.
Phone +45 99 40 92 15. Fax +45 99 40 92 35.

Typeset in LaTeX2$_\varepsilon$ by the author.

Printed in Denmark by Printnord Aps, Hjørring

ISBN 978-87-89195-27-8

Preface

This thesis summarizes the work done during my time as a PhD student at the Department of Physics and Nanotechnology, Aalborg University, Denmark, from August 2006 to July 2009. Throughout my PhD studies I have been under skilled supervision of both Associate Professor Thomas Søndergaard and Professor Dr. Scient. Sergey I. Bozhevolnyi. From April 2008 to October 2008 I had the pleasure of a research stay abroad in the group of Professor Francisco J. Garcia-Vidal at the Department of Theoretical Condensed Matter Physics, Autonomous University of Madrid, Spain. My work during the PhD can be divided into three subjects all related to the interaction between light and metallic micro- and nanostructures. A field of research which has emerged as a subfield of nano-optics and nowadays is known as plasmonics. The three subjects investigated are; guiding of plasmon polariton waves by different metallic waveguides, metallic nanostructures and their resonant field enhancement and light scattering properties, and superlensing properties of holey metal films. The thesis is based on six journal papers and one manuscript which is in review. A full list of all my journal and conference papers can be found in Chap. 7.

Outline of the thesis

Chap. 1 is meant as an introduction to the physics of surface electromagnetic modes bound to and propagating along metal-dielectric interfaces. Such surface modes are known as surface plasmon polaritons (SPPs). After some general remarks on the theoretical foundation, SPPs are defined, the criteria for their existence is discussed, and their fundamental properties for planar metal-dielectric interfaces and in simple metallic nanostructures are presented. Chap. 2 presents the first subject; plasmonic waveguides and is linked to the two first papers presented in App. A and B, respectively. Chap. 3 presents an introduction to nanometer thin and sub-micron wide metal strip resonators and their resonant field enhancement and light scattering properties. A presentation of the Green's function surface integral equation method is given. This presentation is connected to the third paper presented in App. C, and is followed by an introduction to the two papers of App. D and E. Chap. 4 presents a short introduc-

tion to superlenses and to the work on superlensing properties of holey metal films. This includes an introduction to the two papers presented in App. F and G. Lastly a short summary, first in English and second in Danish (Chap. 5 and 6, respectively), is given.

Acknowledgments

There are many people who helped me with the work presented here that I would like to acknowledge. I would like to address a special thanks to both of my supervisors, Thomas Søndergaard and Sergey I. Bozhevolnyi, for their guidance, very useful help, and encouragement throughout my PhD project. Thanks for always being there and always taking the time to talk with me. I would also like to give a special thanks to Francisco J. Garcia-Vidal who was my supervisor for half a year at the Department of Theoretical Condensed Matter Physics at the Autonomous University of Madrid. You took good care of me and made sure that I had a pleasant stay. I have enjoyed many scientific (and non scientific) discussions with you. I would like to acknowledge Jonas Beermannn for cooperation and his willingness to perform experiments that have been very useful for comparison with many of the theoretical investigations made within my PhD project. I acknowledge Alexandra Boltasseva for fabrication of samples for the experiments made by Jonas Beermann. I would also like to acknowledge Luis Martin-Moreno (University of Zaragoza, Zaragoza, Spain) for our cooperation and useful discussions on superlensing. Sir John Pendry (Imperial College, London, United Kingdom) for our cooperation. Esteban Moreno and Antonio Fernandez Dominguez (Autonomous University of Madrid, Madrid, Spain) for our cooperation and many useful discussions on modeling of plasmonic waveguides. Thanks to all colleagues at the Department of Physics and Nanotechnology at Aalborg University for creating a nice atmosphere and for many informal but interesting discussions at the coffee table. Especially Tobias Holmgaard Stær, Jakob Bork, and Thomas Bastholm Lynge, who I also often have enjoyed the company of in my spare time. I furthermore would like to acknowledge Tobias Holmgaard Stær, Christian Fisker, Jens Rafaelsen, Ilya P. Radko, Rafael D. Buscalioni, and Abbas Zarifi for being good office partners. We have had many nice discussions. I would like to acknowledge Ulla Ponsaing for help with administrative tasks. Also thanks to all the other people that I encountered at the Autonomous University of Madrid. Thanks for your hospitality during my stay, you all made sure that I had a pleasant time. Especially Juan Antonio Porto, Esteban Moreno, Antonio Fernandez Dominguez, Johan Christensen, Diego Martin Cano and Pablo Pou who I had launch together with almost everyday. Last, but not least, I would like to thank my girlfriend Sanne, my family, and my friends for always being there and always supporting me, especially during those times where we could not be close together. Your unwavering support has been very valuable for me.

Aalborg, Denmark, July 2009 **Jesper Jung**

Contents

Appendix

List of used acronyms

1D: One dimensional

CPP: Channel plasmon polariton

EOT: Extraordinary optical transmission

GPP: Gap plasmon polariton

LR-SPP: Long-range surface plasmon polariton

LSP: Localized surface plasmon

PhD: Doctor of philosophy

PP: Plasmon polariton

SP: Surface plasmon

SPP: Surface plasmon polariton

SR-SPP: Short-range surface plasmon polariton

SSPPW: Square surface plasmon polariton waveguide

TEM: Transverse electromagnetic

TM: Transverse magnetic

This page is intentionally left blank

Chapter 1

Introduction

The purpose of this introduction is first to present some general remarks on the theoretical foundation of the results presented in this thesis; the macroscopic Maxwell equations, and second to introduce SPPs. In subsequent sections, the fundamental properties of SPPs on planar metal surfaces and in simple nanostructures such as nanometer thin metal films and nanometer thin dielectric gaps between metal surfaces will be presented. Attention will also be given to spoof SPPs and to localized surface plasmons (LSPs) in metallic nano-particles.

1.1 General remarks on the theoretical foundation

The theoretical foundation of the results presented in this thesis is the classical Maxwell equations in macroscopic form which may be written as

$$\nabla \times \mathbf{E}(\mathbf{r},t) = -\frac{\partial \mathbf{B}(\mathbf{r},t)}{\partial t}, \tag{1.1a}$$

$$\nabla \times \mathbf{H}(\mathbf{r},t) = \frac{\partial \mathbf{D}(\mathbf{r},t)}{\partial t} + \mathbf{j}(\mathbf{r},t), \tag{1.1b}$$

$$\nabla \cdot \mathbf{D}(\mathbf{r},t) = \rho(\mathbf{r},t), \tag{1.1c}$$

$$\nabla \cdot \mathbf{B}(\mathbf{r},t) = 0, \tag{1.1d}$$

where $\mathbf{E}(\mathbf{r},t)$ is the space and time dependent macroscopic electric field vector, $\mathbf{H}(\mathbf{r},t)$ is the magnetic field vector, $\mathbf{D}(\mathbf{r},t)$ is the electric displacement, $\mathbf{B}(\mathbf{r},t)$ is the magnetic induction, $\mathbf{j}(\mathbf{r},t)$ is the free current density vector, and $\rho(\mathbf{r},t)$ is the free charge density [1,2]. By solving Maxwell's equations the electromagnetic field can be found, however, in order to use the Maxwell equations to find a solution if material bodies are present, constitutive relations, that describe the electromagnetic properties of the materials, must be available. Within most practical applications, and in all results presented in this thesis, the material parameters are either modeled by simple classical response theory or taken from experiments of other scientists as, e.g., in Refs. [3,4]. Generally the constitutive relations relate $\mathbf{D}(\mathbf{r},t)$ to $\mathbf{E}(\mathbf{r},t)$ and $\mathbf{H}(\mathbf{r},t)$

to $\mathbf{B}(\mathbf{r},t)$ via the macroscopic polarization $\mathbf{P}(\mathbf{r},t)$ and magnetization $\mathbf{M}(\mathbf{r},t)$ as

$$\mathbf{D}(\mathbf{r},t) = \varepsilon_0\mathbf{E}(\mathbf{r},t) + \mathbf{P}(\mathbf{r},t), \tag{1.2a}$$

$$\mathbf{H}(\mathbf{r},t) = \mu_0^{-1}\mathbf{B}(\mathbf{r},t) - \mathbf{M}(\mathbf{r},t), \tag{1.2b}$$

where ε_0 is the vacuum permittivity and μ_0 is the vacuum permeability. In most cases time-harmonic (or monochromatic) fields are assumed. For time-harmonic fields the Maxwell equations take the form

$$\nabla \times \mathbf{E}(\mathbf{r},\omega) = i\omega\mathbf{B}(\mathbf{r},\omega), \tag{1.3a}$$

$$\nabla \times \mathbf{H}(\mathbf{r},\omega) = -i\omega\mathbf{D}(\mathbf{r},\omega) + \mathbf{j}(\mathbf{r},\omega), \tag{1.3b}$$

$$\nabla \cdot \mathbf{D}(\mathbf{r},\omega) = \rho(\mathbf{r},\omega), \tag{1.3c}$$

$$\nabla \cdot \mathbf{B}(\mathbf{r},\omega) = 0, \tag{1.3d}$$

where the dependence of the fields amplitude on ω is explicitly written in the arguments. More generally, the Maxwell equations can be time-Fourier transformed and $\mathbf{E}(\mathbf{r},\omega)$ can be seen as the time-Fourier transformed of $\mathbf{E}(\mathbf{r},t)$. In many cases the media analyzed can be considered local, linear, and isotropic which yield constitutive relations in the frequency domain as

$$\mathbf{D}(\mathbf{r},\omega) = \varepsilon_0\varepsilon(\mathbf{r},\omega)\mathbf{E}(\mathbf{r},\omega), \tag{1.4a}$$

$$\mathbf{B}(\mathbf{r},\omega) = \mu_0\mu(\mathbf{r},\omega)\mathbf{H}(\mathbf{r},\omega), \tag{1.4b}$$

$$\mathbf{j}_c(\mathbf{r},\omega) = \sigma(\mathbf{r},\omega)\mathbf{E}(\mathbf{r},\omega), \tag{1.4c}$$

where $\varepsilon(\mathbf{r},\omega) = 1 + \chi_e(\mathbf{r},\omega)$ is the relative permittivity (often denoted the dielectric constant) and $\mu(\mathbf{r},\omega) = 1 + \chi_m(\mathbf{r},\omega)$ is the relative permeability, where $\chi_e(\mathbf{r},\omega)$ and $\chi_m(\mathbf{r},\omega)$ are the electric and magnetic susceptibilities, respectively. The polarization is given as $\mathbf{P}(\mathbf{r},\omega) = \varepsilon_0\chi_e(\mathbf{r},\omega)\mathbf{E}(\mathbf{r},\omega)$, the magnetization is given as $\mathbf{M}(\mathbf{r},\omega) = \chi_m(\mathbf{r},\omega)\mathbf{H}(\mathbf{r},\omega)$, $\mathbf{j}_c(\mathbf{r},\omega)$ is the induced conduction current density, and $\sigma(\mathbf{r},\omega)$ is the conductivity. By utilizing the Maxwell curl equations in frequency space [Eqs. (1.3a) and (1.3b)], the constitutive relations [Eq. (1.4)], and by spitting the current density vector into a source current density vector $\mathbf{j}_s(\mathbf{r},t)$ and an induced conduction current density vector $\mathbf{j}_c(\mathbf{r},t)$, $\mathbf{j}(\mathbf{r},\omega) = \mathbf{j}_c(\mathbf{r},\omega) + \mathbf{j}_s(\mathbf{r},\omega)$ [2], the wave equation of the macroscopic electric field vector can be expressed as

$$\nabla \times \mu^{-1}(\mathbf{r},\omega)\nabla \times \mathbf{E}(\mathbf{r},\omega) - \frac{\omega^2}{c^2}\left(\varepsilon(\mathbf{r},\omega) + \frac{i\sigma(\mathbf{r},\omega)}{\omega\varepsilon_0}\right)\mathbf{E}(\mathbf{r},\omega) = i\omega\mu_0\mathbf{j}_s(\mathbf{r},\omega), \tag{1.5}$$

where $c = 1/\sqrt{\varepsilon_0\mu_0}$ is the speed of light in vacuum. Commonly a complex dielectric constant is introduced by replacing $\varepsilon(\mathbf{r},\omega) + i\sigma(\mathbf{r},\omega)/(\omega\varepsilon_0)$ in Eq. (1.5) with $\varepsilon(\mathbf{r},\omega)$, which thus becomes complex for materials with $\sigma(\mathbf{r},\omega) \neq 0$ [2]. For non-magnetic materials and for problems without current sources [$\mu(\mathbf{r},\omega) = 1$ and $\mathbf{j}_s(\mathbf{r},t) = 0$], Eq. (1.5) simplifies as

$$\nabla \times \nabla \times \mathbf{E}(\mathbf{r},\omega) - \frac{\omega^2}{c^2}\varepsilon(\mathbf{r},\omega)\mathbf{E}(\mathbf{r},\omega) = 0, \tag{1.6}$$

where it is important to note that $\varepsilon(\mathbf{r},\omega)$ now is the complex dielectric constant where energy dissipation due to Ohmic losses is associated with its imaginary part. Similarly

a homogenous wave equation in terms of the macroscopic magnetic field vector for local, linear, isotropic, and nonmagnetic media, without sources can be constructed as

$$\nabla \times \frac{1}{\varepsilon(\mathbf{r},\omega)} \nabla \times \mathbf{H}(\mathbf{r},\omega) - \frac{\omega^2}{c^2}\mathbf{H}(\mathbf{r},\omega) = 0. \tag{1.7}$$

Both Eq. (1.6) and Eq. (1.7) have the form of eigenvalue equations. In a homogenous medium the dielectric constant is independent of the position $\mathbf{r}$ and Eqs. (1.6) and (1.7) simplify to the homogenous Helmholtz equations

$$\left[\nabla^2 + \varepsilon(\omega)\frac{\omega^2}{c^2}\right] \mathbf{E}(\mathbf{r},\omega) = 0, \tag{1.8a}$$

$$\left[\nabla^2 + \varepsilon(\omega)\frac{\omega^2}{c^2}\right] \mathbf{H}(\mathbf{r},\omega) = 0. \tag{1.8b}$$

For many electromagnetic problems the structures analyzed can be subdivided into several homogenous domains on which the Helmholtz equations can be applied. By utilizing these and by connecting the separate solutions via the electromagnetic boundary conditions, the electromagnetic field of the entire structure can be determined [2]. The homogenous Helmholtz equation for the magnetic field is, e.g., the starting point of the derivation of the Green's function surface integral equation method for p polarization, which is studied and further developed within this PhD project (see Sec. 3.2 for details).

Plane waves are solutions to the Helmholtz equations. From the Helmholtz equations their dispersion relation $\omega(k)$ can be found as

$$\frac{c^2k^2}{\omega^2} = \varepsilon(\omega). \tag{1.9}$$

If the dielectric constat is independent of the frequency, Eq. (1.9) is known as the light line, and form a straight line with a slope of $c/\sqrt{\epsilon}$.

1.2 Introduction to surface plasmon polaritons

It has long been well known that some solids, like an electron gas, support collective motion of the electrons, known as a plasma oscillations [5]. The quantum of elementary excitation (or quasi-particle) associated with such a plasma oscillation is known as a *plasmon* (or volume plasmon to be rigorous). The quanta of energy of a volume plasmon is given as

$$\hbar\omega_p = \hbar\sqrt{\frac{ne^2}{\varepsilon_0 m_0}},$$

where ω_p is the plasma frequency, $\hbar$ is the reduced Planck's constant, n is the free electron density, e is the electron charge, and m_0 is the mass of a free electron. Many properties of solids with free electrons can be determined by studying the electron plasma, where the sea of free conduction electrons can be seen as a high density

electron liquid [6]. Volume plasmons in metals are longitudinal in nature and can be excited by shotting fast electrons into the metal [7,6].

Another quasi-particle is a *polariton*. When photons propagate in a material they excite the medium, and as a consequence the permittivity and/or the permeability of the material are different from unity [8]. Propagation of photons in a medium can therefore be described as an admixture of the electric and magnetic fields associated with the photon and the electric and magnetic polarizations induced in the material by the field of the photon. Hence the propagation of light in a material simply becomes a mixing between a photon and an excitation of the material. Such a composite wave is as a polariton.

Surface electromagnetic waves have been studied for more than a century [9–11], and under certain conditions, which will be discussed below, it is possible for polaritons to propagate along the surface of a material. A *surface polariton* is therefore simply a surface electromagnetic wave that propagates along a surface [12,8]. Surface polaritons have their electric and magnetic fields localized near the surface, meaning that solutions to Maxwell's equations emerge, where the electric and the magnetic fields decay in an exponential manner away from the surface, and vary in a wave like manner along [8]. For the surface polariton to be bound to the interface, one of the two media needs to be surface active. A possible surface active medium is a metal, where the free electrons of the surface will oscillate collectively in a plasmon like resonance with the electromagnetic field of the surface polariton. A surface polariton propagating along the surface of a metal is in this thesis termed a *surface plasmon polariton* (SPP). This name underlines the fact that the electromagnetic field is trapped on the surface due to its interaction with the free conduction electrons of the metal. The name is also nowadays generally accepted within the scientific community of plasmonics[1] [13–16]. However, within the community there is no consistent terminology. Some authors use the term SPP as in this thesis, some use the term surface plasmon (SP) equivalent to the use of SPP in this thesis [6], and other never use SPP, but distinguish between surface polariton and surface plasmon whether retardation terms in the Maxwell equations are important or not [12]. The author of this thesis has decided to use the term SPP for surface electromagnetic waves bound to and propagating along metal-dielectric interfaces independent of the frequency or the momentum of the quasi-particle.

The conditions under which SPPs can exist are related to the relative dielectric constants of two media that constitute the interface. For simplicity the discussions and treatments of SPPs in this thesis are limited to materials where nonlocal effects, such a spatial dispersion are disregarded, and where the magnetic permeability always is unity. A dielectric medium has a relative dielectric constant ε_d which is positive, real, and to a good approximation frequency independent. The dielectric constant of a metal $\varepsilon_m(\omega)$, on the other hand, is strongly frequency dependent and can both be negative and complex. However, in the discussion of the criteria for the existence of SPPs it is assumed that the dielectric constant of the metal is purely real. That $\varepsilon_m(\omega)$ is negative, is a requisite for the existence of SPPs. As argued above, a SPP is an electromagnetic excitation of the surface, where the charged electrons at the metal surface oscillate collectively in resonance with the electromagnetic field. This

[1] Research of the interaction between light and metallic micro- and nanostructures, where SPPs account for most of the interesting and unique optical properties.

means that a SPP involves charges at the surface. For the charges to remain at the surface, the component of the electric field which is normal to the surface $E_\perp(\mathbf{r},\omega)$ must change sign when one moves across the interface [17]. On the other hand, the boundary conditions require that the normal component of the electric displacement $D_\perp$ is continuous, and as $D_\perp(\mathbf{r},\omega) = \varepsilon_0\varepsilon(\mathbf{r},\omega)E_\perp(\mathbf{r},\omega)$, one easily realizes that the relative dielectric constants of the two media that constitute the interface must be of opposite sign in order to support SPPs [17]. Thus, a negative $\varepsilon_m(\omega)$ is a prerequisite for the existence of SPPs. Second if the frequency ω and the wave vector of the SPP is able to match with a bulk polariton in the dielectric, the SPP will radiate into the dielectric. A second requirement can therefore be formulated as $k_\parallel > \sqrt{\varepsilon_d}k_0$, where $k_0 = \omega/c$ and $k_\parallel$ is the in-plane momentum of the SPP along the propagation direction [8]. The inequality ensures that the momentum of the SPP cannot be matched with a bulk polariton in the dielectric which has a real component of the wave vector normal to the surface, meaning that the SPP does not radiate into the dielectric medium [8]. In other words, the dispersion relation of SPPs must lie below the light line. The conditions can therefore be formulated as

$$\omega < \frac{ck_\parallel}{\sqrt{\varepsilon_d}}, \quad \varepsilon_m(\omega) < 0. \tag{1.10}$$

If Eq. (1.10) is satisfied the energy is localized near the surface because it cannot radiate into the dielectric or the metal (the negative dielectric constant of the metal ensures that no bulk polaritons can exists in the metal) [8]. The result of Eq. (1.10) is quite general, and ensures the existence of a surface polariton at any interface between two media with dielectric constants ε_d and ε_m that fulfill the conditions, whether the interface is a metal-dielectric interface or any other interface.

In the simplest case the interaction between light and a metal is described by a dielectric constant on the canonical plasma form as

$$\varepsilon_m(\omega) = 1 - \frac{\omega_p^2}{\omega^2}, \tag{1.11}$$

where scattering of the electrons is ignored [12]. $\varepsilon_m(\omega)$ is negative for frequencies below the plasma frequency ω_p. If we consider a vacuum-metal interface with $\varepsilon_d = 1$, the exact condition for the existence of SPPs is $\varepsilon_m(\omega) < -1$, which can be seen from Eq. (1.10) if the dispersion relation $\omega(k_\parallel)$ is known (see details in Sec. 1.3). $\varepsilon_m(\omega) < -1$ is fulfilled for all frequencies below $\omega_p/\sqrt{2}$. Thus a vacuum-metal interface supports propagation of SPPs in a broad spectrum of frequencies up to $\omega = \omega_p/\sqrt{2}$. The specific eigenfrequency of the SPP mode is, however, strongly dependent on the size of the in-plane SPP wave vector $k_\parallel$, as we shall see in the following section.

As can be seen from Eq. (1.10), there is a momentum mismatch between a photon in the medium outside the metal and a SPP propagating along the metal surface. This means that a photon in the dielectric can not couple to (or excite) a SPP. There are several ways to compensate for the momentum mismatch e.g. by placing a high-index prism close to [18] or at [19] the surface, or to introduce gratings or roughnesses directly on the surface [6,12]. The problem of efficient excitation of SPPs is a huge subfield within plasmonics, and various techniques are utilized in experiments to excite SPPs. However, as these are unimportant for the theoretical investigations and results

presented in this thesis, the practical problem of exciting SPPs in experiments will not be elaborated further.

1.3 Planar metal surfaces

This section presents a brief review of the fundamental properties of SPPs propagating along a smooth infinite metal-dielectric interface. As argued above a metal-dielectric interface can fulfill the criteria for the existence of SPPs. First the coordinate system is chosen such that the xy-plane constitutes the interface and the SPPs propagate along the x-axis. Suppose that for $z > 0$ we have a material with a dielectric constant ε_1 which is positive and frequency independent, and for $z < 0$ we have metal with a dielectric constant which is both frequency dependent and complex $\varepsilon_2(\omega) = \varepsilon_2'(\omega) + i\varepsilon_2''(\omega)$. As a SPP is bound to the surface the electromagnetic field which accompanies the collective electron plasma oscillations at the surface, must decay in an exponential manner away from the interface. SPPs are p polarized as it is easy to show that Maxwell's equations together with the electromagnetic boundary conditions can not be satisfied for s-polarization if $\mu_1(\omega) = \mu_2(\omega) = 1$ [12][2]. The electric field associated with SPPs can therefore be expressed as

$$\mathbf{E}_\alpha(x,z) = E_{0x}\left[\hat{x} \mp \frac{k_x}{k_{z\alpha}}\hat{z}\right]\exp(ik_x x \pm ik_{z\alpha}z) \tag{1.12}$$

where $\alpha = 1$ and the first sign are used for $z > 0$, $\alpha = 2$ and the second sign are used for $z < 0$, k_x is the component of the wave vector along the direction of propagation (often denoted the propagation constant), $k_{z\alpha}$ is imaginary, and $\nabla \cdot \mathbf{D}(x,z) = 0$ has been used to relate E_{0x} to E_{0z}. The boundary conditions are that E_x and D_z must be continuous across the interface. This yields

$$\varepsilon_1 k_{z2} + \varepsilon_2(\omega)k_{z1} = 0. \tag{1.13}$$

As the parallel component of the wave vector always is continuous across an interface, we also have $k_x^2 + k_{z\alpha}^2 = \varepsilon_\alpha \omega^2/c^2$ which combined with Eq. (1.13) yields the well known dispersion relation that relates the propagation constant to the frequency of SPPs

$$k_x^2 = \frac{\omega^2}{c^2}\frac{\varepsilon_1\varepsilon_2(\omega)}{\varepsilon_1 + \varepsilon_2(\omega)}. \tag{1.14}$$

By substituting Eq. (1.14) back into $k_x^2 + k_{z\alpha}^2 = \varepsilon_\alpha\omega^2/c^2$ we can obtain an expression for $k_{z\alpha}^2$

$$k_{z\alpha}^2 = \frac{\varepsilon_\alpha^2}{\varepsilon_1 + \varepsilon_2(\omega)}\frac{\omega^2}{c^2}, \tag{1.15}$$

where ε_α is ε_1 for $z > 0$ and $\varepsilon_2(\omega)$ for $z < 0$, respectively. From Eqs. (1.14) and (1.15) the criteria for the existence of SPPs can, with the discussion in the introduction and Eq. (1.10) in mind, be elaborated a bit. If we shortly again assume that $\varepsilon_2(\omega)$ is

[2]However, the interface between magnetic materials, or a magnetic and a dielectric material can support s-polarized surface polaritons, if the magnetic material is magnetic surface active [8].

purely real (losses in the metal are neglected), and examen Eqs. (1.14) and (1.15), the existence of SPPs can be narrowed down to

$$\varepsilon_1\varepsilon_2(\omega) < 0 \quad \text{and} \quad \varepsilon_1 + \varepsilon_2(\omega) < 0, \tag{1.16}$$

which coincides with Eq. (1.10) if $k_{\|} = k_x$ and k_x is specified in terms of Eq. (1.14). When losses are neglected, k_x must be purely real for the mode to be propagating. From Eq. (1.14) it is seen that this is possible if both the sum and the product of the two dielectric constants are either positive or negative. For the mode to be bound to the interface we must require that $k_{z\alpha}$ is imaginary. From Eq. (1.15) it is seen that this is only possible if the sum of the dielectric constants is negative. Hence both the sum and the product of the dielectric constants must be negative for SPPs to exist [2]. For the metal-vacuum interface this reduces to $\varepsilon_2(\omega) < -1$, as postulated in the introduction.

As the dielectric constant of the metal in general is complex the propagation constant of SPPs is also complex $k_x = k_x^{'} + ik_x^{''}$. The real part of the propagation constant is associated with the wavelength of the SPP mode $\lambda_{spp} = 2\pi/k_x^{'}$, whereas the imaginary part is associated with the internal absorption in the metal. As the metal absorbs energy (Ohmic losses) the SPP intensity decay as the mode propagates along the metal surface. The propagation length L_{spp} is defined as the length after which the intensity has decreased by a factor of e^{-1}, and is given as

$$L_{spp} = \frac{1}{2k_x^{''}}. \tag{1.17}$$

For a good metal like silver, which has a large but negative real part of the dielectric constant and a relatively low imaginary part, the propagation length varies from approximately 10 μm to above 300 μm when one moves from the beginning of the visible spectrum (400 nm) to the near-infrared spectrum ($\sim$ 1600 nm) [17]. The SPP wavelength λ_{spp}, on the other hand, is always smaller than the free space wavelength λ_0. The penetration depth of the SPP mode into the materials that constitute the interface can be found from the z component of the SPP wave vector, which when losses are neglected is purely imaginary. The penetration depths, defined as the distances inside the two media where the field has decayed by a factor of e^{-1}, is given as

$$\delta_\alpha = \frac{1}{|k_{z\alpha}|}, \tag{1.18}$$

where again α is 1 for the dielectric and 2 for the metal. To a first approximation the spatial extension of the field into the dielectric is in the order of the free space wavelength, whereas the penetration into the metal is almost wavelength independent and in the order of 30 nm for the visible and near-infrared spectrum for a good metal like silver [17].

Now we consider the dispersion relation of SPPs [Eq. (1.14)]. By assuming that the dielectric constant $\varepsilon_1 = 1$ and $\varepsilon_2(\omega)$ is on the canonical plasma form, the dispersion curve can be calculated [Fig. 1.1 a)]. The red line is the dispersion relation and the blue line represents the light line. The SPP branch is found below the SP resonance frequency $\omega_{sp} = \omega_p/\sqrt{2}$, and below the light line, where the criteria for true surface

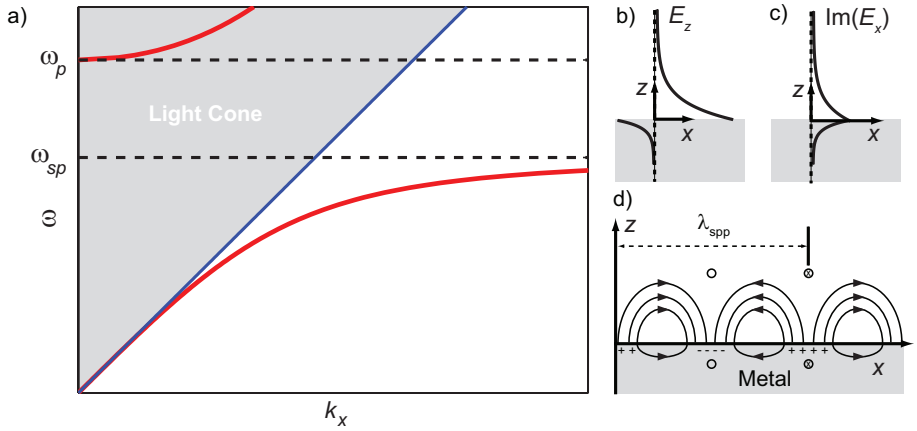

Figure 1.1: a) Dispersion relation of SPPs at a planar metal-dielectric interface. The solid red line is the solution of the SPP dispersion relation [Eq. (1.14)]. In the calculation, the canonical plasma form of the dielectric constant is used for the metal $\varepsilon_2(\omega)$ [Eq. (1.11)] and $\varepsilon_1 = 1$ is used for the dielectric. The solid blue line is the light line, which mark the separation between propagating and evanescent waves in the dielectric. The two horizontal dashed lines are the plasma frequency ω_p and the SP resonance frequency $\omega_{sp} = \omega_p/\sqrt{2}$. b) Sketch of the transverse component of the electric field of the SPP mode. Note how the field decay evanescently away from the interface, both into the metal and the dielectric. c) Sketch of the longitudinal component of the electric field of the SPP mode. d) Sketch of the surface charge and the electric and magnetic field distributions of the SPP mode at the interface. The solid circulating black lines represent the electric field which lies in the xz-plane and $\odot$ (into the paper) and $\otimes$ (out of the paper) denote the orientation of the magnetic field which is directed along the y axis. Note that the wavelength of the SPP mode λ_{spp} is indicated.

states are fulfilled by the dielectric constants. For frequencies well below the SP resonance frequency the SPP dispersion branch is close to the light line, but it is, however, always below. A momentum compensation is always necessary for the non-radiative SPP to transform into light. As the frequency rises, the gap between the light line and the SPP branch increases and the SPP branch goes asymptotically towards the SP resonance frequency. In that limit, the group velocity of the SPP modes becomes almost zero and the mode highly resembles a standing wave resonance in the electron surface plasma. However, in the visible and near-infrared spectrum, where metallic nano components are interesting, the SPP branch is close to the light line [17]. The branch above the plasma frequency, that lies within the light cone, is known as the Brewster mode [2]. Fig. 1.1 b) and c) depict sketches of the transverse and the longitudinal component of the electric field associated with the SPP mode. For a real, but negative, $\varepsilon_2(\omega)$ there is always a $\pi/2$ phase difference between the two electric field components. This explains why $\mathrm{Im}(E_x)$ is depicted in c). Fig. 1.1 d) is a sketch of the spatial variation of the electric field, the magnetic field, and the surface charge distributions associated with the SPP mode. The field patterns can be constructed from the boundary conditions and by remembering that SPPs are p-polarized waves with their magnetic field along the y-axis and their electric field in the xz-plane. The direction of the electric field at a fixed time rotates 360° within the SPP wavelength as one moves along the surface. The sense of the rotation is opposite in the metal and in the dielectric [8]. The direction of the magnetic field is either parallel or antiparallel

with the y-axis and the magnetic field is maximum where the circles are drawn in the sketch [8].

1.4 Nanometer thin metal films

If two metal-dielectric interfaces are placed close together the SPPs supported by the individual surfaces can couple and form new super-SPP modes. An example is a nanometer thin metal film, where two super-SPP modes with different propagation constants emerge. The two SPPs supported by the interfaces can couple in a symmetric and an antisymmetric fashion. If the thickness of the metal film is denoted h and we assume that the metal film is placed in a symmetric environment described by ε_1, and the dielectric constant of the metal film is denoted $\varepsilon_2(\omega)$, the dispersion relation can be written as [20,21]

$$\tanh(\xi_2 h)[\varepsilon_1^2\xi_2^2 + \varepsilon_2^2(\omega)\xi_1^2] + 2\varepsilon_2(\omega)\xi_2\varepsilon_1\xi_1 = 0, \tag{1.19}$$

where $\xi_\alpha^2 = -k_{z\alpha}^2 = k_x^2 - \varepsilon_\alpha\omega^2/c^2$. Eq. (1.19) has two solutions given as

$$\omega^+ \quad \text{LR-SPP}: \ \tanh\left(\frac{h}{2}\xi_2\right)\varepsilon_1\xi_2 + \varepsilon_2(\omega)\xi_1 = 0, \tag{1.20a}$$

$$\omega^- \quad \text{SR-SPP}: \ \coth\left(\frac{h}{2}\xi_2\right)\varepsilon_1\xi_2 + \varepsilon_2(\omega)\xi_1 = 0. \tag{1.20b}$$

where the designations $\omega^\pm$, LR- and SR-SPP will become clear from the following discussion. Note that for $h \to \infty$, the two solutions both converge toward the dispersion relation of a single metal-dielectric interface [Eq. (1.13)]. This makes sense, because if the film is optically thick the two super-SPP modes are completely decoupled and resemble regular SPP modes on each of the two interfaces of the film. The dispersion branches of the two super-SPP modes can be depicted from the solutions of Eq. (1.19) [Fig. 1.2 a)]. For a gold film of thickness $h = 15$ nm the individual SPPs of the two interfaces have coupled and formed a high ω^+ (dashed blue line) and a low ω^- frequency branch (dashed red line) which are positioned above and below (in frequency) the dispersion branch of a regular SPP (solid black line), respectively. The dispersion branches of the two super modes are also depicted for a film thickness of $h = 20$ nm (solid red and blue lines). In general for a increasing thickness h the gap between the two modes, both in propagation constant and in frequency, decreases. Note that both branches always are below the light line (dot-dashed black line). For large propagation constants both modes converge toward the SP plasma frequency $\omega_{sp} = \omega_p/\sqrt{2}$. Fig. 1.2 b) and c) sketch the z component of the electric field of the high and the low frequency branch, respectively. E_z of ω^+ is symmetric with respect to the mid-plan of the film, whereas it for ω^- is antisymmetric.[3] The longitudinal electric field component E_x of the two solutions is sketched in Figs. 1.2 d) and e), respectively. By comparing Fig. 1.2 d) to e) it can be seen that E_x of the low frequency

[3]Due to these symmetry properties ω^+ is often denoted the symmetric SPP mode and ω^- the antisymmetric mode. However, the other electric field component E_x is antisymmetric for ω^+ and symmetric ω^-, which can make the names symmetric and antisymmetric quite confusing. The author of this thesis has therefore decided not to introduce this terminology.

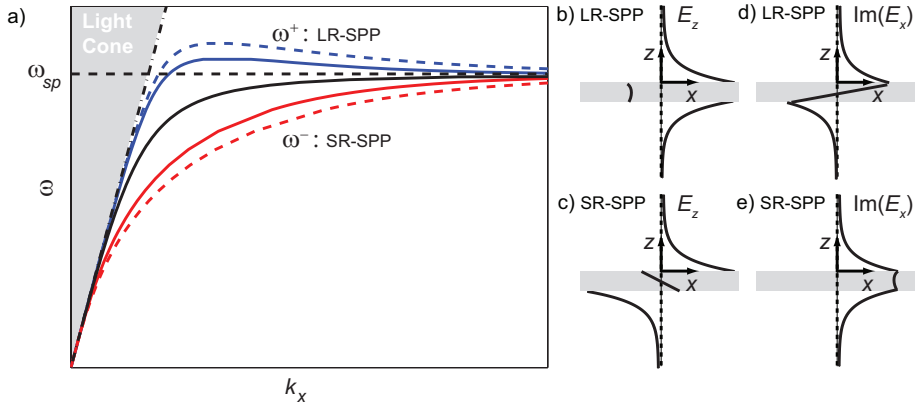

Figure 1.2: a) Dispersion relation of the two super-SPP modes of a thin metal film. A dielectric constant on the canonical plasma form [Eq. (1.11)] is used for the metal. Dispersion relations for two different thicknesses of the film are presented, $h = 15$ (dashed red and blue lines) and $h = 20$ nm (solid red and blue lines). A blue line depicts a dispersion branch from the first solution [Eq. (1.20a)], whereas a red line depicts a branch from the second solution [Eq. (1.20b)]. The solid black line is the dispersion relation of a regular SPP of a single metal-dielectric interface. b) and d) Sketches of the z and the x component of the electric field of the high frequency super-SPP mode, respectively. c) and e) Sketches of the z and x component of the electric field of the low frequency super-SPP mode, respectively.

mode is maximized inside the metal film, whereas it crosses zero in the mid-plane of the film for the high frequency mode. As a consequence the low frequency mode exhibits a strong decay as it propagates along the film. The high frequency mode, on the other hand, exhibits significantly smaller attenuation than the low frequency mode as the zero crossing in the longitudinal field component forces the electromagnetic energy of the mode out of the metal as the film gets thinner. The low frequency mode is therefore often denoted the *short-range* SPP mode (SR-SPP) and the high frequency mode the *long-range* SPP mode (LR-SPP). By examining the dispersion of the LR- and the SR-SPP mode with the thickness of the metal film [Fig. 1.3] it is found that the splitting between them increases dramatically as the thickness of the film is reduced. Non of the two modes exhibit cut-off with respect to the thickness. As the electromagnetic energy of the LR-SPP is pushed out of the metal as the thickness is reduced the LR-SPP converges towards a freely propagating TEM mode in the dielectric. The SR-SPP, on the other hand, becomes more and more confined to the metal, dramatically slowed down, and thus strongly attenuated as the thickness of the film is reduced. The physical reason for this is that a mode with an antisymmetric transverse electric field component cannot exist in a homogenous medium [22]. These very different characteristics of the super-SPP modes when two (or more) SPPs couple between spatially close metal-dielectric interfaces, are extremely essential for the different possible applications of plasmonic micro- and nanostructures. A large subfield within plasmonics is devoted to the study of metallic waveguides which often take advantage of various LR-SPP modes in different waveguide configurations. Another large subfield within plasmonics is the development of metallic nano-antennas and resonators for applications within sensing and spectroscopy. The physics behind many of these resonators can be attributed to standing wave resonances between counter-

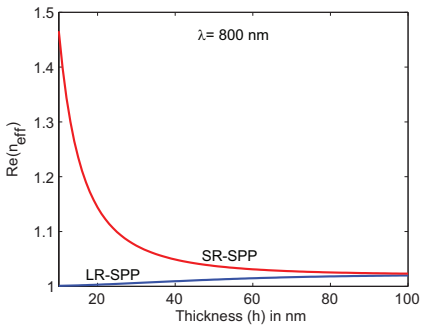

(a) Real part of the normalized propagation constant $n_{\text{eff}} = k_x/k_0$ (also denoted the effective refractive index) of the LR- and the SR-SPP mode as a function of the thickness of the metal film.

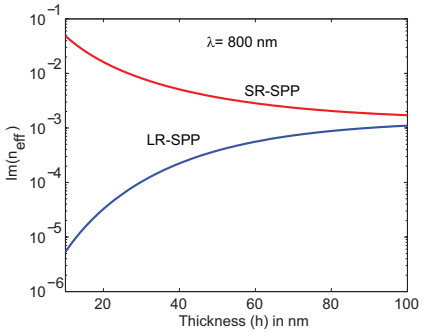

(b) Imaginary part of the normalized propagation constant of the LR- and the SR-SPP mode as a function of the thickness of the metal film.

Figure 1.3: Dispersion with film thickness of the two super-SPP modes of a thin metal film. The free space wavelength is $\lambda_0 = 800$ nm, the metal is gold where the complex dielectric constant is linearly interpolated from the tables presented in Ref. [4], and the environment is vacuum with $\varepsilon_1 = 1$.

propagating SR-SPPs, that strongly enhance both the local and the scattered fields. Both plasmonic waveguides and nano-resonators are studied within this PhD project (see Chap. 2 and Chap 3, respectively).

1.5 Nanometer thin dielectric gaps between metal surfaces

Another super-SPP mode which within this PhD project has been investigated in connection with the development of metallic resonators is the symmetric (with respect to the z-component of the electric field) coupling between SPPs supported by two metal-dielectric interfaces separated by a nanometer thin dielectric gap. This mode is characterized by a large electric field in the gap and is therefore conventionally termed the gap plasmon-polariton (GPP) mode. It is in particular interesting for the development of compact metallic nano-sensors as the large field in the gap allows for a strong interaction between the field and a possible specimen in the gap. If the gap size is denoted d, ε_1 describes the dielectric in the gap, and the dielectric constant of the metal is $\varepsilon_2(\omega)$, the dispersion relation of the GPP mode is given as [21, 23]

$$\text{GPP: } \tanh\left(\frac{\xi_1 d}{2}\right)\varepsilon_2(\omega)\xi_1 + \varepsilon_1\xi_2 = 0, \tag{1.21}$$

where again $\xi_\alpha^2 = k_x^2 - \varepsilon_\alpha\omega^2/c^2$, where k_x now is the propagation constant of the GPP mode. A dielectric gap between either two metal films of finite thickness or two infinitely thick metal surfaces both support the GPP mode. These configurations also support other super-SPP modes, however, if the two films are optically thick, the GPP mode is the only mode that exists when the gap size d approaches zero [21, 23]. The dispersion with the gap size of the GPP mode, is similar to the dispersion with

film thickness of the SR-SPP mode [Fig. 1.4]. As the gap size decrease the GPP mode

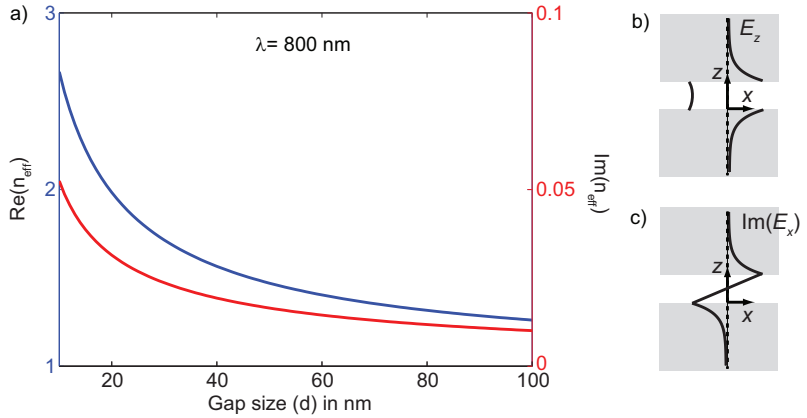

Figure 1.4: a) Dispersion with gap size of the GPP mode for a vacuum gap between two 50 nm thick gold films. The free space wavelength is $\lambda_0 = 800$ nm, the complex dielectric constant of the gold $\varepsilon_2(\omega)$ is linearly interpolated from the tables presented in Ref. [4], and $\varepsilon_1 = 1$. The blue line depicts the real part of the mode index (left y-axis), whereas the red line depicts the imaginary part (right y-axis). b) Sketch of the transverse electric field component E_z of the GPP mode. c) Sketch of the longitudinal electric field component E_x of the GPP mode.

becomes more and more confined, considerably slowed down, and strongly attenuated. For a given gap size d_0, both the real and the imaginary part of k_x of the GPP mode are bigger than the corresponding k_x of the SR-SPP mode for a metal film thickness $t_0 = d_0$. Thus, the GPP mode is even more confined and has a shorter propagation length than the SR-SPP mode. Sketches of the transverse and the longitudinal electric field profiles of the GPP mode [Fig. 1.4 b) and c), respectively], show that E_z is symmetric and E_x is antisymmetric with respect to the mid-plan of the gap. This is similar to the LR-SPP mode of a thin metal film. As the gap size is reduced, the zero crossing of the longitudinal field component forces the field of the GPP mode out of the dielectric gap and into the metal, dissimilar to the LR-SPP mode which for decreasing film thicknesses is forced out of the metal and into the dielectric. This explains the high losses associated with the GPP mode.

1.6 Spoof surface plasmon polaritons

SPPs, as described in Sec. 1.3 to 1.5, are mainly interesting for plasmonic applications in the visible and the near-infrared spectrum because the confinement of the electromagnetic field in the direction perpendicular to the metal-dielectric interface is on the scale of (or below) the free space wavelength. This subwavelength confinement facilitates the used of metallic micro- and nanostructures both as subwavelength waveguides and as ultra compact sensors [13]. At microwave frequencies, however, SPPs are weakly confined. The metals become almost perfect conductors which practically exclude the electromagnetic field, and the field of the SPP in the dielectric above the metal extents over several tens of wavelengths [24]. As a consequence metallic micro- and nanostructures losses their capability to operate both as subwavelength

waveguides and as compact sensors. In fact, the electromagnetic field of SPPs, at microwave frequencies, is to a great extent similar to simple grazing radiation [24], and in the limit of perfect conductors no bound surface mode exists. From the dispersion relation of SPPs of a planar metal-dielectric interface [Fig. 1.1] it can be seen that the propagation constant is large (the SPP is strongly confined) for frequencies which are a considerable amount of the inherent plasma frequency of the metal ω_p. For frequencies well below the inherent plasma frequency the dispersion relation of SPPs is close to the light line, meaning that the SPP is light-like and therefore will resemble simple grazing radiation. Commonly used metals within plasmonics are noble metals like silver and gold which have ω_p in the ultra-violet spectrum. Plasma frequencies in the ultra-violet give rise to subwavelength confined SPPs in the visible and the near-infrared spectrum [25], which explains why plasmonic research predominantly is focused on this spectral region. Thus, it is the intrinsic plasma frequencies of the metals that dictate the applicable spectrums.

It has long been known that the extension of the SPP field into the dielectric can be considerably compressed if the metal surface is perforated by a grating with features on the subwavelength scale [26]. Even in the limit of infinite conductivity, a surface mode can be bound if the surface is perforated with subwavelength features [27,28]. Recently it has been shown that if a perfect conductor is perforated with subwavelength holes, bound surface electromagnetic modes can be supported by the surface [28,29]. Due to their mimicking characteristics and resemble of canonical SPPs such surface modes are usually termed *spoof* SPPs. In Ref. [28] Pendry and coworkers showed that a perfect conductor surface perforated with subwavelength holes behaves as an effective medium, where the electromagnetic waves are governed by an effective dielectric constant which is form invariant with the canonical plasma form of Eq. (1.11). Furthermore they showed that the cut-off frequency of the hole waveguide acts as the effective plasma frequency of the response. This result has two important implications. First, as the dielectric constant is reduced to the canonical plasma form of a metal, it implies that an interface between a dielectric and a holey perfect conductor surface can support bound surface electromagnetic modes. Second it implies that the effective plasma frequency can be custom designed because the cut-off frequency of the hole waveguide scales proportionally with the hole size. This means that the plasma frequency which normally is an intrinsic property of the metal and, as discussed above, uniquely dictates the spectral region of confined SPPs, can more or less be chosen freely. Due to this, spoof SPPs are also commonly referred to as *designer* SPPs, because by designing a structured surface designer SPPs with almost arbitrary dispersion can be constructed. The existence of spoof or designer SPPs at the surface of a two dimensional hole array, as predicted by Pendry and coworkers, has afterwards been verified experimentally in the microwave regime [30]. The dispersion relation of a spoof SPP bound to the interface between a vacuum region and a two dimensional perfect conductor array with square holes can be written as [28,29]

$$k_x^2 c^2 = \omega^2 + \frac{1}{\omega_p^2 - \omega^2} \frac{S^4 \omega^4}{\varepsilon_h}, \tag{1.22}$$

where k_x is the propagation constant, c is the speed of light, $\omega_p = \pi c/(a\sqrt{\varepsilon_h})$ is the effective plasma frequency which is identical to the cut-off frequency of the hole waveguide, ε_h is the dielectric constant of the dielectric within the hole, and $S = 2\sqrt{2}a/(d\pi)$

is the overlap between an incident plane wave and the fundamental waveguide mode of the hole waveguide, where a is the hole size and d is the center to center spacing between the holes. In the case of a one dimensional array of grooves a dispersion relation for the spoof SPPs supported can also be derived, see Ref. [29]. A plot of the spoof SPP dispersion relation from Eq. (1.22) is presented in Fig. 1.5 a). It is seen that the

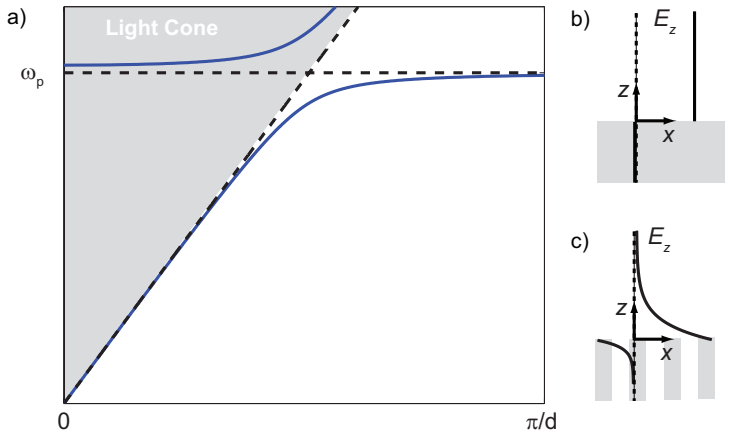

Figure 1.5: a) Dispersion relation of spoof SPPs supported by the surface of a two dimensional perfect conductor square hole array (blue line). The ratio between the hole size a and the unit cell size d is $a/d = 0.8$ and the dielectric constant of the material within the holes is $\varepsilon_h = 6$. The dashed black curves depict the light line and the effective plasma frequency of the two dimensional hole array $\omega_p = \pi c/(a\sqrt{\varepsilon_h})$. b) Sketch of the transverse (z) electric field component of a canonical SPP at microwave frequencies. c) Sketch of the transverse electric field component of a spoof SPP at microwave frequencies at the surface of a hole array.

dispersion relation to a great extent is similar to the dispersion relation of canonical SPPs [Fig. 1.1]. As the frequency is reduced the spoof SPP dispersion branch approaches asymptotically the light line. For large parallel momentums, however, the branch approach the effective plasma frequency of the holey structure ω_p. This is different for canonical SPPs which for large propagation constants approach the surface plasmon resonance $\omega_p/\sqrt{2}$ and not the intrinsic plasma frequency ω_p. This is due to the anisotropy of the holey metal film. Sketches of the transverse component of the electric field of a regular SPP and a spoof SPP at microwave frequencies [Figs. 1.5 b) and c), respectively] show how the field of the regular SPP almost completely is excluded from the metal and is similar to simple grazing radiation. However, by introducing a subwavelength surface structure, in this case in form of holes, the field of the surface mode becomes strongly bounded to surface, very similar to a regular SPP in the visible spectral region. Thus by introducing subwavelength surface perforations the unique properties of canonical SPPs in the visible and the near-infrared spectral region can via the spoof SPP concept be transferred to much lower frequencies, such as microwave frequencies, where metals are almost perfect conductors. One idea within this PhD project, which is described in details in Chap. 4, was to try to transfer the idea of Pendry's near-field perfect lens in the optical regime [31] to lower frequencies by means of the spoof SPP concept. The key to electrostatic near-field superlensing is exponential enhancement of evanescent waves across a thin metal film be means

of resonantly excited SPPs [32]. Hence, it is natural to investigate for superlensing effects at microwave frequencies in holey metal films by trying to take advantage of the spoof SPPs supported.

1.7 Localized surface plasmons

Besides SPPs which are propagating surface modes, that are bound to and propagate along metal-dielectric interfaces, where planar metal surfaces, thin metal films, and dielectric gaps between planar metal surfaces, are just a few examples, localized surface plasma oscillations in small metallic nano particles can also be considered. Such excitations are called localized surface plasmons (LSP) [33,22], and give rise to a resonant behavior in the optical properties of noble-metal nano-particles. In the case of spherical particles, scattering and absorption cross sections can be calculated exactly using the semi-analytical Lorenz-Mie scattering theory [34,35]. Already in 1908 the German physicist Gustav Mie presented an analysis of the optical properties of spherical metal particles [35]. If the radius of a spherical nano-particle a is small compared to the wavelength in the surrounding medium $a \ll \lambda$ it can to a good approximation be treated in the dipole limit. If we assume that the particle is described by a dielectric constant $\varepsilon_m(\omega)$ and the surrounding dielectric by ε_d a quasi-statical analysis yields the particle polarizability as [22]

$$\alpha(\omega) = 4\pi a^3 \frac{\varepsilon_m(\omega) - \varepsilon_d}{\varepsilon_m(\omega) + 2\varepsilon_d}, \tag{1.23}$$

and the scattering cross section of the sphere can be expressed in terms of the polarization as [2]

$$\sigma_{\text{scattering}} = \frac{k^4}{6\pi\varepsilon_0^2}|\alpha(\omega)|^2, \tag{1.24}$$

where k is the wave vector in the surrounding medium. By contemplating Eq. (1.23) it seen that there is a resonance at $\Re\{\varepsilon_m(\omega)\} + 2\varepsilon_d = 0$. This is known as the particle plasmon dipole resonance and is caused by a LSP resonance in the conduction electrons of the small sphere. If the dielectric constant of the metal is on the simple canonical plasma form of Eq. (1.11) this yields a LSP frequency ω_{lsp} as

$$\omega_{lsp} = \frac{\omega_p}{\sqrt{1 + 2\varepsilon_d}}, \tag{1.25}$$

where again ω_p is the intrinsic plasma frequency of the metal. Eq. (1.25) shows how the resonance red-shifts when the dielectric constant of the surrounding material is increased. At this LSP resonance both the local and the scattered fields get strongly enhanced, which make metallic nano-particles interesting for sensing and spectroscopy applications [13]. However, in general the spectral position and the strength of LSP particle resonances can not be determined analytically, because these are dependent on the geometry, the size, and the dielectric constant of the particles as well as the dielectric constant of the surrounding material [22]. Within this PhD project resonant light scattering from sub micron wide and nanometer thin metal nanostrips has been

analyzed using numerical Green's function integral equation techniques (see Chap. 3 for details). In this particular configuration, it has recently been shown that the plasmon resonances of the nanostrips can be attributed to constructive interference between counter-propagating SR-SPPs supported by the nanostrip [36]. Thus even in the case of sub-micron wide nanostrips it makes senses to think about propagating SR-SPP modes.

Chapter 2

Plasmonic waveguides

2.1 Introduction

Ever increasing demands for miniaturization and processing speed of modern microprocessors set high demands to digital information communication techniques, which must be capable of processing larger and larger amounts of data in small and small amounts of times. Interconnects in microprocessors are today made of small copper wires and the digital information is processed from A to B by means of electrical currents. It is these copper interconnects that, to a high extent, limit the speed of modern microprocessors, because the miniaturization of electronic wires strongly increases the propagation delay of the signals [16]. The performance of the transistors, on the other hand, increases when scaled down. Thus the communication speed of electronics is limited by the RC-delay in the wires which, in a simple picture, is proportional to the length squared and inverse proportional to the cross sectional area of the wire. Hence, both as the length increases and as the wires are miniaturized in cross section the propagation delay increases. As an alternative to electronic interconnects on-chip optical data processing can be considered. However, even though optical communication is strongly superior to electronic in terms of operational bandwidth [37], it suffers from one great limitation; the diffraction limit. The size of regular optical waveguides cannot be smaller than half of the operational wavelength of the light that they transmit. Standard fibers for optical communication are therefore quite large compared to electronic interconnects [16]. This means that optical fibers and electronic interconnects are difficult to combine within the same circuit [16].

For an optical technology to be feasible to be utilized as a substitution of electronics one involuntary demand is that the waveguides must be capable of confining and directing light signals in dimensions which are much smaller than the operating wavelength of the light, i.e. subwavelength optical components must be realized. The hybrid nature of SPP propagation along metallic nano-waveguides is one approach to circumvent the problem with the diffraction limit of regular photonic components [37]. As described in Chap. 1, a SPP is a hybrid phenomenon, where the electromagnetic field of the photons is trapped on the surface due to its interaction with the free conduction electrons of the metal. As a consequence of this interaction, SPPs

and super-SPP modes can be strongly confined in the dimensions which are normal to the metal-dielectric interfaces. A thin metal film (as discussed in Sec. 1.4) is an example of a one dimensional SPP waveguide, where the electromagnetic field of the SPP is confined in the dimension perpendicular to the film plane. Due to the Ohmic losses in the metal there exists a tradeoff between confinement and propagation length of SPPs. This can easily be illustrated by contemplating the two super-SPP modes supported by a thin metal film. The LR-SPP mode is close to the light line and thus loosely confined but propagates far when compared to the SR-SPP mode which is strongly confined to the waveguide. The tradeoff between confinement and propagation length of the SPP modes is an intrinsic problem of plasmonic waveguides. In order to achieve compact integrated plasmonic components, waveguides with strongly confined SPP fields are an involuntary requirement. Without a strong confinement of the modes, it is impossible to miniaturize and simultaneously obtain a low level of cross-talk between different waveguides. On the other hand, it is also important that the signals reach their destinations, thus it is important that the SPP modes have long propagation lengths. Hence, the optimization of different metallic waveguides which simultaneously sustain strong confinements and large propagation lengths is one of the primary tasks within research of plasmonic waveguides.

The usage of plasmonic waveguides for future intermediate-level intra-chip interconnects has been investigated in Ref. [38]. The conclusion, was however, that plasmonic interconnects are no obvious replacement of regular electric intermediate-level interconnects. Because of the tradeoff between the mode size and propagation loss, it is questionable if it ever will be possible to exploit plasmonic waveguides as interconnects on the local level between transistors within microprocessors, however, many other applications can be considered. Within plasmonics sensors, plasmonic waveguides can be used to bring plasmonic signals in and out of the sensors. Plasmonic waveguides can also be used as an interface between regular dielectric waveguides, which are ideal for high speed data communication over longer distances, and regular electronic interconnects on the transistor level [38].

A thin metal film which is infinite in the plane of the film (discussed in Sec. 1.4), only offers one-dimensional field confinement of the SPP mode and is therefore of limited practical interest as a plasmonic waveguide. For a plasmonic waveguide to have practical interest, two dimensional field confinement in the plane transverse to the propagation direction is a necessity. One of the most promising configurations, with integrated optics in mind, which offers two-dimensional transverse field confinement, and which recently has been studied, is a thin metal strip embedded in a dielectric [39–42].

2.2 Metal strip waveguides

The metal strip waveguide configuration [Fig. 2.1] was proposed by Berini ten years ago [39]. Typically, dispersion with film thickness t has been analyzed at a fixed width w and wavelength λ. Often $w = 1$ μm and t is in the range $0.01w$ to $0.1w$, hence the width is much larger than the thickness of the strip. Like a thin metal film of infinite width, a metal strip waveguide supports super-SPP modes. These super-SPP modes form from the coupling between the interfaces and the corners of the waveguide. The rectangular metal strip waveguide supports four fundamental modes which can be

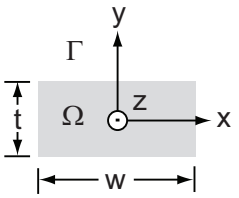

Figure 2.1: Metal strip plasmonic waveguide. A lossy metal core Ω of width w and thickness t (w been much larger than t) is embedded in an infinite dielectric material Γ. The cross section of the waveguide is in the xy plane and the direction of propagation is along the z axis, which is out of the paper.

named according to their symmetries. In the nomenclature developed by Berini the four fundamental modes of the rectangular waveguide are named sa_b^0, aa_b^0, ss_b^0, and as_b^0 [39]. In this nomenclature the two first letters specify the symmetries of the dominating electric field component with respect to the y and x axis, respectively. For rectangular waveguides $t/w \ll 1$ E_y is the dominating field component. The subscript b specify that the mode is bound and the superscript specify the numbers of extrema in the dominating electric field component along the largest transverse dimension of the metal core [40]. Besides the four fundamental modes the metal strip waveguide supports a number of higher order modes.

The mode ss_b^0, also named the dominating symmetric strip mode in Ref. [42][1], is of particular interest with the development of plasmonic waveguides for integrated optics in mind. It has similar characteristics to the LR-SPP mode supported by a thin metal film of infinite width. It has no cut-off with thickness and as the thickness of the metal strip waveguide is reduced it tends asymptotically towards a TEM mode in the surrounding material. Furthermore, the ss_b^0 mode offers longer propagation lengths than the LR-SPP mode of a thin metal film, and it has a field distribution which can be matched by end-fire coupling of a single mode fiber [40]. Different components for integrated optics have been demonstrated utilizing the long-range ss_b^0 mode of the metal strip waveguide [43–46].

As a difference to the super-SPP modes of the infinite wide metal film, the modes of the strip waveguide are not purely p polarized or transverse magnetic (TM), all field components are into play. However, for the rectangular structures investigated in Refs. [39–42], the y component of the electric field is dominating, and in practice the waveguides only support long-range SPP propagation for light polarized with its electric field along the y axis [47]. This is a large disadvantage, which is common for most plasmonic waveguides. A plasmonic waveguide that supports long-range propagation for both polarizations would be a major step towards plasmonic integrated optics, because often the polarization of light in optical communication systems cannot be controlled. As the main component of the electric field of SPPs is oriented perpendicular to the metal-dielectric interface one should look for metal structures with a symmetric cross section in the search of polarization-independent plasmonic waveguides. Very recently, square metal rod waveguides have been investigated experimentally and it was show that these waveguides support long-range propagation

[1]The mode named the dominating antisymmetric strip mode in Ref. [42] is the mode sa_b^1 in the nomenclature of Berini.

of SPPs for both polarizations [47].

A theoretical analysis of a square plasmonic waveguide for long-range polarization-independent waveguiding is the subject of the first paper presented in this thesis [App. A]. The waveguide investigated in the paper is similar to the strip waveguide, analyzed in Refs. [39–42], with the different being that the cross section of the waveguide is square ($t = w$) [Fig. 2.1]. In the paper the bound modes of a square metal rod embedded in a lossless dielectric are determined and characterized. Based on symmetry considerations, a schematic overview of the fundamental modes supported by the waveguide is presented. As a consequence of the 90° rotational symmetry the square surface plasmon-polariton waveguide (SSPPW) can be shown to support four fundamental super modes, which can be constructed from the coupling between four corner or wedge PP modes; one for each of the corners of the waveguide. A metal corner supports a fundamental PP mode which is strongly localized at the tip of the corner. Plasmonic wedge modes have been analyzed both before and after the publication of the paper in App. A, see, e.g., [48–50]. For large metal cores the SSPPW supports four fundamental degenerate modes which all have the mode index of a wedge mode of an isolated 90° corner. However, when the size of the core is reduced, the four corner modes start to overlap and new super modes are formed. By choosing either a positive or a negative sign of the four fundamental corner modes (+/-) four linearly independent super-SPP modes can be constructed. The combinations that are consistent with the symmetry of the waveguide are those involving zero or two negative signs. For naming of the fundamental modes of square plasmonic waveguides, the nomenclature developed by Berini is quite comprehensive and a simpler nomenclature can be introduced. The fundamental modes of the SSPPW can be named via two indices which denote the number of sign changes in the dominating electric field component along the x and the y axis, respectively (the y component along the x axis and the x component along the y axis). If these are appended to E, for the electric field, the four fundamental modes of the SSPPW can be named $E^{(0,0)}$, $E^{(1,0)}$, $E^{(0,1)}$, and $E^{(1,1)}$. As the square geometry makes x and y interchangeable it is evident, from this nomenclature, that the two modes $E^{(1,0)}$ and $E^{(0,1)}$ are degenerate, and it is also evident that $E^{(1,0)}$ is primarily polarized along the x axis, whereas $E^{(0,1)}$ is primarily polarized along the y axis. As $E^{(1,0)}$ and $E^{(0,1)}$ are degenerate (they have the same mode index) it is clear that the SSPPW supports propagation of plasmonic signals independent of the polarization.

A detailed numerical analysis furthermore reveals that the two degenerate modes have characteristics similar to the ss_b^0 mode of rectangular strips and to the LR-SPP of an infinite wide metal film. This means that the SSPPW supports long-rang polarization-independent waveguiding of plasmonic signals. The numerical analysis presented in the paper is performed by means of the finite element method [51,52], utilizing the commercial software provided by COMSOL Multiphysics on a configuration similar to the one experimentally investigated in Ref. [47]. COMSOL Multiphysics solve the eigenvalue wave equation of the electric field [Eq. (1.6)] numerically, looking for solutions on the form

$$\mathbf{E}(\mathbf{r}) = \mathbf{E}(x, y)e^{i\beta z}, \tag{2.1}$$

where here β is the complex propagation constant. The analysis show, among other things, that a square gold rod of core size 200×200 nm^2 embedded in a polymer

of benzocyclobutene (BCB) supports plasmonic guiding for both polarizations with a propagation length of approximately 3 mm. For more details I refer to the paper presented in App. A.

2.3 Gap plasmon polariton based waveguides

The next paper presented in this thesis focus on scaling properties of different SPP waveguides which all offer two dimensional mode confinement and guiding of the PP modes by means of dielectric gaps between metallic surfaces [App. B]. Utilizing the effective index approach [53,54] and an explicit expression of the propagation constant of the GPP mode, obtained for narrow gaps, normalized waveguide parameters (also known as normalized frequency or V-parameter) [55] are introduced for three different GPP based waveguides. The derived V-parameters are investigated by means of the finite element method, where again the commercial solver provided by COMSOL Multiphysics is used. Eq. (1.6) is solved looking for solutions on the form of Eq. (2.1). The three different GPP based waveguides under consideration in the paper are depicted in Fig. 2.2. The idea with all three waveguides is to exploit

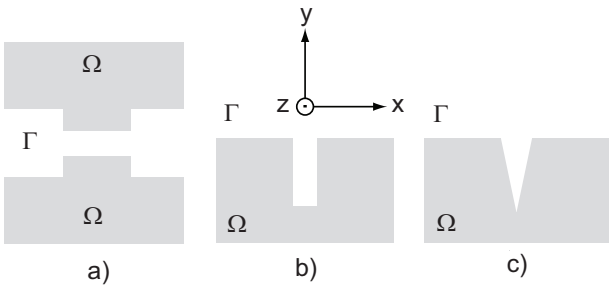

Figure 2.2: The three different waveguides under consideration in the paper presented in App. B. Lossy metal regions Ω are surrounded by lossless dielectrics Γ. All three waveguides offer two dimensional confinement of the mode in the cross section perpendicular to the direction of propagation (the xy plane). The direction of propagation is along the z axis. a) SPP gap waveguide where the field is confined to the domain between the two ridges. b) SPP trench waveguide where the field is confined in the trench. c) SPP V-groove waveguide where the field is confined in the bottom of the groove.

the fact that the mode index of a GPP mode propagating in a dielectric between two parallel metal surfaces increases when the gap is narrowed [see Fig. 1.4 a)]. This can be utilized to achieve two dimensional lateral confinement in plasmonic waveguides. In analogy with the confinement of light in a high index core of an optical fiber, the electromagnetic field of the guided GPP modes of all three waveguides are laterally confined to dielectric gaps between the closest metal surfaces. In the first waveguide configuration [Fig. 2.2 a)] the field is therefore confined and guided along the narrow gap region between the two surfaces. In the second configuration [Fig. 2.2 b)] it is confined and guided in the trench, and in the last configuration [Fig. 2.2 c)] it is confined and guided along the bottom of the groove. All three waveguides in Fig. 2.2 are known and their waveguiding properties have been analyzed before. a) was named SPP gap waveguide and analyzed in Refs. [56,57], and trench waveguides

have been analyzed in Refs. [54,58,59]. V-groove waveguides have been studied extensively both theoretically [58,60–63,54] and experimentally [37,64–66]. Recently fabrication and characterization of V-groove based plasmonic waveguide components, such as Y-splitters, Mach-Zehnder interferometers and waveguide ring resonators have been reported [37]. Guiding of electromagnetic fields by means of channels cut into an otherwise planar metal surface, as in configuration a) and b), was first proposed in Ref. [58]. In Ref. [58] the authors neglected retardation effects and the resulting electrostatic modes were termed channel plasmons. Later the work was extended to include retardation effects [60] and the modes obtained were named channel polaritons. Nowadays however, the plasmonic modes guided by channels cut into metal surfaces are most commonly referred to as channel plasmon polaritons (CPPs) and the waveguides are referred to as CPP waveguides [63,65,66].

The V-parameter, which we consider in the paper [App. B], characterizes the mode field confinement. Using these V-parameters to design waveguides, we demonstrate by means of finite element simulations that plasmonic waveguides of the same type (SPP gap, trench, or V-groove), with the same V-parameter, but with different dimensions and operating at different wavelengths, exhibit very similar normalized field confinements. The general idea of the paper is that the derived expressions for the V-parameters of the GPP based waveguides can be used as practical guidelines in order to provide a simple way to design GPP based waveguides which e.g. can operate within a specified wavelength range and at the same time e.g. ensure a well confined single mode propagation far from cutoff. Simple design criteria for different plasmonic waveguides allowing for two dimensional mode field confinement is of great practical interest, because, the design of plasmonic waveguides with specific properties in general is a complicated task which requires sophisticated and time-consuming computational techniques, see e.g. [50,57,67,60,56,61–63].

In a very recent work [66] the derived V-parameter for V-grooves has been used to design plasmonic candle structures, that can be used for radiation nanofocusing. The nanofocus is obtained by means of CPPs propagating along subwavelength metal grooves that are tapered synchronously in depth and width. An estimated field intensity enhancement of $\sim$90 is shown directly using near-field microscopy. The trick to obtain a good nanofocus by means of CPPs is to taper the channel in such a way that the V-parameter is kept constant. If this is case, the waveguide mode scales in size along with the V-groove cross section, and a tight nanofocus of the electromagnetic energy can be obtained when the size of the channel narrows down [66].

Chapter 3

Metallic nanostructures as resonators

3.1 Introduction

This chapter presents the work made on resonant metallic nanostructures. Such structures are interesting from an optical point of view because of the possibility of strongly enhanced local and scattered fields which make the structures good candidates for applications within e.g. spectroscopy and sensing [13]. As a consequence of excitation of PP modes at the metal-dielectric interfaces when illuminated with light, and the spatial confinement provided by the nanostructures, resonances of the electromagnetic field can be built up. One of the most important features of PP resonances in metallic nanostructures is that the specific resonance wavelength to a large extent can be tuned by means of the geometrical parameters of the structures. Recently the resonant optical properties of metallic nanowires have attracted some attention [68–71], and it has also been suggested that such wires can be used for optical antennas which can be much smaller than the wavelength of the light considered [72, 73]. Squeezing of light into nanometer thin dielectric cavities between metallic structures and associated scattering resonances has also been considered [74, 75].

Within this PhD project sub-micron wide and nanometer thin metal strip resonators have been studied in various configurations [Apps. C - E]. The metal strips are treated as two dimensional structures and considered invariant under translation along the last spatial dimension. Resonant scattering properties of such structures have been studied both for single strips [36, 23, 76–79], for two strips separated by a small dielectric gap [23, 80], and in configurations where a strip (or an assembly of strips) is coupled to a thin metal film [81–85]. Schematics of different resonators involving metal strips which have been studied within this PhD project are depicted in Fig. 3.1. As noted in Chap. 1, the physics of the scattering resonances of metallic nano-strips has recently been related to excitation of SR-SPPs (or GPPs in the case of gap PP based resonators) [36, 76, 80]. As in the case of a thin metal film, SR-SPPs, propagating along the x direction, are supported by a metal strip. However, as the metal strip has a finite width, the SR-SPP mode will, because of its strongly bound nature, be efficiently reflected when it reaches the terminations (along the x-axis) of the strip, and as a consequence of constructive interference between contour-propagating

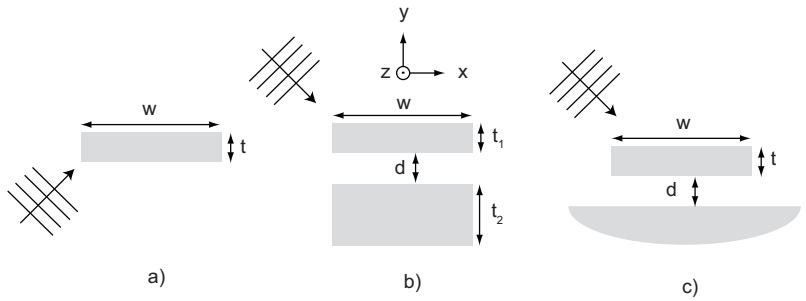

Figure 3.1: Different two dimensional strip and gap resonators. All structures are considered invariant along the z axis and are illuminated by p polarized plane wave (the electric field is in the xy plane and the magnetic field is along the z axis). Ω regions consist of lossy metals and Γ regions are lossless dielectrics. a) Metal nanostrip resonator of thickness t and width w. b) GPP resonator consisting of two metal strips both of width w and with thicknesses t_1 and t_2 separated by a dielectric gap of size d. c) Metal strip resonator of width w and thickness t placed in a distance d of an infinite surface.

SR-SPPs standing wave resonances can be built up at some wavelengths. These standing wave resonances strongly enhance not only the local field in the near-field region of the strips but also the scattered fields. A metal strip resonator can therefore be thought of as a Fabry-Pérot like resonator for SR-SPPs, where the spectral position of the resonance fulfill an equation as [78]

$$w\frac{2\pi}{\lambda}n_{pp} = m\pi - \phi, \tag{3.1}$$

where w is the width of the metal strip, n_{pp} is the real part of the mode index of the SR-SPP mode, $m = 1, 2, 3, ...$ is the order of the resonance, ϕ is the phase acquired upon reflection at a termination of the strip, and λ is the free space excitation wavelength. Eq. (3.1) can also be used for the two other GPP based resonator configurations [Figs. 3.1 b) and c)] if the real part of the mode index of the GPP mode is used for n_{pp}. From Eq. (3.1) it can be seen that if w is increased by $\Delta w = \lambda/(2n_{pp})$ ($w_f = w_i + \Delta w$) one would expect a one order higher resonance to appear at approximately the same wavelength as the resonance of the initial strip of width w_i. Fig. 3.2 presents calculations of scattering cross sections and resonant fields of silver nanostrips of different widths that verify that this is indeed true. The calculations are performed utilizing the Green's function surface integral equation method. The configurations studied are $t = 10$ nm thick silver strips of width w which are illuminated by p polarized plane waves at an angle of 45° with respect to the x axis [see Fig. 3.1 a)]. It is seen that a silver strip of $w = 100$ nm has a scattering resonance at a free space wavelength of $\lambda_0 = 538$ nm. This is also the case for strips having $w = 253$ nm and $w = 406$ nm, though the resonance of the strip with $w = 406$ nm is slightly hidden as a shoulder in the broader and larger resonance at $\lambda_0 = 762$ nm. A strip of $w = 202$ nm, however, has a resonance at $\lambda_0 = 493$ nm. The four different strip widths have been chosen carefully, in order to verify Eq. (3.1). The real part of the mode index of the SR-SPP mode supported by a silver film of thickness 10 nm at $\lambda_0 = 538$ nm is $n_{pp} = 1.756$ and thus $\lambda_{pp}/2 = \lambda_0/(2n_{pp}) \approx 153$ nm. This is exactly the difference in strip widths considered in first three calculations presented in Fig. 3.2 a) [$w = 100$, 253 and 406 nm]. The strip of $w = 202$ nm corresponds to a difference

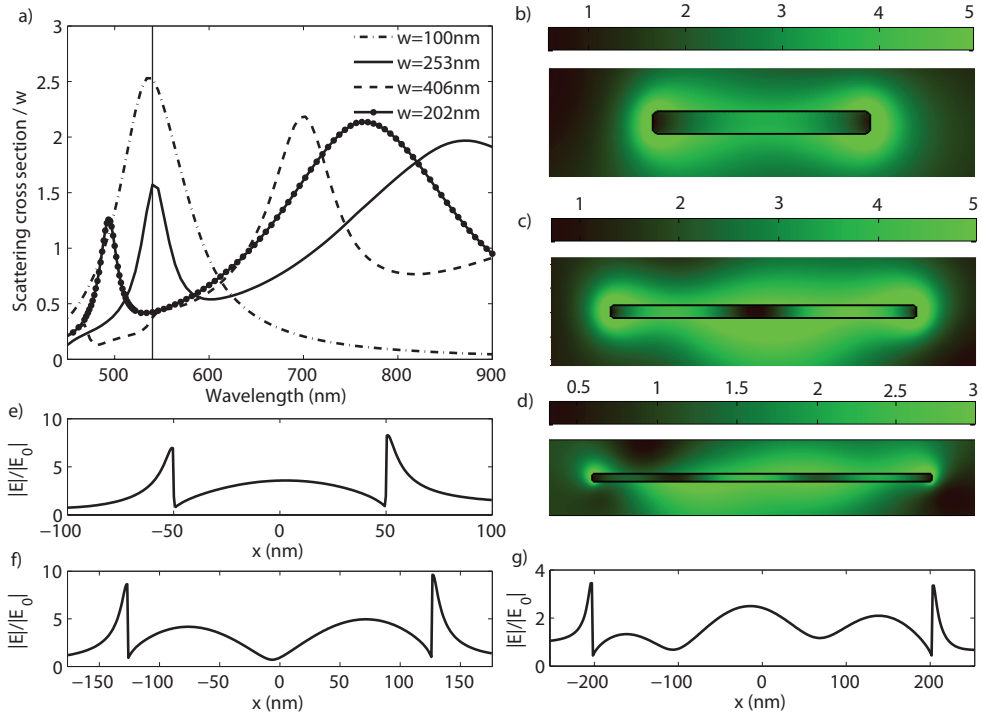

Figure 3.2: a) Scattering cross section normalized with the width of the strip as a function of the free space wavelength. The strips are t =10 nm thick silver strips of width w and are illuminated by a p polarized plane wave at an angle of 45° with respect to the x axis [see Fig. 3.1 a)]. b) Electric field magnitude for a strip with w = 100 nm at the resonance wavelength λ_0 = 538 nm. c) The same as in b) but for w = 253 nm. d) The same as in b) but for w = 406 nm. e) Cross section of the electric field magnitude through the center of the strip for w = 100 nm and at the resonance wavelength λ_0 = 538 nm. f) The same as in e) but for w = 253 nm. g) The same as in e) but for w = 406 nm. The slightly asymmetric seen in the field patterns is because an angle of incident of 45° is chosen in the calculations.

in strip width of $\lambda_{pp}/3$ and this strip does therefore not have a resonance as the other three strips at λ_0 = 538 nm. The field distributions in Figs. 3.2 b) to g) for strips with widths w = 100, 253, and 406 nm at λ_0 = 538 nm clearly illustrate the first, second, and third order nature of the resonances, respectively. In all three configurations a standing wave pattern is seen. Thus, the calculations presented clearly demonstrate that metallic nanostrips can indeed be seen as Fabry-Pérot resonators for SR-SPPs and that strips of different widths can be tuned to have scattering resonances at similar wavelengths through the knowledge of the wavelength of the SR-SPP mode supported by the strip.

Configuration b) and c) in Fig. 3.1 are examples of structures, where the resonances are built up from constructive interference between counter propagating GPP modes that are strongly bound to a dielectric gap between two strips or a strip and an infinite metal surface, respectively. Both structures have been investigated within this PhD project utilizing Green's function integral equation methods.

Three papers on resonant metallic nanostructures are included in the thesis [App. C

to E]. App. C presents a further development of the Green's function surface integral equation method which enables an exact analysis of configuration c). App. D presents a work, where configuration c) is studied for gold strips in air placed directly on a quartz substrate. In that paper the theoretical calculations are compared with carefully conducted reflection spectroscopy experiments. Lastly, App. E presents a study, where the resonances of configuration c) for a silver strip close to a silver surface are investigated for launching of SPPs. Furthermore this configuration is compared to an asymmetric configuration b) where a silver strip is close to a large block of silver with same width as the strip. Most of the results presented in the three papers are performed using the Green's function surface integral equation method. This method is presented in the next section, which also is an introduction to the paper presented in App. C.

3.2 The Green's function surface integral equation method

The Green's function surface integral equation method is an appropriate and efficient method for analysis of two dimensional scattering problems involving small metallic nanoscatterer in open infinite domains [52,86]. This is because the method allows for a good description of the boundary of the scatterers, and because the method only involves an integral over the boundary of the scatterers as the radiating boundary conditions are automatically satisfied through an appropriate choice of Green's function. A good description of the surfaces of the scatterers is crucial for scattering problems involving metallic scatterers where PP modes, which have field maxima at the metal surfaces, are responsible for most of the interesting resonant optical properties. As only the boundary of the scatterers needs to be discretized, the method is efficient from a computational point of view, especially for small scatterers such as nanostructures. The method has been successfully utilized before, both for electromagnetic scattering and eigenvalue problems and also within quantum mechanics [87–92,36,80]. Essentially the field in any closed domain is related to the field and its normal derivative at the domain boundary by means of Green's function integral equations, and different domains are related via the field boundary conditions.

If we consider a scattering problem where an arbitrary simply connected two-dimensional homogenous isotropic scatterer Ω_2 is placed in an infinite homogenous isotropic surrounding Ω_1 and it is illuminated by a strictly monochromatic ω_0 p polarized incident field ($\mathbf{H}(\mathbf{r},\omega_0) = H(\mathbf{r},\omega_0)\hat{z}$) [Fig. 3.3], scalar magnetic field Helmholtz equations for the piecewise homogenous medium can be formulated as [see Eq. (1.8) in Sec. 1.1]

$$\left[\nabla^2 + k_0^2\varepsilon_1(\omega_0)\right] H_1(\mathbf{r},\omega_0) = 0, \tag{3.2a}$$

$$\left[\nabla^2 + k_0^2\varepsilon_2(\omega_0)\right] H_2(\mathbf{r},\omega_0) = 0, \tag{3.2b}$$

which must be used within Ω_1 and Ω_2, respectively. We also define two Green's function as

$$\left[\nabla^2 + k_0^2\varepsilon_1(\omega_0)\right] g_1(\mathbf{r},\mathbf{r}',\omega_0) = -\delta(\mathbf{r},\mathbf{r}'), \tag{3.3a}$$

$$\left[\nabla^2 + k_0^2\varepsilon_2(\omega_0)\right] g_2(\mathbf{r},\mathbf{r}',\omega_0) = -\delta(\mathbf{r},\mathbf{r}'), \tag{3.3b}$$

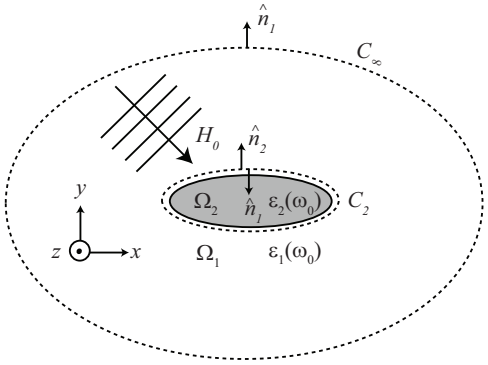

Figure 3.3: A scatterer Ω_2 in a homogenous medium Ω_1. The incident field H_0 is a strictly monochromatic p-polarized wave and is propagating in the xy plane. The system is considered invariant under translation along the z axis. The dielectric constants of the surrounding medium and the scatterer are $\varepsilon_1(\omega_0)$ and $\varepsilon_2(\omega_0)$, respectively.

which also must be used within Ω_1 and Ω_2, respectively. If we for each domain, multiply Eq. (3.3) with $H(\mathbf{r},\omega_0)$, subtract the resulting equation with Eq. (3.2) multiplied with $g(\mathbf{r},\mathbf{r}',\omega_0)$, integrate over the entire domain, and used Green's second integral identity in the plane, the surface integral equations can be set up. If the total field outside Ω_2 is furthermore divided into the incident field $H_0(\mathbf{r},\omega_0)$ and the scattered field $H_s(\mathbf{r},\omega_0)$ $[H(\mathbf{r},\omega_0) = H_0(\mathbf{r},\omega_0) + H_s(\mathbf{r},\omega_0)]$ the surface integral equations in the two regions Ω_1 and Ω_2 become

$$H(\mathbf{r},\omega_0) = \begin{cases} H_0(\mathbf{r},\omega_\mathbf{0}) + \oint_{C_2} \{H(\mathbf{s}',\omega_0)\hat{n}'\cdot\nabla' g_1(\mathbf{r},\mathbf{s}',\omega_0) \\ -g_1(\mathbf{r},\mathbf{s}',\omega_0)\hat{n}'\cdot\nabla' H_1(\mathbf{s}',\omega_0)\}\, dl' \text{ for } \mathbf{r}\in\Omega_1 \\ \\ -\oint_{C_2}\{H(\mathbf{s}',\omega_0)\hat{n}'\cdot\nabla' g_2(\mathbf{r},\mathbf{s}',\omega_0) \\ -\, g_2(\mathbf{r},\mathbf{s}',\omega_0)\frac{\varepsilon_2(\omega_0)}{\varepsilon_1(\omega_0)}\hat{n}'\cdot\nabla' H_1(\mathbf{s}',\omega_0)\Big\}\, dl' \text{for } \mathbf{r}\in\Omega_2 \end{cases} \tag{3.4}$$

where $\mathbf{s}'$ is a point on the boundary of Ω_2, $\hat{n} = \hat{n}_2 = -\hat{n}_1$ is the outward normal of Ω_2 [Fig. 3.3], the boundary condition $\hat{n}'\cdot\nabla' H_2(\mathbf{s}',\omega_0) = \varepsilon_2(\omega_0)/\varepsilon_1(\omega_0)\hat{n}'\cdot\nabla' H_1(\mathbf{s}',\omega_0)$ has been used, where H_1 and H_2 refer to the magnetic field approaching the boundary from medium Ω_1 or Ω_2, respectively, it has been used that the incident field $H_0(\mathbf{r},\omega_0)$ satisfies

$$H_0(\mathbf{r},\omega_0) = \oint_{C_\infty} \{g_1(\mathbf{r},\mathbf{s}',\omega_0)\hat{n}_1'\cdot\nabla' H_0(\mathbf{s}',\omega_0) - H_0(\mathbf{s}',\omega_0)\hat{n}_1'\cdot\nabla' g_1(\mathbf{r},\mathbf{s}',\omega_0)\}\, dl', \tag{3.5}$$

and that the scattered field satisfies

$$\oint_{C\infty} \{g_1(\mathbf{r},\mathbf{s}',\omega_0)\hat{n}_1'\cdot\nabla' H_s(\mathbf{s}',\omega_0) - H_s(\mathbf{s}',\omega_0)\hat{n}_1'\cdot\nabla' g_1(\mathbf{r},\mathbf{s}',\omega_0)\}\, dl' = 0, \tag{3.6}$$

which is true if $g_1(\mathbf{r},\mathbf{s}',\omega_0)$ satisfy the radiating boundary condition. The Green's functions are the solutions of Eq. (3.3) and are given by the zero order Hankel function of second kind $g_{1,2}(\mathbf{r},\mathbf{s}',\omega_0) = H_0^{(2)}\left(k_0\sqrt{\varepsilon_{1,2}(\omega_0)}|\mathbf{r}-\mathbf{s}'|\right)/(4i)$.

In the paper presented in App. C, we present a further development of the Green's function surface integral equation method suitable for scattering analysis of metallic nanostructures placed close to an infinite planar surface. The standard formulation of the method is not well suited for such scattering problems. This is because one would have to integrate along the surface and this boundary is usually considered to be infinite long. The idea of the further developed version of the Green's function surface integral equation method is that light scattering by an object near a planar interface can be analyzed exactly using Green's function surface integral equations form invariant with the standard formulation of the method [Eq. (3.4)]. All effects of the planar interface structure are built into the Green's function $g_1(\mathbf{r}, \mathbf{r}', \omega_0)$. Thus, the integral along the infinite surface is omitted by the use of an appropriate Green's function outside the scatterer. Related examples of Green's functions and their applications can be found in Refs. [2, 93–102]. The Green's function used inside Ω_2 is the same as in the case of a scatterer in homogenous space and is therefore analytically given by the zero order Hankel function of second kind. However, the Green's function used outside Ω_2, for a reference structure consisting of two half planes, can not be evaluated analytically. For $g_1(\mathbf{r}, \mathbf{r}', \omega_0)$ to be correctly constructed it must account for the interaction of the field with the boundary. We consider the situation where the scatterer is placed in a reference structure consisting of two half planes, where the boundary between the two half planes is located at $y = 0$ along the x axis. If both the source and observation point $\mathbf{r}'$ and $\mathbf{r}$, respectively, are above the boundary [Fig. 3.4(a)] both the direct propagation from the source to the observation

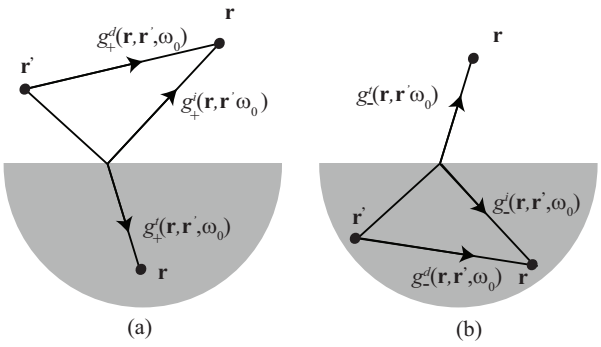

Figure 3.4: (a) Construction of the Green's function for $\mathbf{r} \notin \Omega_2$ with the source point above the boundary. (b) The same as in a) but with the source point below the boundary.

point $g_+^d(\mathbf{r}, \mathbf{r}', \omega_0)$ and the indirect propagation due to reflection from the interface $g_+^i(\mathbf{r}, \mathbf{r}', \omega_0)$ must be taken into account. If $\mathbf{r}$ is below the boundary, the propagation that has been transmitted, $g_+^t(\mathbf{r}, \mathbf{r}', \omega_0)$, must be taken into account. Thus for $y' > 0$

$$g_1(\mathbf{r}, \mathbf{r}', \omega_0) = g_+^d(\mathbf{r}, \mathbf{r}', \omega_0) + g_+^i(\mathbf{r}, \mathbf{r}', \omega_0) \text{ for } y, y' > 0, \tag{3.7a}$$

$$g_1(\mathbf{r}, \mathbf{r}', \omega_0) = g_+^t(\mathbf{r}, \mathbf{r}', \omega_0) \text{ for } y' > 0,\ y < 0, \tag{3.7b}$$

where the direct propagator $g_+^d(\mathbf{r}, \mathbf{r}', \omega_0)$ can be evaluated analytically by means of the zero order Hankel function of second kind. The propagator of the indirect propagation and the propagation that have been transmitted must, however, be constructed by

means of Sommerfeld integrals. For explicit expressions of the Sommerfeld integrals I refer to App. C. If the source point is below the boundary $y' < 0$ [Fig. 3.4(b)] the observation point can either be above or below the boundary. In that case, the Green's function is given as

$$g_1(\mathbf{r},\mathbf{r}',\omega_0) = g_-^t(\mathbf{r},\mathbf{r}',\omega_0) \text{ for } y > 0,\ y' < 0, \tag{3.8a}$$

$$g_1(\mathbf{r},\mathbf{r}',\omega_0) = g_-^d(\mathbf{r},\mathbf{r}',\omega_0) + g_-^i(\mathbf{r},\mathbf{r}',\omega_0) \text{ for } y, y' < 0. \tag{3.8b}$$

Again for explicit expressions of the Sommerfeld integrals and in general for the proof of the further developed Green's function surface integral equation method I refer to App. C.

In order to solve Eq. (3.4) we need self consistent equations. These can be obtained, by taking the limit $\mathbf{r} \to \mathbf{s}$, where $\mathbf{s}$ is a point on the boundary of Ω_2. This yield the following self-consistent equations

$$\begin{aligned}\frac{1}{2}H(\mathbf{s},\omega_0) =& H_0(\mathbf{s},\omega_0) + \mathrm{PV}\oint_{C_2}\{H(\mathbf{s}',\omega_0)\hat{n}'\cdot\nabla' g_1(\mathbf{s},\mathbf{s}',\omega_0) \\ & - g_1(\mathbf{s},\mathbf{s}',\omega_0)\hat{n}'\cdot\nabla' H_1(\mathbf{s}',\omega_0)\}\, dl', \end{aligned}\tag{3.9a}$$

$$\begin{aligned}\frac{1}{2}H(\mathbf{s},\omega_0) =& -\mathrm{PV}\oint_{C_2}\{H(\mathbf{s}',\omega_0)\hat{n}'\cdot\nabla' g_2(\mathbf{s},\mathbf{s}',\omega_0) \\ & - g_2(\mathbf{s},\mathbf{s}',\omega_0)\frac{\varepsilon_2}{\varepsilon_1}\hat{n}'\cdot\nabla' H_1(\mathbf{s}',\omega_0)\} dl,' \end{aligned}\tag{3.9b}$$

where the integrals have been rewritten as Cauchy principal values in order to handle the singularities of $\hat{n}\cdot\nabla g_{1,2}(\mathbf{s},\mathbf{s}',\omega_0)$. The singularities of $g_{1,2}(\mathbf{s},\mathbf{s}',\omega_0)$ are handled in the implementation of the method. At the singularity $\mathbf{s} = \mathbf{s}'$ the terms in the integrals involving $\hat{n}\cdot\nabla g_{1,2}(\mathbf{s},\mathbf{s}',\omega_0)$ give a contribution of $\pm H(\mathbf{s},\omega_0)/2$ for a smooth surface, where the $\pm$ depends on from which side the boundary curve is approached.

In order to implement the method, Eq. (3.9b) must be discretized and solved numerically. In the implementation of the method it is assumed that the scatterer Ω_2 is placed in the upper half plane. Eq. (3.9b) is solved numerically by subdividing the boundary curve C_2 into N segments $\{C^i\}$ on which $H(\mathbf{s},\omega_0)$ and $\hat{n}\cdot\nabla H(\mathbf{s},\omega_0)$ are sampled in the center and assumed to be constant. We therefore rewrite Eq. (3.9b) as a sum of integrals over each of the curve segments $\{C^i\}$, as

$$\frac{1}{2}H(s_i,\omega_0) = H_0(s_i,\omega_0) + \sum_{j=1}^{N}\left[H(s_j,\omega_0)\Phi_{ij}^{(1)} - \Psi_{ij}^{(1)}\hat{n}_j\cdot\nabla_j H(s_j,\omega_0)\right] \tag{3.10a}$$

$$\frac{1}{2}H(s_i,\omega_0) = -\sum_{j=1}^{N}\left[H(s_j,\omega_0)\Phi_{ij}^{(2)} - \Psi_{ij}^{(2)}\hat{n}_j\cdot\nabla_j H(s_j,\omega_0)\right] \tag{3.10b}$$

where $\hat{n}_j\cdot\nabla_j H(s_j,\omega_0)$ is the normal derivative of the magnetic field in the point s_j and the interaction matrix elements are given and evaluated as

$$\Phi_{ij}^{(1,2)} = \int_{C^j}\hat{n}'\cdot\nabla' g_{1,2}(s_i,\mathbf{s}',\omega_0)dl' \approx \sum_{p=1}^{M}\hat{n}_p\cdot\nabla_p g_{1,2}(s_i,s_p,\omega_0)l_p \tag{3.11a}$$

$$\Psi_{ij}^{(1,2)} = \int_{C^j} g_{1,2}(s_i,\mathbf{s}',\omega_0)dl' \approx \sum_{p=1}^{M} g_{1,2}(s_i,s_p,\omega_0)l_p \tag{3.11b}$$

where each curve segment is subdivided into M sub segments in order to account for the variation in $\hat{n} \cdot \nabla g_{1,2}(\mathbf{s}, \mathbf{s}', \omega_0)$ and $g_{1,2}(\mathbf{s}, \mathbf{s}', \omega_0)$, and l_p is the length of the p'th sub segment. For $s_i = s_p$ both $\Phi_{ij}^{(1,2)}$ and $\Psi_{ij}^{(1,2)}$ become singular. As described above the singularities of $\hat{n} \cdot \nabla g_2(\mathbf{s}, \mathbf{s}', \omega_0)$ and $\hat{n} \cdot \nabla g_1(\mathbf{s}, \mathbf{s}', \omega_0)$ are handled explicitly in the formulation of the self consistent surface integral equations [Eq. 3.9b] and the remaining singularities are handled in the evaluation of diagonal matrix elements. The contribution to diagonal matrix elements for $s_i = s_p$ is evaluated as

$$C_{\Phi_{ii}^{(2)}} = 0, \tag{3.12a}$$

$$C_{\Phi_{ii}^{(1)}} = \hat{n}_p \cdot \nabla_p g_+^i(s_p, s_p, \omega_0) l_p, \tag{3.12b}$$

$$C_{\Psi_{ii}^{(2)}} = \frac{1}{4i} - \frac{1}{2\pi}\left[\ln\left(\frac{k_0\sqrt{\varepsilon_2(\omega_0)}l_p}{4}\right) - 1\right], \tag{3.12c}$$

$$C_{\Psi_{ii}^{(1)}} = \frac{1}{4i} - \frac{1}{2\pi}\left[\ln\left(\frac{k_0\sqrt{\varepsilon_1(\omega_0)}l_p}{4}\right) - 1\right] + g_+^i(s_p, s_p, \omega_0) l_p, \tag{3.12d}$$

where the Hankel function at the singularity, in Eqs. (3.12c) and (3.12d), is evaluated as the average value over the p'th sub segment containing the singularity.

Setting up Eq. (3.10) for all N sampling points on C_2 yields $2N$ equations with $2N$ unknowns, which can be collected in a matrix equation and solved using standard techniques.

In the paper presented in App. C we furthermore present far-field approximations of the Green's function that enable efficient evaluation of scattering into waves propagating out of the surface plane and, in the case of a reference structure consisting of a metal-dielectric interface, evaluation of scattering into SPPs propagating along the planar surface of the reference structure. The out-of-plane scattering cross section is obtained from the scattered power through a semicircle with infinite radius in the upper half plane, and the SPP scattering cross section is obtained from the power going into SPP. In order to calculate the SPP scattering cross section the SPP contribution to the total Green's function must be extracted. This is the subject of App. A in the paper presented in App. C. For further details, tests, and applications of the further developed Green's function surface integral equation method I refer to App. C.

3.3 Metal nanostrip and gap plasmon-polariton resonators

This section is devoted to introduce two papers [App. D and E]. Both papers present an analysis of resonant light scattering from different metal strip based resonator configurations.

In App. D we present both a theoretical analysis and an experimental demonstration of resonant light scattering for gold nanostrip resonators situated on a quartz substrate. The theoretical analysis is performed using the Green's tensor area integral equation method [86], where the out-of-plane scattering cross section is calculated. For the experiments, samples were fabricated using electron beam lithography. Several samples of 5 μm long w wide and t thick nanostrips were fabricated. To

reduce cross-talk between the individual strips all samples were fabricated such that the strips are far apart [the strips are separated by 10 μm along the x dimension, see Fig. 3.1 c)]. In the experiments the fabricated samples were investigated using reflection spectroscopy, where the samples were illuminated by a p polarized plane wave under normal incidence. The theoretical modeling and the experiments were compared for two different thicknesses and several widths, and all scattering peaks observed in the experiments were also predicted by the theoretical analysis. Thus, the paper in App. D presents results where theory and experiments display an almost perfect match. For more details I refer to App. D.

The last paper [App. E] presents a theoretical analysis where two different GPP based resonator configurations are compared. The first GPP resonator analyzed consists of a nanometer thin silver strip of width w placed close to a w wide and optically thick block of silver [configuration b) in Fig. 3.1 with $t_2 \gg t_1$]. The second GPP resonator consists of a nanometer thin silver strip of width w placed close to an infinite planar silver surface [configuration c) in Fig. 3.1]. We show that the scattering resonances of both configurations have a common origin and can be related to the GPP mode supported by the gap between the metal dielectric interfaces. Standing wave resonances are built up from constructive interference between counter-propagating GPPs. As the terminations of the resonator in the configuration where the strip is close to the infinite surface are less sharp, the resonances of this structure are both red-shifted and broader than the resonances of the configuration where the strip is placed close to the silver block. In the configuration where the strip is close to the infinite silver surface two main scattering channels exist viz. scattering into waves propagating out of the surface plane and scattering of light into SPPs that propagate along the surface. Thus a metal strip resonator close to a metal surface can be utilized to launch SPPs. For small gaps the excitation of SPPs in this configuration can be quite efficient and feature a SPP scattering cross section that even exceeds the strip width. Both out-of-plane and SPP scattering can be evaluated utilizing the generalized version of the Green's function surface integral equation method presented in the section above and in App. C. For more details I refer to App. E.

This page is intentionally left blank

Chapter 4

Superlensing effects in metallic micro- and nanostructures

4.1 Introduction

The resolution of imaging using conventional optics is limited by diffraction [103, 104]. When a lens is used to construct an image, e.g. by means of a camera, fine details of the image disappear. This is because of the fundamental diffraction limit. Features smaller than approximately the wavelength of the light disappear because they are carried by evanescent waves that decay exponentially away from the source [105]. This means that when a far-field image is constructed by means of a conventional lens the subwavelength features of the source are permanently lost. When light is scattered from a specimen it contains information that specify the features of the specimen. Scattered light can be divided into two parts; evanescent waves and propagating waves. Evanescent waves carry the components with high spatial frequencies which identify the fine details of the specimen, whereas the propagating waves carry the remaining far-field information. If the information is picked up in the near-field zone of the specimen both evanescent and propagating waves can contribute to the reconstruction of an image with subwavelength resolution. This is the general idea behind the scanning near-field optical microscope which breaks the diffraction limit by means of a sharp fiber tip which is brought into the near-field zone of the specimen in order to pickup the subwavelength information of the evanescent waves [106, 107]. Other scanning probe techniques such as e.g. scanning tunneling microscopy [108, 109] and atomic force microscopy [110] which do not rely on an optical interaction are nowadays extensively used to create images of surfaces with resolutions on the atomic scale [111].

The idea of a superlens which can be used to construct an image on the subwavelength scale is attractive, both from an application and a theoretical point of view. In order to achieve subwavelength imaging such a superlens must be able, not only to cancel the phase delay of propagating waves, but it must also be able to exponentially enhance the evanescent waves in order to cancel their exponential decay. This is possible using a slab of negative refractive index material [31]. Using arguments from macroscopic electromagnetism it was proved that a thin slab of material with a refractive index of -1 surrounded by vacuum yields a perfect lens,

apparently with unlimited resolution [31]. Although it is known from microscopic electrodynamics that unlimited spatial resolution is physically incorrect, even when all evanescent waves are included [112], it has been underlined with experiments that the superlens proposed by Pendry [31] can be utilized to achieve subwavelength imaging [32,113–117]. In order to achieve the superlensing effect for both polarizations the slab must have a refractive index of -1. This can only be achieved if both ε and μ are -1 simultaneously [118]. There are no natural materials that display such exotic properties. Thus the primary challenge in the hunt for the perfect lens lies in the engineering of artificial metamaterials with the desired optical properties. At optical wavelengths, the experimental verification of Pendry's superlens was demonstrated for p polarization using a thin metal film as a superlens [32,117]. This is possible in the electrostatic limit where the two polarizations become decoupled. In Pendry's seminal paper he showed that electrostatic superlensing, for p polarization, can be achieved at the frequency where the dielectric constant of the thin slab is $\varepsilon = -1$, as the dependence of μ gets completely eliminated [31]. Likewise for s polarization electrostatic superlensing can be realized at the frequency where $\mu = -1$ because the dependence of ε gets eliminated. Thus for one polarization, electrostatic superlensing can be achieved without a negative refractive index of the lens. $\varepsilon = -1$ is exactly the surface plasmon resonance frequency of a metal, and as noted in Sec. 1.6 and by Pendry [31], there is a link between electrostatic superlensing using a thin metal film and the existence of well defined SPPs. The physical mechanism behind electrostatic superlensing using a thin metal film is resonant excitation of SPPs that help to enhance the evanescent waves across the film. At the spectral location where the size of the dielectric constant of the metal matches the dielectric constant of the surrounding material with opposite sign, the SPP dispersion relation becomes virtually flat for large parallel momentums, meaning that the band where it is possible to excite SPPs becomes very broad, which results in the superlensing effect [119,32]. Examples of metamaterials that have been investigated in connection with superlensing (here not meaning imaging with unlimited resolution, but structures that can be used for subwavelength imaging in the sense that they overcome the diffraction limit of conventional lenses) are layered metal-dielectric structures [120–125], metallic wire media [126–129] and photonic crystals [130–133].

Within this PhD project we have analyzed whether superlensing can be realized at lower frequencies by taking advantage of spoof SPPs which, as described in Sec. 1.6, emerge as electromagnetic surface modes when a perfect conductor film is perforated by an array of subwavelength holes. Holey metal films have been studied extensively since the pioneering work of Ebbesen *et al.* in 1998 [134]. Ebbesen and co-workers discovered that a metal film perforated with subwavelength holes exhibits transmission resonances that are orders of magnitudes larger than predicted by standard diffraction theory [135], and that this extraordinary optical transmission (EOT) is connected to the excitation of SPPs on the surface of the film. The physics of the EOT phenomenon was reveal a few years after its discovery, where it was clarified, using a full three-dimensional theoretical model, that the enhancement of the optical transmission is due to photon tunneling through SPPs formed on the individual surface of the holey metal film [136]. Both before and after this discovery, EOT has been studied both for a single subwavelength hole in a metal film [137–143] and for various configurations of subwavelength hole arrays [144–148].

4.2 Optical superlensing effects in holey metal films

This section is devoted to introduce the two papers of App. F and G. In these two papers, superlensing properties of holey metal films in the effective medium limit, where the unit length of the periodic hole array is much smaller than the operating wavelength, are analyzed using the multiple-scattering formalism, the modal expansion formalism, and the finite element method. As stated in the introduction the original idea was to try to take advantage of spoof SPPs on holey metal films in order to investigate if it is possible to design a spoof SPP superlens. Contrary to our expectations we found that spoof SPPs on holey metal films are not able to enhance the electromagnetic field associated with the incident evanescent waves as canonical SPPs do on an uncorrugated thin metal slab. Instead the analysis showed that within the perfect conductor and effective medium limit, and at some resonant frequencies, holey metal films can act as endoscopes, meaning that they are capable of transforming an image from the input to the output surface of the film with subwavelength resolution. A similar resonant regime, where all incoming plane waves, both propagating and evanescent, are transmitted through the structure with unit efficiency have been discovered before for wire media [130,126–129]. In Ref. [130] this regime was named *canalization*. Holey metal films, however, are much more attractive from an application point of view because they are, unlike wire media, relatively easy to fabricate.

In the paper presented in App. F, holey metal films are analyzed first in the perfect conductor approximation and at a second stage the effect of finite absorption is checked. In the first analysis presented, an analytical expression of the transmission coefficients of holey metal films is derived utilizing the multiple scattering formalism. The idea of the formalism is that the electromagnetic field is expanded in terms of plane wave eigenmodes outside the film and in terms of waveguide eigenmodes inside the film. As we assume that the metal regions are perfect conductors the fields inside those regions are zero. Inside the holes several waveguide modes will be excited by an incident field but only the fundamental waveguide mode is included in the calculation. This is because the fundamental mode is the only mode important for the transmission properties, as all higher order modes are strongly evanescent. This is a good approximation, see e.g. Ref. [136]. A similar analysis based on the modal expansion formalism is given in the paper presented in App. G.

In both papers we show that, in the perfect conductor and effective medium limit, the transmission coefficient of a holey metal film can be rewritten in a form which is invariant with the expression for the transmission coefficient of a homogenous isotropic slab. Exactly the same expression as Pendry used to demonstrate electrostatic superlensing for p polarization [31]. Pendry showed that in the electrostatic limit the z component of the wave vector both outside and inside a homogenous isotropic slab become identical independent of the parallel momentum, and in the limit of $\varepsilon = -1$ the transmission coefficient reduces to

$$t = \exp\left(-ik_z h\right) \quad \forall \quad k_{\parallel}, \tag{4.1}$$

where it is important to notice that this is true independent of the parallel momentum $k_{\parallel} = \sqrt{k_x^2 + k_y^2}$ [31]. Thus, all plane waves, both propagating and evanescent, have a transmission coefficient on the form of Eq. (4.1). This means that propagating waves

are phase corrected and evanescent waves are exponentially amplified across the lens. Hence, if the distance that the plane waves travel outside the lens is identical to the distance that they travel inside the lens an image where both propagating and evanescent waves helps in the reconstruction can be obtained. In practice, at optical wavelength, the lens/metal film has to be nanometer thin both in order to be in the electrostatic limit and also because of the absorption in the metal which eventually, when the film gets thick, will kill the enhancement of the evanescent waves [149]. As a consequence Pendry's superlens is sometimes referred to as the near-sighted superlens [150]. In Ref. [32] subwavelength imaging is experimentally demonstrated 75 nm away from the source plane at a wavelength $\lambda = 365$ nm using a 35 nm thin silver film as a superlens.

For holey metal films, a transmission coefficient on the form of Eq. (4.1) can not be realized independent of the parallel momentum. As noted above, the trick that Pendry utilized was that the z component of the wave vector both inside and outside the film become identical independent of the parallel momentum. This is not possible with holey metal films, as the z component of the wave vector inside the film is fixed by the fundamental waveguide mode. However, as described with more details in the papers [App. F and G], because the z component of the wave vector is fixed by the fundamental waveguide mode, a transmission coefficient which, depending on the resonance order m, is either 1 or -1 independent of the parallel momentum can be realized at some resonant frequencies. This means that holey metal films, with all above mentioned assumptions in mind, at these frequencies, transfer perfectly all plane waves both propagating and evanescent across the lens. Hence, they make perfect endoscopes. For more details and examples of calculations where the subwavelength imaging properties of a slit array based endoscope are investigated, first in the perfect conductor limit using the semi-analytical multiple scattering formalism and the modal expansion formalism, and second with losses included in the terahertz regime using the commercial finite element solver provided by COMSOL Multiphysics, I refer to App. F and G.

Chapter 5

Summary

This PhD thesis presents theoretical investigations of the interaction between light and metallic micro- and nanostructures. This interaction is interesting because such structures support surface plasmon polaritons (SPPs). Research of the interaction between light and metallic structures has emerged as a subfield of nano-optics and is nowadays known as plasmonics. The work presented in this thesis contributes to three topics within plasmonics; guiding of plasmon polaritons by means of metallic waveguides, resonant light scattering and field enhancement properties of metallic nanoresonators, and superlensing properties of holey metal films. Besides these three topics, a general introduction to SPPs and their fundamental properties is given. After some general remarks on the theoretical foundation, SPPs are defined, the criteria for their existence is discussed, and their fundamental properties for planar metal-dielectric interfaces and in simple metallic nanostructures are presented.

Concerning the first topic, theoretical investigations have been made using effective index modeling and finite element analysis. All finite element calculations are made by utilizing the commercial solver provided by COMSOL Multiphysics. Two papers are presented. The first paper presents a theoretical analysis of a square metal rod waveguide, where it is shown that such a plasmonic waveguide is unique because it supports propagation of long-range SPPs for both polarizations. A common drawback for most plasmonic waveguides is that they only allow for propagation of SPPs for one polarization. Based on the symmetry of the square rod waveguide a schematic overview of the modes supported is presented, and it is shown that all fundamental modes can be constructed from the coupling of the corner modes supported by the individual corners of the square metal rod. In the second paper scaling rules for gap plasmon based waveguides are presented. A normalized waveguide parameter (or V-parameter) is introduced for three different gap plasmon based waveguides; a SPP gap, a trench, and a V-groove waveguide. Utilizing finite element simulations it is demonstrated that two waveguides of the same type and with same V-parameter, but with different dimensions and operating at different wavelengths exhibit very similar field confinements. Thus, the introduced V-parameters provide a means to design plasmonic waveguides without advanced numerical modeling.

Concerning the second subject, resonant light scattering and field enhancement

properties of metallic resonators, theoretical investigations utilizing Green's function integral equation methods are presented, and experiments utilizing reflection spectroscopy are performed for verification. Three papers have been included in the thesis. The first paper presents a further development of the Green's function surface integral equation method for theoretical analysis of scatterers close to a metal surface. It is shown how the choice of an appropriate Green's function makes it possible to analysis scatterers close to planar interfaces with a set of integral equations which are form invariant with the equations used if the scatterers are placed in homogenous reference media. An approach for calculating the Green's function is presented along with far-field approximations that enable efficient evaluation of scattering out of the surface plane and, in case of a metal surface, scattering into SPPs that propagate along the metal surface. In the second paper we present both a theoretical analysis and an experimental demonstration of resonant light scattering from metal nanostrips on quartz substrates. The samples are fabricated using electron-beam lithography, the experiments are performed utilizing reflection spectroscopy, and the theoretical modeling is made using the Green's tensor area integral equation method. Theory and experiments are compared and found in a good agreement. In the last paper presented, the Green's function surface integral equation method is used to analyze two different resonator configurations. A metal nanostrip close to either a metal surface or a metal block. It is shown that the resonances of both structures occur due to constructive interference between counter-propagating GPPs which form standing waves in the gap for certain wavelengths. In the configuration where the nanostrip is close to a metal surface, light can, besides from scattering out of the surface plane, scatter into SPPs that propagate along the metal surface. These two scattering channels are evaluated separately and it is shown that, even though the out-of-plane scattering is dominating, scattering into SPPs can be very efficient for small gaps ($\sim$ 10 nm) and feature a cross section that at resonance even exceeds the strip width.

Concerning the third and last subject, superlensing properties of metal films, theoretical investigations using the multiple scattering formalism, the modal expansion formalism, and the finite element method are presented. Within the third topic two papers are presented. The first paper is a short overview paper which presents possible superlensing effects in holey metal films. We show that within the perfect conductor and effective medium limit and at some resonant frequencies, holey metal films make perfect endoscopes. Meaning that they are capable of transforming an image from the input to the output side of the film with subwavelength resolution. It is presented that under the above assumptions the transmission coefficient of light through a holey film is unity independent of the parallel momentum. Thus all waves, both propagating and evanescent, are transmitted with unit efficiency. Calculations presenting the subwavelength imaging properties of a 1D endoscope, based on a slit array, are given both with and without absorption in the metal included. The second paper is a more thorough paper, which presents a derivation of the transmission coefficients of holey metal film using the modal expansion formalism in details. In the paper it is furthermore illustrated how holey metal films effectively can be mapped into homogenous anisotropic films with effective optical properties controlled by the geometrical parameters of the holes. Lastly the paper presents a detailed analysis of the subwavelength imaging properties of a 1D silt array endoscope, which among other things, presents an estimate of the ultimate resolution of the 1D slit array endoscope.

Chapter 6

Resume (in Danish)

Dette ph.d. projekt præsenterer teoretiske undersøgelser af vekselvirkningen mellem lys og metalliske mikro- og nanostrukturer. Denne vekselvirkning er interessant, fordi metalliske strukturer understøtter overflade plasmon polariton bølger. Forskningen i vekselvirkningen mellem lys og metalliske strukturer er opstået som et underområde af nanooptik og kendes i dag under navnet plasmon optik (plasmonics). Arbejdet, som præsenteres i denne afhandling, bidrager til tre emner indenfor plasmon optik; ledning af plasmon polaritoner med metalliske bølgeledere, resonant lysspredning og feltforstærkningsegenskaber af metalliske nanoresonatorer og til sidst superlinse egenskaber af tynde metal film med små huller i. Udover disse tre emner gives der en generel introduktion til overflade plasmon polaritoner og deres fundamentale egenskaber. Efter nogle generelle bemærkninger omkring det teoretiske fundament, defineres overflade plasmon polaritoner, deres eksistenskriterium diskuteres og deres fundamentale egenskaber præsenteres for plane overflader samt for simple metalliske nanostrukturer.

Indenfor det første emne, metalliske bølgeledere, er der lavet teoretiske undersøgelser med effektiv indeks metoden og finite element metoden. Alle finte element beregninger er lavet med det kommercielle program COMSOL Multifysik. To artikler er skrevet og publiceret. I den første artikel præsenteres en teoretisk analyse af en kvadratisk metallisk bølgeleder. Det vises, at denne plasmon optiske bølgeleder er unik, idet den kan lede langtrækkende overflade plamon polaritoner for begge polarisationer. En fælles svaghed for mange plasmon optiske bølgeledere er, at de kun tillader udbredelse for en polarisation. Baseret på symmetrierne af bølgelederen præsenteres et skematisk overblik over de bølgetilstande, som bølgelederen understøtter og det vises, at de fundamentale bølgetilstande kan konstrueres ved at koble hjørne plasmon bølgetilstandene, som de fire individuelle hjørner af bølgelederen understøtter. I den anden artikel præsenteres skaleringsregler for gab plasmon baserede bølgeledere. Normaliserede bølgeleder parametre (også kendt som V parametre) introduceres for tre forskellige bølgeledere; en gab overflade plasmon polariton bølgeleder, en rektangulær grøft bølgeleder og en V bølgeleder. Ved hjælp af finite element simuleringer demonstreres det, at to bølgeledere af samme type og med samme V parameter, men med forskellige dimensioner og arbejdsbølgelængde, har stort set ens normaliserede

feltfordelinger. Dette betyder at de introducerede V parametre kan bruges til at designe plasmon optiske bølgeledere i forskellige størrelser med specifikke feltfordelinger uden, at komplicerede og tidstunge numeriske beregninger behøves.

I forbindelse med det andet emne, resonant lysspredning og feltforstærkningsegenskaber af metalliske resonatorer, præsenteres teoretiske undersøgelser lavet med Greens funktion integralligningsmetoder og eksperimenter lavet med refleksionsspektroskopi. Tre artikler er inkluderet i afhandlingen. I den første artikel præsenteres en yderligere udvikling af Greens funktion overflade integralligningsmetoden, som kan anvendes til at analysere lysspredning fra en spreder, som er placeret tæt på en metal overflade. Det vises, at man ved at vælge en hensigtsmæssig Greens funktion kan undersøge en spreder tæt på en overflade med integralligninger, som er forminvariante med dem, som bruges til at analysere en spreder placeret i et homogent medie. Der præsenteres en fremgangsmåde til at beregne denne Greens funktion og der præsenteres fjernfeltsapproksimationer, som muliggør en effektiv evaluering af både ud af planen spredningen og, i tilfældet hvor sprederen er tæt på en metal overflade, spredningen ind i overflade plasmon polaritoner, som udbreder sig langs overfladen. I den anden artikel præsenteres både en teoretisk analyse og en eksperimentel demonstration af resonant lysspredning fra guld nanostriber på glassubstrater. Prøverne er lavet ved hjælp af elektronstråle litografi, eksperimenterne er lavet ved hjælp af refleksionsspektroskopi, og beregninger er lavet ved hjælp af Greens tensor areal integralligningsmetoden. En sammenligning af beregningerne og eksperimenterne viser, at der er god overensstemmelse mellem de beregnede og de målte spredningstværsnit. I den tredje artikel, som præsenteres, bruges Greens funktion overflade integralligningsmetoden til at analysere to forskellige resonator konfigurationer; en metalstribe tæt på enten en metal overflade eller en metal blok. I artiklen vises, at den resonante lysspredning i begge konfigurationer kan relateres til konstruktiv interferens mellem fremad og bagud løbende gab plasmon polaritoner, som for visse bølgelængder danner stående bølger i gabet. I konfigurationen hvor striben er tæt på en metal overfalde, kan lys både blive spredt ud af planen men også ind i overflade plasmon polaritoner, som udbreder sig langs metal overfladen. I artiklen bliver disse to spredningskanaler evalueret separat, og det vises, at selvom ud af planen spredningen dominerer for de valgte parametre, så kan spredningen ind i overflade plasmon polaritoner være meget kraftig, især for små gab ($\sim$10 nm), hvor overflade plasmon polariton spredningstværsnittet kan overgå bredden af striben.

I forbindelse med det tredje og sidst emne, superlinse egenskaber af metalliske film med små huller i, præsenteres to artikler. Den første artikel er en kort artikel, som præsenterer superlinse egenskaberne af metal film med små huller i, på et overordnet plan. Det vises, at en perfekt ledende metal film med huller, som er meget små i forhold til bølgelængden af lyset, kan virke som et perfekt endoskop ved bestemte frekvenser. Dette betyder, at en hullet metal film er i stand til at overføre et billede fra den ene side til den anden side af filmen med en opløsning, som bryder diffraktionsgrænsen. I artiklen vises det, at under de ovenstående forudsætninger bliver transmissionskoefficienten for lys igennem en hullet metal film $t = 1$ for alle bølgevektorer. Dette betyder, at alle plane bølger, både propagerende og eksponentielt aftagende, transmitteres igennem filmen med en effektivitet på 1. Den anden artikel er en mere dybdegående artikel, som i detaljer præsenter, hvordan transmissionskoefficienterne for lys igennem hullede metal film udledes. Ydermere vises det i artiklen, hvordan

hullede metal film effektivt kan erstattes med en homogen anisotropisk film, hvor de effektive optiske egenskaber er bestemt af de geometriske dimensioner af hullerne i metal filmen. Til sidst i artiklen gives en detaljeret gennemgang af afbildningsegenskaberne af et en-dimensionalt endoskop, hvor der blandt andet gives et bud på den maksimale opløsningsevne af endoskopet.

This page is intentionally left blank

Chapter 7

List of publications

Papers in peer-reviewed journals

1: J. Jung, T. Søndergaard, and S. I. Bozhevolnyi, "Theoretical analysis of square surface plasmon-polariton waveguides for long-range polarization-independent waveguiding", Phys. Rev. B **76**, 035434 (2007).

2: S. I. Bozhevolnyi and J. Jung, "Scaling for gap plasmon based waveguides", Opt. Express 16, 2676–2684 (2008).

3: J. Jung and T. Søndergaard, "Green's function surface integral equation method for theoretical analysis of scatterers close to a metal interface", Phys. Rev. B **77**, 245310 (2008).

4: T. Søndergaard, J. Jung, S. I. Bozhevolnyi, and G. Della Valle, "Theoretical analysis of gold nano-strip gap plasmon resonators", New J. of Phys. **10**, 105008 (2008).

5: J. Jung, T. Søndergaard, and S. I. Bozhevolnyi, "Gap plasmon-polariton nanoresonators: Scattering enhancement and launching of surface plasmon polaritons", Phys. Rev. B **79**, 035401 (2009).

6: J. Jung, T. Søndergaard, J. Beermann, A. Boltasseva, and S. I. Bozhevolnyi, "Theoretical analysis and experimental demonstration of resonant light scattering from metal nanostrips on quartz", J. Opt. Soc. Am. B **26**, 121–124 (2009).

7: J. Jung, F. J. Garcia-Vidal, L. Martin-Moreno, and J. B. Pendry, "Holey metal films make perfect endoscopes", Phys. Rev. B **79**, 153407 (2009).

8: J. Jung, L. Martin-Moreno, and F. J. Garcia-Vidal, Transmission properties of holey films: effective medium theory and superlensing effects, *New J. of Phys.*, in review (2009).

Peer-reviewed conference papers

1: A. Boltasseva, K. Leosson, T. Rosenzveig, R. B. Nielsen, R. H. Pedersen, K. B. Jørgensen, I. Fernandez-Cuesta, J. Jung, T. Søndergaard, S. I. Bozhevolnyi, and A. Kristensen, "Fabrication of plasmonic waveguides for device applications", *Proceedings of the Society of Photo-Optical Instrumentation Engineers (SPIE)* **6638**, 663804 (2007).

2: J. Jung and T. Søndergaard, "Theoretical analysis of surface-plasmon-polariton resonators in free space and close to an interface", *Proceedings of the Society of Photo-Optical Instrumentation Engineers (SPIE)* **6988**, N69881 (2008).

3: T. Søndergaard, S. I. Bozhevolnyi, J. Jung, J. Beermann, G. Della Valle, and A. Boltasseva, "Slow-light plasmonic metal nano-strip resonators", *Proceedings of the Society of Photo-Optical Instrumentation Engineers (SPIE)* **7099**, G991 (2008).

Presentations

1: Oral presentation at a NABIIT meeting, University of Southern Denmark, December 2006, Odense, Denmark.

2: Poster presentation at the 13th International Conference on Integrated Optics, April 2007, Copenhagen, Denmark.

3: Poster presentation at the 3rd International Conference on Surface Plasmon Photonics, June 2007, Dijon, France.

4: Poster presentation at the Danish Optical Society annual meeting, December 2007, Risø National Laboratory, Roskilde, Denmark.

5: Poster presentation at the SPIE Photonics Europe Conference, April 2008, Strasbourg, France.

6: Poster presentation at the 4th International Conference on Surface Plasmon Photonics, June 2009, Amsterdam, The Netherlands.

References

[1] J. D. Jackson, *Classical Electrodynamics* (John Wiley & Sons, Inc., New York, 1998).

[2] L. Novotny and B. Hecht, *Principles of nano-optics* (Cambridge University Press, Cambridge, 2006).

[3] E. Palik, *Handbook of Optical Constants of Solids* (Academic, New York, 1985).

[4] P. B. Johnson and R. W. Christy, "Optical Constants of the Noble Metals," Phys. Rev. B **6**, 4370 (1972).

[5] D. Pines, "Collective Energy Losses in Solids," Revs. Mod. Phys. **28**, 184–198 (1956).

[6] H. Raether, *Surface Plasmons on Smooth and Rough Surfaces and on Gratings* (Springer-Verlag, New York, 1986).

[7] R. H. Ritchie, "Plasma Losses by Fast Electrons in Thin Films," Phys. Rev. **106**, 874–881 (1957).

[8] D. L. Mills and E. Burstein, "Polaritons: the electromagnetic modes of media," Rep. Prog. Rhys. **37**, 817–926 (1974).

[9] A. Sommerfeld, "Fortpffanzung elektrodynamischer Wellen an einem zylindnschen Leiter," Ann. Physik and Chemie **67**, 233–290 (1899).

[10] J. Zenneck, "Über die Fortplfanzung ebener elektromagnetischer Wellen längs einer ebenen Leiterfläche und ihre Beziehung zur drahtlosen Telegraphie," Ann. Physik **23**, 846–866 (1907).

[11] A. Sommerfeld, "Über die Ausbreitung der Wellen in der drahtlosen Telegraphie," Ann. Physik **28**, 665–736 (1909).

[12] V. M. Agranovich and A. A. Maradudin, *Surface polaritons - Electromagnetic Waves at surface and Interfaces* (North-Holland, New York, 1982).

[13] S. Lal, S. Link, and N. J. Halas, "Nano-optics from sensing to waveguiding," Nature Phot. **1**, 641–648 (2007).

[14] W. Murray and W. L. Barnes, "Plasmonic Materials," Adv. Mater. **19**, 3771–3782 (2007).

[15] W. L. Barnes, A. Dereux, and T. W. Ebbesen, "Surface plasmon subwavelength optics," Nature **424**, 824–830 (2003).

[16] E. Ozbay, "Plasmonics: Merging Photonics and Electronics at Nanoscale Dimensions," Science **311**, 189–193 (2006).

[17] W. L. Barnes, "Surface plasmon-polariton length scales: a route to subwavelength optics," J. Opt. A: Pure Appl. Opt. **8**, S87–S93 (2006).

[18] A. Otto, "Excitation of Nonradiative Surface Plasma Waves in Silver by the method of Frustrated total reflection," Z. Phys. **216**, 398–410. (1968).

[19] E. Kretschmann and H. Raether, "Radiative decay of nonradiative surface plasmons excited by light," Z. Naturforsch. **23**, 2135 (1968).

[20] J. J. Burke, G. I. Stegeman, and T. Tamir, "Surface-polariton-like waves guided by thin, lossy metal films," Phys. Rev. B **33**, 5186 (1986).

[21] E. N. Economou, "Surface Plasmons in Thin Films," Phys. Rev. **182**, 539 (1969).

[22] S. A. Maier and H. A. Atwater, "Plasmonics: Localization and guiding of electromagnetic energy in metal/dielectric structures," J. Appl. Phys. **98**, 1–10. (2005).

[23] S. I. Bozhevolnyi and T. Søndergaard, "General properties of slow-plasmon resonant nanostructures: nano-antennas and resonators," Opt. Express **15**, 10869 (2007).

[24] R. Sambles, A. Hibbins, and M. Lockyear, "Manipulating microwaves with spoof surface plasmons," SPIE Newsroom (2009). DOI: 10.1117/2.1200902.1532.

[25] A. I. Fernandez-Dominguez, L. Martin-Moreno, F. J. Garcia-Vidal, S. R. Andrews, and S. A. Maier, "Spoof Surface Plasmon Polariton Modes Propagating Along Periodically Corrugated Wires," IEE J. Quantum Elec. **14**, 1515 (2008).

[26] G. Goubau, "Surface waves and their application to transmission lines," J. Appl. Phys. **21**, 1119 (1950).

[27] D. L. Mills and A. A. Maradudin, "Suface corrugation and surface-polariton binding in the infrared frequency range," Phys. Rev. B **39**, 1569 (1989).

[28] J. B. Pendry, L. Martin-Moreno, and F. J. Garcia-Vidal, "Mimicking Surface Plasmons with Structed Surfaces," Science **305**, 847 (2004).

[29] F. J. Garcia-Vidal, L. Martin-Moreno, and J. B. Pendry, "Surface with holes in them: new plasmonic metamaterials," J. Opt. A: Pure Appl. Opt. **7**, 97–101 (2005).

[30] A. P. Hibbins, B. J. Evans, and J. R. Sambles, "Experimental verification of designer surface plasmons," Science **308**, 670–672 (2005).

[31] J. B. Pendry, "Negative Refraction Makes a Perfect Lens," Phys. Rev. Lett. **85**, 3966–3969 (2000).

[32] N. Fang, H. Lee, C. Sun, and X. Zhang, "Sub-Diffraction-Limited Optical Imaging with a Silver Superlens," Science **308**, 534–537 (2005).

[33] A. V. Zayats and I. I. Smolyaninov, "Near-field photonics: surface plasmon polaritons and localized surface plasmons," J. Opt. A: Pure Appl. Opt. **5**, 16–50. (2003).

[34] L. Lorenz, "Lysbevaegelsen i og uden for en af plane Lysbolger belyst Kugle," Det Kongelige Danske Videnskabernes Selskabs Skrifter **6**, 1–62. (1890).

[35] G. Mie, "Beiträge zur Optik trüber Medien, speziell kolloidaler Metallösungen," Ann. Physik **25**, 377–445 (1908).

[36] T. Søndergaard and S. Bozhevolnyi, "Slow-plasmon resonant nanostructures: Scattering and field enhancement," Phys. Rev. B **75**, 073402 (2007).

[37] S. I. Bozhevolnyi, V. S. Volkov, E. Devaux, J.-Y. Laluet, and T. W. Ebbesen, "Channel plasmon subwavelengthwaveguide components including interferometers and ring resonators," Nature Lett. **440**, 508–511 (2006).

[38] J. A. Conway, S. Sahni, and T. Szkopek, "Plasmonic interconnects versus conventional interconnects: a comparison of latency, cross-talk and energy costs," Opt. Express **15**, 4474–4484 (2007).

[39] P. Berini, "Plasmon-polariton modes guided by a metal film of finite width," Opt. Lett **24**, 1011–1013 (1999).

[40] P. Berini, "Plasmon-polriton waves guided by thin lossy metal films of finite width: Bound modes of symmetric structures," Phys. Rev. B **61**, 10484–10503 (2000).

[41] P. Berini, "Plasmon-polriton modes guided by a metal film of finite width bounded by differnt dielectrics," Opt. Express **7**, 329–335 (2000).

[42] S. J. Al-Bader, "Optical Transmission on Metallic Wires - Fundamental Modes," IEEE J. Ouantum Electron. **40**, 325–329 (2004).

[43] A. Boltasseva, T. Nikolajsen, K. Leosson, K. Kjaer, M. S. Larsen, and S. I. Bozhevolnyi, "Integrated Optical Components Utilizing Long-Range Surface Plasmon Polaritons," IEE J. Lightwave Technol. **23**, 413–422 (2005).

[44] T. Nikolajsen, K. Leosson, and S. I. Bozhevolnyi, "In-line extinction modulator based on long-range surface plasmon polaritons," Opt. Commun. **244**, 455–459 (2005).

[45] S. I. Bozhevolnyi, T. Nikolajsen, and K. Leosson, "Integrated power monitor for long-range surface plasmon polaritons," Opt. Commun. **255**, 51–56 (2005).

[46] R. Charbonneau, N. Lahoud, G. Mattiussi, and P. Berini, "Demonstration of integrated optics elements based on long-ranging surface plasmon polaritons," Opt. Express **13**, 977–983 (2005).

[47] K. Leosson, T. Nikolajsen, A. Boltasseva, and S. I. Bozhevolnyi, "Long-range surface plasmon polariton nanowire waveguides for device applications," Opt. Express **14**, 314–319 (2006).

[48] D. F. P. Pile, T. Ogawa, D. K. Gramotnev, T. Okamoto, M. Haraguchi, M. Fukui, and S. Matsuo, "Theoretical and experimental investigation of strongly localized plasmons on triangular metal wedges for subwavelength waveguiding," Appl. Phys. Lett. **87**, 061106 (2005).

[49] E. Feigenbaum and M. Orenstein, "Nano plasmon polariton modes of a wedge cross section metal waveguide," Opt. Express **14**, 8779–8784 (2006).

[50] E. Moreno, S. G. Rodrigo, S. I. Bozhevolnyi, L. Martin-Moreno, and F. J. Garcia-Vidal, "Guiding and Focusing of Electromagnetic Fields with Wedge Plasmon Polaritons," Phys. Rev. Lett. **100**, 023901 (2008).

[51] T. Ioth, *Nummerical Techniques for Microwave and Millimeter-Wave Passive Structures* (Wiley, New York, 1989).

[52] J. Jin, *The Finite Element Method in Electromagnetics* (Wiley, New York, 2002).

[53] A. B. Buckman, *Guided-Wave Photonics*, 1st ed. (Saunders College Publishing, 1992).

[54] S. I. Bozhevolnyi, "Effective index modeling of channel plasmon polaritons," Opt. Express **14**, 9467 (2006).

[55] H. Kogelnik and V. Ramaswamy, "Scaling Rules for Thin-Film Optical Waveguides," Appl. Opt. **13**, 1857–1862 (1974).

[56] K. Tanaka and M. Tanaka, "Simulations of nanometric optical circuits based on surface plasmon polariton gap waveguide," Appl. Phys. Lett. **82**, 1158 (2003).

[57] K. Tanaka, M. Tanaka, and T. Sugiyama, "Simulations of practical nanometric optical circuits based on surface plasmon polariton gap waveguides," Opt. Express **13**, 256 (2005).

[58] J. Q. Lu and A. A. Maradudin, "Channel plasmons," Phys. Rev. B **42**, 11159 (1990).

[59] I. Lee, J. Jung, J. Park, and B. Lee, "Dispersion characteristics of channel plasmon polariton waveguides with step trench type grooves," Opt. Express **15**, 16596 (2007).

[60] I. V. Novikov and A. A. Maradudin, "Channel polaritons," Phys. Rev. B **66**, 035403 (2002).

[61] D. F. P. Pile and D. K. Gramotnev, "Channel plasmon-polariton in a triangular groove on a metal surface," Opt. Lett. **29**, 1069 (2004).

[62] D. K. Gramotnev and D. F. P. Pile, "Single-mode subwavelength waveguide with channel plasmon-polaritons in triangular grooves on a metal surface," Appl. Phys. Lett. **85**, 6323 (2004).

[63] E. Moreno, F. J. Garcia-Vidal, S. G. Rodrigo, L. Martin-Moreno, and S. I. Bozhevolnyi, "Channel plasmon-polaritons: modal shape, dispersion, and losses," Opt. Lett. **31**, 3447 (2006).

[64] S. I. Bozhevolnyi, V. S. Volkov, E. Devaux, and T. W. Ebbesen, "Channel Plasmon-Polariton Guiding by Subwavelength Metal Grooves," Phys. Rev. Lett. **95**, 046802 (2005).

[65] V. S. Volkov, S. I. Bozhevolnyi, E. Devaux, J.-Y. Laluet, and T. W. Ebbesen, "Wavelength Selective Nanophotonic Components Utilizing Channel Plasmon Polaritons," Nano Lett. **7**, 880 (2007).

[66] V. S. Volkov, S. I. Bozhevolnyi, S. G. Rodrigo, L. Martin-Moreno, F. J. Garcia-Vidal, E. Devaux, J.-Y. Laluet, and T. W. Ebbesen, "Nanofocusing with Channel Plasmon Polaritons," Nano Lett. **9**, 1278 (2009).

[67] T. Holmgaard and S. I. Bozhevolnyi, "Theoretical analysis of dielectric-loaded surface plasmon-polariton waveguides," Phys. Rev. B **75**, 245405 (2007).

[68] H. Ditlbacher, A. Hohenau, D. Wagner, U. Kreibig, M. Rogers, F. Hofer, F. R. Aussenegg, and J. R. Krenn, "Silver Nanowires as Surface Plasmon Resonators," Phys. Rev. Lett. **95**, 257403 (2005).

[69] F. Neubrech, T. Kolb, R. Lovrincic, G. Fahsold, A. Pucci, J. Aizpurua, T. W. Cornelius, M. E. Toimil-Molares, R. Neumann, and S. Karim, "Resonances of individual metal nanowires in the infrared," Appl. Phys. Lett. **89**, 253104 (2006).

[70] K. Imura, T. Nagahara, and H. Okamoto, "Near-field optical imaging of plasmon modes in gold nanorods," J. Chem. Phys. **122**, 154701 (2005).

[71] T. Laroche and C. Girard, "Near-field optical properties of single plasmonic nanowires," Appl. Phys. Lett. **89**, 233119 (2006).

[72] P. Mühlschlegel, H.-J. Eisler, O. J. F. Martin, B. Hecht, and D. W. Pohl, "Resonant Optical Antennas," Sceince **308**, 1607 (2005).

[73] L. Novotny, "Effective Wavelength Scaling for Optical Antennas," Phys. Rev. Lett. **98**, 266802 (2007).

[74] H. T. Miyazaki and Y. Kurokawa, "Squeezing Visible Light Waves into a 3-nm-Thick and 55-nm-Long Plasmon Cavity," Phys. Rev. Lett. **96**, 097401 (2006).

[75] Y. Kurokawa and H. T. Miyazaki, "Metal-insolator-metal plasmon nanocavities: Analysis of optical properties," Phys. Rev. B **75**, 035411 (2007).

[76] T. Søndergaard and S. I. Bozhevolnyi, "Metal nano-strip optical resonators," Opt. Express **15**, 4198–4204 (2007).

[77] G. D. Valle, T. Søndergaard, and S. I. Bozhevolnyi, "Plasmon-polariton nano-strip resonators: from visible to infrared," Opt. Express **16**, 6867–6876 (2008).

[78] T. Søndergaard, J. Beermann, A. Boltasseva, and S. I. Bozhevolnyi, "Slow-plasmon resonant-nanostrip antennas: Analysis and demonstration," Phys. Rev. B **77**, 115420 (2008).

[79] G. D. Valle, T. Søndergaard, and S. I. Bozhevolnyi, "Efficient suppression of radiation damping in resonant retardation-based plasmonic structures," Phys. Rev. B **79**, 113410 (2009).

[80] T. Søndergaard and S. I. Bozhevolnyi, "Strip and gap plasmon polariton optical resonators," Phys. Stat. Sol. B **245**, 9–19 (2008).

[81] G. Lévêque and O. J. F. Martin, "Tunable composite nanoparticle for plasmonics," Opt. Lett. **31**, 2750 (2006).

[82] G. Lévêque and O. J. F. Martin, "Optical interactions in a plasmonic particle coupled to a metallic film," Opt. Express **14**, 9971 (2006).

[83] A. Christ, T. Zentgraf, S. G. Tikhodeev, N. A. Gippius, O. J. F. Martin, J. Kuhl, and H. Giessen, "Interaction between localized and delocalized surface plasmon polariton modes in a metallic photonic crystal," Phys. Stat. Sol. B **243**, 2344 (2006).

[84] A. Christ, T. Zentgraf, S. G. Tikhodeev, N. A. Gippius, J. Kuhl, and H. Giessen, "Controlling the interaction between localized and delocalized surface plasmon modes: Experiment and numerical calculations," Phys. Rev. B **74**, 155435 (2006).

[85] A. Christ, G. Lévêque, O. J. F. Martin, T. Zentgraf, J. Kuhl, C. Bauer, H. Giessen, and S. G. Tikhodeev, "Near-field-induced tunability of surface plasmon polaritons in composite metallic nanostructures," J. Microscopy **229**, 344–353 (2008).

[86] T. Søndergaard, "Modeling of plasmonic nanostructures: Green's function integral eqaution methods," Phys. Stat. Sol. B **244**, 3448–3462 (2007).

[87] D. W. Prather, M. S. Mirotznik, and J. N. Mait, "Boundary integral methods applied to the analysis of diffractive optical elements," J. Opt. Soc. Am. A **14**, 34–43 (1997).

[88] D. W. Prather, J. N. Mait, M. S. Mirotznik, and J. P. Collins, "Vector-based synthesis of finite aperiodic subwavelength diffractive optical elements," J. Opt. Soc. Am. A **15**, 1599–1607 (1998).

[89] J. Liu, B.-Y. Gu, B.-Z. Dong, and G.-Z. Yang, "Interference effect of dual diffractive cylindrical microlenses analyzed by rigorous electromagnetic theory," J. Opt. Soc. Am. A **18**, 526–536 (2001).

[90] M. K. Choi, "Numerical calculation of light scattering from a layered sphere by the boundary-element method," J. Opt. Soc. Am. A **18**, 577–583 (2001).

[91] J. Wiersig, "Boundary element method for resonances in dielectric microcavities," J. Opt. A, Pure Appl. Opt. **5**, 53–60 (2003).

[92] P. A. Knipp and T. L. Reinecke, "Boundary-element method for the calculation of electronic states in semiconductor nanostructures," Phys. Rev. B **54**, 1880–1891 (1996).

[93] L. M. Brekhovskikh, *Waves in Layered Media* (Academic, New York, 1980).

[94] L. Novotny, B. Hecht, and D. W. Pohl, "Interference of locally excited surface plasmons," J. Appl. Phys. **81**, 1798–1806 (1997).

[95] M. S. Tomaš, "Green function for multilayers: Light scattering in planar cavities," Phys. Rev. A **51**, 2545–2559 (1995).

[96] P. I. Geshev, S. Klein, T. Witting, K. Dickmann, and M. Heitschold, "Calculation of the electric-field enhancement at nanoparticles of arbitrary shape in close proximity to a metallic surface," Phys. Rev. B **70**, 075402 (2004).

[97] P. I. Geshev and K. Dickmann, "Enhanced radiation of a dipole placed between a metallic surface and a nanoparticle," J. Opt. A, Pure Appl. Opt. **8**, S161–S173 (2006).

[98] C. Hooijer, G.-X. Li, K. Allaart, and D. Lenstra, "Spontaneous Emission in Multilayer Semiconductor Structures," IEEE J. Ouantum Electron. **37**, 1161–1170 (2001).

[99] M. Paulus, P. Gay-Balmaz, and O. J. F. Martin, "Accurate and efficient computation of the Greens tensor for stratified media," Phys. Rev. E **62**, 5797–5807 (2000).

[100] M. Paulus and O. J. F. Martin, "Light propagation and scattering in stratified media: a Greens tensor approach," J. Opt. Soc. Am. A **18**, 854–861 (2001).

[101] C. Girard, A. Dereux, O. J. F. Martin, and M. Devel, "Generation of optical standing waves around mesoscopic surface structures: Scattering and light confinement," Phys. Rev. B **52**, 2889–2898 (1995).

[102] P. Gay-Balmaz and O. J. F. Martin, "Validity domain and limitation of nonretarded Green's tensor for electromagnetic scattering at surfaces," Opt. Commun. **184**, 37–47 (2000).

[103] E. Abbe, "Beiträge zur Theorie des Mikroskops und der mikroskopischen Wahrnehmung," Arch. Mikrosk. Anat. **9**, 413–468 (1873).

[104] L. Rayleigh, "Investigations in optics, with special reference to the spectroscope," Phil. Mag. **8**, 261–274 (1879).

[105] X. Zhang and Z. Liu, "Superlenses to overcome the diffraction limit," Nature materials **7**, 435–441 (2008).

[106] E. H. Synge, "A suggested method for extending the microscopic resolution into the ultramicroscopic region," Phil. Mag. **6**, 356–362 (1928).

[107] D. Pohl, W. Denk, and M. Lanz, "Optical stethoscopy: Image recording with resolution $\lambda/20$," Appl. Phys. Lett. **44**, 651–653 (1984).

[108] G. Binnig, H. Rohrer, C. Gerber, and E. Weibel, "Tunneling through a controllable vacuum gap," Appl. Phys. Lett. **40**, 178–180 (1982).

[109] G. Binnig, H. Rohrer, C. Gerber, and E. Weibel, "Surface Studies by Scanning Tunneling Microscopy," Phys. Rev. Lett. **49**, 57–61 (1982).

[110] G. Binnig, C. F. Quate, and C. Gerber, "Atomic Force Microscope," Phys. Rev. Lett. **56**, 930–933 (1986).

[111] R. Wiesendanger, *Scanning Probe Microscopy and Spectroscopy: Methods and Applications*, 1st ed. (Cambridge University Press, 1994).

[112] O. Keller, "Spatial resolution beyond the Rayleigh limit," J. Opt. A: Pure Appl. Opt. **8**, S174–S182 (2006).

[113] A. A. Houck, J. B. Brock, and I. L. Chuang, "Experimental Observations of a Left-Handed Material That Obeys Snells Law," Phys. Rev. Lett. **90**, 137401 (2003).

[114] A. N. Lagarkov and V. N. Kissel, "Near-Perfect Imaging in a Focusing System Based on a Left-Handed-Material Plate," Phys. Rev. Lett. **92**, 077401 (2004).

[115] A. Grbic and G. V. Eleftheriades, "Overcoming the Diffraction Limit with a Planar Left-Handed Transmission-Line Lens," Phys. Rev. Lett. **92**, 117403 (2004).

[116] H. Lee, Y. Xiong, N. Fang, W. Srituravanich, S. Durant, M. Ambati, C. Sun, and X. Zhang, "Realization of optical superlens imaging below the diffraction limit," New J. Phys. **7**, 255 (2005).

[117] D. O. S. Melville and R. J. Blaikie, "Super-resolution imaging through a planar silver layer," Opt. Express **13**, 2127–2134 (2005).

[118] V. G. Veselago, "The electrodynamics of substances with simultaneously negative values of ε and μ," Sov. Phys. Usp. **10**, 509–514 (1968).

[119] N. Fang, Z. Liu, T.-J. Yen, and X. Zhang, "Regenerating evanescent waves from a silver superlens," Opt. Express **11**, 682–687 (2003).

[120] S. A. Ramakrishna, J. B. Pendry, M. C. K. Wiltshire, and W. J. Stewart, "Imaging the near field," J. Mod. Opt. **50**, 1419 (2003).

[121] P. A. Belov and Y. Hao, "Subwavelength imaging at optical frequencies using a transmission device formed by a periodic layered metal-dielectric structure operating in the canalization regime," Phys. Rev. B **73**, 113110 (2006).

[122] B. Wood, J. B. Pendry, and D. P. Tsai, "Directed subwavelength imaging using a layered metal-dielectric system," Phys. Rev. B **74**, 115116 (2006).

[123] Y. Xiong, Z. Liu, and X. Zhang, "Projecting deep-subwavelength patterns from diffraction-limited masks using metal-dielectric multilayers," Appl. Phys. Lett. **93**, 111116 (2008).

[124] Z. Liu, H. Lee, Y. Xiong, C. Zong, and X. Zhang, "Far-Field Optical Hyperlens Magnifying Sub-Diffraction-Limited Objects," Science **315**, 1686 (2007).

[125] I. I. Smolyaninov, Y.-J. Hung, and C. C. Davis, "Magnifying Superlens in the Visible Frequency Range," Science **315**, 1699 (2007).

[126] P. A. Belov, Y. Hao, and S. Sudhakaran, "Subwavelength microwave imaging using an array of parallel conducting wires as a lens," Phys. Rev. B **73**, 033108 (2006).

[127] G. Shvets, S. Trendafilov, J. B. Pendry, and A. Sarychev, "Guiding, Focusing, and Sensing on the Subwavelength Scale Using Metallic Wire Arrays," Phys. Rev. Lett. **99**, 053903 (2007).

[128] S. Kawata, A. Ono, and P. Verma, "Subwavelength colour imaging with a metallic nanolens," Nat. Photonics **2**, 438–442 (2008).

[129] P. A. Belov, Y. Zhao, S. Tse, P. Ikonen, M. G. Silveirinha, C. R. Simovski, S. Tretyakov, Y. Hao, and C. Parini, "Transmission of images with subwavelength resolution to distances of several wavelengths in the microwave range," Phys. Rev. B **77**, 193108 (2008).

[130] P. A. Belov, C. R. Simovski, and P. Ikonen, "Canalization of subwavelength images by electromagnetic crystals," Phys. Rev. B **71**, 193105 (2005).

[131] P. Ikonen, P. A. Belov, C. R. Simovski, and S. Maslovski, Phys. Rev. B **73**, 073102 (2006).

[132] C. Lou, S. G. Johnson, J. D. Joannopoulos, and J. B. Pendry, "All-angle negative refraction without negative effective index," Phys. Rev. B **65**, 201104(R) (2002).

[133] P. V. Parimi, W. T. Lu, P. Vodo, and S. Sridhar, "Photonic crystals: Imaging by flat lens using negative refraction," Nature **426**, 404 (2003).

[134] T. W. Ebbesen, H. J. Lezec, H. F. Ghaemi, T. Thio, and P. A. Wolff, "Extraordinary optical transmission through sub-wavelength hole arrays," Nature **391**, 667–669 (1998).

[135] H. A. Bethe, "Theory of Diffraction by Small Holes," Phys. Rev. **66**, 163–182 (1944).

[136] L. Martin-Moreno, F. J. Garcia-Vidal, H. J. Lezec, K. M. Pellerin, T. Thio, J. B. Pendry, and T. W. Ebbesen, "Theory of Extraordinary Optical Transmission through Subwavelength Hole Arrays," Phys. Rev. Lett. **86**, 1114–1117 (2001).

[137] M. J. Lockyear, A. P. Hibbins, J. R. Sambles, and C. R. Lawrence, "Microwave Transmission through a Single Subwavelength Annular Aperture in a Metal Plate," Phys. Rev. Lett. **94**, 193902 (2005).

[138] D. E. Grupp, H. J. Lezec, T. Thio, and T. W. Ebbesen, "Beyond the Bethe Limit: Tunable Enhanced Light Transmission Through a Single Sub-Wavelength Aperture," Adv. Mater. **11**, 860–862 (1999).

[139] F. J. G. de Abajo, "Light transmission through a single cylindrical hole in a metallic film," Opt. Express **10**, 1475–1484 (2002).

[140] H. J. Lezec, A. Degiron, E. Devaux, R. A. Linke, L. Martin-Moreno, F. J. Garcia-Vidal, and T. W. Ebbesen, "Beaming Light from a Subwavelength Aperture," Science **297**, 820–822 (2002).

[141] A. Degiron, H. J. Lezec, and N. Y. T. W. Ebbesen, "Optical transmission properties of a single subwavelength aperture in a real metal," Opt. Commun. **239**, 61–66 (2004).

[142] J. A. Matteo, D. P. Fromm, Y. Yuen, P. J. Schuck, W. E. Moerner, and L. Hesselink, "Spectral analysis of strongly enhanced visible light transmission through single C-shaped nanoapertures," Appl. Phys. Lett. **85**, 648–650 (2004).

[143] F. J. Garcia-Vidal, E. Moreno, J. A. Porto, and L. Martin-Moreno, "Transmission of Light through a Single Rectangular Hole," Phys. Rev. Lett. **95**, 103901 (2005).

[144] U. Schröter and D. Heitmann, "Surface-plasmon-enhanced transmission through metallic gratings," Phys. Rev. B **58**, 15419 (1998).

[145] J. A. Porto, F. J. Garcia-Vidal, and J. B. Pendry, "Transmission Resonances on Metallic Gratings with Very Narrow Slits," Phys. Rev. Lett. **83**, 2845–2848 (1999).

[146] J. Bravo-abad, F. J. Garcia-Vidal, and L. Martin-Moreno, "Resonant Transmission of Light Through Finite Chains of Subwavelength Holes in a Metallic Film," Phys. Rev. Lett. **93**, 227401 (2004).

[147] K. L. van der Molen, K. J. K. Koerkamp, S. Enoch, F. B. Segerink, N. F. van Hulst, and L. Kuipers, "Role of shape and localized resonances in extraordinary transmission through periodic arrays of subwavelength holes: Experiment and theory," Phys. Rev. B **72**, 045421 (2005).

[148] A. Mary, S. G. Rodrigo, F. J. Garcia-Vidal, and L. Martin.Moreno, "Theory of Negative-Refractive-Index Response of Double-Fishnet Structures," Phys. Rev. Lett. **101**, 103902 (2008).

[149] Z. Liu, N. Fang, T.-J. Yen, and X. Zhang, "Rapid growth of evanescent wave by a silver superlens," Appl. Phys. Lett. **83**, 5184–5186 (2003).

[150] V. A. Podolskiy and E. E. Narimanov, "Near-sighted superlens," Opt. Lett. **30**, 75–77 (2005).

Appendix A

Phys. Rev. B **76**, 035434 (2007)

Theoretical analysis of square surface plasmon-polariton waveguides for long-range polarization-independent waveguiding

by

Jesper Jung, Thomas Søndergaard, and Sergey I. Bozhevolnyi.

This page is intentionally left blank

Theoretical analysis of square surface plasmon-polariton waveguides for long-range polarization-independent waveguiding

Jesper Jung,* Thomas Søndergaard, and Sergey I. Bozhevolnyi
Department of Physics and Nanotechnology, Aalborg University, Skjernvej 4A, DK-9220 Aalborg Øst, Denmark
(Received 8 March 2007; revised manuscript received 20 April 2007; published 26 July 2007)

Bound electromagnetic modes supported by a square metal rod embedded in a lossless dielectric medium are determined and characterized. Based on the symmetry of the waveguide configuration, a schematic overview of the supported fundamental modes is given. These fundamental modes are related to coupling between four corner modes associated with individual metal corners of the square rod waveguide. Utilizing the finite element method a numerical analysis of the waveguide is performed at telecom wavelengths (~1550 nm). The mode dispersion with the rod size, mode field orientations, profiles, and widths are presented. Unlike thin metal stripe waveguides, the square metal waveguide is shown to support long-range surface plasmon-polariton modes for both polarizations. The configuration studied is a gold core embedded in a polymer (benzocyclobutene). Surface plasmon-polariton modes of both polarizations are shown to be guided with a propagation length of approximately 3 mm for a metal core size of 200×200 nm^2. The possibility of long-range polarization-independent transmission of surface plasmon-polariton modes makes the square surface plasmon-polariton waveguide unique and a promising optical component, from which future plasmonic interconnects and circuits can benefit.

DOI: 10.1103/PhysRevB.76.035434 PACS number(s): 42.79.Gn, 42.25.Ja, 71.36.+c, 73.20.Mf

I. INTRODUCTION

The ability to transmit or direct optical signals along waveguide structures of subwavelength dimensions is crucial for the further development of integrated optics in the context of ever increasing demands for miniaturization. One way of achieving subwavelength confinement of light is by means of surface electromagnetic waves, known as surface plasmon polaritons (SPPs), propagating along an interface between a metal and a dielectric medium.[1] Over the last two decades, the research and development of different SPP waveguide configurations have considerably intensified. One of the most promising configurations studied recently, with integrated optics in mind, is a thin metal stripe (its width being much larger than its thickness) embedded in a dielectric.[2–5] This waveguide configuration offers the possibility of the mode confinement to match that of a single-mode fiber and its propagation length to extend into the millimeter range. There is, however, an important drawback, which is common for most SPP waveguide configurations, that the long-range propagation is supported only for one polarization of the electric field. A plasmonic waveguide allowing for long-range propagation of both polarizations would be a major advance in plasmonic integrated optics.

The main component of the SPP electric field is oriented perpendicular to the metal surface (due to the boundary conditions), implying thereby that when searching for the polarization-independent guiding of SPP modes, one should look at metal structures with symmetric cross sections. Indeed, experimental studies by Leosson *et al.*[6] have recently verified long-range SPP guiding along square metal rods for both polarizations. At telecom wavelengths, optical radiation was shown to propagate up to several millimeters. In this paper, the surface electromagnetic modes of square surface plasmon-polariton waveguides (SSPPWs) are determined and characterized at telecom wavelengths (~1550 nm) by means of the finite element method.[7,8] To some extent, SSPPWs have been studied theoretically by the method of lines.[9] The finite element method is known as a successful numerical technique for analyzing optical waveguide structures and has previously been utilized to characterize SPP modes in metal-clad optical waveguides[10] and to analyze gain assisted SPPs in metal slab and stripe geometries.[11]

This paper is organized as follows. In Sec. II, the waveguide structure, the SPP modes supported by the structure, and the numerical technique used in the analysis are presented. The numerical results are presented in Sec. III. The electromagnetic modes supported by a SSPPW are characterized from sub- to suprawavelength metal core sizes. The mode dispersion with the size, field orientations, and field profiles, including mode width, are presented. Lastly, the electromagnetic modes supported by the square waveguide configuration are related to the modes supported by the rectangular metal stripe configuration. Section IV presents the conclusion.

II. STRUCTURE AND NUMERICAL TECHNIQUE

A. Structure

The waveguide structure studied consists of two regions Ω and Γ. Ω is a lossy metal core with thickness t and width w. The metal core is surrounded by Γ, which is an infinite lossless dielectric material [Fig. 1(a)]. The direction of propagation is along the z axis, which is out of the paper. The metal is characterized by a complex dielectric constant ϵ_Ω, whereas the dielectric constant of the surrounding medium ϵ_Γ is real. If the width and the thickness of the metal core are identical, $t=w$, the waveguide structure is a SSPPW.

The formation of super SPP modes supported by thin metal films (metal slabs), which exhibit dispersion with film thickness, can be explained by mode coupling, due to field

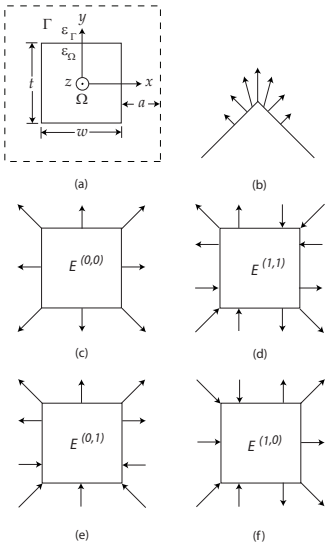

FIG. 1. (a) The waveguide structure. A lossy metal core with dielectric constant ϵ_Ω, thickness t, and width w is surrounded by a lossless dielectric material with dielectric constant ϵ_Γ. The direction of propagation is along the z axis. a is the distance between the metal-dielectric interface and the border of the computational window indicated by the outer dashed square. (b) Field orientation profile of the fundamental plasmon polariton mode supported by a single isolated corner. (c)–(f) Field orientation profiles of the possible fundamental SPP modes supported by the SSPPW configuration. The naming of the modes is according to the nomenclature described.

tunneling through the metal film, between the SPP modes guided by the two interfaces as the film becomes thin enough. In a similar way, the fundamental SPP modes supported by the SSPPW can be explained by a mode coupling of wedge or corner plasmon polariton (PP) modes supported by isolated corners [Fig. 1(b)]. Wedge modes of single isolated corners have been analyzed before.[12–16] The SSPPW configuration consists of four corners connected by four planar surfaces. One approach for determining the SPP modes supported by the SSPPW is to construct the super modes from proper combinations of the four corner modes, taking into account the symmetries of the SSPPW. As an isolated corner supports one fundamental corner mode, it is expected that the SSPPW with four corners at least supports four SPP modes. These four SPP modes will be referred to as the fundamental modes of the SSPPW. If the metal core is optically large, the four corners are far apart and there is no coupling between the four isolated corner modes. Furthermore, side modes where SPPs are propagating along each of the four planar surfaces are supported. These modes are almost zero at the corners and are localized along the sides of the metal core. Such side modes, both leaky and bound, have been analyzed for air-exposed metal stripes on glass substrates by Zia *et al.*[17] For optically large metal cores, the four fundamental modes are practically degenerate and have the mode index of a PP of a single isolated corner. As the size of the metal core decreases, the mode fields of the four corner modes start to overlap, and the degeneracy of the four fundamental modes is lifted. New modes are formed from the coupling between the four corner modes. By choosing one or the other sign (+ or −) for each corner mode, four linearly independent field combinations can be constructed (Fig. 1). The four super SPP modes are constructed from combinations of the four PP corner modes involving zero or two negative signs. Combinations with one or three negative signs are inconsistent with the overall symmetry of the system. The super modes must be symmetric or antisymmetric with respect to the x and y axes. The fundamental SPP modes supported by the SSPPW are labeled in terms of two indices. The first and second indices denote the number of nodes or sign changes in the dominant component of the electric field along the x and y axes, respectively (the y component along the x axis and the x component along the y axis). These two indices are appended as superscripts to the symbol E for the electric field. The $E^{(0,0)}$ mode [Fig. 1(c)] and the $E^{(1,1)}$ mode [Fig. 1(d)] remain unchanged after a 90° rotation around the z axis (except for a sign change in the $E^{(1,1)}$ mode). The two last modes, $E^{(0,1)}$ [Fig. 1(e)] and $E^{(1,0)}$ [Fig. 1(f)], transform into one another by a 90° rotation around the z axis. Because the square geometry of the SSPPW makes the x and the y axes interchangeable, it is evident that $E^{(0,1)}$ and $E^{(1,0)}$ are degenerate, and there is a 90° rotational symmetry around the z axis in the sum of the norm squared of $E^{(0,1)}$ and $E^{(1,0)}$. Note that it is possible to construct corner fields located on each of the four corners from a superposition of the fields of the four fundamental SSPPW modes depicted in Figs. 1(c)–1(f). Some of the super modes of the SSPPW can, in a simple manner, be related to the two super SPP modes of a thin metal film. If a metal rod is transformed into a thin and infinitely wide metal stripe, the field orientation of the $E^{(0,0)}$ mode [Fig. 1(c)] becomes similar to the field orientation of the short-range super SPP mode of a thin metal film. At the same time, the field orientation of the $E^{(0,1)}$ mode [Fig. 1(e)] becomes similar to the field orientation of the long-range SPP mode of a thin metal film. Hence, the $E^{(0,1)}$ and $E^{(1,0)}$ modes (due to the 90° rotational symmetry) can be seen as the SSPPW analogs of the long-range SPP mode of a thin metal film, while the $E^{(0,0)}$ mode can be seen as the SSPPW analog of the short-range SPP mode.

In summary, a schematic overview of the four fundamental modes supported by the SSPPW can be constructed from proper combinations of field coupling between four corner modes, taking into account the symmetries of the square waveguide structure. However, detailed information on mode dispersion, field orientation, and distribution can only be obtained from a numerical analysis of the waveguide.

It should be noted that the SPP modes of the SSPPW studied in this paper can be excited by means of end-fire or butt coupling, in which a SPP mode is excited by focusing light onto the end face of the waveguide [light incidence is along the z axis in Fig. 1(a)]. An efficient excitation can be achieved by matching the incident light field distribution (in the xy plane) to that of the SPP mode. It is thereby clear

(from symmetry considerations) that when conveniently using a linearly polarized mode of a single-mode fiber for the SSPPW excitation, only long-range $E^{(0,1)}$ and/or $E^{(1,0)}$ modes (depending on the fiber mode polarization) can be efficiently excited. The latter circumstance renders practical applications of SSPPWs for optical interconnects and integrated circuits.

B. Numerical technique

The starting point of the numerical analysis of the waveguide is the wave equation of the electric field

$$\nabla \times \nabla \times \mathbf{E} - k_0^2 \epsilon_r \mathbf{E} = 0, \tag{1}$$

where $k_0 = \omega\sqrt{\epsilon_0 \mu_0}$ is the vacuum wave number and ϵ_r is the relative dielectric constant. The solutions are sought of the form

$$\mathbf{E}(x,y,z,t) = \mathbf{E}(x,y)e^{j(\beta z - \omega t)}, \tag{2}$$

where β is the (complex) phase or propagation constant.

In order to perform a finite element analysis of the waveguide structure, the infinite dielectric medium that surrounds the metal core must be truncated. This is done by placing a square computational window that surrounds enough of the waveguide, metal core, and surrounding dielectric medium for the mode field to be negligible at the computational window boundary [dashed curve in Fig. 1(a)]. The boundary of the computational window is considered as an electric wall with $\mathbf{n} \times \mathbf{E} = 0$. It is important that the distance between the metal surface and the computational window a [see Fig. 1(a)] is large in order to prevent the size of the computational window from influencing the result of the calculation. For bounded SPP modes, the mode field must be close to zero at the boundary of the computational window. The minimum size of the computational window is directly related to the SPP mode confinement. If the SPP mode is loosely confined to the metal core, the computational window must be large compared to the size of the core. Using the finite element method, the domain within the computational window is dizcretized in a mesh of small finite triangular elements. In all calculations, the number of finite elements is increased until convergence of the phase constant is reached. The number of elements necessary to reach convergence is dependent on both the size of the metal core and the confinement of the SPP mode and changes from 15.000 to 50.000. If the mode confinement is weak, the field stretches out in the dielectric medium, and more elements are often needed to achieve convergence. The mesh of the finite elements is constructed such that the concentration of elements are high in subregions where the field distribution varies rapidly. A high concentration of elements is needed close to the metal surface and especially at the four corners. All finite element calculations are made utilizing the commercial program COMSOL MULTIPHYSICS.

III. NUMERCIAL RESULTS

In all calculations, the free space wavelength λ_0 is set to 1550 nm. This wavelength is used in optical communication because the silicon dioxide used in optical fibers has a low loss around this wavelength. The dielectric constants of the two regions are set to $\epsilon_\Omega = -131.9475 + 12.65j$[9] and $\epsilon_\Gamma = 2.356\,225$,[18] which corresponds to a gold core surrounded by a dielectric polymer of benzocyclobutene (BCB). This configuration is identical to the configuration studied experimentally by Leosson *et al.*[6] First corner rounding is briefly discussed.

TABLE I. Mode index of the fundamental corner mode vs radius of curvature calculated utilizing the finite element method.

Radius of curvature (nm)	Mode index β/k_0
2	$1.5599 + 0.0026j$
5	$1.5599 + 0.0026j$
10	$1.5591 + 0.0026j$
20	$1.5585 + 0.0025j$
50	$1.5441 + 0.0011j$

A. Corner rounding

In order to investigate the effect of corner rounding, a single isolated 90° corner [Fig. 1(b)] is analyzed for different radii of curvature by means of the finite element method. The mode index of the fundamental corner PP modes is presented in Table I. The corner mode becomes less confined and has a longer propagation length as the radius of curvature is increased. However, it is seen that if the corner rounding is below 20 nm, the effect is small. In all calculations, the corners of the metal core are rounded with a radius of curvature of 10 nm. This is mainly for numerical reasons because the field tends to become singular at sharp corners, and is furthermore justified as it is practically difficult to fabricate real structures with very sharp corners.

B. Square metal waveguide

The electromagnetic modes supported by the SSPPW are characterized for both sub- and suprawavelength sizes starting at $t = w = 200$ nm and ending at 5000 nm.

1. Mode dispersion with size

Figure 2 depicts the dispersion of the real part of the mode index [$\mathrm{Re}(\beta/k_0)$], with the size of the metal core for the electromagnetic modes supported by the SSPPW. Three of the SPP modes supported by the configuration do not have a transmission cutoff as the metal core size decreases. These modes are the $E^{(0,0)}$ mode and two degenerate modes $E^{(1,0)}$ and $E^{(0,1)}$. The last of the four fundamental modes $E^{(1,1)}$ is not supported for metal core sizes below 1500 nm. For metal cores sizes above 3000 nm, a side mode is, on the other hand, supported. As the size of the metal core decreases, the real part of the mode index of the $E^{(0,0)}$ mode increases. This corresponds to the fact that the confinement of the $E^{(0,0)}$ mode increases as the size of the metal core decreases. The real part of the mode index of two degenerate modes $E^{(1,0)}$

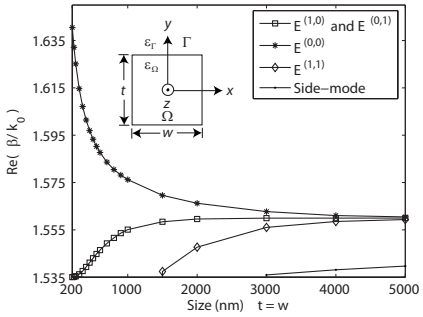

FIG. 2. The dispersion of the real part of the mode effective index of the SPP modes supported by the square waveguide with the size of the metal core.

and $E^{(0,1)}$ decreases as the size of the metal core decreases and tends asymptotically toward the refractive index of the surrounding dielectric medium. In the suprawavelength region, the four fundamental modes converge toward a four-time degenerate SPP mode with a mode index of a PP mode supported by a single isolated corner. The analysis of an isolated corner with a 10 nm radius of curvature yielded $\mathrm{Re}(\beta/k_0)=1.5591$. This value corresponds well to the value of the four fundamental modes of a SSPPW with a metal core size of 5000 nm (Fig. 2). The side mode is a mode where SPPs propagate along each of the four sides of the square metal core. The side mode has transmission cutoff for metal core sizes below approximately 3000 nm.

Figure 3 depicts the dispersion of the propagation length $L=[2\ \mathrm{Im}(\beta)]^{-1}$ with the size of the metal core. The two degenerate modes $E^{(1,0)}$ and $E^{(0,1)}$ become long range, with propagation lengths above 1 mm, when the size of the metal core is decreased below 300 nm. For a metal core size of 200 nm, the propagation length of the two degenerate modes is approximately 3 mm. 3 mm is not long range if compared to the propagation length of optical signals in standard optical fibers. However, it is long range measured in wavelengths and can be sufficient for plasmonic communication on an optical chip. The propagation length of the $E^{(0,0)}$ mode decreases as the size of the metal core decreases. If the metal core size is 200 nm, $L_{E^{(0,0)}}\approx 16$. For suprawavelength metal core sizes, the propagation lengths of the four fundamental SPP modes converge toward the propagation length of a PP mode supported by a single isolated corner with $L\approx 48\ \mu$m. The propagation length of the less confined side mode is larger than the propagation lengths of the four fundamental modes. A comparison of Figs. 2 and 3 reveals that the $E^{(1,1)}$ mode has both a lower $\mathrm{Re}(\beta/k_0)$ and a smaller propagation length than the $E^{(0,0)}$ for suprawavelength metal core sizes. This is not physically intuitive because a lower $\mathrm{Re}(\beta/k_0)$ normally implies that the mode is less confined and should therefore have a longer propagation length. This phenomenon is also observed, but not commented on, in the theoretical study of metal stripes by Berini.[2] The numerical technique utilized by Berini is the method of lines, which is another numerical approach besides the finite element method utilized in this paper. As both approaches imply the same tendency, it is not considered as an error.

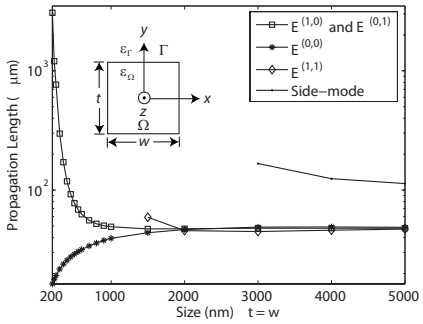

FIG. 3. The dispersion of the propagation length of the SPP modes supported by the square waveguide with the size of the metal core. The propagation length is calculated as $L=[2\ \mathrm{Im}(\beta)]^{-1}$.

The $E^{(0,0)}$ mode is the SSPPW analog of the fundamental SPP mode supported by the circular SPP waveguide, which was theoretically analyzed by Takahara *et al.*[19] With the $E^{(0,0)}$ mode, it is possible to achieve high mode confinement at the price of a high propagation loss. The $E^{(0,0)}$ mode, is therefore not suitable for plasmonic communication but could possibly be used in a SPP resonator based on slow SPP modes propagating back and forth along a thin metal wire of finite length.[20]

The $E^{(1,0)}$ and $E^{(0,1)}$ modes can be utilized for polarization-independent long-range SPP guiding. The $E^{(1,0)}$ mode is almost entirely polarized along the x axis and guides x-polarized light. The $E^{(0,1)}$ mode is polarized along the y axis and guides y-polarized light. As $E^{(1,0)}$ and $E^{(0,1)}$ are degenerate, excitation by means of end-fire or butt coupling will allow SPP guiding with the same mode index (and propagation loss) for both polarizations of the incident light. This makes the SSPPW unique because, as argued in the Introduction, metal stripe waveguides are very polarization dependent. The theoretically predicted propagation lengths of the $E^{(1,0)}$ and $E^{(0,1)}$ modes in Fig. 3 correspond well to the experimental results reported by Leosson *et al.*[6]

2. Electric field orientation in the xy plane

Arrow plots of the electric field orientation in the xy plane are presented for the four fundamental modes. The orientation of the electric field is indicated by arrows (Figs. 4–6). The length of the x (y) component of the arrow is proportional to the amplitude of the E_x (E_y) component of the electric field. The norm of the electric field is also depicted in the arrow plots. The electric field orientation of the $E^{(0,0)}$ mode (Fig. 4) has a mirror symmetry with respect to both x and y axes and is perpendicular to the metal surface along all four sides. This is in good agreement with the schematic overview of the $E^{(0,0)}$ mode presented in Fig. 1(c). Figure 5 shows how the $E^{(0,1)}$ mode has a main field polarization along the y axis. The field orientation plot of the $E^{(1,0)}$ mode is obtained by a

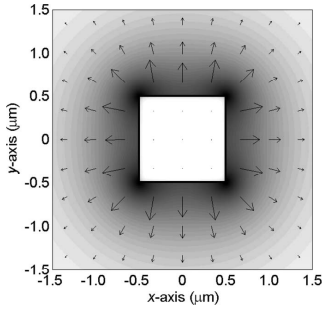

FIG. 4. Magnitude and orientation of the electric field in the xy plane of the $E^{(0,0)}$ mode for a metal core size of 1 μm.

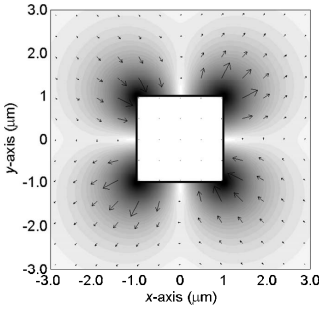

FIG. 6. Magnitude and orientation of the electric field in the xy plane of the $E^{(1,1)}$ mode for a metal core size of 2 μm.

90° rotation of the plot of the $E^{(0,1)}$ mode around the z axis. Thus, the $E^{(1,0)}$ mode has a main polarization along the x axis. The numerical results of the $E^{(0,1)}$ and $E^{(1,0)}$ modes are also in good agreement with Figs. 1(e) and 1(f). However, the numerical results show very clearly that these two degenerate modes are strongly polarized along the y and x axes, respectively. The arrow plot of the $E^{(1,1)}$ mode shows the orientation and magnitude of the electric field for a metal core size of 2 μm. This mode has a transmission cutoff for metal core sizes below approximately 1500 nm. The plot shows that the mode field (x and y components) is zero at the middle of all four sides of the metal core. As the metal core size decreases, there is not enough space along the sides to sustain these zeros, and the mode therefore has a transmission cutoff.

3. Mode width

The mode width is determined for metal core sizes below 1000 nm. The mode width $2r_w$ is defined as two times the distance from the center of the metal core to the point where the norm of the electric field has decayed to $1/e$ of its maximum value. The mode width of the $E^{(0,0)}$ is determined along the x axis. For $E^{(1,0)}$ and $E^{(0,1)}$, the mode width is determined along the x and y axes, respectively. The mode width is defined by the following equation:

$$E_{norm}(r_w) = \frac{1}{e} E_{norm}^{max}, \tag{3}$$

where E_{norm}^{max} is the maximum value of the norm of the electric field and r_w is the half of the mode width. A schematic illustration of how the mode width is estimated is depicted in the inset in Fig. 7. The mode width is illustrated by the double arrow. The solid square represents the size of the metal core. It can be seen that the skin depth of the electric field in the

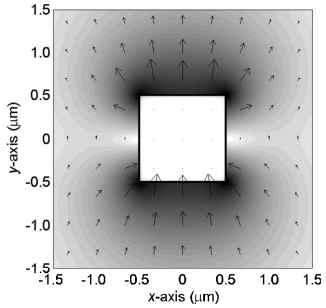

FIG. 5. Magnitude and orientation of the electric field in the xy plane of the $E^{(0,1)}$ mode for a metal core size of 1 μm. The field orientation plot of the $E^{(1,0)}$ mode is obtained by a counterclockwise rotation of 90° around the z axis, which is out of the paper.

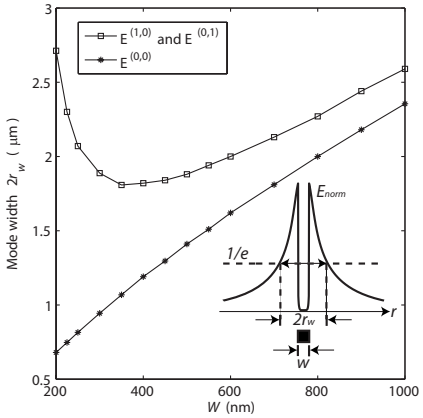

FIG. 7. Mode width versus metal core size for the $E^{(1,0)}$, $E^{(0,1)}$, and $E^{(0,0)}$ modes for metal core sizes below 1000 nm. The inset shows schematically how the mode width $2r_w$ is defined. The solid line represents the norm of the electric field along the axis by which the mode width is determined, and the dashed line is $1/e$ of the maximum of the norm of the electric field. The size of the metal core is indicated by the black square.

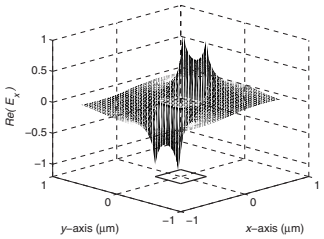

(a) Re(E_x) of the $E^{(0,0)}$ mode.

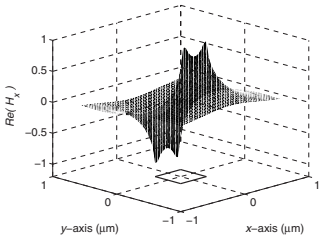

(b) Re(H_x) of the $E^{(0,0)}$ mode.

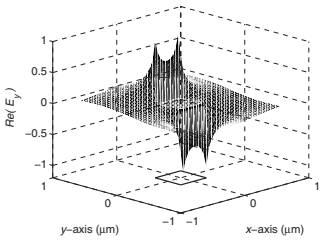

(c) Re(E_y) of the $E^{(0,0)}$ mode.

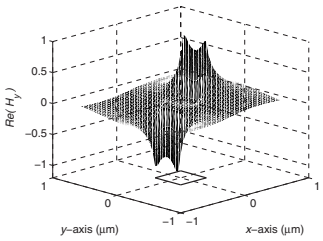

(d) Re(H_y) of the $E^{(0,0)}$ mode.

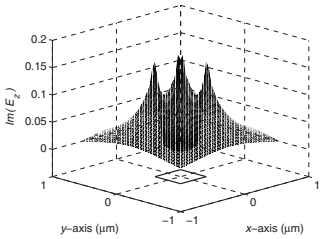

(e) Im(E_z) of the $E^{(0,0)}$ mode.

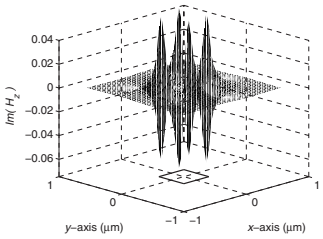

(f) Im(H_z) of the $E^{(0,0)}$ mode.

FIG. 8. Field distribution profiles of the electric and magnetic field components of the $E^{(0,0)}$ mode over a cross section of the waveguide for a metal core size of 400 nm. The electric and magnetic field components are normalized by $\max(|E_y|)=1$ and $\max(|H_x|)=1$.

metal is very small and that the electric field decays in an exponential manner in the dielectric. The mode width versus metal core size of the two degenerate modes $E^{(1,0)}$ and $E^{(0,1)}$ (Fig. 7) shows that the mode width increases rapidly when the metal core decreases below 300 nm. This indicates that the $E^{(1,0)}$ and $E^{(0,1)}$ modes are weakly confined to the metal structure when the metal core decreases below 300 nm. The mode width of the two degenerate modes has a distinct minimum at a metal core size of approximately 400 nm. Thus, the smallest mode field of the long-range modes is achieved for a metal core size of approximately 400 nm. The mode width of the $E^{(0,0)}$ mode decreases as the metal core size decreases. When the size of the metal core becomes large, the mode width of all the fundamental modes tends asymptotically toward the size of the metal core. In general, it can be seen that it is possible to tune the size of the SPP mode by choosing the right size of the metal core. From a technological point of view, this is valuable because the mode size of the SSPPW can be custom designed to match, e.g., the size of an optical fiber mode. Thus, by choosing the right size of the metal core, a good overlap with an optical fiber mode can be achieved. An optical fiber has two degenerate fundamental guided modes. In comparison, the SSPPW has four fundamental modes, but only three of them are supported for subwavelength metal core sizes. These three modes are the two degenerate long-range modes ($E^{(1,0)}$ and $E^{(0,1)}$) and the

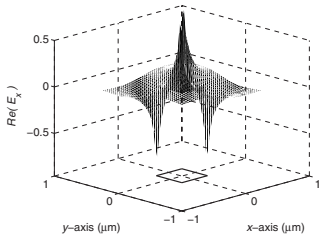

(a) Re(E_x) of the $E^{(0,1)}$ mode.

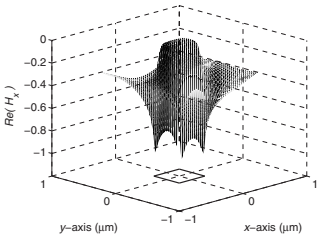

(b) Re(H_x) of the $E^{(0,1)}$ mode.

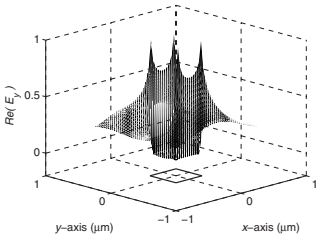

(c) Re(E_y) of the $E^{(0,1)}$ mode.

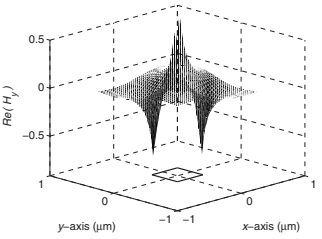

(d) Re(H_y) of the $E^{(0,1)}$ mode.

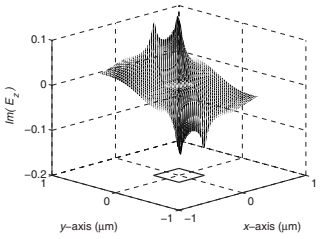

(e) Im(E_z) of the $E^{(0,1)}$ mode.

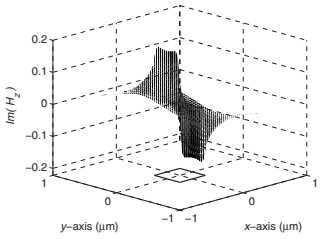

(f) Im(H_z) of the $E^{(0,1)}$ mode.

FIG. 9. Field distribution profiles of the electric and magnetic field components of the $E^{(0,1)}$ mode over a cross section of the waveguide for a metal core size of 400 nm. The electric and magnetic field components are normalized by $\max(|E_y|)=1$ and $\max(|H_x|)=1$. The field distribution of the $E^{(1,0)}$ is obtained by rotating the entire waveguide structure 90° around the z axis.

short-range mode ($E^{(0,0)}$). Regarding plasmonic communication, it is preferable to couple light from an optical fiber to the long-range modes. However, if the short-range mode is also excited, it will die out fast due to absorption. Furthermore, a good overlap between an optical fiber mode and the long-range modes will result in a poor overlap with the short-range mode because the mode size of the short-range mode is small compared to the long-range mode and because of symmetry mismatch with the optical fiber mode. This is especially pronounced for metal core sizes below approximately 400 nm. Roughness along the waveguide could, aside from scattering, also result in a continuous coupling of energy from the long-range to the short-range mode. However, in experiments, this does not seem to be a problem.[6]

4. Field distribution profiles

Field distribution profiles of the fundamental SSPPW modes are presented. All field components are, in general, complex but are presented as Re(E_x), Re(E_y), Re(H_y), Re(H_y), Im(E_z), and Im(H_z). This is chosen because the real parts of the transverse components are larger than (and equal in distribution to) the imaginary parts and because the real parts of the longitudinal components are small compared to the imaginary parts. Figure 8 shows the field distribution profiles of the six field components of the $E^{(0,0)}$ mode over a cross section of the waveguide for a metal core size of 400 nm. The electric field components are normalized such that the absolute maximum of E_y is unity. The magnetic field

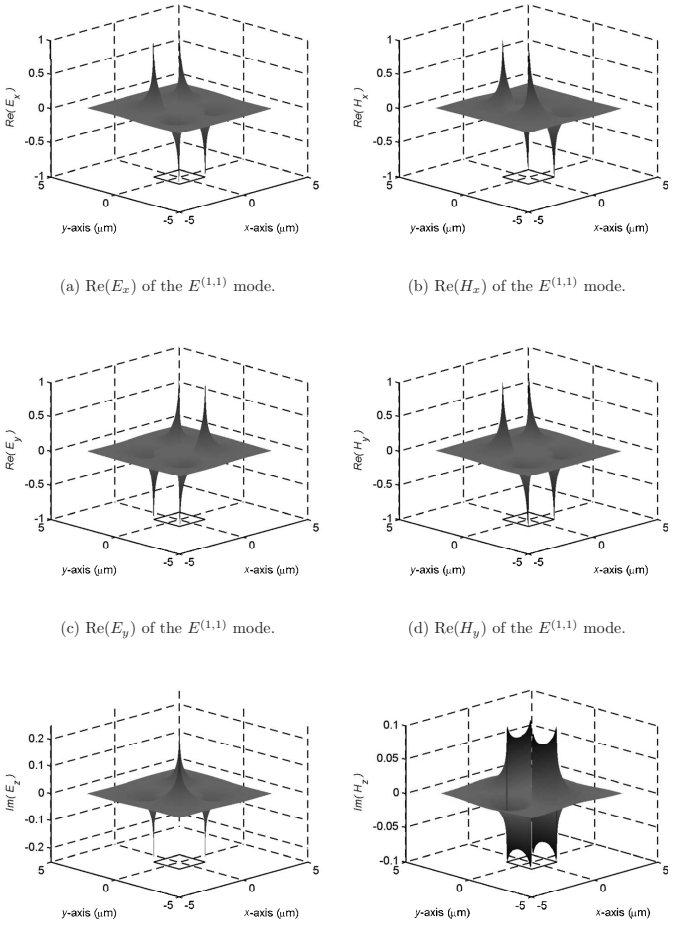

(a) Re(E_x) of the $E^{(1,1)}$ mode.

(b) Re(H_x) of the $E^{(1,1)}$ mode.

(c) Re(E_y) of the $E^{(1,1)}$ mode.

(d) Re(H_y) of the $E^{(1,1)}$ mode.

(e) Im(E_z) of the $E^{(1,1)}$ mode.

(f) Im(H_z) of the $E^{(1,1)}$ mode.

FIG. 10. Field distribution profiles of the electric and magnetic field components of the $E^{(1,1)}$ mode over a cross section of the waveguide for a metal core size of 2000 nm. The electric and magnetic field components are normalized by $\max(|E_y|)=1$ and $\max(|H_x|)=1$.

components are normalized such that the absolute maximum of H_x is unity. E_x and E_y are equal in size, and $E^{(0,0)}$ has therefore no dominating electric field component. H_x and H_y are also identical in size. The maximum of all six components are located at the corners of the metal core, and all six components decay in an exponential-like manner away from metal surfaces. Figure 9 shows the field distribution profiles of the $E^{(0,1)}$ mode. Because $E^{(1,0)}$ and $E^{(0,1)}$ are degenerate, the field distribution profiles calculated by means of the finite element method utilizing COMSOL MULTIPHYSICS are often a mixture of the two modes. In order to avoid this, it was necessary to place electric walls ($\mathbf{n}\times\mathbf{E}=0$) along the x and y axes for the $E^{(0,1)}$ and $E^{(1,0)}$ modes, respectively. The dominating electric and magnetic field components of the $E^{(0,1)}$ mode is E_y and H_x, respectively. As the SSPPW has a 90° rotational symmetry around the z axis, the field components of the $E^{(1,0)}$ mode can be directly deduced from the field components of the $E^{(0,1)}$ mode. The $E^{(1,0)}$ mode is simply the $E^{(0,1)}$ mode rotated 90° around the z axis. Utilizing this, it is readily seen that the dominating electric and magnetic field components of the $E^{(1,0)}$ mode is E_x and H_y, respectively. The guiding of both x- and y-polarized long-range SPP modes of the SSPPW is thus a direct consequence of the 90° rotational symmetry of the physical structure of the waveguide. The six electromagnetic field components of the $E^{(1,1)}$ are presented in Fig. 10. The x and y components of the

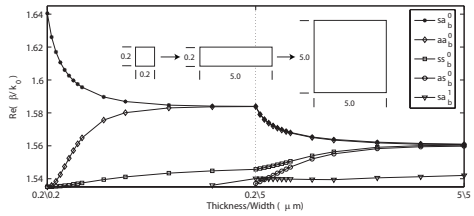

FIG. 11. The mode dispersion vs size of the structure is calculated starting from a subwavelength size SSPPW going through the rectangular waveguide and ending at a suprawavelength size SSPPW. The inset in the figure shows how the dimensions of the metal core changes during the finite element analysis. All sizes are given in micrometers.

electric field of this mode dominate equally, and the mode therefore has no dominating electric field component. This is also the case for the transverse magnetic components.

C. Rectangular vs square metal waveguides

In order to investigate how the SPP modes supported by the square metal waveguide are related to the modes supported by the rectangular metal waveguide (the metal stripe $t \ll w$), the mode dispersion is calculated starting from a subwavelength size SSPPW going through the rectangular waveguide and ending at a suprawavelength size SSPPW (Fig. 11). Starting with a SSPPW of 200 nm, the width w is increased to 5000 nm (the metal stripe structure), and subsequently the thickness t is increased to 5000 nm (see inset in Fig. 11). The four modes transforming into the corner modes of the SSPPW are in the nomenclature developed by Berini,[2] named sa_b^0, aa_b^0, ss_b^0, and as_b^0. In this nomenclature, the first two characters specify the symmetries of the dominating electric field component with respect to the y and x axes, respectively. The subscript b specifies that the mode is bound. The subscript could be l if the mode is leaky. The superscript specifies the number of extrema observed in the field distribution of the dominating electric field component along the largest transverse dimension of the metal core. As the two degenerate modes of the SSPPW have the same symmetry and number of extrema in the dominating field component, Berini introduced a second subscript[9] in order to separate the two modes from each other. The extra subscript is either x or y, which indicates that the dominating electric field component is either E_x or E_y. The four fundamental modes of the SSPPW $E^{(0,0)}$, $E^{(0,1)}$, $E^{(1,0)}$, and $E^{(1,1)}$ are with Berini's notation, named sa_b^0, ss_{bx}^0, ss_{by}^0, and as_b^0. In the metal stripe configuration, these are named sa_b^0, aa_b^0, ss_b^0, and as_b^0, respectively. For a SSPPW with a metal core size of 5000 nm, the latter four modes are practically degenerate with a mode index equal to the mode index of a PP mode supported by an isolated corner. In the SSPPW configuration, these modes are named $E^{(0,0)}$, $E^{(1,0)}$, $E^{(0,1)}$, and $E^{(1,1)}$. When the thickness is decreased, the four modes split up into two almost degenerate upper branches, sa_b^0 and aa_b^0, and into two lower branches, ss_b^0 and as_b^0. sa_b^0 and aa_b^0 are named corner modes and ss_b^0 is named the dominant symmetric stripe mode.[3] The two upper branches have an antisymmetry in the dominating electric field component across the x axis, whereas the two lower branches have a symmetry. The side mode supported by the suprawavelength size SSPPW is also supported by the metal stripe configuration and is named sa_b^1 with Berini's notation. The sa_b^1 is also named the dominant antisymmetric stripe mode.[3] When the width of the metal stripe is decreased, the degeneracy of the two upper branches are lifted and the two modes split up. When the metal core becomes square, the sa_b^0, aa_b^0, and ss_b^0 modes of the metal stripe becomes the $E^{(0,0)}$, $E^{(1,0)}$, and $E^{(0,1)}$ modes of the SSPPW, respectively. In the configuration studied here (BCB, gold, and $\lambda_0 = 1550$ nm), the as_b^0 and sa_b^1 modes have transmission cutoffs for $w \approx 5000$ nm and $w \approx 4000$ nm, respectively. The dispersion branch of the as_b^0 mode crosses the dispersion branch of the sa_b^1 mode as the thickness of the metal stripe is reduced. Such crossing is also observed in the analysis of metal stripe waveguides by Berini.[2] An investigation of the field distribution profiles of the two modes in the crossing region shows that the two modes are very different in distribution.

IV. CONCLUSION

In conclusion, we have described and characterized the surface electromagnetic modes supported by SSPPWs at telecom wavelengths ($\sim$1550 nm) for both sub- and suprawavelength metal core sizes. It was shown how mode coupling between four plasmon polariton modes of isolated corners and the symmetries of the SSPPW can be used to deduce a schematic overview of the fundamental SPP modes supported by the structure. The technique utilized for the numerical analysis of the SSPPWs was the finite element method. The configuration studied was a square gold core surrounded by an infinite lossless dielectric polymer of BCB. The mode dispersion with the size, field orientations, and field profiles, including mode width, have been presented. The SPP modes supported by the SSPPW have been related to the modes supported by the rectangular metal stripe configuration, and it was shown how three of the fundamental stripe modes transform into three of the fundamental modes of the SSPPW as the stripe is gradually changed to a SSPPW. For subwavelength metal core sizes, the three modes supported by the SSPPW are one short range and two degenerate long range. The short-range mode is the SSPPW analog of the fundamental SPP mode supported by the circular SPP waveguide.[19] With the short-range SSPPW mode, it is possible to achieve high mode confinement at the price of a significant increase in the propagation loss. The short-range mode can possibly be used in SPP resonators based on slow SPP modes propagating back and forth along a thin metal wire of finite length. The two degenerate modes become long range as the size of the metal core decreases and can be utilized for long-range SPP guiding. For a metal core size of 200 nm, the two degenerate modes have a propagation

length of approximately 3 mm. One of the long-range modes is polarized along the x axis, whereas the other is polarized along the y axis. These modes allow for polarization-independent plasmonic communication. Thus, unlike the thin metal stripe waveguides, the SSPPW supports long-range SPP waves for both polarizations. This makes the SSPPW unique and a promising optical component from which future plasmonic communication can benefit.

ACKNOWLEDGMENTS

The authors gratefully acknowledge the financial support (J.J., T.S. and S.I.B.) from the NABIIT project financed by the Danish Research Agency (Contract No. 2106-05-033), (T.S.) from the Danish Research Council for Technology and Production, and (S.I.B.) from the European Network of Excellence, Plasmo-nano-devices (FP6-2002-IST-1-507879).

*jung@physics.aau.dk

[1] H. Raether, *Surface Plasmons: On Smooth and Rough Surfaces and on Gratings*, 1st ed. (Springer-Verlag, New York, 1988).
[2] P. Berini, Phys. Rev. B **61**, 10484 (2000).
[3] S. J. Al-Bader, IEEE J. Quantum Electron. **40**, 325 (2004).
[4] P. Berini, Opt. Express **7**, 327 (2000).
[5] P. Berini, Opt. Lett. **24**, 1011 (1999).
[6] K. Leosson, T. Nikolajsen, A. Boltasseva, and S. I. Bozhevolnyi, Opt. Express **14**, 314 (2006).
[7] T. Itoh, *Numerical Techniques for Microwave and Millimeter-Wave Passive Structures*, 1st ed. (Wiley, New York, 1989).
[8] J. Jin, *The Finite Element Method in Electromagnetics*, 2nd ed. (Wiley, New York, 2002).
[9] P. Berini, U.S. Patent No. 6,741,782 (25 May 2004) (http://www.uspto.gov/).
[10] C. Themistos, B. M. A. Rahman, M. Rajarajan, K. Kalli, and K. T. V. Grattan, Appl. Opt. **45**, 8523 (2006).
[11] M. P. Nezhad, K. Tetz, and Y. Fainman, Opt. Express **12**, 4072 (2004).
[12] E. Feigenbaum and M. Orenstein, Opt. Express **14**, 8779 (2006).
[13] A. Eguiluz and A. A. Maradudin, Phys. Rev. B **14**, 5526 (1976).
[14] D. F. P. Pile, T. Ogawa, D. K. Gramotnev, T. Okamoto, M. Haraguchi, M. Fukui, and S. Matsuo, Appl. Phys. Lett. **87**, 061106 (2005).
[15] A. D. Boardman, R. Garcia-Molina, A. Gras-Marti, and E. Louis, Phys. Rev. B **32**, 6045 (1985).
[16] L. Dobrzynski and A. A. Maradudin, Phys. Rev. B **6**, 3810 (1972).
[17] R. Zia, M. D. Selker, and M. L. Brongersma, Phys. Rev. B **71**, 165431 (2005).
[18] A. Boltasseva, T. Nikolajsen, K. Leosson, K. Kjaer, M. S. Larsen, and S. I. Bozhevolnyi, J. Lightwave Technol. **23**, 413 (2005).
[19] J. Takahara, S. Yamagishi, H. Taki, A. Morimoto, and T. Kobayashi, Opt. Lett. **22**, 475 (1997).
[20] T. Søndergaard and S. I. Bozhevolnyi, Phys. Rev. B **75**, 073402 (2007).

Appendix B

Opt. Express **16**, 2676 (2008)

Scaling for gap plasmon based waveguides
by
Sergey I. Bozhevolnyi and Jesper Jung

This page is intentionally left blank

Scaling for gap plasmon based waveguides

Sergey I. Bozhevolnyi[1,2] **and Jesper Jung**[1]

[1]*Department of Physics and Nanotechnology, Aalborg University, Skjernvej 4A, DK-9220 Aalborg Øst, Denmark*
[2]*Institute of Sensors, Signals and Electrotechnics (SENSE), University of Southern Denmark, Niels Bohrs Allé 1, DK-5230 Odense M, Denmark*
seib@sense.sdu.dk

Abstract: Using the effective-index approach and an explicit expression for the propagation constant of gap surface plasmon polaritons (G-SPPs) obtained for moderate gap widths, we introduce a normalized waveguide parameter characterizing the mode field confinement and obtain the corresponding expressions for various (gap, trench and V-groove) G-SPP based waveguides. Usage of the obtained relations is investigated with a finite-element method, demonstrating that waveguides with different dimensions and operating at different wavelengths, but having the same normalized parameter, exhibit very similar field confinement. These relations allow one to design G-SPP waveguides for single-mode operation supporting a well-confined fundamental mode.

OCIS codes: (240.6680) Surface plasmons; (230.7380) Waveguides, channeled ; (250.5300) Photonic integrated circuits

References and links

1. H. Raether, *Surface Plasmons* (Springer-Verlag, Berlin, 1988).
2. E. N. Economou, "Surface plasmons in thin films," Phys. Rev. **182**, 539-554 (1969).
3. S. I. Bozhevolnyi, "Effective-index modeling of channel plasmon polaritons," Opt. Express **14**, 9467-9476 (2006).
4. K. Tanaka and M. Tanaka, "Simulations of nanometric optical circuits based on surface plasmon polariton gap waveguide," Appl. Phys. Lett. **82**, 1158-1160 (2003).
5. K. Tanaka, M. Tanaka, and T. Sugiyama, "Simulation of practical nanometric optical circuits based on surface plasmon polariton gap waveguides," Opt. Express **13**, 256-266 (2005).
6. S. H. Chang, T. C. Chiu, and C.-Y. Tai, "Propagation characteristics of the supermode based on two coupled semi-infinite rib plasmonic waveguides," Opt. Express **15**, 1755-1761 (2007).
7. I. V. Novikov and A. A. Maradudin, "Channel polaritons," Phys. Rev. B **66**, 035403 (2002).
8. D. K. Gramotnev and D. F. P. Pile, "Single-mode subwavelength waveguide with channel plasmon-polaritons in triangular grooves on a metal surface," Appl. Phys. Lett. **85**, 6323-6325 (2004).
9. S. I. Bozhevolnyi, V. S. Volkov, E. Devaux, and T. W. Ebbesen, "Channel plasmon-polariton guiding by subwavelength metal grooves," Phys. Rev. Lett. **95**, 046802 (2005).
10. S. I. Bozhevolnyi, V. S. Volkov, E. Devaux, J.-Y. Laluet, and T. W. Ebbesen, "Channel plasmon subwavelength waveguide components including interferometers and ring resonantors," Nature **440**, 508-511 (2006).
11. V. S. Volkov, S. I. Bozhevolnyi, E. Devaux, J.-Y. Laluet, and T. W. Ebbesen, "Wavelength selective nanophotonic components utilizing channel plasmon polaritons," Nano Lett. **7**, 880-884 (2007).
12. E. Moreno, F. J. Garcia-Vidal, S. G. Rodrigo, L. Martin-Moreno, and S. I. Bozhevolnyi, "Channel plasmon-polaritons: modal shape, dispersion, and losses," Opt. Lett. **31**, 3447-3449 (2006).
13. G. B. Hocker and W. K. Burns, "Mode dispersion in diffused channel waveguides by the effective index method," Appl. Opt. **16**, 113-118 (1977).
14. A. Boltasseva, T. Nikolajsen, K. Leosson, K. Kjaer, M. S. Larsen, and S. I. Bozhevolnyi, "Integrated optical components utilizing long-range surface plasmon polaritons," J. Lightwave Technol. **23**, 413-422 (2005).
15. R. Zia, A. Chandran, and M. L. Brongersma, "Dielectric waveguide model for guided surface polaritons," Opt. Lett. **30**, 1473-1475 (2005).
16. H. Kogelnik and V. Ramaswamy, "Scaling rules for thin-film optical waveguides," Appl. Opt. **13**, 1857-(1974).
17. S. I. Bozhevolnyi, V. S. Volkov, E. Devaux, J.-Y. Laluet, and T. W. Ebbesen, "Channelling surface plasmons," Appl. Phys. A **89**, 225-231 (2007).
18. E. D. Palik, *Handbook of Optical Constants of Solids* (Academic, New York, 1985).

19. M. Yan and M. Qiu, "Guided plasmon polariton at 2D metal corners," J. Opt. Soc. Am. B **24**, 2333-2342 (2007).

1. Introduction

Photonic components are superior to electronic ones in terms of operational bandwidth but suffer from the diffraction limit that constitutes a major problem on the way towards miniaturization and high density integration of optical circuits. The degree of light confinement in dielectric structures, including those based on the photonic band-gap effect, is fundamentally limited by the light wavelength in the dielectric used. The main approach to circumvent this problem is to take advantage of the hybrid nature of surface plasmon polaritons (SPPs) whose subwavelength confinement is achieved due to the very short (nanometer-sized) penetration of light in metals [1]. The important issue in this context is to strongly confine the SPP field in the cross section perpendicular to the SPP propagation direction (smaller cross sections ensure smaller bend losses and higher densities of components), while keeping relatively low propagation loss. Among various SPP guiding configurations, waveguides utilizing SPP modes supported by a dielectric gap between two metal surfaces [2] promise the possibility of achieving a better trade-off between the lateral confinement and the propagation loss [3]. Gap-SPP (G-SPP) based configurations include waveguides having the gap width varying in the lateral direction [4, 5], trench [3, 6] and V-groove [7-9] waveguides. The latter configuration has recently been exploited to realize various subwavelength waveguide components, including Mach-Zehnder interferometers and waveguide-ring resonators [10] as well as add-drop multiplexers and grating filters [11].

Modeling of SPP waveguides allowing for the two-dimensional (2D) mode field confinement (in the cross section perpendicular to the propagation direction) is, in general, a rather complicated problem requiring the usage of sophisticated computational techniques [4-6, 7, 8, 12], which is often time-consuming due to the very detailed discretization required near metal edges. Even though very careful and detailed simulations are crucial for understanding intricate physical phenomena involved (e.g., hybridization of channel and wedge SPP modes [12]), it has been found that the effective-index method (EIM) [13] can be quite helpful in judging upon the existence of guided (bound) SPP modes [3, 9, 14, 15]. The main attractive feature of the EIM is that it allows one to combine the results of modeling conducted for one-dimensional (1D) waveguide configurations so that the characteristics of 2D (channel) waveguides can be described [13]. For a rectangular-core waveguide, one should first analyze a planar (slab) waveguide obtained by letting one dimension of the original 2D waveguide approach infinity. The obtained in this way mode propagation constant(s) is then used to define the corresponding effective dielectric index(es) assigned to the core index(es) of another 1D waveguide considered in the perpendicular direction. The propagation constant(s) of this second waveguide are taken to represent those of the original rectangular waveguide [13]. Furthermore, for the purpose of evaluating the guiding potential one can make use of the normalized waveguide parameter (normalized frequency [16]) avoiding the implementation of the second step in the EIM [3]. Note that the waveguide parameter can be rigorously introduced only for 1D (thin-film) waveguide configurations [16], and that its usage for 2D SPP-based waveguides should thus be carefully examined.

In this work, using the EIM along with an explicit (approximate) expression for the G-SPP propagation constant obtained for moderate gap widths, we introduce a normalized waveguide parameter characterizing the mode field confinement and obtain the corresponding expressions for various (gap, trench and V-groove) G-SPP based waveguides. Usage of the obtained relations is investigated with a finite-element method (FEM), demonstrating that waveguides with different dimensions and operating at different wavelengths, but having the same normalized parameter, exhibit very similar field confinement. These exceedingly simple relations allow one to properly choose the system parameters in a broad range so as to realize the single-mode operation of G-SPP waveguides with a well-confined fundamental mode.

2. G-SPP propagation constant for moderate gap widths

Many different SPP modes can be found in multiple-interface systems [2], when the SPPs associated with individual metal-dielectric interfaces start interacting with each other. Considering the SPP modes associated with two metal-dielectric interfaces one finds that the SPP modes can be guided within a thin dielectric layer surrounded by metals (i.e. inside a gap between metals), constituting (for even symmetry of the transverse field component) G-SPP modes that can be found for *any gap* width [2-4]. The G-SPP characteristics were discussed in detail elsewhere [17], paying special attention to the non-trivial dependence of the G-SPP propagation length on the gap width that indicates that G-SPPs exploit in the most efficient way the available dielectric space (gap) between the metal walls minimizing thereby the absorption loss [3]. This remarkable feature stimulates investigations of various G-SPP based waveguide geometries. Since the G-SPP effective index is strongly dependent on the gap width (increasing with its decrease) it is natural to exploit this dependence for achieving the 2D lateral mode confinement by laterally varying the gap width forming gap [4, 5], trench [3, 6] and V-groove [7-9] waveguides (Fig. 1). In general, guided modes in all these configurations are laterally confined to a dielectric space between the *closest* metal surfaces, where the G-SPP effective index reaches its largest value, i.e. to a gap [Fig. 1(a)], in a trench [Fig. 1(b)] or to the bottom of a V-groove [Fig. 1(c)]. In the EIM, the corresponding waveguide modes can be evaluated by considering a 1D multilayer structure whose layers feature the refractive indexes associated with the relevant G-SPP modes [3].

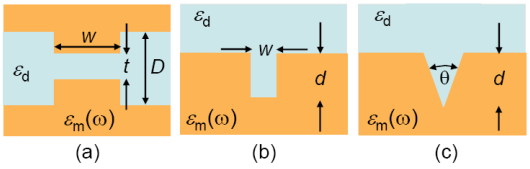

Fig. 1. Schematic of the G-SPP based waveguides under consideration.

For the purpose of obtaining simple design guidelines, we start with deriving an explicit expression for the G-SPP propagation constant that can be used for moderate gap widths. Applying the appropriate boundary conditions for the electric field components and the aforementioned field symmetry, allows one to obtain the G-SPP dispersion relation [2]:

$$\tanh\left(k_z^{(d)}t/2\right)=-\left(\varepsilon_d k_z^{(m)}\right)/\left(\varepsilon_m k_z^{(d)}\right),\ \text{with}\ k_z^{(m,d)}=\sqrt{k_{gsp}^2-\varepsilon_{m,d}k_0^2}\ \text{and}\ k_0=\frac{2\pi}{\lambda}\ , \quad (1)$$

where t is the gap width, ε_d and ε_m are the dielectric constants of correspondingly dielectric and metal, and k_{gsp} denotes the propagation constant of the fundamental G-SPP mode with the transverse field component having the same sign across the gap. For sufficiently small gap widths ($t \to 0$), one can use the approximation $\tanh x \approx x$ resulting in the following expression:

$$k_{gsp} \approx k_0\sqrt{\varepsilon_d+0.5\left(k_{gsp}^0/k_0\right)^2+\sqrt{\left(k_{gsp}^0/k_0\right)^2\left[\varepsilon_d-\varepsilon_m+0.25\left(k_{gsp}^0/k_0\right)^2\right]}} \quad (2)$$

$$\text{with} \quad k_{gsp}^0=-\frac{2\varepsilon_d}{t\varepsilon_m} \quad .$$

Here, k_{gsp}^0 represents the G-SPP propagation constant in the limit of vanishing gaps ($t \to 0$), for which the real part of the correspondent effective index, $\mathrm{Re}\{k_{gsp}\lambda/(2\pi)\}$, becomes much larger than the dielectric refractive index. At the same time, the imaginary part of the G-SPP

propagation constant increases rapidly as well, resulting in a decrease of the G-SPP propagation length. For our purpose, it is desirable to further simplify the small-gap approximation given by Eq. (2), which is somewhat cumbersome to handle. Considering different gap-width-dependent terms in Eq. (2), one notices that for not too small gaps, i.e. when $\left|k_{gsp}^{0}\right| < k_0 \Leftrightarrow t > (\lambda\varepsilon_d)/(\pi|\varepsilon_m|)$, it can be approximated as follows:

$$k_{gsp} \approx k_0 \sqrt{\varepsilon_d + \frac{2\varepsilon_d\sqrt{\varepsilon_d - \varepsilon_m}}{k_0 t\left(-\varepsilon_m\right)}} \quad . \tag{3}$$

The G-SPP characteristics were calculated for air gaps in gold for several wavelengths in the interval between visible and telecom wavelengths using the exact (implicit) dispersion relation [Eq. (1)] and the above explicit (analytic) formula (Fig. 2). The following dielectric constants of gold were used in the simulations: n = 0.166 + 3.15i (λ = 653 nm), 0.174 + 4.86i (775 nm), 0.272 + 7.07i (1033 nm), and 0.55 + 11.5i (1550 nm) [18].

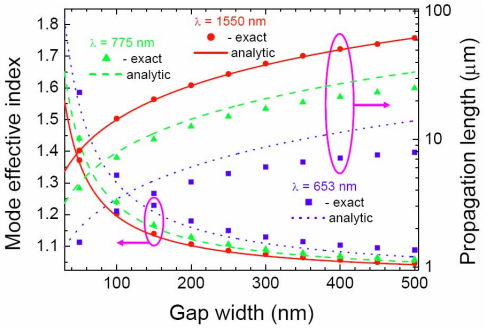

Fig. 2. The G-SPP mode effective index and its propagation length as a function of the width t of the air gap in gold for several light wavelengths calculated exactly [Eq. (1)] and using the analytic (moderate gap) approximation [Eq. (3)].

It is seen that the above approximation gives quite accurate values for both the G-SPP propagation length and effective index. In fact progressively more accurate values are obtained for longer wavelengths because of the large values of $|\varepsilon_m|$. Even for shorter wavelengths and other materials, the obtained relation is still fairly accurate. For example, considering the system parameters used for simulations of G-SPP waveguides [4], i.e. λ = 532 nm, ε_d = 1, Re(ε_m) ≅ - 12.6 (silver), t = 34 and 85 nm, results, when using Eq. (3), in effective G-SPP indexes N_{eff} ≅ 1.57 and 1.26, respectively. These values agree well with the values N_{eff} ≅ 1.61 and 1.28 obtained directly from the dispersion relation [4].

3. Gap waveguides

The lateral G-SPP mode confinement in gap waveguides [4, 5] is achieved by decreasing the gap within a stripe of width w [Fig. 1(a)]. The corresponding waveguide modes can be described within the EIM framework by considering TE (electric field is parallel to interfaces) modes in a *symmetric* three-layer structure whose refractive indexes are given by the appropriate G-SPP effective indexes [3]. The normalized waveguide parameter (normalized frequency [16]) of a symmetric optical waveguide, consisting of a film (core) with the thickness w and the refractive index n_1 embedded in a medium (cladding) with the refractive index n_2, is given by [16]:

$$V = w k_0 \sqrt{n_1^2 - n_2^2} \quad . \tag{4}$$

For the considered waveguide configuration [Fig. 1(a)], the core and cladding refractive indexes correspond to the effective indexes of G-SPP modes supported by gaps having the width t and D, accordingly. These indexes can be approximated using the explicit relation for the G-SPP propagation constant [Eq. (3)], resulting thereby in the following expression for the normalized waveguide parameter:

$$V_{gsp} \cong 2w \sqrt{\frac{\pi \varepsilon_d \sqrt{|\varepsilon_d - \varepsilon_m|}}{\lambda |\varepsilon_m|} \left(\frac{1}{t} - \frac{1}{D} \right)} \quad . \tag{5}$$

It is seen that this waveguide parameter depends explicitly on the light wavelength, reflecting the fact that the gap widths considered are relatively large. In the limit of very narrow gaps, i.e. when $t << (\lambda \varepsilon_d)/(\pi |\varepsilon_m|)$, the G-SPP propagation constant becomes equal to k_{gsp}^0 [Eq. (2)] and the wavelength dependence disappears as expected for SPP waveguides whose operation is not limited by diffraction. Note that the above condition is rather stringent requiring extremely narrow gaps. Thus, for example, a gap width $t << 13$ nm is required for the system parameters used in the aforementioned gap waveguide made of silver.

The usage of the waveguide parameter V allows one to choose the system parameters that ensure a well-confined fundamental mode. In fact, the design of single-mode waveguides is often aimed at achieving the best lateral mode confinement, because this confinement strongly influences the maximum density of waveguide components in integrated optical circuits [3]. For the fundamental TE_0 mode, there is no cutoff (with respect to the width w) in a symmetric waveguide, but the effective mode width diverges in the limit of both very wide ($w \to \infty$) and very narrow($w \to 0$) waveguides, reaching its minimum at $V_0 = 1.73$ [16]. The parameter space for the single-mode symmetric waveguide, within which the fundamental mode is well confined, can thereby be determined by the following unequality: $1.73 \le V \le \pi$ [16]. In order to illustrate the usage of the waveguide parameter we modeled (using the FEM and above dielectric constants) two different gap waveguides made of gold, operating at two different wavelengths, but characterized by the same waveguide parameter $V_{gsp} = 1.73$ (Fig. 3).

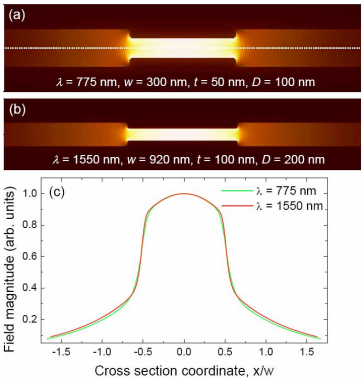

Fig. 3. (a, b). The G-SPP mode field magnitude distributions and (c) their lateral mid-plane cross sections shown by a dotted line in (a) for two waveguide configurations having the same waveguide parameter $V_{gsp} = 1.73$.

It is seen that the fundamental waveguide mode, when displayed using the normalized (with respect to the waveguide width w) cross section coordinate, exhibits the same confinement and field distribution in the lateral direction. All FEM simulations presented in this paper were conducted using the commercial software COMSOL with all sharp corners being rounded with a 10-nm radius, which is usually used in similar calculations [12, 19], and with the convergence achieved for a total number of unknowns in the range of $2{\cdot}10^5 - 4{\cdot}10^5$. The fact that the modes found for two rather different waveguide configurations exhibit such a striking similarity in their lateral distributions is related to the circumstance that the EIM, which was used to introduce the waveguide parameter [Eq. (5)], is quite accurate when applied to the gap waveguides [3]. Thus, for the considered configurations, the mode effective indexes calculated with the FEM, $N_{\mathrm{FEM}}(\lambda = 775\ \mathrm{nm}) \cong 1.365 + 0.014i$ and $N_{\mathrm{FEM}}(\lambda = 1550\ \mathrm{nm}) \cong 1.161 + 0.0080i$, are found being quite similar to those obtained with the EIM, $N_{\mathrm{EIM}}(\lambda = 775\ \mathrm{nm}) \cong 1.326 + 0.013i$ and $N_{\mathrm{EIM}}(\lambda = 1550\ \mathrm{nm}) \cong 1.145 + 0.0073i$.

4. Trench waveguides

The waveguide modes supported by rectangular trenches [Fig. 1(b)] can be described within the EIM framework by considering TE modes in a three-layer structure, in which a dielectric core, having the effective index of the corresponding G-SPP, is sandwiched between the air cladding and the gold substrate [3]. Using the approximation [Eq. (3)] of moderately narrow gaps (trenches) and the approach similar to that employed in the previous section, one obtains for the normalized waveguide parameter [16] of trench waveguides:

$$V_{tpp} \cong 2d\sqrt{\frac{\pi\,\varepsilon_d\sqrt{|\varepsilon_d - \varepsilon_m|}}{\lambda\, w|\varepsilon_m|}} \quad . \tag{6}$$

The trench SPP (TPP) mode fields decrease to (nearly) zero at the trench bottom because of the large magnitude of dielectric constant of the metal substrate and the boundary condition for the electric field [3]. For this reason, the TPP mode characteristics are nearly identical to the corresponding (odd) modes of the symmetrical gap waveguide having the double width, a circumstance that allows one to deduce a simple relation for the single-mode TPP guiding: $0.5\pi < V_{\mathrm{tpp}}(w, d) < 1.5\pi$ [3]. It is then reasonable to take as a compromise the waveguide parameter value $V_{\mathrm{tpp}} = \pi$ for the design of single-mode waveguides supporting a well-confined fundamental TPP mode. As in the previous case, we modeled two different trench waveguides characterized by the same waveguide parameter $V_{\mathrm{tpp}} = \pi$ (Fig. 4).

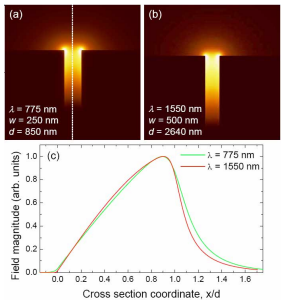

Fig. 4. (a, b). The TPP mode field magnitude distributions and (c) their lateral mid-plane cross sections shown by a dotted line in (a) for two waveguide configurations having the same waveguide parameter $V_{\mathrm{tpp}} = \pi$.

It is seen that the correspondence of the calculated TPP field magnitude distributions is rather good, albeit not as perfect as in the case of gap waveguides [cf. Figs. 4(c) and 3(c)]. We relate this fact to the circumstance that the correspondence between the EIM (approximate) simulations and accurate numerical modeling (e.g., when using the FEM) is generally worse for channel waveguides [12]. Thus, for the considered configurations, the mode effective indexes calculated with the FEM, $N_{FEM}(\lambda = 775\text{ nm}) \cong 1.097 + 0.0050i$ and $N_{FEM}(\lambda = 1550\text{ nm}) \cong 1.035 + 0.0022i$, are found to be quite different from those obtained with the EIM, $N_{EIM}(\lambda = 775\text{ nm}) \cong 1.056 + 0.0037i$ and $N_{EIM}(\lambda = 1550\text{ nm}) \cong 1.022 + 0.0018i$. It should be noted that the FEM modeling of the first trench waveguide (at $\lambda = 775$ nm) revealed the existence of an additional mode associated with the coupling of two wedge SPP modes that cannot be described within the EIM framework. The latter mode is very close to the cutoff (its effective index is larger than that of the corresponding SPP by only $\sim 7\cdot10^{-4}$) and therefore only weakly confined to the trench, extending in the lateral direction along the metal surface (away from each side of the trench) over several microns. We believe that, in practice, the existence of such a mode, whose characteristics are most strongly influenced by the curvature of wedges, can be disregarded.

5. V-groove waveguides

The SPP modes supported by metal grooves, in particular V-grooves [Fig. 1(c)], are conventionally called channel SPPs (CPPs) [7]. Careful analysis of CPP waveguides requires elaborate numerical modelling [7, 8, 12, 19], but the design guidelines can be worked out using the EIM [3, 9]. Within the framework of the EIM, one can find the CPP modes supported by a V-groove through analyzing a one-dimensional layered (in depth) guiding structure, in which a top layer of air and a bottom layer of metal abut a stack of layers having refractive indexes determined by the layer depth: the refractive index is equal to the G-SPP effective index for a gap width corresponding to the groove width at this depth [9]. The normalized CPP waveguide parameter can be obtained by integrating the index contrast over the groove depth, a straightforward procedure when using the moderate gap approximation [Eq. (3)] that results in the following expression:

$$V_{cpp} \cong 2\sqrt{\frac{k_0 d\,\varepsilon_d\sqrt{|\varepsilon_d - \varepsilon_m|}}{|\varepsilon_m|\tan(\theta/2)}} \quad . \tag{7}$$

It is seen that, since $\tan(\theta/2) = 0.5w/d$ (w being the groove width at the top of the groove), the CPP waveguide parameter is exactly twice that of TPP [Eq. (6)]: $V_{cpp} = 2V_{tpp}$. The latter relation is somewhat surprising as the cross section of a CPP waveguide is twice smaller than that of the TPP waveguide having the same width and depth [cf. Figs. 1(b) and 1(c)]. However, the G-SPP effective index increases with the decrease in the gap width and, thereby, *narrower* channels (trench and V-grooves) represent *stronger* waveguides (i.e., with larger waveguide parameters), as is also transparent from Eqs. (6) and (7), which accounts for the relation above. Note that the above relation for the CPP waveguide parameter [Eq. (7)] involves additional approximations as compared to Eq. (6). Thus, when using the EIM for CPP waveguides, it is implicitly assumed that the CPP electric field is polarized parallel to the sample surface, an approximation that can be justified only for narrow ($\theta << 1$) grooves [12]. Furthermore, when obtaining Eq. (7), the moderate gap approximation was applied for the gap widths varying all the way from 0 to the (maximum) groove width at the top of the groove.

Within the EIM framework, the CPP mode fields decrease to (nearly) zero at the groove bottom similarly to the TPP modes [3], and the single-mode CPP guiding should be, in principle, governed by the same condition as for the TPP guiding: $0.5\pi < V_{cpp}(w, d) < 1.5\pi$. On the other hand, it has been noticed that the EIM *overestimates* the guiding capability of V-groove waveguides [12]. In the course of this work, we have also found that, contrary to the EIM simulations, the FEM modeling could not locate bound modes for the V-groove

waveguides characterized with a normalized waveguide parameter of π. On the other hand, the behavior of V-groove waveguides might still follow the *scaling* described by the waveguide parameter [Eq. (7)]. In order to asses this scaling, we modeled two different waveguides characterized with $V_{cpp}(w, d) = 1.34\pi$, a value which is still smaller than the cutoff value (1.5π) for the second mode (within the EIM framework). The two simulated CPP field magnitude distributions (of the fundamental modes) are shown in Fig. 5.

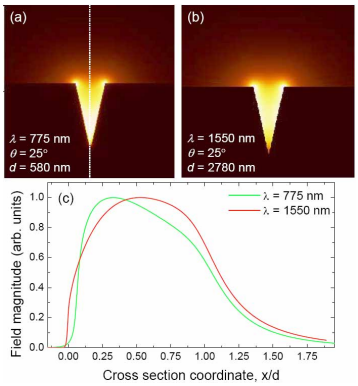

Fig. 5. (a, b). The CPP mode field magnitude distributions and (c) their lateral mid-plane cross sections shown by a dotted line in (a) for two waveguide configurations having the same waveguide parameter $V_{cpp} = 1.34\pi$.

It is seen that, even though the correspondence between the calculated CPP field magnitude distributions is worse than that found for the TPP distributions [cf. Figs. 5(c) and 4(c)], the CPP confinement to the groove region is rather similar for both configurations, with the major part of the CPP field being concentrated within the groove (i.e., for $0 \le x \le d$). The observed differences in the CPP distributions should be related to the aforementioned approximations introduced when applying the EIM and moderate gap approximation [Eq. (3)] for obtaining the CPP waveguide parameter. Influence of the EIM approximation is also reflected in the differences between the effective mode indexes calculated with the FEM, $N_{FEM}(\lambda = 775\text{ nm}) \cong 1.086 + 0.0074i$ and $N_{FEM}(\lambda = 1550\text{ nm}) \cong 1.012 + 0.0015i$, and those with the EIM, $N_{EIM}(\lambda = 775\text{ nm}) \cong 1.118 + 0.010i$ and $N_{EIM}(\lambda = 1550\text{ nm}) \cong 1.022 + 0.0023i$. It is in fact surprising that, despite all the approximations, the very simple formula obtained [Eq. (7)] reflects accurately enough the relations between the V-groove parameters that should be maintained in order to keep the same degree of CPP mode confinement. Finally, it is worth mentioning that the scaling established [Eqs. (5) – (7)] includes also the material dispersion, which is especially important for metals, resulting in the requirement of *progressively* wider (gap) or deeper (trench and V-groove) waveguides for longer wavelengths. Consequently, these waveguide configurations cannot be realized in the limit of ideal metals (when $\lambda \to \infty$), even though the G-SPP guiding does persist existing in this limit.

6. Conclusion

In summary, using the EIM along with an explicit expression for the G-SPP propagation constant obtained for moderate gap widths, we have obtained simple relations describing the normalized waveguide parameter for gap, trench and V-groove waveguides that characterizes the mode field confinement. Usage of the obtained relations was investigated with FEM simulations, demonstrating that waveguides with different dimensions and operating at

different wavelengths but having the same normalized parameter exhibit very similar field confinement. In the case of the gap waveguides, this confinement determines the lateral mode width, whereas for the TPP and CPP waveguides that are far from cutoff (which can be judged with the help of the corresponding waveguide parameters) the lateral mode width is simply set by the groove width *w* at the groove top. Note that it is the lateral mode width that governs both the bend loss and crosstalk between the neighbor waveguides, determining thereby the maximum density of waveguide components [3]. It should also be borne in mind that, as the TPP or CPP modes approach the cutoff and the mode fields become progressively larger at the groove edges, one should expect the occurrence of mode coupling to wedge SPP modes leading to their hybridization [12] that cannot be described with the EIM. These (sub-critical) waveguides are therefore outside the validity domain for the introduced waveguide parameter. However, the obtained expressions for the normalized waveguide parameter can still be used as *practical guidelines* to design G-SPP based gap, trench and V-groove waveguides for operation within a given wavelength range, so as to ensure the single-mode operation with a well-confined fundamental mode being far away from the cutoff. The latter is very important not only for minimizing the lateral mode width but also for avoiding additional loss, since, in practice, any structural irregularities would result in coupling of waveguide modes (especially those close to the cutoff) to plane SPPs propagating away from the waveguide and thereby result in additional propagation loss.

Acknowledgments

The authors acknowledge the support by the European Network of Excellence, PLASMO-NANO-DEVICES (FP6-2002-IST-1-507879), the Danish Agency for Science, Technology and Innovation (contract No. 274-07-0258), and from the NABIIT project financed by the Danish Research Agency (contract No. 2106-05-033).

This page is intentionally left blank

Appendix C

Phys. Rev. B **77**, 245310 (2008)

Greens function surface integral equation method for theoretical analysis of scatterers close to a metal interface

by

Jesper Jung and Thomas Søndergaard

This page is intentionally left blank

Green's function surface integral equation method for theoretical analysis of scatterers close to a metal interface

Jesper Jung* and Thomas Søndergaard
Department of Physics and Nanotechnology, Aalborg University, Skjernvej 4A, DK-9220 Aalborg Øst, Denmark
(Received 24 January 2008; revised manuscript received 16 April 2008; published 10 June 2008)

A method for theoretical analysis of light scattering by arbitrary shaped two-dimensional scatterers placed near a planar surface between two media is presented. We show that light scattering by an object near a planar interface can be analyzed (exactly) using Green's function surface integral equations that are form invariant with those for a scatterer in free space. All effects of the planar interface structure are built into the Green's function. An approach for calculating the Green's function is presented along with far-field approximations that enable efficient evaluation of scattering into waves propagating out of the surface plane and, in the case of a planar metal-dielectric interface, evaluation of scattering into surface plasmon-polariton (SPP) waves propagating along the interface. Finally, the method is exemplified by analysis of light scattering by a nm-thin and sub-μm-wide gold strip (resonator) placed between 5 and 200 nm above a planar gold surface. We compare the amount of scattering going into the out-of-plane propagating waves and SPPs, respectively, and, for our configuration, scattering into out-of-plane propagating waves dominates. Scattering into SPP waves has a maximum if the strip is placed approximately 20 nm from the surface. We also find that when placing the gold strip more than 50 nm from the interface, the scattering resonance wavelength is practically independent of the distance, whereas changing the distance from 50 to 5 nm results in a ~400 nm redshift of the resonance wavelength.

DOI: 10.1103/PhysRevB.77.245310 PACS number(s): 73.20.Mf, 71.36.+c, 02.30.Rz, 02.60.Cb

I. INTRODUCTION

The Green's function surface integral equation method (GFSIEM) is well established for electromagnetic scattering problems in the microwave regime (see Ref. 1), and, more recently in the optical regime, the method has been applied to, e.g., analysis of diffractive optical elements,[2–4] resonances in dielectric microcavities,[5] scattering from layered spheres,[6] and metal nanostrip resonators.[7,8] The method has also been applied within quantum mechanics to calculate wave functions and eigenenergies, scattering cross sections, and spectral density functions of electrons of arbitrarily shaped nanostructures.[9] Essentially the method relates the field at any position inside a closed domain to the field and its normal derivative at the domain boundary via Green's function integral equations, and different domains are related via field boundary conditions. For scattering from objects in open infinite domains, the GFSIEM involves only integrals over the boundary of the scatterers and the radiating boundary condition is satisfied by an appropriate choice of the Green's function, which makes this approach computationally very efficient for small scatterers such as nanostructures.

The standard formulation of the GFSIEM is generally not well suited for scattering problems where a nanostructure is placed close to a planar surface, with the case of a perfect conducting surface as an exception.[1] This is because the GFSIEM will involve also boundary integrals over the planar surface, which is usually considered infinitely long. One approach to work around this problem in a diffractive-optics scattering problem has been to simply truncate this surface integral and ignore the part of the integral related to positions at a larger distance than some threshold from a surface nanostructure.[3] While this approximation might work for surface microstructures of very small height or depth, this approach is, in general, not practical nor satisfying from a theoretical point of view. In particular, for the case of a nanostructure close to a metal surface, scattering of light can involve the excitation of surface-plasmon polaritons (SPPs)[10] propagating hundreds of wavelengths along the surface and at least similar distances would have to be included in the surface integral when using the GFSIEM. As an exception, when, instead of a scattering problem, the GFSIEM is applied to find, e.g., plasmon polariton modes bound to and propagating along a triangular indentation in a metal surface, the assumption of negligible guided mode field at some limited distance from the indentation is an excellent approximation.[11]

In this paper we present a version of the GFSIEM that is well suited for theoretical analysis of scatterers close to a planar interface. Our primary motivation for this work is to extend previous modeling of metal nanostrip resonators in a homogeneous medium[7,8] to the case of such resonators placed close to a surface. Essentially, by construction of an appropriate Green's function, we eliminate the integral over the planar surface and, similar to the case of a scatterer in free space, it becomes sufficient to consider only integrals over the boundary of the scatterer itself, whereas all effects of the planar surface are accounted for by the Green's function. Related examples of Green's functions and their applications can be found in Refs. 12–23. In the case of a perfect conducting surface, such a version of the GFSIEM was arrived at by noticing that the field and Green's function were zero at the surface for *s* polarization, and the normal derivatives of the field and Green's function were zero at the surface for *p* polarization, resulting in no contribution from the surface integral.[1] In the general case considered here, where any refractive index for the material below the surface is allowed, the argument, which we present in the paper, is more complicated.

In order to be able to investigate the amount of light scattered separately into out-of-plane propagating and SPP waves, we define scattering cross sections, and introduce analytical far-field approximations for the Green's function containing the part of the Green's function related to out-of-plane propagating and SPP waves, respectively. Especially the latter part of the Green's function is obtained in the Appendix via an eigenmode-expansion technique.

The GFSIEM will then finally be exemplified for a gold nanostrip resonator placed close to a gold surface; in which case, we will investigate and compare how much light is scattered into SPP and out-of-plane propagating waves depending on the distance of the resonator to the gold surface, and how the presence of the gold surface influences the resonance wavelength.

The paper is organized as follows. Section II contains a presentation of the GFSIEM generalized to the case of scatterers placed close to an interface, including also a construction of the required Green's function and a discussion of the proof of the method. Far-field approximations of the Green's function and scattering cross-section definitions are presented in Sec. III where we separately consider out-of-plane propagating waves (Sec. III A) and excitation of SPPs in the case of a metal-dielectric interface (Sec. III B). The method is exemplified in Sec. IV for a gold nanostrip resonator placed close to a gold surface. Section V presents the conclusion. Lastly, the part of the Green's function that governs excitation of SPPs is derived in the Appendix.

II. METHOD

The situation that we consider is scattering of a monochromatic plane wave (angular frequency ω_0) by an arbitrary shaped two-dimensional scatterer Ω_2 (Fig. 1). The problem is reduced to a two-dimensional problem in the xy plane as the structure and fields are considered invariant under translation along the z axis. The incident wave is propagating in the xy plane. Both s and p polarizations of the incident field can be considered. For s polarization, the scalar surface integral equations are formulated by means of the electric field $[\mathbf{E}(\mathbf{r},\omega_0)=E(\mathbf{r},\omega_0)\hat{z}]$ and the magnetic field is afterward found using $\mathbf{H}(\mathbf{r},\omega_0)=i/(\mu_0\omega_0)\nabla\times\mathbf{E}(\mathbf{r},\omega_0)$. For p polarization, they are formulated by means of the magnetic field $[\mathbf{H}(\mathbf{r},\omega_0)=H(\mathbf{r},\omega_0)\hat{z}]$ and the electric field is afterward found using $\mathbf{E}(\mathbf{r},\omega_0)=-i/[\omega_0\varepsilon_0\varepsilon(\omega_0)]\nabla\times\mathbf{H}(\mathbf{r},\omega_0)$. When analyzing metal nanostrip resonators, the case where the incident field is p polarized is the interesting one because plasmons are p polarized. In the following, we therefore consider the case of p polarization.

We begin by introducing the scalar wave equation of the magnetic field $H(\mathbf{r},\omega_0)$

$$\left[-\frac{\nabla\varepsilon(\mathbf{r},\omega_0)\cdot\nabla}{\varepsilon(\mathbf{r},\omega_0)}+\nabla^2+k_0^2\varepsilon(\mathbf{r},\omega_0)\right]H(\mathbf{r},\omega_0)=0, \quad (1)$$

where $\varepsilon(\mathbf{r},\omega_0)$ is the space and frequency dependent complex relative dielectric constant, $k_0=\omega_0/c$ is the free space wave number, and c is the speed of light in vacuum. Outside Ω_2 the solution $H(\mathbf{r},\omega_0)$ to Eq. (1) that we search for is in the form of $H(\mathbf{r},\omega_0)=H_0(\mathbf{r},\omega_0)+H_s(\mathbf{r},\omega_0)$, where $H_0(\mathbf{r},\omega_0)$

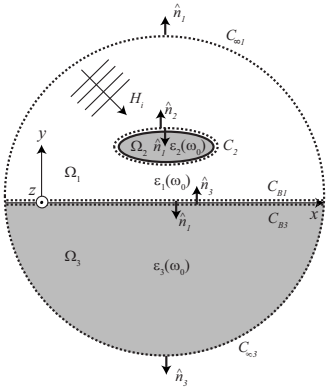

FIG. 1. A scatterer Ω_2 in a reference structure of two half planes Ω_1 and Ω_3. The incident field H_i is a monochromatic p-polarized wave propagating in the xy plane. The dielectric constants of the two half planes and the scatterer are $\varepsilon_1(\omega_0)$, $\varepsilon_3(\omega_0)$, and $\varepsilon_2(\omega_0)$, respectively. The boundary curve C_2 surrounds the scatterer Ω_2, C_{B1} is a boundary curve along the interface between the two half planes at $y=0^+$, C_{B3} is along the interface in the lower half plane at $y=0^-$, and the curves $C_{\infty 1}$ and $C_{\infty 3}$ are semicircles with infinite radii in the upper and the lower half planes, respectively.

is a solution to the wave equation of the reference structure [described by the relative dielectric constant $\varepsilon_{\mathrm{ref}}(\mathbf{r},\omega_0)$] with Ω_2 removed,

$$\left[-\frac{\nabla\varepsilon_{\mathrm{ref}}(\mathbf{r},\omega_0)\cdot\nabla}{\varepsilon_{\mathrm{ref}}(\mathbf{r},\omega_0)}+\nabla^2+k_0^2\varepsilon_{\mathrm{ref}}(\mathbf{r},\omega_0)\right]H_0(\mathbf{r},\omega_0)=0, \quad (2)$$

and $H_s(\mathbf{r},\omega_0)$ is the scattered field moving away from Ω_2. We define two scalar Green's functions; $g_1(\mathbf{r},\mathbf{r}',\omega_0)$ of the reference structure and $g_2(\mathbf{r},\mathbf{r}',\omega_0)$, which is used inside Ω_2. $g_1(\mathbf{r},\mathbf{r}',\omega_0)$ and $g_2(\mathbf{r},\mathbf{r}',\omega_0)$ must satisfy

$$\left[-\frac{\nabla\varepsilon_{\mathrm{ref}}(\mathbf{r},\omega_0)\cdot\nabla}{\varepsilon_{\mathrm{ref}}(\mathbf{r},\omega_0)}+\nabla^2+k_0^2\varepsilon_{\mathrm{ref}}(\mathbf{r},\omega_0)\right]g_1(\mathbf{r},\mathbf{r}',\omega_0)=-\delta(\mathbf{r},\mathbf{r}'), \quad (3)$$

$$[\nabla^2+k_0^2\varepsilon_2(\omega_0)]g_2(\mathbf{r},\mathbf{r}',\omega_0)=-\delta(\mathbf{r},\mathbf{r}'). \quad (4)$$

A. GFSIEM for scatterers close to an interface

The problem with the usual GFSIEM (Ref. 1) is that, when the reference structure consists of two half planes (Fig. 1), the boundary curve that we must integrate over is infinitely long. To circumvent this problem, we have developed a generalized version of the GFSIEM where the boundary between Ω_1 and Ω_3 is handled by constructing the Green's function and the incident field such that the boundary conditions of the electromagnetic field are satisfied for the reference structure. As we will prove using this special

constructed Green's function and this special constructed incident field of the reference structure, the usual surface integral equations are still valid and it is sufficient to integrate only over C_2 (Fig. 1),

$$H(\mathbf{r},\omega_0)=\begin{cases} H_0(\mathbf{r},\omega_0)+\oint_{C_2}[H(\mathbf{s}',\omega_0)\hat{n}'\cdot\nabla' g_1(\mathbf{r},\mathbf{s}',\omega_0)-g_1(\mathbf{r},\mathbf{s}',\omega_0)\hat{n}'\cdot\nabla' H_1(\mathbf{s}',\omega_0)]dl' & \text{for } \mathbf{r}\notin\Omega_2 \\ -\oint_{C_2}\left[H(\mathbf{s}',\omega_0)\hat{n}'\cdot\nabla' g_2(\mathbf{r},\mathbf{s}',\omega_0)-g_2(\mathbf{r},\mathbf{s}',\omega_0)\dfrac{\varepsilon_2(\omega_0)}{\varepsilon_1(\omega_0)}\hat{n}'\cdot\nabla' H_1(\mathbf{s}',\omega_0)\right]dl' & \text{for } \mathbf{r}\in\Omega_2 \end{cases} \tag{5}$$

where $\mathbf{s}'$ is a point on the boundary of Ω_2, $\hat{n}=\hat{n}_2=-\hat{n}_1$ is the outward normal of Ω_2, and the boundary condition $\hat{n}'\cdot\nabla' H_2(\mathbf{s}',\omega_0)=\varepsilon_2(\omega_0)/\varepsilon_1(\omega_0)\hat{n}'\cdot\nabla' H_1(\mathbf{s}',\omega_0)$ has been used, where H_1 and H_2 refer to the magnetic field approaching the boundary from mediums Ω_1 and Ω_2, respectively.

In the absence of the surface ($\varepsilon_3=\varepsilon_1$), the Green's functions $g_{1,2}(\mathbf{r},\mathbf{s}',\omega_0)$ are given by the zero-order Hankel function of second kind $g_{1,2}(\mathbf{r},\mathbf{s}',\omega_0)=H_0^{(2)}[k_0\sqrt{\varepsilon_{1,2}(\omega_0)}|\mathbf{r}-\mathbf{s}'|]/(4i)$. However, for a reference structure consisting of two half planes (Fig. 1), the Green's function used outside Ω_2, $g_1(\mathbf{r},\mathbf{r}',\omega_0)$, must be constructed such that the boundary condition of the electromagnetic field across the interface is fulfilled. The Green's function $g_1(\mathbf{r},\mathbf{s}',\omega_0)$ must be the solution to Eq. (3) that describes a field that propagates away from the source point. If it is assumed that the source point is in the upper half plane $y'>0$, the Green's function of the reference structure may be written as

$$g_1(\mathbf{r},\mathbf{r}',\omega_0)=g_+^d(\mathbf{r},\mathbf{r}',\omega_0)+g_+^i(\mathbf{r},\mathbf{r}',\omega_0)\quad \text{for}\quad y,\ y'>0, \tag{6a}$$

$$g_1(\mathbf{r},\mathbf{r}',\omega_0)=g_+^t(\mathbf{r},\mathbf{r}',\omega_0)\quad \text{for}\quad y'>0,\ y<0, \tag{6b}$$

where $g_+^d(\mathbf{r},\mathbf{r}',\omega_0)$ is the direct propagation from $\mathbf{r}'$ to $\mathbf{r}$ that can be evaluated analytically by means of the zero-order Hankel function of second kind, $g_+^i(\mathbf{r},\mathbf{r}',\omega_0)$ is the indirect propagation that includes a reflection at the boundary, and $g_+^t(\mathbf{r},\mathbf{r}',\omega_0)$ is the transmitted propagation. The propagators of the indirect and transmitted propagations cannot be evaluated analytically and must therefore be constructed by means of Sommerfeld integrals. This is accomplished by writing the propagators as expansions in the in-plane wave number k_x,

$$g_+^d(\mathbf{r},\mathbf{r}',\omega_0)=\frac{-i}{2\pi}\int_{k_x=0}^{\infty}\frac{1}{k_{y_1}}\cos(k_x|x-x'|)e^{-ik_{y_1}|y-y'|}dk_x \quad \text{for}\quad y,y'>0, \tag{7a}$$

$$g_+^i(\mathbf{r},\mathbf{r}',\omega_0)=\frac{-i}{2\pi}\int_{k_x=0}^{\infty}\frac{1}{k_{y_1}}\cos(k_x|x-x'|)r^p(k_x)e^{-ik_{y_1}(y+y')}dk_x \quad \text{for}\quad y,y'>0, \tag{7b}$$

$$g_+^t(\mathbf{r},\mathbf{r}',\omega_0)=\frac{-i}{2\pi}\int_{k_x=0}^{\infty}\frac{1}{k_{y_1}}\cos(k_x|x-x'|)t^p(k_x)e^{-i(k_{y_1}y'-k_{y_3}y)}dk_x \quad \text{for}\quad y'>0\quad\text{and}\quad y<0, \tag{7c}$$

where $k_x^2+k_{y_{1,3}}^2=\varepsilon_{1,3}(\omega_0)k_0^2$, $\mathrm{Im}(k_{y_{1,3}})\le 0$, and $r^p(k_x)$ and $t^p(k_x)$ are the Fresnel reflection and transmission coefficients for p-polarized light, which fulfill the boundary conditions of the electromagnetic field at the interface. From Eqs. (6a), (6b), and (7a)–(7c), it can be seen that if the observation point is above the boundary, a reflection term is added in order to construct the total propagator for each k_x, and if the observation point is below the boundary, a transmission term is constructed for each k_x. If the source point is below the boundary ($y'<0$), the Green's function is given as

$$g_1(\mathbf{r},\mathbf{r}',\omega_0)=g_-^t(\mathbf{r},\mathbf{r}',\omega_0)\quad \text{for}\quad y>0,\ y'<0, \tag{8a}$$

$$g_1(\mathbf{r},\mathbf{r}',\omega_0)=g_-^d(\mathbf{r},\mathbf{r}',\omega_0)+g_-^i(\mathbf{r},\mathbf{r}',\omega_0)\quad \text{for}\quad y,\ y'<0, \tag{8b}$$

where

$$g_-^d(\mathbf{r},\mathbf{r}',\omega_0)=\frac{-i}{2\pi}\int_{k_x=0}^{\infty}\frac{1}{k_{y_3}}\cos(k_x|x-x'|)e^{-ik_{y_3}|y-y'|}dk_x \quad \text{for}\quad y,y'<0, \tag{9a}$$

$$g_-^i(\mathbf{r},\mathbf{r}',\omega_0)=\frac{-i}{2\pi}\int_{k_x=0}^{\infty}\frac{1}{k_{y_3}}\cos(k_x|x-x'|)r^{p2}(k_x)e^{ik_{y_3}(y+y')}dk_x \quad \text{for}\quad y,y'<0, \tag{9b}$$

$$g_-^t(\mathbf{r},\mathbf{r}',\omega_0)=\frac{-i}{2\pi}\int_{k_x=0}^{\infty}\frac{1}{k_{y_3}}\cos(k_x|x-x'|)t^{p2}(k_x)e^{i(k_{y_3}y'-k_{y_1}y)}dk_x \quad \text{for}\quad y'<0\quad\text{and}\quad y>0. \tag{9c}$$

Here $r^{p2}(k_x)$ and $t^{p2}(k_x)$ are Fresnel reflection and transmission coefficients for light incident from the other side of the interface.

The field of the reference structure without the scatterer present, $H_0(\mathbf{r},\omega_0)$, must also be constructed such that the

boundary condition of the incident field is satisfied. If it is assumed that the incident field $H_i(\mathbf{r},\omega_0)$ is a monochromatic p-polarized plane wave and that Ω_2 is illuminated from the upper half plane (Fig. 1), then $H_0(\mathbf{r},\omega_0)$ may be written as

$$H_0(\mathbf{r},\omega_0) = e^{-ik_x x}[e^{ik_{y1}y} + r^p(k_x)e^{-ik_{y1}y}] \quad \text{for} \quad y > 0, \tag{10}$$

$$H_0(\mathbf{r},\omega_0) = e^{-ik_x x}t^p(k_x)e^{ik_{y3}y} \quad \text{for} \quad y < 0. \tag{11}$$

1. Proof of the generalized GFSIEM

In this section it is proved that Eq. (5) can [using the Green's function specified in Eqs. (6a), (6b), and (7a)–(7c), and the $H_0(\mathbf{r},\omega_0)$ specified in Eqs. (10) and (11)] be used to analyze scatterers close to a planar interface. The idea is to prove that the integral along the infinite boundary between Ω_1 and Ω_3 vanish. This is proven in the two cases where the observation point is either in the upper or the lower half plane; $\mathbf{r}\in\Omega_1$ and $\mathbf{r}\in\Omega_3$, respectively.

a. $\mathbf{r}\in\Omega_1$. Starting from Fig. 1, we set up a curve integral expression of the magnetic field as

$$\begin{aligned} H(\mathbf{r},\omega_0) = H_0(\mathbf{r},\omega_0) &+ \oint_{C_2} [g_1(\mathbf{r},\mathbf{s}',\omega_0)\hat{n}_1' \cdot \nabla' H(\mathbf{s}',\omega_0) \\ &- H(\mathbf{s}',\omega_0)\hat{n}_1' \cdot \nabla' g_1(\mathbf{r},\mathbf{s}',\omega_0)]dl' \\ &+ \int_{C_{B1}} [g_1(\mathbf{r},\mathbf{s}',\omega_0)\hat{n}_1' \cdot \nabla' H_s(\mathbf{s}',\omega_0) \\ &- H_s(\mathbf{s}',\omega_0)\hat{n}_1' \cdot \nabla' g_1(\mathbf{r},\mathbf{s}',\omega_0)]dl' \quad \text{for} \quad \mathbf{r} \in \Omega_1 \end{aligned} \tag{12}$$

where we have used that the surface integral expression involving $H_s(\mathbf{s}',\omega_0)$ along $C_{\infty 1}$ vanishes because the scattered field and $g_1(\mathbf{r},\mathbf{s}',\omega_0)$ satisfy the radiating boundary condition, and that the integral involving $H_0(\mathbf{s}',\omega_0)$ along $C_{\infty 1}+C_{B1}$ gives $H_0(\mathbf{r},\omega_0)$.

Now we must prove that the last integral along C_{B1} is zero. A closed-loop curve integral along $C_{\infty 3}+C_{B3}$ (Fig. 1) with the observation point $\mathbf{r}\in\Omega_1$ for the scattered part of the field may be written as

$$\begin{aligned} \int_{C_{B3}} &[g_1(\mathbf{r},\mathbf{s}',\omega_0)\hat{n}_3' \cdot \nabla' H_s(\mathbf{s}',\omega_0) \\ &- H_s(\mathbf{s}',\omega_0)\hat{n}_3' \cdot \nabla' g_1(\mathbf{r},\mathbf{s}',\omega_0)]dl' = 0 \quad \text{for} \quad \mathbf{r} \in \Omega_1, \end{aligned} \tag{13}$$

where it has been used that the scattered field and $g_1(\mathbf{r},\mathbf{s}',\omega_0)$ satisfy the radiating boundary condition such that there is no contribution to the integral along the semicircle with infinite radius, boundary curve $C_{\infty 3}$. Eq. (13) reveals that the integral along the interface at $y=0^-$ is zero. From Eqs. (6a), (6b), (7a)–(7c), (8a), (8b), and (9a)–(9c), it is given that

$$g_1(x,y;x',y'=0^+;\omega_0) = \frac{\varepsilon_3(\omega_0)}{\varepsilon_1(\omega_0)} g_1(x,y;x',y'=0^-;\omega_0), \tag{14a}$$

$$\frac{\partial}{\partial y'} g_1(x,y;x',y'=0^+;\omega_0) = \frac{\partial}{\partial y'} g_1(x,y;x',y'=0^-;\omega_0), \tag{14b}$$

which, together with the boundary conditions of both the magnetic field and the normal derivative of the magnetic field, show that the integrand of the curve integral along C_{B1} [Eq. (12)] is, with an opposite sign, identical to the integrand of the curve integral along C_{B3}, where the primed coordinate has been moved across the boundary from $y=0^+$ to $y=0^-$. Thus the integral along the boundary curve C_{B1} is proportional to the integral along C_{B3}, meaning that the integral along C_{B1} also vanishes. Eq. (12), therefore, becomes form invariant with the usual surface integral equation for $\mathbf{r}\in\Omega_1$ [cf. Eq. (5)].

b. $\mathbf{r}\in\Omega_3$. A curve integral expression of the magnetic field, where the integral is taken along the closed boundary curve $C_{B3}+C_{\infty 3}$ (cf. Fig. 1), may be written as

$$\begin{aligned} H(\mathbf{r},\omega_0) = H_0(\mathbf{r},\omega_0) &+ \int_{C_{B1}} [g_1(\mathbf{r},\mathbf{s}',\omega_0)\hat{n}_3' \cdot \nabla' H_s(\mathbf{s}',\omega_0) \\ &- H_s(\mathbf{s}',\omega_0)\hat{n}_3' \cdot \nabla' g_1(\mathbf{r},\mathbf{s}',\omega_0)]dl' \quad \text{for} \quad \mathbf{r} \in \Omega_3 \end{aligned} \tag{15}$$

where the integral along C_{B3} has been replaced by an integral along C_{B1}, similar to the integration shift above. A closed-loop curve integral expression for the scattered part of the field along the boundary of Ω_1 ($C_{\infty 1}+C_{B1}+C_2$) is zero if the observation point $\mathbf{r}\in\Omega_3$; thus, we may write

$$\begin{aligned} \oint_{C_2} &[g_1(\mathbf{r},\mathbf{s}',\omega_0)\hat{n}_1' \cdot \nabla' H_s(\mathbf{s}',\omega_0) \\ &- H_s(\mathbf{s}',\omega_0)\hat{n}_1' \cdot \nabla' g_1(\mathbf{r},\mathbf{s}',\omega_0)]dl' \\ = \int_{C_{B1}} &[g_1(\mathbf{r},\mathbf{s}',\omega_0)\hat{n}_3' \cdot \nabla' H_s(\mathbf{s}',\omega_0) \\ &- H_s(\mathbf{s}',\omega_0)\hat{n}_3' \cdot \nabla' g_1(\mathbf{r},\mathbf{s}',\omega_0)]dl' \quad \text{for} \quad \mathbf{r} \in \Omega_3. \end{aligned} \tag{16}$$

From Eq. (16) it can be seen that the curve integral along C_{B1} in Eq. (15) can be replaced with a curve integral along C_2. Eq. (15) can therefore be rewritten as

$$\begin{aligned} H(\mathbf{r},\omega_0) = H_0(\mathbf{r},\omega_0) &+ \oint_{C_2} [H(\mathbf{s}',\omega_0)\hat{n}_2' \cdot \nabla' g_1(\mathbf{r},\mathbf{s}',\omega_0) \\ &- g_1(\mathbf{r},\mathbf{s}',\omega_0)\hat{n}_2' \cdot \nabla' H(\mathbf{s}',\omega_0)]dl' \quad \text{for} \quad \mathbf{r} \in \Omega_3, \end{aligned} \tag{17}$$

where we have used

$$\oint_{C_2} [g_1(\mathbf{r},\mathbf{s}',\omega_0)\hat{n}_1' \cdot \nabla' H_0(\mathbf{s}',\omega_0) - H_0(\mathbf{s}',\omega_0)\hat{n}_1' \cdot \nabla' g_1(\mathbf{r},\mathbf{s}',\omega_0)]dl' = 0 \quad \text{for} \quad \mathbf{r} \in \Omega_3, \tag{18}$$

and $H(\mathbf{r},\omega_0)=H_0(\mathbf{r},\omega_0)+H_s(\mathbf{r},\omega_0)$.

Equation (17) reveals that the surface integral equation of the magnetic field for $\mathbf{r}\in\Omega_3$, also [as Eq. (12) for $\mathbf{r}\in\Omega_1$] is form invariant with the usual surface integral equation used outside the scatterer in the case of a homogenous reference space [cf. Eq. (5)]. This completes the proof of the generalized GFSIEM.

2. Self-consistent equations

In order to achieve self-consistent equations, we take the limit $\mathbf{r}\to\mathbf{s}$ of Eq. (5), where $\mathbf{s}$ is a point on C_2,

$$\frac{1}{2}H(\mathbf{s},\omega_0) = H_0(\mathbf{s},\omega_0) + \mathrm{PV}\oint_{C_2} [H(\mathbf{s}',\omega_0) \times \hat{n}' \cdot \nabla' g_1(\mathbf{s},\mathbf{s}',\omega_0) - g_1(\mathbf{s},\mathbf{s}',\omega_0) \times \hat{n}' \cdot \nabla' H_1(\mathbf{s}',\omega_0)]dl',$$

$$\frac{1}{2}H(\mathbf{s},\omega_0) = -\mathrm{PV}\oint_{C_2} \left[H(\mathbf{s}',\omega_0)\hat{n}' \cdot \nabla' g_2(\mathbf{s},\mathbf{s}',\omega_0) - g_2(\mathbf{s},\mathbf{s}',\omega_0)\frac{\varepsilon_2}{\varepsilon_1}\hat{n}' \cdot \nabla' H_1(\mathbf{s}',\omega_0)\right] dl,' \tag{19}$$

where the integrals have been rewritten as Cauchy principal values in order to handle the singularities of $\hat{n}\cdot\nabla g_{1,2}(\mathbf{s},\mathbf{s}',\omega_0)$. The singularities of $g_{1,2}(\mathbf{s},\mathbf{s}',\omega_0)$ are handled in the implementation of the method. At the singularity $\mathbf{s}=\mathbf{s}'$ the terms in the integrals involving $\hat{n}\cdot\nabla g_{1,2}(\mathbf{s},\mathbf{s}',\omega_0)$ give a contribution of $\pm H(\mathbf{s},\omega_0)/2$, where the $\pm$ depends on from which side the boundary curve is approached. Eq. (19) can be discretized and solved numerically, which yields the field and the normal derivative of the field on the surface of the scatterer. Using these, the field elsewhere can be found using Eq. (5).

Similar equations can be obtained for the *s*-polarization case by replacing the magnetic field with the electric field, by replacing the Fresnel reflection and transmission coefficients for *p* polarization with those for *s* polarization, and by using different boundary conditions when the self-consistent integral equations are constructed.

III. FAR-FIELD APPROXIMATIONS OF THE GREEN'S FUNCTION AND SCATTERING CROSS SECTIONS

In this section two different far-field approximations of the Green's function $g_1(\mathbf{r},\mathbf{r}',\omega_0)$ for a reference structure consisting of two half planes are presented and evaluated numerically, and related scattering cross sections are defined.

A. Out-of-plane scattering cross section

In order to evaluate the out-of-plane scattering, meaning the light scattered out of the surface plane (Fig. 2), an out-of-plane scattering cross section $\sigma_{\mathrm{ops}}(\omega_0)$ is defined as the time averaged flux of the Poynting vector of the scattered field through a semicircle with infinite radius in the upper half plane ($C_{\infty 1}$, cf. Fig. 2) divided by the time averaged Poynting vector of the incident field. As the electric and magnetic fields of the scattered field are proportional, perpendicular, and can locally be regarded as plane waves in the far field, the out-of-plane scattering cross section can be expressed as

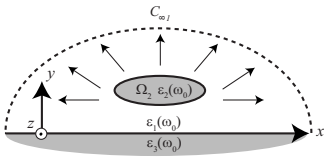

FIG. 2. The out-of-plane scattering cross section is evaluated by integrating the time averaged flux of the Poynting vector of the scattered field through the boundary curve $C_{\infty 1}$.

$$\sigma_{\mathrm{ops}}(\omega_0) = \frac{\int_{C_{\infty 1}} |H_s^{ff}(\mathbf{r},\omega_0)|^2 dl}{|H_i(\mathbf{r},\omega_0)|^2}, \tag{20}$$

where $H_i(\mathbf{r},\omega_0)$ is the incident monochromatic plane wave (Fig. 1) and $H_s^{ff}(\mathbf{r},\omega_0)$ is the resulting scattered far field, which can be evaluated as

$$H_s^{ff}(\mathbf{r},\omega_0) = \oint_{c_2} [H(\mathbf{s}',\omega_0)\hat{n}' \cdot \nabla' g_1^{ff}(\mathbf{r},\mathbf{s}',\omega_0) - g_1^{ff}(\mathbf{r},\mathbf{s}',\omega_0)\hat{n}' \cdot \nabla' H(\mathbf{s}',\omega_0)]dl', \tag{21}$$

where $g_1^{ff}(\mathbf{r},\mathbf{r}',\omega_0)$ is the far-field approximation of $g_1(\mathbf{r},\mathbf{r}',\omega_0)$ for $y,y'>0$, given as

$$g_1^{ff}(\mathbf{r},\mathbf{r}',\omega_0) = \frac{-i}{4}\sqrt{\frac{2}{\pi k_0\sqrt{\varepsilon_1(\omega_0)}r}}e^{i\pi/4}e^{-ik_0\sqrt{\varepsilon_1(\omega_0)}r} \times [e^{ik_0\sqrt{\varepsilon_1(\omega_0)}[\cos(\theta)x'+\sin(\theta)y']} + r^p(\theta) \times e^{ik_0\sqrt{\varepsilon_1(\omega_0)}[\cos(\theta)x'-\sin(\theta)y']}], \tag{22}$$

where θ is the positive angle measured from the x axis, which defines the direction of $\mathbf{r}=r(\hat{x}\cos\theta+\hat{y}\sin\theta)$. In the far field, the wave vector of the scattered field is parallel with $\mathbf{r}$. This is used in the calculation of $r^p(\theta)$.

B. Surface-plasmon polariton scattering cross section

If the lower half plane is a metal, light can be scattered into SPPs propagating along the metal surface. In order to evaluate how strongly light is scattered into SPPs, a SPP scattering cross section $\sigma_{\mathrm{SPP}}(\omega_0)$ is introduced as

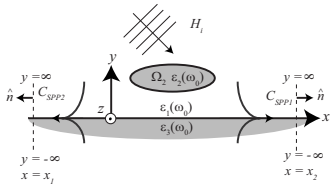

FIG. 3. The SPP scattering cross section is calculated by integrating the SPP contribution of the time averaged flux of the Poynting vector of the scattered field through the boundary curves C_{SPP1} and C_{SPP2}.

$$\sigma_{\mathrm{SPP}}(\omega_0) = \int_C \mathrm{Re}[\mathbf{E}_s^{\mathrm{SPP}}(\mathbf{r},\omega_0) \times \mathbf{H}_s^{\mathrm{SPP}*}(\mathbf{r},\omega_0)] \cdot \hat{n} dl \times \frac{1}{\mathrm{Re}[\mathbf{E}_i(\mathbf{r},\omega_0) \times \mathbf{H}_i^*(\mathbf{r},\omega_0)] \cdot \mathbf{k}/k}, \tag{23}$$

where the integral is over the two curves C_{SPP1} and C_{SPP2} (Fig. 3), the asterisk $*$ means complex conjugated, $\mathbf{E}_s^{\mathrm{SPP}}(\mathbf{r},\omega_0)$ and $\mathbf{H}_s^{\mathrm{SPP}}(\mathbf{r},\omega_0)$ are the field components of the scattered field that are related to SPPs, $\mathbf{E}_i(\mathbf{r},\omega_0)$ and $\mathbf{H}_i(\mathbf{r},\omega_0)$ are the field components of the incident wave, $\hat{n}$ is the normal vector to the curves C_{SPP1} and C_{SPP2} that points away from Ω_2, and $\mathbf{k}$ is the wave vector of the incident field with magnitude k. In order to calculate the scattered field that is related to SPPs propagating along the interface, the SPP contribution to the Green's function must be derived. The SPP Green's function is related to the SPP eigenmodes and can (cf. Appendix) in the far-field approximation be written as

$$g_{\mathrm{SPP}}^{ff}(\mathbf{r},\mathbf{r}',\omega_0) = -i\frac{\varepsilon_1(\omega_0)\varepsilon_3(\omega_0)}{\varepsilon_1(\omega_0)+\varepsilon_3(\omega_0)} \times \frac{1}{\sqrt{\frac{\varepsilon_1(\omega_0)}{(-\varepsilon_3(\omega_0))}}[\varepsilon_1(\omega_0)-\varepsilon_3(\omega_0)]} \times e^{-k_{\mathrm{SPP}}\sqrt{\varepsilon_1(\omega_0)/[-\varepsilon_3(\omega_0)]}(y+y')} e^{-ik_{\mathrm{SPP}}|x-x'|}, \tag{24}$$

for $y,y'>0$ and

$$g_{\mathrm{SPP}}^{ff}(\mathbf{r},\mathbf{r}',\omega_0) = -i\frac{\varepsilon_1(\omega_0)\varepsilon_3(\omega_0)}{\varepsilon_1(\omega_0)+\varepsilon_3(\omega_0)} \times \frac{1}{\sqrt{\frac{\varepsilon_1(\omega_0)}{(-\varepsilon_3(\omega_0))}}[\varepsilon_1(\omega_0)-\varepsilon_3(\omega_0)]} \times e^{-k_{\mathrm{SPP}}[\sqrt{\varepsilon_1(\omega_0)/[-\varepsilon_3(\omega_0)]}y' - \sqrt{[-\varepsilon_3(\omega_0)]/\varepsilon_1(\omega_0)}y]} \times e^{-ik_{\mathrm{SPP}}|x-x'|}, \tag{25}$$

for $y<0$ and $y'>0$, where k_{SPP} is the SPP wave number given as

$$k_{\mathrm{SPP}} = k_0\sqrt{\frac{\varepsilon_1(\omega_0)\varepsilon_3(\omega_0)}{\varepsilon_1(\omega_0)+\varepsilon_3(\omega_0)}}. \tag{26}$$

The SPP scattered far field can, using an expression similar to Eq. (21) where $g_1^{ff}(\mathbf{r},\mathbf{r}',\omega_0)$ has been replaced with $g_{\mathrm{SPP}}^{ff}(\mathbf{r},\mathbf{r}',\omega_0)$, be written as

$$H_s^{\mathrm{SPP}}(\mathbf{r},\omega_0) = H_s^{\mathrm{SPP}}(x,0)e^{-k_{\mathrm{SPP}}\sqrt{\frac{\varepsilon_1(\omega_0)}{(-\varepsilon_3(\omega_0))}}y} \quad \text{for} \quad y>0,$$

$$H_s^{\mathrm{SPP}}(\mathbf{r},\omega_0) = H_s^{\mathrm{SPP}}(x,0)e^{k_{\mathrm{SPP}}\sqrt{\frac{(-\varepsilon_3(\omega_0))}{\varepsilon_1(\omega_0)}}y} \quad \text{for} \quad y<0, \tag{27}$$

where $H_s^{\mathrm{SPP}}(x,0)$ is given as

$$H_s^{\mathrm{SPP}}(x,0) = A_{\mathrm{SPP}}(\omega_0)e^{\pm ik_{\mathrm{SPP}}x}, \tag{28}$$

where + is used for $x<x'$, − is used for $x>x'$, and $A_{\mathrm{SPP}}(\omega_0)$ is given as

$$A_{\mathrm{SPP}}(\omega_0) = \frac{-i\varepsilon_1(\omega_0)\varepsilon_3(\omega_0)}{[\varepsilon_1(\omega_0)+\varepsilon_3(\omega_0)]\sqrt{\frac{\varepsilon_1(\omega_0)}{(-\varepsilon_3(\omega_0))}}[\varepsilon_1(\omega_0)-\varepsilon_3(\omega_0)]} \times \oint_{C_2}\left\{H(\mathbf{s}',\omega_0)\left[\pm ik_{\mathrm{spp}}\hat{n}_x' - k_{\mathrm{SPP}}\sqrt{\frac{\varepsilon_1(\omega_0)}{[-\varepsilon_3(\omega_0)]}}\hat{n}_y'\right] - \hat{n}'\cdot\nabla' H(\mathbf{s}',\omega_0)\right\} e^{-k_{\mathrm{SPP}}\sqrt{\frac{\varepsilon_1(\omega_0)}{[-\varepsilon_3(\omega_0)]}}y'} e^{\pm ik_{\mathrm{SPP}}x'} dl' \tag{29}$$

where + is used for $x>x'$ and − is used for $x<x'$. Given $H_s^{\mathrm{SPP}}(\mathbf{r},\omega_0)$, $\sigma_{\mathrm{SPP}}(x_1,x_2,\omega_0)$ can readily be found as

$$\sigma_{\mathrm{SPP}}(x_1,x_2,\omega_0) = \frac{\varepsilon_1(\omega_0)}{k|H_i(\mathbf{r},\omega_0)|^2}[|H_{s,x_1<x'}^{\mathrm{SPP}}(x_1,0)|^2 + |H_{s,x_2>x'}^{\mathrm{SPP}}(x_2,0)|^2]\frac{1}{2}\left(\frac{\mathrm{Re}[k_{\mathrm{SPP}}/\varepsilon_1(\omega_0)]}{\mathrm{Re}\left\{k_{\mathrm{SPP}}\sqrt{\frac{\varepsilon_1(\omega_0)}{[-\varepsilon_3(\omega_0)]}}\right\}} + \frac{\mathrm{Re}[k_{\mathrm{SPP}}/\varepsilon_3(\omega_0)]}{\mathrm{Re}\left\{k_{\mathrm{SPP}}\sqrt{\frac{[-\varepsilon_3(\omega_0)]}{\varepsilon_1(\omega_0)}}\right\}}\right), \tag{30}$$

where the integration along y is from $-\infty$ to ∞, and x_1 and x_2 are the position of C_{SPP1} and C_{SPP2} on the x axis (cf. Fig. 3).

C. Testing the far-field approximation of the Green's function

In order to evaluate the far-field approximation of the Green's function [Eq. (22)], the exact Green's function and the far-field approximation of the Green's function are calculated for a fixed source point $\mathbf{r}'=(5\ \mathrm{nm})\hat{y}$ and for observation points along semicircles in the upper half plane with different radii (Figs. 4 and 5). At a wavelength of 500 nm, we consider an air-silver interface with $\varepsilon_3=-9.75748-0.31241i$ [24] and $\varepsilon_1=1$. Three different radii are used, 1, 10, and 100 μm. All curves on the figures are scaled with $\sqrt{r}$,

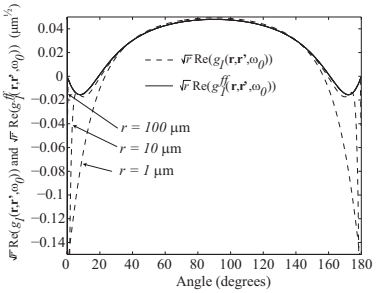

FIG. 4. The real part of the exact Green's function and the far-field approximation of the Green's function are calculated at semicircles in the upper half plane with different radii. All curves are scaled with $\sqrt{r}$. The configuration analyzed is an air-silver interface at $\lambda=500$ nm.

which means that the far-field approximation for all three radii becomes identical. The figures show that the difference between the far-field approximation and the exact Green's function decreases when r increases. The figures also show that for $r=1$ μm and $r=10$ μm, the deviations are large for angles close to 0° and 180°. This is partly because the far-field approximation of the Green's function does not contain a SPP contribution, which is contained in the exact Green's function (cf. Appendix). For $r=100$ μm, the SPP contribution to the Green's function will extinguish due to the losses in the metal. The propagation length of a SPP at $\lambda=500$ nm for an air-silver interface is approximately 20.6 μm. However, it must also be noted that for $r=100$ μm, a 100 times smaller angle is needed to get as close to the surface as for $r=1$ μm.

D. Testing the SPP approximation of the Green's function

The far-field approximation of the SPP contribution to the Green's function for $y,y'>0$ [Eq. (24)] is also investigated.

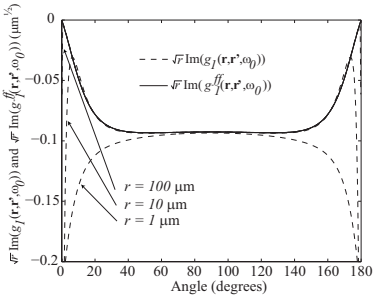

FIG. 5. The imaginary part of the exact Green's function and the far-field approximation of the Green's function are calculated at semicircles in the upper half plane with different radii. All curves are scaled with $\sqrt{r}$. The configuration analyzed is an air-silver interface at $\lambda=500$ nm.

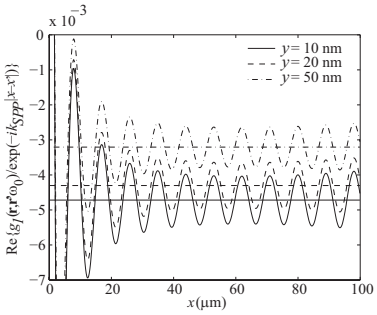

FIG. 6. The x dependence of the real part of the exact Green's function normalized with $\exp(-ik_{\mathrm{SPP}}|x-x'|)$ for $x'=0$, $y'=5$ nm, and for three different values of y. Also depicted is the real part of the front factor of the far-field SPP contribution to the Green's function $A(y,y')$ for the different values of y.

As above, at a wavelength of 500 nm, we consider an air-silver interface with $\varepsilon_3=-9.75748-0.31241i$. The far-field approximation of the SPP contribution to the Green's function can be written as $g_{\mathrm{SPP}}^{ff}(x,y,x',y',\omega_0)=A(y,y')\times\exp(-ik_{\mathrm{SPP}}|x-x'|)$. Fig. 6 (Fig. 7) depicts the real (imaginary) part of the exact Green's function $g_1(\mathbf{r},\mathbf{r}',\omega_0)$ normalized with $\exp(-ik_{\mathrm{SPP}}|x-x'|)$ as a function of x for a fixed source point $[\mathbf{r}'=5(\mathrm{nm})\hat{y}]$ and for three different values of y. Also depicted in Fig. 6 (Fig. 7) is the real (imaginary) part of the front factor $A(y,y',\omega_0)$. The fact that both the real and the imaginary parts of the exact Green's function for x, which is approximately larger than 20 μm, are fluctuating about the real and the imaginary parts of $A(y,y',\omega_0)$, respectively, show that the far-field approximation to the SPP contribution in some cases also works as an approximation to the exact Green's function.

IV. EXAMPLE OF A GOLD NANOSTRIP RESONATOR CLOSE TO A GOLD SURFACE

The out-of-plane and the SPP scattering cross sections [cf. Eqs. (20) and (30)] of a gold nanostrip resonator close to a

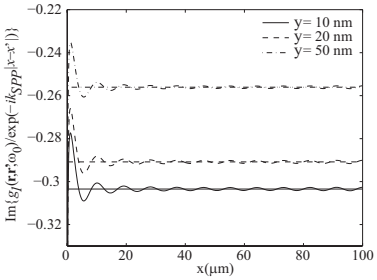

FIG. 7. The x dependence of the imaginary part of the exact Green's function normalized with $\exp(-ik_{\mathrm{SPP}}|x-x'|)$ for $x'=0$, $y'=0$, and for three different values of y. Also depicted is the imaginary part of the front factor of the far-field SPP contribution to the Green's function $A(y,y')$ for the different values of y.

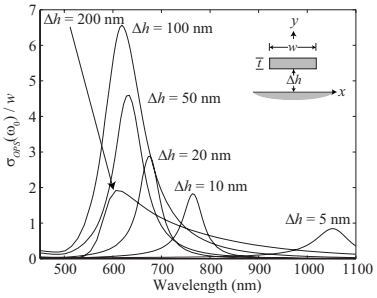

FIG. 8. The out-of-plane scattering cross section, as a function of the wavelength, for a rectangular gold nanostrip resonator ($t=10$ nm and $w=80$ nm) for different values of Δh, above a planar gold surface.

planar gold surface are calculated as a function of the wavelength for different distances between the resonator and the surface (Figs. 8 and 9). The relative dielectric constant of gold used in the calculations is interpolated from Ref. 25.

We consider a rectangular gold nanostrip resonator with $t=10$ nm and $w=80$ nm, where the corners have been rounded 2 nm (insets of Figs. 8 and 9). Both the out-of-plane and the SPP scattering cross sections are normalized with w, and are calculated for an incident p-polarized plane wave propagating at a $-90°$ angle with respect to the x axis. By comparing the out-of-plane (Fig. 8) scattering cross section with the SPP (Fig. 9) scattering cross section, it can be seen that the resonance wavelength of the out-of-plane and SPP scatterings are, within a few nanometers, identical. By increasing Δh, it is seen that the scattering resonance wavelength is blueshifted. This is expected since the mode index of a gap plasmon decreases with Δh in a related resonator configuration.[8] Going from $\Delta h=20$ nm to 100 nm, it is seen that the out-of-plane scattering is enhanced, whereas the scattering into SPPs are reduced. For distances below 50 nm the resonance wavelength is a strong function of Δh and,

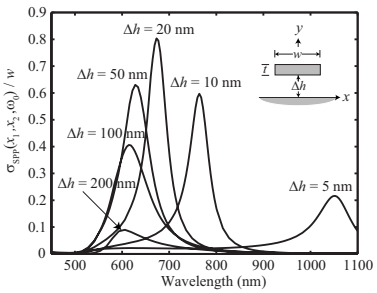

FIG. 9. The SPP scattering cross section, as a function of the wavelength, for a rectangular gold nanostrip resonator ($t=10$ nm and $w=80$ nm) for different values of Δh, above a planar gold surface. $\sigma_{\mathrm{SPP}}(x_1,x_2,\omega_0)$ is calculated for $-x_1=x_2=1$ μm (cf. Fig. 3).

e.g., by changing Δh from 5 to 50 nm, the resonance wavelength is blueshifted more than 400 nm. For distances above 50 nm, no significant resonance shift is observed. This is similar to what has been observed in Refs. 26–30.

V. CONCLUSION

In conclusion, we presented an approach for analyzing light scattering of a scatterer close to a planar surface. A version of the GFSIEM, where all effects of the planar surface are built into the Green's function of the reference structure, was derived. By using a special Green's function, we showed that scatterers placed above a planar surface can be analyzed using surface integral equations that are form invariant with those for the case of a scatterer in free space. We also presented analytical far-field approximations of the Green's function that enabled calculation of out-of-plane scattering and, in the case of a metal-dielectric interface, scattering of light into SPPs bound to and propagating along the interface. Both the out-of-plane and the SPP far-field approximations of the Green's function were tested against the exact Green's function, and it was justified that both approximations were applicable. Lastly, the method was utilized to analyze light scattering from a rectangular nanostrip gold resonator placed within close proximity of a planar gold surface. Both the out-of-plane and the SPP scattering cross sections were calculated over a wide range of wavelengths. For distances between the scatterer and the surface below 50 nm, we showed that, for the configuration studied, the resonance wavelength is a strong function of the distance. The scattering resonance wavelength is redshifted more than 400 nm when the distance is changed from 50 to 5 nm. This property enables one to tune the resonance wavelength of such a scattering system, meaning that a given configuration can be tuned to match, e.g., a laser frequency or a given transition in a molecule. The latter renders applications within sensing.

ACKNOWLEDGMENTS

The authors gratefully acknowledge the financial support (J.J. and T.S.) from the NABIIT project financed by the Danish Research Agency (Contract No. 2106-05-033) and (T.S.) from the Danish Research Council for Technology and Production.

APPENDIX: ANALYTICAL STUDY OF THE GREEN'S FUNCTION OF A METAL-DIELECTRIC INTERFACE IN TWO DIMENSIONS

In this Appendix, the Green's function of a two-dimensional ($\mathbf{r}=x\hat{x}+y\hat{y}$) reference structure is studied analytically for p polarization. The configuration studied is a dielectric medium for $y>0$ and a metal for $y<0$. We present a formulation of the Green's function for $y,y'>0$, where the Green's function is constructed from a summation over eigenfunctions. Two types of eigenfunctions must be considered; p-polarized plane waves being reflected at the surface and the SPP eigenmodes propagating along the metal-dielectric interface. Furthermore, the far-field approximation of the SPP contribution to the total Green's function is de-

rived. A detailed description of a similar method for constructing Green's tensors through an eigenmode expansion can be found in Ref. 31. For the three dimensional case a similar investigation of the Green's tensor has been made in Ref. 32.

We start the derivation with the wave equation of the magnetic field for a metal-dielectric interface, which can be written as

$$\Theta H(\mathbf{r},\omega_0) = 0, \tag{A1}$$

and the Green's function, which is a solution to

$$\Theta g(\mathbf{r},\mathbf{r}'\omega_0) = -\delta(\mathbf{r}-\mathbf{r}'), \tag{A2}$$

where the operator Θ is given as

$$\Theta = -\frac{\nabla\varepsilon(\mathbf{r},\omega_0)\cdot\nabla}{\varepsilon(\mathbf{r},\omega_0)} + \nabla^2 + k_0^2\varepsilon(\mathbf{r},\omega_0). \tag{A3}$$

It is, however, convenient to introduce a related Green's function $G_g(\mathbf{r},\mathbf{r}',\omega_0)$ defined by

$$\Theta_g G_g(\mathbf{r},\mathbf{r}',\omega_0) = -\delta(\mathbf{r}-\mathbf{r}'), \tag{A4}$$

where

$$\Theta_g = -\frac{\nabla\varepsilon(\mathbf{r},\omega_0)\cdot\nabla}{\varepsilon(\mathbf{r},\omega_0)^2} + \frac{\nabla^2}{\varepsilon(\mathbf{r},\omega_0)} + k_0^2. \tag{A5}$$

The Green's function that we seek is then given by $G_g(\mathbf{r},\mathbf{r}',\omega_0)=g(\mathbf{r},\mathbf{r}',\omega_0)\varepsilon(\mathbf{r}',\omega_0)$. In general for a complex $\varepsilon(\mathbf{r},\omega_0)$, Θ_g is non-Hermitian. However, for passive dielectric media, $\varepsilon(\mathbf{r},\omega_0)$ is real and Θ_g is Hermitian. If we assume that Θ_g is Hermitian and that $\{g_i(\mathbf{r})\}$ form a complete orthogonal set of eigenfunctions to Θ_g with corresponding eigenvalues $\{\lambda_i\}$, the Green's function can be constructed as

$$G_g(\mathbf{r},\mathbf{r}',\omega_0) = -\sum_i \frac{g_i(\mathbf{r},\omega_0)[g_i(\mathbf{r}',\omega_0)]^*}{N\lambda_i}, \tag{A6}$$

where the symbol Σ_i must be interpreted as $\Sigma_i' + \int di$, where Σ_i' is a genuine summation of the eigenfunctions belonging to the discrete part of the spectrum of Θ_g, and $\int di$ is an integral over the continuous part of the spectrum.[33] The constant N is calculated from normalization of the eigenfunctions as

$$N\delta_{ij} = \int [g_i(\mathbf{r},\omega_0)]^* g_j(\mathbf{r},\omega_0) d^2r, \tag{A7}$$

and the eigenfunctions $g_i(\mathbf{r},\omega_0)$ are solutions to the eigenvalue equation

$$\Theta_g g_i(\mathbf{r},\omega_0) = \lambda_i g_i(\mathbf{r},\omega_0). \tag{A8}$$

1. Contribution from *p*-polarized plane waves

For $y>0$, the eigenfunctions of the p-polarized plane waves may be written as

$$g_{k_x,k_{y1}}(\mathbf{r},\omega_0) = e^{-ik_x x}(e^{ik_{y1}y} + r^p(k_x)e^{-ik_{y1}y}), \tag{A9}$$

which, using Eq. (A8), yields the eigenvalues

$$\lambda_{k_x,k_{y1}} = k_0^2 - \frac{1}{\varepsilon_1}(k_x^2 + k_{y1}^2). \tag{A10}$$

The normalization factor is found using Eq. (A7),

$$\begin{aligned} &N\delta(k_x - k_x')\delta(k_{y1} - k_{y1}') \\ &= \int_{x=-\infty}^{\infty}\int_{y=0}^{\infty} [g_{k_x,k_{y1}}(\mathbf{r},\omega_0)]^* g_{k_x',k_y'}(\mathbf{r},\omega_0) dy dx \\ &= (2\pi)^2\delta(k_x - k_x')\delta(k_y - k_y'), \end{aligned} \tag{A11}$$

where it has been used that $r^p[r^p]^*=1$, because all dielectric constants are assumed to be real. From Eq. (A11) it is seen that $N=4\pi^2$. Using Eqs. (A6) and (A9)–(A11), the contribution to $G_g(\mathbf{r},\mathbf{r}',\omega_0)$ from the summation over the p-polarized plane waves can, for $y,y'>0$, be written as

$$\begin{aligned} G_g^P(\mathbf{r},\mathbf{r}',\omega_0) = \frac{-\varepsilon_1(\omega_0)}{4\pi^2}\int_{-\infty}^{\infty} e^{-ik_x(x-x')} \\ \times \int_{-\infty}^{\infty} \frac{e^{-ik_{y1}(y-y')} + r^p(k_x)e^{-ik_{y1}(y+y')}}{\varepsilon_1(\omega_0)k_0^2 - k_x^2 - k_{y1}^2 - i0^+} dk_{y1}dk_x, \end{aligned} \tag{A12}$$

where the $-i0^+$ term in the denominator effectively adds a homogenous solution to Eq. (A4) and leads to the retarded Green's function, describing waves propagating away from the point $\mathbf{r}'$, and it has been used that $[r^p(-k_{y1})]^*=r^p$ and $r^p[r^p]^*=1$. The integration over k_{y1} can be handled using the residue theorem where the poles in $1/[\varepsilon_1(\omega_0)k_0^2-k_x^2-k_{y1}^2 - i0^+]$ and r^p must be considered. In order to find the residues at the poles in $1/[\varepsilon_1(\omega_0)k_0^2-k_x^2-k_{y1}^2-i0^+]$, Eq. (A12) is rewritten as

$$G_g^P(\mathbf{r},\mathbf{r}',\omega_0) = \frac{-\varepsilon_1(\omega_0)}{4\pi^2}\int_{-\infty}^{\infty} e^{-ik_x(x-x')}\int_{-\infty}^{\infty} f(k_{y1})dk_{y1}dk_x, \tag{A13}$$

where

$$\begin{aligned} f(k_{y1}) = \frac{-e^{-ik_{y1}(y-y')} - r^p(k_x)e^{-ik_{y1}(y+y')}}{(k_{y1} - \sqrt{\varepsilon_1(\omega_0)k_0^2 - k_x^2 - i0^+})} \\ \times \frac{1}{(k_{y1} + \sqrt{\varepsilon_1(\omega_0)k_0^2 - k_x^2 - i0^+})}. \end{aligned} \tag{A14}$$

From Eq. (A14) it can be seen that the pole of the first fraction is in the lower half plane and that the pole of the second fraction is in the upper half plane [due to our sign convention $\sqrt{-a}=-i\sqrt{a}$, where a is a real positive number]. Using the residue theorem to handle the k_{y1} integration, considering only the poles of $1/[\varepsilon_1(\omega_0)k_0^2-k_x^2-k_{y1}^2]$, yields

$$G_g^{P1}(\mathbf{r},\mathbf{r}',\omega_0) = \frac{-\varepsilon_1(\omega_0)i}{4\pi}\int_{-\infty}^{\infty} e^{-ik_x(x-x')} \times\left[\frac{1}{k_{y1}}e^{-ik_{y1}|y-y'|} + \frac{r^p(k_x)}{k_{y1}}e^{-ik_{y1}(y+y')}\right]dk_x, \tag{A15}$$

where now $k_{y1}^2+k_x^2=\varepsilon_1(\omega_0)k_0^2$, $\mathrm{Im}(k_{y1})\leq 0$. In order to prevent the exponential from exploding, the integral of the term involving $e^{-ik_{y1}(y-y')}$ must be taken counterclockwise around a simple closed part in the upper half plane for $y<y'$, and for $y>y'$, it must be taken clockwise in the lower half plane. This explains why the absolute value is introduced in the result. For the term involving $e^{-ik_{y1}(y+y')}$, the contour integral is always taken clockwise in the lower half plane.

In order to calculate the total contribution to the Green's function from the p-polarized eigenfunctions, the contribution from the residue at the pole in $r^p(k_x)$ must also be calculated. Thus the pole $k_{y1}^{\mathrm{pole}}=-\varepsilon_1(\omega_0)k_{y3}/\varepsilon_3(\omega_0)$ in $r^p(k_x)$ must be considered. Here it is important to remember that k_{y3} is a function of k_{y1}. The relation between k_{y1} and k_{y3} can be written as

$$k_{y3}^2 = k_x^2\left[\frac{\varepsilon_3(\omega_0)}{\varepsilon_1(\omega)}-1\right]+\frac{\varepsilon_3(\omega_0)}{\varepsilon_1(\omega)}k_{y1}^2. \tag{A16}$$

Using Eq. (A16), the pole can be rewritten as $k_{y1}^{\mathrm{pole}} =-i\sqrt{\varepsilon_1(\omega_0)/(-\varepsilon_3(\omega_0))}|k_x|$. The denominator of $r^p(k_x)$ divided by $\varepsilon_3(\omega_0)$ can, using Eq. (A16), be written as

$$k_{y1}-i\frac{\varepsilon_1(\omega_0)}{\varepsilon_3(\omega_0)}\sqrt{\frac{-\varepsilon_3(\omega_0)}{\varepsilon_1(\omega_0)}k_{y1}^2+k_x^2\left[\frac{-\varepsilon_3(\omega_0)}{\varepsilon_1(\omega_0)}+1\right]}. \tag{A17}$$

If Eq. (A17) around the simple pole $k_{y1}^{\mathrm{pole}} =-i\sqrt{\varepsilon_1(\omega_0)/(-\varepsilon_3(\omega_0))}|k_x|$ is written as a Taylor series, $r^p(k_x)$ can be expressed as

$$r^p(k_x)\approx\frac{k_{y1}-\frac{\varepsilon_1(\omega_0)}{\varepsilon_3(\omega_0)}k_{y3}}{\left[k_{y1}+i\sqrt{\frac{\varepsilon_1(\omega_0)}{-\varepsilon_3(\omega_0)}}|k_x|\right]\left[1-\frac{\varepsilon_1(\omega_0)}{\varepsilon_3(\omega_0)}\right]}. \tag{A18}$$

Using the residue theorem and Eq. (A18), the contribution to $G_g^P(\mathbf{r},\mathbf{r}',\omega_0)$ from the pole in $r^p(k_x)$, $G_g^{P2}(\mathbf{r},\mathbf{r}',\omega_0)$, is calculated as

$$G_g^{P2}(\mathbf{r},\mathbf{r}',\omega_0) = \frac{\varepsilon_1(\omega_0)\varepsilon_3(\omega_0)}{\pi[\varepsilon_1(\omega_0)+\varepsilon_3(\omega_0)]} \times\int_{k_x=-\infty}^{\infty}\frac{|k_x|e^{-ik_x(x-x')}e^{-|k_x|\sqrt{\frac{\varepsilon_1(\omega_0)}{-\varepsilon_3(\omega_0)}}(y+y')}}{(k_{\mathrm{SPP}}^2-k_x^2-i0^+)\sqrt{\frac{\varepsilon_1(\omega_0)}{[-\varepsilon_3(\omega_0)]}}} \times\frac{1}{\left[\frac{-\varepsilon_3(\omega_0)}{\varepsilon_1(\omega_0)}+1\right]}dk_x, \tag{A19}$$

where $k_{\mathrm{SPP}}=k_0\sqrt{\varepsilon_1(\omega_0)\varepsilon_3(\omega_0)/[\varepsilon_1(\omega_0)+\varepsilon_3(\omega_0)]}$.

The total contribution to the Green's function for the p-polarized plane wave eigenfunctions is given as

$$G_g^P(\mathbf{r},\mathbf{r}',\omega_0) = G_g^{P1}(\mathbf{r},\mathbf{r}',\omega_0)+G_g^{P2}(\mathbf{r},\mathbf{r}',\omega_0). \tag{A20}$$

2. Contribution from surface-plasmon polaritons

For $y>0$, the SPP eigenfunction of the metal-dielectric interface may be written as

$$g_{k_x}(\mathbf{r},\omega_0) = e^{-ik_x x}e^{-|k_x|\sqrt{\frac{\varepsilon_1(\omega_0)}{[-\varepsilon_3(\omega_0)]}}y}, \tag{A21}$$

and for $y<0$,

$$g_{k_x}(\mathbf{r},\omega_0) = e^{-ik_x x}e^{|k_x|\sqrt{\frac{[-\varepsilon_3(\omega_0)]}{\varepsilon_1(\omega_0)}}y}, \tag{A22}$$

which, using Eq. (A8), yields the eigenvalues

$$\lambda_{k_x} = k_0^2 - k_x^2\frac{\varepsilon_1(\omega_0)+\varepsilon_3(\omega_0)}{\varepsilon_1(\omega_0)\varepsilon_3(\omega_0)}. \tag{A23}$$

The normalization factor is found using Eq. (A7) as

$$\begin{aligned} N\delta(k_x-k_x') &= \int_{x=-\infty}^{\infty}\int_{y=-\infty}^{\infty}[g_{k_x}(\mathbf{r},\omega_0)]^* g_{k_x'}(\mathbf{r},\omega_0)dxdy \\ &= \delta(k_x-k_x')2\pi\left\{\int_{y=0}^{\infty}e^{-2|k_x|\sqrt{\varepsilon_1(\omega_0)/[\varepsilon_3(\omega_0)]}y}dy\right. \\ &\quad \left.+\int_{y=-\infty}^{0}e^{2|k_x|\sqrt{[-\varepsilon_3(\omega_0)]/\varepsilon_1(\omega_0)}y}dy\right\}, \end{aligned} \tag{A24}$$

which yields

$$N = \frac{\pi}{|k_x|}\sqrt{\frac{\varepsilon_1(\omega_0)}{[-\varepsilon_3(\omega_0)]}}\left[1-\frac{\varepsilon_3(\omega_0)}{\varepsilon_1(\omega_0)}\right]. \tag{A25}$$

For $y,y'>0$, the contribution to the total Green's function $G_g(\mathbf{r},\mathbf{r}',\omega_0)$ from the SPP eigenfunctions $G_g^{\mathrm{SPP}}(\mathbf{r},\mathbf{r}',\omega_0)$ can, using Eq. (A6), be written as

$$G_g^{\mathrm{SPP}}(\mathbf{r},\mathbf{r}',\omega_0) = -\frac{\varepsilon_1(\omega_0)\varepsilon_3(\omega_0)}{\pi[\varepsilon_1(\omega_0)+\varepsilon_3(\omega_0)]} \times\int_{k_x=-\infty}^{\infty}\frac{|k_x|e^{-ik_x(x-x')}e^{-|k_x|\sqrt{\frac{\varepsilon_1(\omega_0)}{-\varepsilon_3(\omega_0)}}(y+y')}}{(k_{\mathrm{SPP}}^2-k_x^2-i0^+)\sqrt{\frac{\varepsilon_1(\omega_0)}{[-\varepsilon_3(\omega_0)]}}} \times\frac{1}{\left[\frac{-\varepsilon_3(\omega_0)}{\varepsilon_1(\omega_0)}+1\right]}dk_x, \tag{A26}$$

where $k_{\mathrm{SPP}}=k_0\sqrt{\varepsilon_1(\omega_0)\varepsilon_3(\omega_0)/[\varepsilon_1(\omega_0)+\varepsilon_3(\omega_0)]}$ and $i0^+$ has been subtracted in the denominator in order to get the retarded Green's function. By comparing Eq. (A26) to Eq. (A19), it is seen that the SPP contribution to the total Green's function is, with an opposite sign, identical to the contribution related to the pole in $r^p(k_x)$, $G_g^{P2}(\mathbf{r},\mathbf{r}',\omega_0)$. This means that the two terms cancel each other in the total Green's function $G_g(\mathbf{r},\mathbf{r}',\omega_0)$.

3. Total Green's function

The total Green's function $G_g(\mathbf{r},\mathbf{r}',\omega_0)$ for $y,y'>0$ is the sum of Eqs. (A20) and (A26), thus,

$$G_g(\mathbf{r},\mathbf{r}'\omega_0) = G_g^P(\mathbf{r},\mathbf{r}'\omega_0) + G_g^{\mathrm{SPP}}(\mathbf{r},\mathbf{r}'\omega_0)$$
$$= G_g^{P1}(\mathbf{r},\mathbf{r}'\omega_0)$$
$$= \frac{-\varepsilon_1(\omega_0)i}{2\pi}\int_0^\infty \frac{1}{k_{y1}}\cos[k_x(x-x')]$$
$$\times[e^{-ik_{y1}|y-y'|} + r^p(k_x)e^{-ik_{y1}(y+y')}]dk_x, \tag{A27}$$

where the integral over k_x from $-\infty$ to ∞, has been rewritten as an integral from zero to ∞.

The Green's function that we seek can now be determined using $G_g(\mathbf{r},\mathbf{r},\omega_0)=g(\mathbf{r},\mathbf{r},\omega_0)\varepsilon_1(\omega_0)$, yielding

$$g(\mathbf{r},\mathbf{r}'\omega_0) = \frac{-i}{2\pi}\int_0^\infty \frac{1}{k_{y1}}\cos[k_x(x-x')]$$
$$\times[e^{-ik_{y1}|y-y'|} + r^p(k_x)e^{-ik_{y1}(y+y')}]dk_x, \tag{A28}$$

which, by comparison with Eqs. (6a), (7a), and (7b), is identical to the Green's function used for $y,y'>0$ outside Ω_2. If the lower medium is a dielectric, Eq. (A28) is still a valid Green's function because then there is no pole in $r^p(k_x)$ and $G^{\mathrm{SPP}}(\mathbf{r},\mathbf{r}',\omega_0)$ does not exist.

4. Far-field approximation of the SPP contribution to the Green's function

Using that $\lim y\to 0$ for $1/(x\pm iy)=PV(1/x)\mp i\pi\delta(x)$, where PV is defined as Cauchy principal value, $G_g^{\mathrm{SPP}}(\mathbf{r},\mathbf{r}'\omega_0)$ in Eq. (A26) can be rewritten as

$$G_g^{\mathrm{SPP}}(\mathbf{r},\mathbf{r}'\omega_0) = -\frac{\varepsilon_1(\omega_0)\varepsilon_3(\omega_0)}{\varepsilon_1(\omega_0)+\varepsilon_3(\omega_0)}$$
$$\times\left[PV\int_{k_x=-\infty}^{\infty}\frac{|k_x|e^{-ik_x(x-x')}e^{-|k_x|\sqrt{\frac{\varepsilon_1(\omega_0)}{-\varepsilon_3(\omega_0)}}(y+y')}}{\pi(k_{\mathrm{SPP}}^2-k_x^2)\sqrt{\frac{\varepsilon_1(\omega_0)}{[-\varepsilon_3(\omega_0)]}}}\right.$$
$$\times\frac{1}{\left[\frac{-\varepsilon_3(\omega_0)}{\varepsilon_1(\omega_0)}+1\right]}dk_x + \frac{i}{\sqrt{\frac{\varepsilon_1(\omega_0)}{[-\varepsilon_3(\omega_0)]}}\left[\frac{-\varepsilon_3(\omega_0)}{\varepsilon_1(\omega_0)}+1\right]}$$
$$\times e^{-k_{\mathrm{SPP}}\sqrt{\varepsilon_1(\omega_0)/[-\varepsilon_3(\omega_0)]}(y+y')}$$
$$\left.\times\cos[k_{\mathrm{SPP}}(x-x')]\right]. \tag{A29}$$

The far-field approximation must be on the form

$$G_{g,\mathrm{SPP}}^{ff}(\mathbf{r},\mathbf{r}'\omega_0) = Ae^{-ik_{\mathrm{SPP}}|x-x'|}\times e^{-k_{\mathrm{SPP}}\sqrt{\varepsilon_1(\omega_0)/[-\varepsilon_3(\omega_0)]}(y+y')}. \tag{A30}$$

From Eq. (A29), we identify the constant A as

$$A = \frac{-i\varepsilon_1(\omega_0)\varepsilon_3(\omega_0)}{[\varepsilon_1(\omega_0)+\varepsilon_3(\omega_0)]\left(\sqrt{\frac{\varepsilon_1(\omega_0)}{[-\varepsilon_3(\omega_0)]}}\left[\frac{-\varepsilon_3(\omega_0)}{\varepsilon_1(\omega_0)}+1\right]\right)}. \tag{A31}$$

The far-field approximation of the Green's function that we seek is given from $g_{\mathrm{SPP}}^{ff}(\mathbf{r},\mathbf{r}',\omega_0)=G_{g,\mathrm{SPP}}^{ff}(\mathbf{r},\mathbf{r}',\omega_0)/\varepsilon_1(\omega_0)$, which yields

$$g_{\mathrm{SPP}}^{ff}(\mathbf{r},\mathbf{r}',\omega_0) = -i\frac{\varepsilon_1(\omega_0)\varepsilon_3(\omega_0)}{\varepsilon_1(\omega_0)+\varepsilon_3(\omega_0)}$$
$$\times\frac{1}{\sqrt{\frac{\varepsilon_1(\omega_0)}{(-\varepsilon_3(\omega_0))}}[\varepsilon_1(\omega_0)-\varepsilon_3(\omega_0)]}$$
$$\times e^{-k_{\mathrm{SPP}}\sqrt{\varepsilon_1(\omega_0)/[-\varepsilon_3(\omega_0)]}(y+y')}e^{-ik_{\mathrm{SPP}}|x-x'|}, \tag{A32}$$

for $y,y'>0$. For $y<0$ and $y'>0$, both eigenfunctions on the form of Eqs. (A21) and (A22) must be used to construct the Green's function. This results in the far-field approximation

$$g_{\mathrm{SPP}}^{ff}(\mathbf{r},\mathbf{r}',\omega_0) = -i\frac{\varepsilon_1(\omega_0)\varepsilon_3(\omega_0)}{\varepsilon_1(\omega_0)+\varepsilon_3(\omega_0)}$$
$$\times\frac{1}{\sqrt{\frac{\varepsilon_1(\omega_0)}{(-\varepsilon_3(\omega_0))}}[\varepsilon_1(\omega_0)-\varepsilon_3(\omega_0)]}$$
$$\times e^{-k_{\mathrm{SPP}}\{\sqrt{\varepsilon_1(\omega_0)/[-\varepsilon_3(\omega_0)]}y'-\sqrt{[-\varepsilon_3(\omega_0)]/\varepsilon_1(\omega_0)}y\}}$$
$$\times e^{-ik_{\mathrm{SPP}}|x-x'|}. \tag{A33}$$

These two far-field approximations of the SPP contribution to the total Green's function are used in the evaluation of the SPP scattering cross section in Sec. IV.

*jung@nano.aau.dk

[1] J. Jin, *The Finite Element Method in Electromagnetics*, 2nd ed. (Wiley, New York, 2002).
[2] D. W. Prather, M. S. Mirotznik, and J. N. Mait, J. Opt. Soc. Am. A **14**, 34 (1997).
[3] D. W. Prather, J. N. Mait, M. S. Mirotznik, and J. P. Collins, J. Opt. Soc. Am. A **15**, 1599 (1998).
[4] J. Liu, B.-Y. Gu, B.-Z. Dong, and G.-Z. Yang, J. Opt. Soc. Am. A **18**, 526 (2001).
[5] J. Wiersig, J. Opt. A, Pure Appl. Opt. **5**, 53 (2003).
[6] M. K. Choi, J. Opt. Soc. Am. A **18**, 577 (2001).
[7] T. Søndergaard and S. I. Bozhevolnyi, Phys. Rev. B **75**, 073402 (2007).
[8] T. Søndergaard and S. I. Bozhevolnyi, Phys. Status Solidi B **245**, 9 (2008)
[9] P. A. Knipp and T. L. Reinecke, Phys. Rev. B **54**, 1880 (1996).
[10] H. Raether, *Surface Plasmons–on Smooth and Rough Surfaces and on Gratings*, 1st ed. (Springer-Verlag, Berlin, 1988).
[11] I. V. Novikov and A. A. Maradudin, Phys. Rev. B **66**, 035403 (2002).
[12] L. Novotny, B. Hecht, and D. W. Pohl, J. Appl. Phys. **81**, 1798 (1997).

[13] M. S. Tomaš, Phys. Rev. A **51**, 2545 (1995).
[14] P. I. Geshev, S. Klein, T. Witting, K. Dickmann, and M. Hietschold, Phys. Rev. B **70**, 075402 (2004).
[15] P. I. Geshev and K. Dickmann, J. Opt. A, Pure Appl. Opt. **8**, S161 (2006).
[16] C. Hooijer, G.-X. Li, K. Allaart, and D. Lenstra, IEEE J. Quantum Electron. **37**, 1161 (2001).
[17] L. Novotny and B. Hecht, *Principles of Nano-Optics*, 1st ed. (Cambridge University Press, Cambridge, England, 2006).
[18] L. M. Brekhovskikh, *Waves in Layered Media*, 2nd ed. (Academic, New York, 1980).
[19] M. Paulus, P. Gay-Balmaz, and O. J. F. Martin, Phys. Rev. E **62**, 5797 (2000).
[20] M. Paulus and O. J. F. Martin, J. Opt. Soc. Am. A **18**, 854 (2001).
[21] O. J. F. Martin, J. Microsc. **194**, 235 (1999).
[22] C. Girard, A. Dereux, O. J. F. Martin, and M. Devel, Phys. Rev. B **52**, 2889 (1995).
[23] P. Gay-Balmaz and O. J. F. Martin, Opt. Commun. **184**, 37 (2000).
[24] E. Palik, *Handbook of Optical Constants of Solids*, 1st ed. (Academic, New York, 1985).
[25] P. B. Johnson and R. W. Christy, Phys. Rev. B **6**, 4370 (1972).
[26] G. Lèvêque and O. J. F. Martin, Opt. Lett. **31**, 2750 (2006).
[27] G. Lèvêque and O. J. F. Martin, Opt. Express **14**, 9971 (2006).
[28] A. Christ, T. Zentgraf, S. G. Tikhodeev, N. A. Gippius, O. J. F. Martin, J. Kuhl, and H. Giessen, Phys. Status Solidi B **243**, 2344 (2006)
[29] A. Christ, T. Zentgraf, S. G. Tikhodeev, N. A. Gippius, J. Kuhl, and H. Giessen, Phys. Rev. B **74**, 155435 (2006).
[30] A. Christ, G. Lèvêque, O. J. F. Martin, T. Zentgraf, J. Kuhl, C. Bauer, H. Giessen, and S. G. Tikhodeev, J. Microsc. **229**, 344 (2008).
[31] T. Søndergaard and B. Tromborg, Phys. Rev. A **64**, 033812 (2001).
[32] T. Søndergaard and S. I. Bozhevolnyi, Phys. Rev. B **69**, 045422 (2004).
[33] E. Economou, *Green's Functions in Quantum Physics*, 1st ed. (Springer-Verlag, Berlin, 1979).

Appendix D

J. Opt. Soc. Am. B **26**, 121 (2009)

Theoretical analysis and experimental demonstration of resonant light scattering from metal nanostrips on quartz

by

Jesper Jung, Thomas Søndergaard, Jonas Beermann, Alexandra Boltasseva, and Sergey I. Bozhevolnyi

This page is intentionally left blank

Theoretical analysis and experimental demonstration of resonant light scattering from metal nanostrips on quartz

Jesper Jung,[1,*] Thomas Søndergaard,[1] Jonas Beermann,[2] Alexandra Boltasseva,[3] and Sergey I. Bozhevolnyi[1,2]

[1]*Department of Physics and Nanotechnology, Aalborg University, Skjernvej 4A, DK-9220 Aalborg Øst, Denmark*
[2]*Institute of Sensors, Signals and Electrotechnics (SENSE), University of Southern Denmark, Niels Bohrs Allé 1, DK-5230 Odense M, Denmark*
[3]*Current address: School of Electrical and Computer Engineering, Birck Nanotechnology Center, Purdue University, West Lafayette, Indiana 47907, USA*
[*]*Corresponding author: jung@nano.aau.dk*

Received October 27, 2008; accepted November 4, 2008;
posted November 5, 2008 (Doc. ID 103330); published December 18, 2008

Using the Green's tensor area integral equation method and reflection spectroscopy, resonant light scattering from rectangular gold nanostrips on quartz substrates fabricated with electron-beam lithography is analyzed theoretically and demonstrated experimentally. Theory and experiments are compared and found in a good agreement. Design curves presenting the scattering resonance wavelength as a function of the nanostrip width allow one, by carefully choosing the strip width and thickness, to realize the resonance at a given wavelength in a broad wavelength spectrum ranging from the visible (~600 nm) to the near infrared including telecommunication wavelengths (~1600 nm). © 2008 Optical Society of America

OCIS codes: 290.0290, 290.5850, 300.6550.

1. INTRODUCTION

Resonant excitation of plasmon polaritons (PPs) in different metallic nanostructures has recently been a subject of intense research and is widely utilized to enhance electromagnetic near and scattered fields. The possibility of customizing the PP resonance wavelength by carefully optimizing geometrical parameters makes metallic nanostructures interesting in sensing and spectroscopical applications [1]. Metal nanowires of finite length [2–5], also suggested as optical antennas [6,7], gaps between adjacent metal nanostrips [8–10], and gaps between metal nanostrips and surfaces [11,12] are just a few recent examples of metallic nanostructures, where attention has been given to their resonant optical properties.

We have previously, in theoretical papers, shown that resonant light scattering from metal nanostrips [13–15] (and gap-resonators [16–19]) can physically be understood if the strip is thought of as a Fabry–Perot resonator for the slow surface plasmon polariton (SPP) mode. As an effect of constructive interference between forward and backward propagating slow SPPs, standing wave resonances that enhance not only local but also scattered fields, are built up. In this paper, we analyze resonant light scattering from gold nanostrips of different widths and thicknesses, which are fabricated on quartz substrates using electron-beam lithography. We present theoretical investigations utilizing the Green's tensor area integral equation method, comparing the calculated scattering spectra with those obtained experimentally in the course of carefully conducted reflection spectroscopy measurements. Previously, similar investigations have been carried out for the (simpler) case of metal nanostrips placed in a homogeneous environment [20]. This paper is organized as follows. In Section 2 the sample fabrication, theoretical modeling, and experimental arrangement are described. Section 3 presents the results, including a comparison between the calculated and experimentally obtained scattering spectra. Section 4 terminates the paper with our conclusions.

2. METHOD

The samples were fabricated using electron-beam lithography. Several samples with 100 μm × 100 μm arrays of 5 μm long, w wide (w from 100 to 500 nm at 50 nm increments), and t thick ($t=17$ and $t=23$ nm) gold nanostrips on quartz substrates were fabricated. To reduce cross talk between the strips, they are positioned such that there is a separation of 1 μm along and 10 μm across the strips and arrays are separated by at least 500 μm. The samples are the same as in [20] except for not being covered with index-matching oil.

A schematic of the structure analyzed with the area integral equation method is presented in Fig. 1. A rectangular gold nanostrip of width w and thickness t is placed directly onto a quartz substrate and above the quartz it is surrounded by air. As the fabricated nanostrips are very long (in the z direction) compared to their widths and thicknesses, the mode index of the slow SPP, responsible for the resonant buildup, is only slightly affected by the confinement in the length direction, and all calculations can therefore safely be reduced to two dimensions, where structure and fields are considered invariant under translation along the z axis. The optical properties of the gold

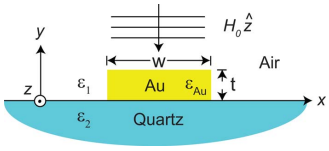

Fig. 1. (Color online) Rectangular gold nanostrip on top of a quartz surface surrounded by air is illuminated by a p polarized plane wave $H_0\hat{z}$ propagating in the xy plane antiparallel with the y axis.

nanostrip are described by a frequency dependent complex dielectric constant ε_{Au}, which is linearly interpolated from the table presented in [21]. The dielectric constants used for quartz and air are $\varepsilon_2=1.452^2$ and $\varepsilon_1=1$, respectively. The structure is illuminated by a p polarized plane wave ($H_0\hat{z}$) propagating in the xy plane antiparallel with the y axis, and the out-of-plane scattering cross section is calculated by integrating the time averaged flux of the Poynting vector of the scattered field through a semicircle of infinite radius in the upper half plane. We have checked, that except for a scaling factor the scattering cross section obtained by integrating along the entire semicircle is similar to scattering cross sections obtained when considering only the limit angular range of which the experimental setup can collect light. A presentation of the method including also scatterers in a stratified reference medium can be found in [22]. As an alternative, the generalized Green's function surface integral equation method [23] could also be used if further developed to handle strips placed directly onto the quartz substrate. Calculations with the strip placed within a few nanometers of the quartz substrate give very similar out-of-plane scattering cross sections.

The experiments presented in this paper are similar to those presented in [20]. Light scattering from the fabricated nanostrips are investigated using reflection spectroscopy, where the samples are illuminated by p polarized light propagating antiparallel to the y axis. The light source is a halogen bulb, which delivers sufficient radiation up to ~850 nm. After each measurement of a spectrum from gold strips R, a reference spectrum R_{quartz}, away from the strips, is also recorded. As the experimental setup and the experiments are described in detail in [20] they will not be further elaborated here. However, it is important to notice that the nanostrips investigated in this paper are not covered with an index-matching oil that matches the refractive index of the quartz substrate.

3. RESULTS

It has recently been clarified that resonant light scattering from metal strips in homogeneous surroundings can be ascribed to standing wave resonances, built up from constructive interference between counterpropagating slow SPPs that are strongly bound to the metal strips [13,14]. If the strip width is increased in increments of $\lambda/(2n_{slow})$ (λ being the wavelength and n_{slow} being the mode index of the slow SPP mode) higher order resonances appear at approximately the same wavelength. This interpretation is also valid for gold nanostrips on quartz substrates. If the width of the nanostrip is increased by $\lambda/(2n_{slow})$ (e.g., $\Delta w \sim 207$ nm and $\Delta w \sim 204$ nm for gold thicknesses 17 and 23 nm in an air-gold-quartz sandwich, respectively) a one order higher resonance at approximately the same wavelength appears [Fig. 2].

To illustrate that it is possible to obtain resonant light scattering from the fabricated gold nanostrips on quartz in a large wavelength spectrum, scattering cross section spectra for 17 nm thick gold strips of different widths w (from 100 to 500 nm in increments of 50 nm) are presented for wavelengths ranging from 550 nm to the near infrared including also telecommunication wavelengths (up to 1600 nm) [Fig. 3]. The scattering resonances revealed are of first and third order. Second order resonances, or in general even order resonances, are suppressed in calculations where the angle of incidence is −90°, because of symmetry mismatch between the resonant field and the incident field. A gold strip with a width of, e.g., 100 nm has a first order resonance at a wavelength of approximately 645 nm, and as the width of the strip is increased the resonance is significantly redshifted, and, e.g., a strip of width 500 nm has a first order resonance at approximately 1520 nm. In the considered wavelength spectrum all strips present a first order resonance and all strips with widths larger than 250 nm also present a third order resonance. From the investigations, it is clear that it is possible to obtain resonant light scattering from the fabricated nanostrips in a broad wavelength spectrum.

By mapping the resonance wavelengths versus the width (or thickness) of the nanostrips, design curves useful for designing optical resonators that support resonances at specific wavelengths can be obtained [Fig. 4]. Two strip thicknesses ($t=17$ and $t=23$ nm, those of the fabricated samples) are considered both for gold strips on quartz substrates and in homogeneous quartz surroundings. As the strips, for normal incidence, support both first and third order scattering resonances, we get two

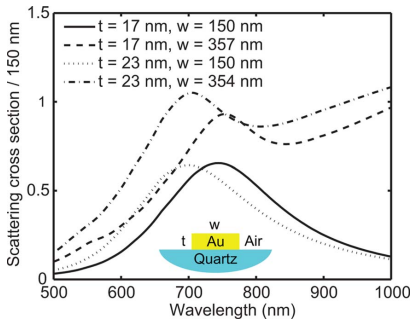

Fig. 2. (Color online) Normalized out-of-plane scattering cross section calculated for configurations designed to have first and second order scattering resonances at approximately the same wavelength. The two thicknesses of the fabricated samples (17 and 23 nm) are considered. The gold nanostrips on quartz (see inset) are illuminated by a p polarized plane wave at an angle of −45° relative to the x axis.

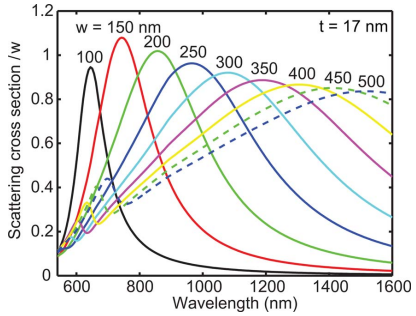

Fig. 3. (Color online) Normalized out-of-plane scattering cross section for 17 nm thick gold nanostrips of different widths w on quartz. The angle of incidence is −90° relative to the x axis, and the incident field is p polarized.

curves for each configuration. For all four configurations, the first order resonance follows a close to linear relationship with the strip width. This is similar to what has been found for strip and gap PP based resonators in homogeneous surroundings [15,17]. When designing optical resonators, it is obvious that the smallest resonators are obtained when the first order resonances are utilized. Note that the slope of the curves gets steeper for thinner strips, meaning that thinner strips have longer resonance wavelengths for a given strip width and resonance order. The curves for the strips embedded in homogeneous surroundings of quartz are steeper than the curves for strips on quartz substrates. This can easily be explained as the mode index of the slow SPP mode in a quartz-gold-quartz configuration is larger than the mode index of the mode in an air-gold-quartz configuration.

The results of the theoretical analysis are validated by comparing with reflection spectroscopy measurements, which also present an experimental demonstration of

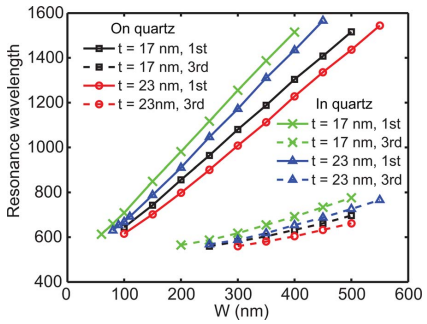

Fig. 4. (Color online) Design curves mapping first and third order resonance wavelengths versus the strip width. Two thicknesses (t=17 and t=23 nm) are considered. The curves marked with squares (t=17 nm) and circles (t=25 nm) are for gold strips or quartz substrates, and the curves marked with x (t=17 nm) and triangles (t=23 nm) are for gold strips embedded in a homogeneous medium of quartz. The angle of incidence is −90° relative to the x axis.

resonant light scattering from gold nanostrips on quartz [Figs. 5 and 6]. To minimize effects from fluctuations in the radiation spectrum from the halogen bulb in the experiments the experimental results are presented as $(R\text{-}R_{\text{quartz}})/R_{\text{quartz}}$, where R is the spectrum measured from the strips and R_{quartz} is the reference spectrum taken after each measurement. For normal incidence, and in the available wavelength spectrum of the experiments, the fabricated nanostrips exhibit both first and third order scattering resonances. The comparison is presented for two different strip thicknesses (t=17 and t=23 nm, Figs. 5 and 6, respectively) and several strip widths (from w=100 to w=500 nm in increments of 50 nm) (with the exception of t=17 and w=250 nm, where a large piece of gold in the array disturbs the experiment.) In both Figs. 5 and 6 the lower subplot presents the experiment and the upper subplot presents the corresponding theoretical out-of-plane scattering cross section. For both thicknesses and all widths all scattering resonances predicted by the theory are also observed in the experiments. A tendency of a small redshift (~20 nm) of the scattering peaks and a decrease for wavelengths above 750 nm of the experiments are the only obstacles hindering an almost perfect match between the theoretical predictions and the experimental results. However, it should be noted that our theoretical analysis captures accurately all the main features observed in the experiments.

4. CONCLUSION

In conclusion, we have both theoretically and experimentally demonstrated resonant light scattering from samples of rectangular gold nanostrips on quartz substrates. The theoretical analysis of the samples was performed utilizing the Green's tensor area integral equation method, and the measurements were conducted using re-

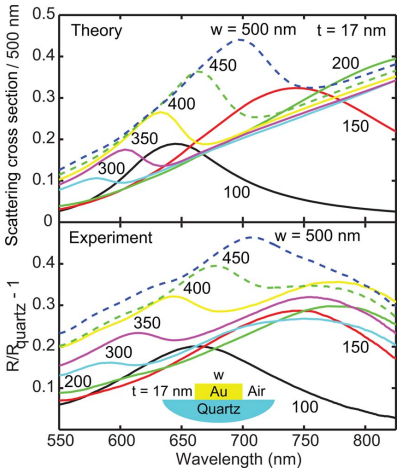

Fig. 5. (Color online) Calculated and measured out-of-plane scattering cross sections for 17 nm thick gold nanostrips of different widths w on quartz.

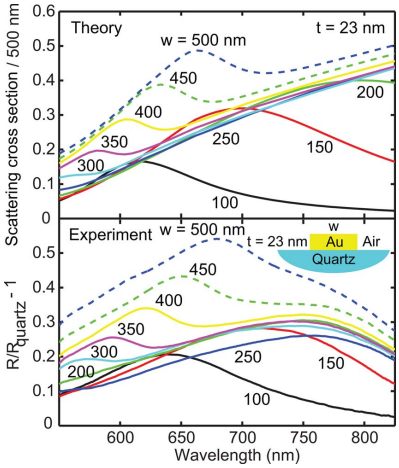

Fig. 6. (Color online) Calculated and measured out-of-plane scattering cross sections for 23 nm thick gold nanostrips of different widths w on quartz.

flection spectroscopy. In a wavelength interval ranging from 550 to 825 nm we have shown good agreement between theoretical predictions and experiments. Several first and third order scattering resonances observed in the experiments were all predicted by our theoretical investigations, and only a small wavelength-shift of ~20 nm is hindering an almost perfect match between the theory and experiments. Design curves mapping out the resonance wavelengths have been calculated, and these show how it is possible, by carefully optimizing the width and the thickness of the gold strips, to place scattering resonances in a broad wavelength spectrum ranging from the mid visible to the near infrared including also telecommunication wavelengths.

ACKNOWLEDGMENTS

The authors gratefully acknowledge the financial support from the NABIIT project financed by the Danish Research Agency (contract 2106-05-0033), T. Søndergaard from the Danish Research Council for Technology and Production, and S. I. Bozhevolnyi from the European Network of Excellence, PLASMO-NANO-DEVICES (FP6-2002-IST-1-507879).

REFERENCES

1. S. Lal, S. Link, and N. J. Halas, "Nano-optics from sensing to waveguiding," Nat. Photonics **1**, 641–648 (2007).
2. H. Ditlbacher, A. Hohenau, D. Wagner, U. Kreibig, M. Rogers, F. Hofer, F. R. Aussenegg, and J. R. Krenn, "Silver nanowire as surface plasmon resonators," Phys. Rev. Lett. **95**, 257403 (2005).
3. K. Imura, T. Nagahara, and H. Okamoto, "Near-field optical imaging of plasmon modes in gold nanorods," J. Chem. Phys. **122**, 154701 (2005).
4. F. Neubrech, T. Kolb, R. Lovrincic, G. Fahsold, A. Pucci, J. Aizpurua, T. W. Cornelius, M. E. Toimil-Molares, R. Neumann, and S. Karim, "Resonances of individual metal nanowires in the infrared," Appl. Phys. Lett. **89**, 253104 (2006).
5. T. Laroche and C. Girard, "Near-field optical properties of single plasmonic nanowires," Appl. Phys. Lett. **89**, 233119 (2006).
6. P. Mühlschlegel, H. J. Eisler, O. J. F. Martin, B. Hecht, and D. W. Pohl, "Resonant optical antennas," Science **308**, 1607–1609 (2005).
7. L. Novotny, "Effective wavelength scaling for optical antennas," Phys. Rev. Lett. **98**, 266802 (2007).
8. H. T. Miyazaki and Y. Kurokawa, "Squeezing visible light waves into a 3-nm thick and 55-nm-long plasmon cavity," Phys. Rev. Lett. **96**, 097401 (2006).
9. Y. Kurokawa and H. T. Miyazaki, "Metal-insulator-metal plasmon nanocavities: analysis of optical properties," Phys. Rev. B **75**, 035411 (2007).
10. P. Ghenuche, S. Cherukulappurath, T. H. Taminiau, N. F. van Hulst, and R. Quidant, "Spectroscopic mode mapping of resonant plasmon nanoantennas," Phys. Rev. Lett. **101**, 116805 (2008).
11. G. Lèvêque and O. J. F. Martin, "Tunable composite nanoparticle for plasmonics," Opt. Lett. **31**, 2750–2752 (2006).
12. G. Lèvêque and O. J. F. Martin, "Optical interactions in a plasmonic particle coupled to a metallic film," Opt. Express **14**, 9971–9981 (2006).
13. T. Søndergaard and S. I. Bozhevolnyi, "Slow-plasmon resonant nanostructures: scattering and field enhancements," Phys. Rev. B **75**, 073402 (2007).
14. T. Søndergaard and S. I. Bozhevolnyi, "Metal nano-strip optical resonators," Opt. Express **15**, 4198–4204 (2007).
15. G. D. Valle, T. Søndergaard, and S. I. Bozhevolnyi, "Plasmon-polariton nano-strip resonators: from visible to infra-red," Opt. Express **16**, 6867–6876 (2008).
16. T. Søndergaard and S. I. Bozhevolnyi, "Strip and gap plasmon polariton optical resonators," Phys. Status Solidi B **245**, 9–19 (2008).
17. T. Søndergaard, J. Jung, S. I. Bozhevolnyi, and G. D. Valle, "Theoretical analysis of gold nano-strip gap plasmon resonators," New J. Phys. **10**, 105008 (2008).
18. J. Jung and T. Søndergaard, "Theoretical analysis of surface-plasmon-polariton resonators in free space and close to an interface," Proc. SPIE **6988**, 69881N (2008).
19. J. Jung, T. Søndergaard, and S. I. Bozhevolnyi, "Gap plasmon-polariton nano-resonators: scattering enhancement and launching of surface plasmon polaritons," (accepted for publication in Phys. Rev. B).
20. T. Søndergaard, J. Beermann, A. Boltasseva, and S. I. Bozhevolnyi, "Slow-plasmon resonant-nanostrip antennas: analysis and demonstration," Phys. Rev. B **77**, 115420 (2008).
21. P. B. Johnson and R. W. Christy, "Optical constants of the noble metals," Phys. Rev. B **6**, 4370–4379 (1972).
22. T. Søndergaard, "Modeling of plasmonic nanostructures: Green's function integral equation methods," Phys. Status Solidi B **244**, 3448–3462 (2007).
23. J. Jung and T. Søndergaard, "Green's function surface integral equation method for theoretical analysis of scatterers close to a metal interface," Phys. Rev. B **77**, 245310 (2008).

Appendix E

Phys. Rev. B **79**, 035401 (2009)

Gap plasmon-polariton nanoresonators: Scattering enhancement and launching of surface plasmon polaritons

by

Jesper Jung, Thomas Søndergaard, and Sergey I. Bozhevolnyi

This page is intentionally left blank

Gap plasmon-polariton nanoresonators: Scattering enhancement and launching of surface plasmon polaritons

Jesper Jung* and Thomas Søndergaard
Department of Physics and Nanotechnology, Aalborg University, Skjernvej 4A, DK-9220 Aalborg Øst, Denmark

Sergey I. Bozhevolnyi
Institute of Sensors, Signals and Electrotechnics (SENSE), University of Southern Denmark, Niels Bohrs Allé 1, DK-5230 Odense M, Denmark

(Received 10 June 2008; revised manuscript received 12 August 2008; published 5 January 2009)

Gap plasmon-polariton (GPP) nanoresonators based on a metal nanostrip separated with a small gap from a metal surface or metal block are considered. Scattering resonances and field enhancements are studied for two-dimensional structures using the Green's-function surface integral equation method (GFSIEM). For small gaps, we show that the scattering resonances occur due to the constructive interference of counterpropagating GPPs, forming standing waves. By varying the gap size we find that the resonance wavelength can be tuned over a wide range of wavelengths, which makes the resonators interesting for spectroscopic and sensing applications, and observe the transition between GPP-based resonators (for narrow gaps) and slow surface plasmon-polariton (SPP) strip resonators (for wide gaps). Considering the resonant field distributions, we find that, for an insulator thickness of 10 nm, the maximum field enhancement (with respect to the incident field) can reach values close to 50 along the line passing through the gap center. For the case of a strip placed close to a metal surface, two scattering channels, viz., the out-of-plane scattering and the scattering into SPPs (propagating along the surface) are evaluated separately using a generalized version of the GFSIEM. We find that, even though the out-of-plane scattering is in general dominating in the considered range of parameters, scattering into SPPs can be very efficient for smaller gaps featuring a cross section that at resonance even exceeds the strip width. The considered properties of GPP nanoresonators, i.e., resonant scattering and local-field enhancements along with efficient scattering into SPPs, hold promises for their useful applications within plasmonic sensing devices.

DOI: 10.1103/PhysRevB.79.035401 PACS number(s): 78.67.−n, 71.36.+c, 73.20.Mf, 02.70.Pt

I. INTRODUCTION

Metallic nanorods, nanowires, and nanostrips have recently attracted a great deal of attention in the design of optical resonators and optical antennas[1–23] because they show strong resonant enhancement in light scattering or extinction and also because of the possibility of strong electromagnetic field-enhancement effects in the near-field region of the structures. Especially gaps between adjacent metal nanostructures allow for very high fields and localization of light way beyond the diffraction limit.[2,16–18,22,23] These properties make metallic nanostructures interesting for sensing and spectroscopic purposes.[24]

Composite metal nanostructures support super plasmon-polariton (PP) modes, which in some cases can become more localized and more strongly bound than regular surface plasmon polaritons (SPPs).[25,26] An example of such a highly localized PP mode is the gap plasmon-polariton (GPP) mode between two metal surfaces. In this paper, we are particularly interested in what happens when a metal strip is placed close to a metal surface. In such a configuration a GPP mode can be formed in the gap, and similar to resonances of metal strips and slow SPP strip modes,[14,15,20] scattering resonances of the strip-surface configuration can be related to the GPP mode. We analyze two different configurations: one where the metal surface is of finite width (a metal block) and one where the width of the metal surface is infinite, configurations (a) and (b), respectively (Fig. 1). Coherent presentation of these configurations, showing also the link to (individual) nanostrip resonators,[14,15] is one of the goals of this paper. Another goal is to consider the usage of configuration (b), where light can be scattered both out of the surface plane and into SPPs that propagate along the surface, for launching of SPPs. The directional (left and right) SPP excitation is evaluated using the generalized version of the Green's-function surface integral equation method (GFSIEM) we presented in Ref. 27.

In the latter context, it should be noted that scattering into SPPs is a subject of great interest in plasmonics, and many different configurations have been considered for local SPP

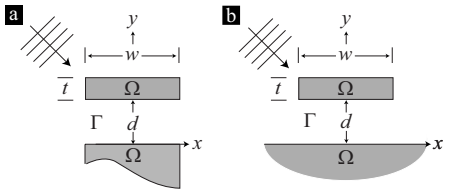

FIG. 1. The two GPP resonators analyzed. (a) A plane wave propagating in the *xy* plane is scattered by a lossy metal strip of thickness *t* and width *w* placed at a distance *d* from a lossy metal surface of width *w*. The metals are surrounded by Γ, a lossless dielectric medium. (b) The situation is the same as in (a) except for the width of the surface, which is infinite.

excitation, e.g., SPP launching through an array of nanoholes,[28] through a subwavelength slit supplemented with a periodic set of grooves[29] or by a surface protrusion defect in the form of a particle or a single ridge,[30] as well as by a periodic set of those.[31] The efficiency of SPP excitation for some configurations has been evaluated both experimentally and numerically.[31,32] A very recent study of SPP excitation by a single subwavelength hole in a gold film[32] revealed an efficiency of up to 28%. Note though that this is the value normalized with respect to the power incident onto the hole area, implying that the corresponding scattering (into SPPs) cross section is smaller than one-third of the hole area.

This paper is organized as follows. In Sec. II, the resonator structures and the theoretical method used in the numerical analysis are presented. Section III presents the results. We start with a brief discussion of the GPP mode. Hereafter we present the numerical analysis of the two GPP-based nanoresonator configurations (Sec. III A and Sec. III B, respectively). This is followed by the conclusion in Sec. IV.

II. STRUCTURES AND METHOD

A. Structures

The GPP resonators that we investigate consist of lossy metals Ω surrounded by lossless dielectrics Γ (Fig. 1). The optical properties of the metals are characterized by a complex-frequency-dependent dielectric constant ε_Ω, and the dielectric is characterized by a real-frequency-independent dielectric constant ε_Γ. The problem is reduced to two dimensions by considering both the structure and fields invariant under translation along the z axis, which is out of the paper. The situation that we analyze is the scattering of a monochromatic p-polarized plane wave propagating in the xy plane. p polarization is chosen because plasmons are p polarized. Two different GPP-based resonator configurations are analyzed (Fig. 1).

In configuration (a), a plane wave is scattered by a metal strip of thickness t and width w placed at a distance d from a metal surface of width w. In configuration (b), the width of the metal surface is infinite.

B. Method

The numerical analysis of the two configurations (Fig. 1) is performed using the GFSIEM which is an appropriate and efficient method for the analysis of two-dimensional scattering problems in open infinite domains.[27,33,34] This is primarily because the GFSIEM only involves integrals over the boundary of the scatterers as the radiating boundary conditions are satisfied through an appropriate choice of Green's function and, secondarily, because the GFSIEM allows for a good description of the metal surfaces. The latter is important since we are particularly interested in SPPs and GPPs, which have field maxima at the metal surfaces. As we consider p polarization $[\mathbf{H}(\mathbf{r})=H(\mathbf{r})\hat{z}]$ it is convenient to formulate the surface integral equations by means of the magnetic field as this yields scalar equations. The standard scalar surface integral equations for the magnetic field read as[33,34]

$$H(\mathbf{r}) = H_0(\mathbf{r}) + \oint_{\partial\Omega} [H(\mathbf{s}')\hat{n}' \cdot \nabla' g_\Gamma(\mathbf{r},\mathbf{s}') - g_\Gamma(\mathbf{r},\mathbf{s}')\hat{n}' \cdot \nabla' H_\Gamma(\mathbf{s}')]dl' \quad \text{for} \quad \mathbf{r} \in \Gamma, \tag{1a}$$

$$H(\mathbf{r}) = -\oint_{\partial\Omega} \left[H(\mathbf{s}')\hat{n}' \cdot \nabla' g_\Omega(\mathbf{r},\mathbf{s}') - g_\Omega(\mathbf{r},\mathbf{s}')\frac{\varepsilon_\Omega}{\varepsilon_\Gamma}\hat{n}' \cdot \nabla' H_\Gamma(\mathbf{s}') \right] dl' \quad \text{for} \quad \mathbf{r} \in \Omega, \tag{1b}$$

where $H_0(\mathbf{r})$ is the incident field, $\mathbf{s}'$ is a point on the boundary of Ω, $\hat{n}$ is the outward normal of Ω, $\partial\Omega$ is the boundary of Ω, and the boundary condition $\hat{n}' \cdot \nabla' H_\Omega(\mathbf{s}') = \varepsilon_\Omega/\varepsilon_\Gamma \hat{n}' \cdot \nabla' H_\Gamma(\mathbf{s}')$ has been used, where H_Γ and H_Ω refer to the magnetic field approaching the boundary from medium Γ and Ω, respectively, and the Green's functions $g_{\Gamma,\Omega}(\mathbf{r},\mathbf{s}')$ are given by the zero-order Hankel function of second kind $g_{\Gamma,\Omega}(\mathbf{r},\mathbf{s}') = H_0^{(2)}(k_0\sqrt{\varepsilon_{\Gamma,\Omega}}|\mathbf{r}-\mathbf{s}'|)/(4i)$, where k_0 is the vacuum wave number.

Configuration (b) [Fig. 1(b)] is, however, not suitable for the standard GFSIEM [Eq. (1)] because the boundary of Ω is infinite, and one would have to integrate along this infinite boundary. In configuration (a) this can very simply be avoided by assuming that the lower metal has a finite thickness. If the thickness of the lower metal is much larger than the skin depth of the electromagnetic field, this assumption is very good. Configuration (b) is, however, much more difficult to handle because even though a finite thickness of the metal surface is assumed the boundary is still infinite. In order to work around this problem, we developed a generalized version of the GFSIEM,[27] where the integral along the infinite surface is omitted by the use of an appropriate Green's function outside of the metal strip. Using this method an exact numerical analysis of configuration (b) can be made without truncations of integrals or assumptions of finite structures. The tradeoff is that the Green's function used outside the metal strip cannot be represented by means of a simple Hankel function but must be evaluated by means of more complicated, numerically difficult, and computationally time-consuming Sommerfeld integrals. For further details we refer to Ref. 27.

III. RESULTS

In all calculations presented, the optical properties of the dielectric regions Γ are described using the refractive index of quartz $n_\Gamma = 1.452$. The metal chosen is silver as it is known from previously presented results[14,17,23] that strong plasmon resonances occur in related geometries based on silver. The dielectric constant of silver is obtained by linear interpolation of the data in Ref. 35. In all calculations sharp corners have been rounded with a radius of curvature of 2 nm for numerical reasons.

Our physical interpretation of the scattering resonances of the configurations [(a) and (b), Fig. 1] is in the following section related to the GPP mode supported by a gap sand-

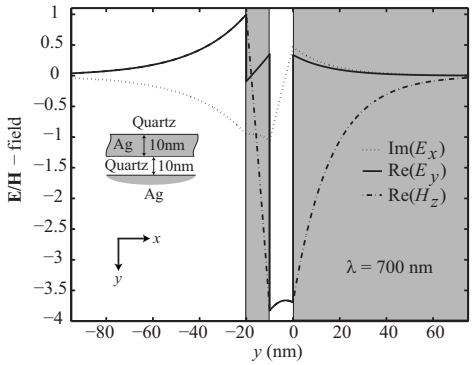

FIG. 2. The distribution of the components of the electric and the magnetic fields of the GPP mode supported by a 10 nm quartz gap sandwiched between a silver half plane and a thin silver film of 10 nm thickness, for $\lambda=700$ nm. According to the coordinate system chosen, the direction of propagation of the GPP wave is along the x axis and the field distributions are displayed along the y axis (see inset).

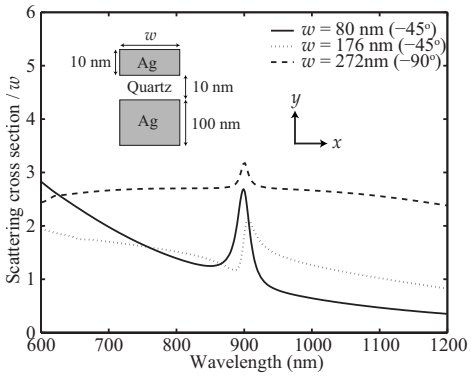

FIG. 3. The scattering cross section versus free space wavelength for configuration (a). A plane wave propagating at an angle (relative to x) axis indicated in the legend is scattered by the structure [$t=10$ nm, $d=10$ nm, and $t_2=100$ nm (see inset)]. Three different widths w are considered.

wiched between a thin metal film and a metal surface (Fig. 2). It is seen how the GPP mode is characterized by a large electric field in the gap and how the field decays exponentially away from the structure in the direction transverse to the propagation direction, which is along the x axis (see inset of Fig. 2).

To justify the assumption of a finite thickness of the lower metal block in configuration (a) we have investigated the dependence of the mode index of the GPP mode on the thickness of the lower metal block. We find that for thicknesses larger than ~50 nm the mode index is practically constant. In all scattering calculations performed on configuration (a) a thickness of $t_2=100$ nm is used for the lower metal block.

Also, the dependence of the mode index of the GPP mode versus the gap size has been investigated. Two distinct regimes were observed: for small gaps (below ~50 nm), the mode index decreases for an increasing gap size, and for larger gaps, the mode index becomes constant. Interestingly, for large gaps (above ~200 nm) the mode index of the GPP mode converges toward the mode index of the slow SPP strip mode. This indicates that the GPP mode for wide gaps transforms into a slow SPP strip mode and therefore becomes decoupled from the lower surface.

A. Configuration (a)

In the analysis of configuration (a), we start by relating the scattering resonances to the GPP mode. Even though the width of the metals is finite, the GPP mode can still propagate along the x axis, and because the GPP is strongly bound to the gap, it will be efficiently reflected when it reaches the end of the resonator. Similar to the case of symmetric nanostrip configurations,[14,17,22] constructive interference between forward- and backward-propagating GPPs can give rise to standing-wave resonances at certain wavelengths, which will show up in the scattering spectrum.

To demonstrate this, we have calculated the scattering cross section for three different widths, which corresponds to first, second, and third order resonances at the wavelength $\lambda_0=900$ nm, respectively (Fig. 3). The configuration with $w=80$ nm has a first-order resonance at $\lambda_0=900$ nm. The real part of the mode index of the GPP mode supported by the configuration is $n_{GPP}=4.69$, which yields $\lambda_{GPP}/2 \approx 96$ nm. It is known that if the width of the resonator is increased by half the wavelength of the PP mode responsible for the resonance, a one-order higher resonance will be positioned at approximately the same wavelength.[14,17,22] Thus a resonator with $w=176$ nm should have a second-order resonance around $\lambda_0=900$ nm, and a resonator with $w=272$ nm should have a third-order resonance. For the third-order resonance, the angle of incidence has been changed to −90°. This has been done in order to better reveal the scattering peak from the spectrum. This angle (−90°) cannot be used to excite the second-order resonance due to symmetry mismatch between the incident field and the resonance field. The field patterns in Fig. 4 clearly illustrate the third, second, and first-order natures of the GPP resonance for the different widths. In (a) three minima of the field are seen in the gap, in (b) two, and in (c) one. The field patterns show how the mode field, at resonance, is highly localized in the gap. From (d)–(f) the standing-wave pattern of the field is clearly seen.

With sensing and spectroscopical applications in mind, an important feature of resonant nanostructures is tunability of the resonance wavelength. It is known that the resonance wavelength is a strong function of the gap size in related configurations.[7–10,18] To investigate the tunability of the resonance wavelength, and furthermore to study the transition from a GPP resonator to a slow SPP strip resonator, we have calculated the scattering cross section of a monochromatic plane wave scattered at an angle of −45° (with respect to the

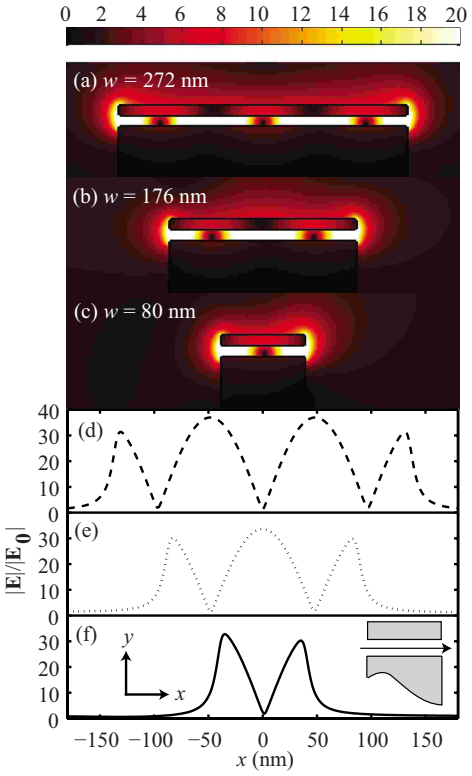

FIG. 4. (Color online) Electric-field magnitude in the xy plane for three different resonator widths: (a) $w=272$ nm, (b) $w=176$ nm, and (c) $w=80$ nm [$t=10$ nm, $d=10$ nm, and $t_2=100$ nm (see inset of Fig. 3)]. Cross-sectional plot of the electric-field magnitude (parallel to the x axis) through the center of the gap [see inset in (f)]. (d) $w=272$ nm, (e) $w=176$ nm, and (f) $w=80$ nm. All field plots have been calculated at the resonance wavelength $\lambda_0=900$ nm.

x axis) by configuration (a) for varying gap sizes (Fig. 5). It is seen that the resonance wavelength is a strong function of the gap size, and by changing the gap size from 80 to 5 nm, the resonance wavelength is redshifted more than 400 nm, from 690 to 1110 nm. The resonance shift is far from linear with the gap size. For small gaps it is shifted much more than for larger gaps, e.g., λ_0 shifts more than 200 nanometers (from 900 to 1110 nm) when the gap size is reduced by only 5 nm, from 10 to 5 nm, and it shifts only 15 nm (from 690 to 705 nm) when the gap size is reduced by 30 nm, from 80 to 50 nm. This behavior is in good agreement with our interpretation of the resonances as a smaller gap results in a larger GPP mode index and thus a larger GPP wavelength.

Another expectation from the investigation of the GPP mode is that when the gap size becomes large, the resonator

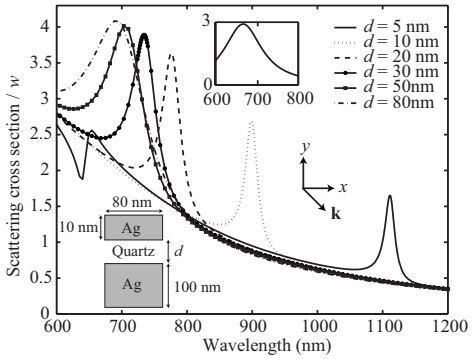

FIG. 5. Scattering cross section versus wavelength for a monochromatic plane wave propagating at an angle of −45° with respect to the x axis scattered of configuration (a) [$t=10$ nm, $w=80$ nm, and $t_2=100$ nm (see inset)]. Six different gap sizes have been considered. The second inset depicts the scattering cross section versus wavelength of a strip resonator [$t=10$ nm and $w=80$ nm] surrounded by quartz.

no longer resembles a GPP resonator but instead acts as a slow SPP strip resonator. The second inset in Fig. 5 shows the scattering cross section versus wavelength for a single strip resonator [$t=10$ nm and $w=80$ nm] surrounded by quartz. This scattering peak is similar to the scattering peak of configuration (a) for $d=80$ nm. The resonance wavelength of the strip resonator is $\lambda_0=665$ nm, and the resonance wavelength of configuration (a) for $d=80$ nm is 690 nm. This illustrates that configuration (a) for $d=80$ nm is relatively close in resembling a strip resonator. However, it must be noted that a large increase in gap size is needed to blueshift the resonance wavelength the last 25 nm as for gap sizes above 80 nm the resonance wavelength dependence on the gap size is weak. To further study the transition from a GPP resonator to a slow SPP strip resonator in configuration (a), and to study field-enhancement effects in the gap, we have calculated the electric-field magnitude in the xy plane for different gap sizes (Fig. 6). The electric-field magnitude for a gap size of $d=10$ nm [Fig. 4(c)] shows that the field is highly concentrated in the gap. The field is large, close to the terminations of the resonator, and has a clear minimum close to the center of the gap. The reason that the minimum is not completely in the center of the gap is that the angle of incidence is −45°. From the cross-sectional plot through the center of the gap [Fig. 4(f)] a maximum field enhancement, with respect to the incident field, above 30 is found. A higher value is possible with the angle of incidence −90°, where a maximum enhancement of 49 is found for $d=10$ nm and $w=80$ nm. For $d=30$ nm, at resonance ($\lambda_0=734$ nm), most of the characteristics of the GPP mode are still found in the field pattern [Fig. 6(a)]; the mode still has a tendency of being connected to the lower metal surface through the gap. However, the largest field is no longer found in the gap but rather at the terminations of the strip. From the cross-

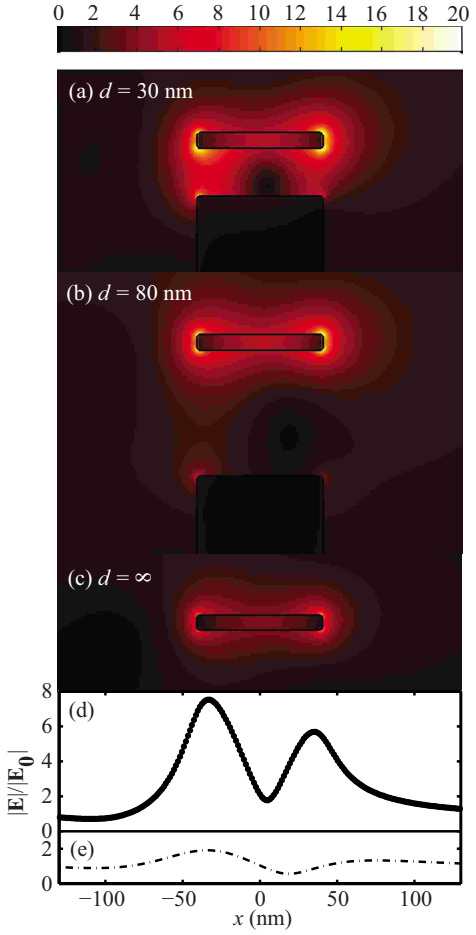

FIG. 6. (Color online) Electric-field magnitude in the xy plane for different gap sizes [$t=10$ nm, $w=80$ nm, and $t_2=100$ nm (see inset of Fig. 5)]. (a) $d=30$ nm and $\lambda_0=734$ nm, (b) $d=80$ nm and $\lambda_0=690$ nm, and (c) $d=\infty$ and $\lambda_0=665$ nm. Cross-sectional plot of the electric-field magnitude parallel to the x axis through the center of the gap. (d) $d=30$ nm and (e) $d=80$ nm.

sectional plot through the center of the gap [Fig. 6(d)] the maximum field enhancement is also considerably lower than for $d=10$ nm, approximately 7.5 which is at least four times smaller. For $d=80$ nm [Figs. 6(b) and 6(e)], the field mostly resembles a metal strip resonator [Fig. 6(c)], where the field is confined to the strip and not in the gap. For $d=80$ nm, the maximum field enhancement through the center of the gap is below 2 [Fig. 6(e)].

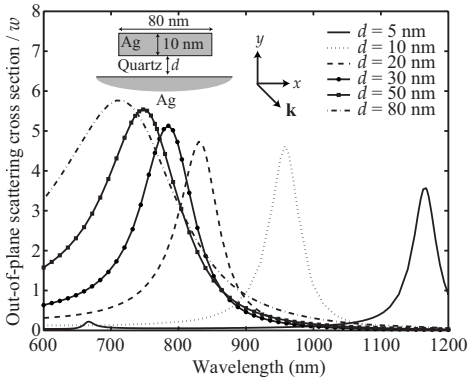

FIG. 7. The out-of-plane scattering cross section versus wavelength. A plane wave propagating at an angle of −45° (with respect to the x axis) is scattered by configuration (b) [$t=10$ nm, $w=80$ nm, and for six values of d (see inset and legend)].

B. Configuration (b)

Using the method we presented in Ref. 27, we have calculated the scattering cross sections of the two main scattering channels of configuration (b), viz., the out-of-plane scattering (Fig. 7) and scattering into SPPs (Fig. 8). All the same tendencies as in the scattering analysis of configuration (a) (Fig. 5) are seen. When the gap size is decreased the resonance wavelength is redshifted. However, when compared to configuration (a), a larger redshift is seen, the resonance peaks are broader, and also larger values of the peak maxima are seen. That the resonances of configuration (b) are redshifted compared to configuration (a) is in good agreement with our interpretation of them. Due to the infinite surface, the terminations of the resonator in configuration (b) are less sharp than in configuration (a). This makes the effective length of the resonator in configuration (b) larger than in configuration (a), and the resonances therefore get redshifted. More rapid coupling of energy out of the resonator, in this case both into out-of-plane propagating waves (the peak values in Fig. 7 are higher than in Fig. 5) and SPPs, results in broadening of the scattering peaks. The SPP scattering cross section is calculated as an integral of the time averaged flux of the Poynting vector of the scattered field related to SPPs. Due to losses in the metal, SPPs are damped as they propagate along the surface, and thus the SPP scattering cross section is a function of the distance that the SPPs have propagated as

$$\sigma_{\mathrm{SPP}}(x) = A_{\mathrm{SPP}} \exp(-2\,\mathrm{Im}(k_{\mathrm{SPP}})|x|), \tag{2}$$

where A_{SPP} is a constant, k_{SPP} is the SPP wave number, and $|x|$ is related to the distance that the SPPs have propagated along the x axis. In order to compare the amount of light scattered into SPPs to the out-of-plane propagating waves, x should be chosen to be small and close to the resonator. In the results presented (Fig. 8) we have chosen $|x|=1000$ nm, where $x=0$ is in the center of the strip. When the SPP scat-

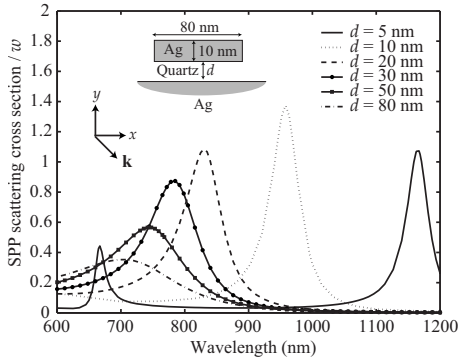

FIG. 8. The SPP scattering cross section versus wavelength. See caption of Fig. 7 for details.

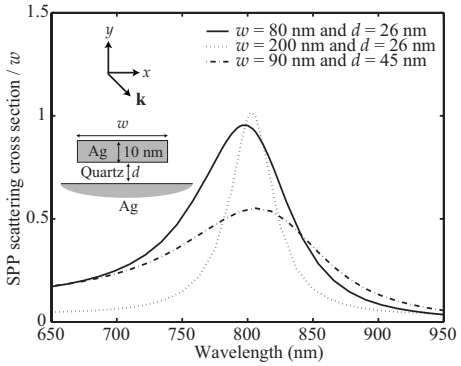

FIG. 9. The SPP scattering cross section versus wavelength for silver strips of different width, where the gap is adjusted such that a resonant launching of SPPs is achieved around a free space wavelength of λ_0=800 nm. For details of configurations see inset and legends.

tering is compared to the out-of-plane scattering, it is seen that the resonance wavelengths are, within a few nanometers, identical. However, the SPP scattering cross section is smaller. The SPP scattering cross section increases when the gap size is reduced and has a maximum around a gap size of 10 nm, with a value close to 1.4. This is about 30% of the out-of-plane scattering cross section which is close to 5. For comparison, in a very recent study of SPP excitation by a single subwavelength hole in a gold film,[32] the highest efficiency achieved (normalized with respect to the power incident onto the hole area) was below 30%, implying that the normalized scattering (into SPPs) cross section was below 0.3. The close to fivefold increase in the efficiency predicted for the 10-nm-wide gap structure is related to the occurrence of strong resonance in the scattering configuration (Fig. 8) that enhances not only local but also scattered fields.

To demonstrate structure optimization of configuration (b) with respect to SPP launching, we have calculated a series of SPP scattering cross sections in which the strip width and gap are adjusted such that the structures show resonant launching of SPPs around a free space wavelength of 800 nm (Fig. 9). The calculations show how it is possible to achieve resonant SPP launching at a desired wavelength by carefully playing with the structural parameters (in Fig. 9 the width of the strip and the gap size) of configuration (b). Note that both first- (e.g., w=80 nm and d=26 nm) and second- (w =200 nm, d=26 nm, and $\lambda_{GPP}/2 \approx 120$ nm) order resonances can be utilized for resonant launching of SPPs. It should also be taken in consideration that, in terms of the absolute efficiency of SPP excitation, the second-order resonance shown in Fig. 9 ensures a 2.5-fold efficiency increase when compared to the first-order one.

With development of plasmonic devices in mind, a strong unidirectional coupling into SPPs is often favorable.[36] In order to investigate the directionality of the launched SPPs of configuration (b) under oblique incidence, we have calculated two SPP scattering cross sections related to SPPs that propagate in the negative (to the left) and positive (to the right) x directions (Fig. 10). It is seen how the SPP scattering cross section of SPPs that propagate to the left is blueshifted a few nanometers compared to the scattering cross section of SPPs that propagate to the right. At resonance, however, the strength of the two scattering cross sections are almost identical. Thus, even under oblique incidence (−45° with respect to the x axis), SPPs that propagate along the surface are launched with almost equal strength in both directions. However, this is expected as scattering into SPPs is related to the occurrence of the strong resonant buildup of the standing waves in the gap, and these standing waves are only slightly asymmetric [see field calculations for configuration (b) presented in Fig. 11].

To investigate the transition from GPP resonator to SPP strip resonator, and to study the field enhancement in the gap, we have calculated the field for three different gap sizes for

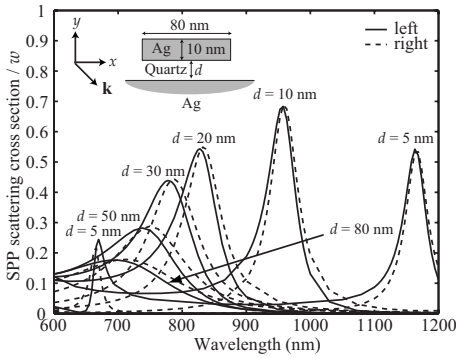

FIG. 10. The SPP scattering cross section versus wavelength. The solid lines represent the scattering cross section of SPPs that propagate to the left and the dashed lines SPPs that propagate to the right. See caption of Fig. 7 and inset for details about the configuration.

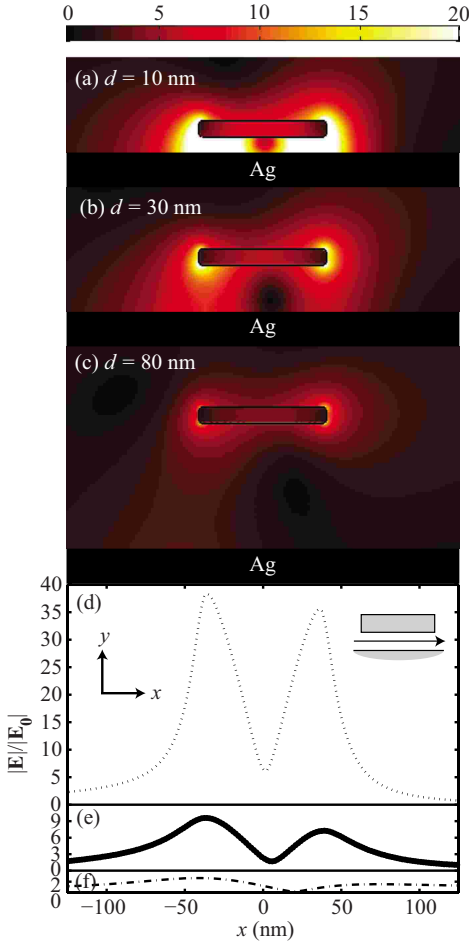

FIG. 11. (Color online) Electric-field magnitude at resonance in the xy plane of configuration (b) ($t=10$ nm, $w=80$ nm, and three different gap sizes). A plane wave is incident at an angle of $-45°$ with respect to the x axis. (a) $d=10$ nm and $\lambda_0=958$ nm. (b) $d=30$ nm and $\lambda_0=785$ nm. (c) $d=80$ nm and $\lambda_0=712$ nm. Cross sectional plots of the field magnitude through the center of the gap along the x axis. (d) $d=10$ nm, (e) $d=30$ nm, and (f) $d=80$ nm.

configuration (b) (Fig. 11). When compared to the fields of configuration (a) (Fig. 6), the fields in the gaps are slightly increased. The maximum field enhancement in the gap ($d=10$ nm) is close to 40 [Fig. 11(d)], and again a higher value can be obtained for the angle of incidence of $-90°$. In this case the maximum value is 48. Also, the modes at resonance in configuration (b) are wider than in configuration (a). This makes the effective resonator width larger, which makes sense, as argued above. In configuration (b) the field for $d=80$ nm is, as in configuration (a), mostly localized around the strip and not within the gap. Thus for a gap size of $d=80$ nm, the field of configuration (b) also mostly resembles the field of a strip resonator.

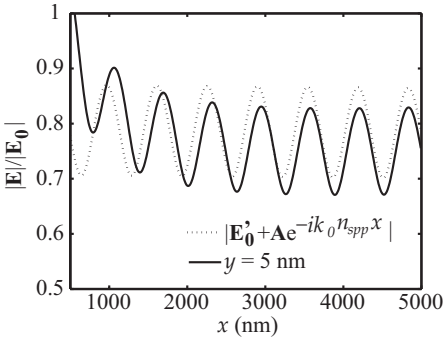

FIG. 12. A cut along the x axis of the magnitude of the electric field at $y=5$ nm. The cut is shown at resonance $\lambda_0=958$ nm for the configuration $t=d=10$ nm, $w=80$ nm, and an angle of incidence of $-90°$. Also shown is $|\mathbf{E}_0'+\mathbf{A}\exp(-ik_0 n_{\mathrm{SPP}}x)|$, where $\mathbf{E}_0'$ is the incident field including its reflection from the surface and $\mathbf{A}$ is the amplitude vector of the SPP electric field.

In order to reveal the launched SPPs that propagate along the silver surface from the near-field plots, a cut along the x axis at $y=5$ nm of the electric-field magnitude is presented together with $|\mathbf{E}_0'+\mathbf{A}\exp(-ik_0 n_{\mathrm{SPP}}x)|$, where $\mathbf{E}_0'$ is the incident field including its reflection from the surface and $\mathbf{A}$ is the amplitude vector of the SPP electric field, determined using Eqs. (27)–(29) of Ref. 27 (Fig. 12). As the two curves are quite similar, it is seen how the characteristics of the electric-field magnitude are mainly dominated by the interference between $\mathbf{E}_0'$ and the SPP that propagates along the surface. The reason that the two curves deviate slightly is that the electric-field magnitude also contains propagating scattered waves.

From the above analysis of configuration (b) it is clear that the scattering resonances of both resonator configurations [(a) and (b)] have a common origin. The resonances in the scattering spectra are due to constructive interference of counterpropagating GPPs that are trapped in the quartz gap below the strip. For certain wavelengths these form standing-wave resonances. As the terminations of the resonator in configuration (b) are weaker than in (a), the resonances of (b) are broader and redshifted.

IV. CONCLUSION

In conclusion, we have, using the GFSIEM, theoretically analyzed two GPP resonator configurations, viz., a metal strip close to a metal block of finite width [configuration (a)] and a metal strip close to an infinitely wide metal surface [configuration (b)]. We have shown that the scattering resonances of both configurations (a) and (b) have a common origin and can be related to the GPP mode supported by the

gap between the strip and the block/surface. As the GPP mode is efficiently reflected at the resonator terminations due to its strongly bound nature, standing-wave patterns can form from constructive interference between forward- and backward-propagating GPPs, which gives rise to the scattering resonances. As the terminations of the resonator in configuration (b) are less sharp, the scattering resonances are redshifted and broader than in configuration (a). We have shown how the scattering resonance wavelength can be tuned over a wide range of frequencies from the upper visible to the near infrared by varying the gap size of the configurations. For wide gaps, we have established a link between gap and strip resonators, as the two GPP resonator configurations for wide gaps clearly resemble slow SPP strip resonators. Also field-enhancement effects in the gap of the two configurations were analyzed. The largest field enhancement in the gap was found in configuration (b). For a gap size of 10 nm a field enhancement close to 40, with respect to the incident field, was found for a nonoptimized angle of incidence. For an optimized angle of incidence a value close to 50 was found in both configurations. Finally, noticing that in configuration (b) there appears the possibility of exciting SPPs, we have considered the efficiency of this process. We were able to evaluate scattering into out-of-plane propagating waves and into SPPs separately and found that for a gap size of 10 nm scattering into SPPs is about 30% of the out-of-plane scattering. The considered properties of the GPP resonators make them attractive for use within plasmonic sensing devices.

ACKNOWLEDGMENTS

The authors (J.J., T.S., and S.B.) gratefully acknowledge the financial support from the NABIIT project financed by the Danish Research Agency (Contract No. 2106-05-033), (T.S.) from the Danish Research Council for Technology and Production, and (S.B.) from the European Network of Excellence, PLASMO-NANO-DEVICES (Contract No. FP6-2002-IST-1-507879).

*jung@nano.aau.dk

[1] H. Ditlbacher, A. Hohenau, D. Wagner, U. Kreibig, M. Rogers, F. Hofer, F. R. Aussenegg, and J. R. Krenn, Phys. Rev. Lett. **95**, 257403 (2005).
[2] P. Mühlschlegel, H. J. Eisler, O. J. F. Martin, B. Hecht, and D. W. Pohl, Science **308**, 1607 (2005).
[3] K. Imura, T. Nagahara, and H. Okamoto, J. Chem. Phys. **122**, 154701 (2005).
[4] H. T. Miyazaki and Y. Kurokawa, Phys. Rev. Lett. **96**, 097401 (2006).
[5] F. Neubrech, T. Kolb, R. Lovrincic, G. Fahsold, A. Pucci, J. Aizpurua, T. W. Cornelius, M. E. Toimil-Molares, R. Neumann, and S. Karim, Appl. Phys. Lett. **89**, 253104 (2006).
[6] T. Laroche and C. Girard, Appl. Phys. Lett. **89**, 233119 (2006).
[7] G. Lèvêque and O. J. F. Martin, Opt. Lett. **31**, 2750 (2006).
[8] G. Lèvêque and O. J. F. Martin, Opt. Express **14**, 9971 (2006).
[9] A. Christ, T. Zentgraf, S. G. Tikhodeev, N. A. Gippius, O. J. F. Martin, J. Kuhl, and H. Giessen, Phys. Status Solidi B **243**, 2344 (2006).
[10] A. Christ, T. Zentgraf, S. G. Tikhodeev, N. A. Gippius, J. Kuhl, and H. Giessen, Phys. Rev. B **74**, 155435 (2006).
[11] L. Novotny, Phys. Rev. Lett. **98**, 266802 (2007).
[12] Y. Kurokawa and H. T. Miyazaki, Phys. Rev. B **75**, 035411 (2007).
[13] O. L. Muskens, V. Giannini, J. A. Sánchez-Gil, and J. G. Rivas, Opt. Express **15**, 17736 (2007).
[14] T. Søndergaard and S. I. Bozhevolnyi, Phys. Rev. B **75**, 073402 (2007).
[15] T. Søndergaard and S. I. Bozhevolnyi, Opt. Express **15**, 4198 (2007).
[16] S. I. Bozhevolnyi and T. Søndergaard, Opt. Express **15**, 10869 (2007).
[17] T. Søndergaard and S. I. Bozhevolnyi, Phys. Status Solidi B **245**, 9 (2008).
[18] A. Christ, G. Lèvêque, O. J. F. Martin, T. Zentgraf, J. Kuhl, C. Bauer, H. Giessen, and S. G. Tikhodeev, J. Microsc. **229**, 344 (2008).
[19] G. A. Wurtz, W. Dickson, D. O'Connor, R. Atkinson, W. Hendren, P. Evans, R. Pollard, and A. V. Zayats, Opt. Express **16**, 7460 (2008).
[20] T. Søndergaard, J. Beermann, A. Boltasseva, and S. I. Bozhevolnyi, Phys. Rev. B **77**, 115420 (2008).
[21] G. Della Valle, T. Søndergaard, and S. I. Bozhevolnyi, Opt. Express **16**, 6867 (2008).
[22] T. Søndergaard, J. Jung, S. I. Bozhevolnyi, and G. Della Valle, New J. Phys. **10**, 105008 (2008).
[23] J. Jung and T. Søndergaard, Proc. SPIE **6988**, 69881N (2008).
[24] S. Lal, S. Link, and N. J. Halas, Nat. Photonics **1**, 641 (2007).
[25] H. Raether, *Surface Plasmons-on Smooth and Rough Surfaces and on Gratings*, 1st ed. (Springer-Verlag, Berlin, 1988).
[26] W. L. Barnes, A. Dereux, and T. W. Ebbesen, Nature (London) **424**, 824 (2003).
[27] J. Jung and T. Søndergaard, Phys. Rev. B **77**, 245310 (2008).
[28] E. Devaux, T. W. Ebbesen, J.-C. Weeber, and A. Dereux, Appl. Phys. Lett. **83**, 4936 (2003).
[29] F. López-Tejeira, S. G. Rodrigo, L. Martín-Moreno, F. J. García-Vidal, E. Devaux, J. Dintinger, T. W. Ebbesen, J. R. Krenn, I. P. Radko, and S. I. Bozhevolnyi, New J. Phys. **10**, 033035 (2008).
[30] H. Ditlbacher, J. R. Krenn, N. Felidj, B. Lamprecht, G. Schider, M. Salerno, A. Leitner, and F. R. Aussenegg, Appl. Phys. Lett. **80**, 404 (2002).
[31] H. Ditlbacher, J. R. Krenn, A. Hohenau, A. Leitner, and F. R. Aussenegg, Appl. Phys. Lett. **83**, 3665 (2003).
[32] A.-L. Baudrion, F. de León-Pérez, O. Mahboub, A. Hohenau, H. Ditlbacher, F. J. García-Vidal, J. Dintinger, T. W. Ebbesen, L. Martín-Moreno, and J. R. Krenn, Opt. Express **16**, 3420 (2008).
[33] J. Jin, *The Finite Element Method in Electromagnetics*, 2nd ed. (Wiley, New York, 2002).
[34] T. Søndergaard, Phys. Status Solidi B **244**, 3448 (2007).
[35] E. Palik, *Handbook of Optical Constants of Solids*, 1st ed. (Academic, U.S., 1985).
[36] F. López-Tejeira *et al.*, Nat. Phys. **3**, 324 (2007).

Appendix F

Phys. Rev. B **79, 153407 (2009)**

Holey metal films make perfect endoscopes

by

Jesper Jung, Francisco J. Garcia-Vidal, Luis Martin-Moreno, and John B. Pendry

This page is intentionally left blank

Holey metal films make perfect endoscopes

J. Jung,[1,2] F. J. García-Vidal,[2,*] L. Martín-Moreno,[3] and J. B. Pendry[4]
[1]*Department of Physics and Nanotechnology, Aalborg University, Skjernvej 4A, DK-9220 Aalborg Øst, Denmark*
[2]*Departamento de Física Teórica de la Materia Condensada, Universidad Autónoma de Madrid, E-28049 Madrid, Spain*
[3]*Departamento de Física de la Materia Condensada and Instituto de Ciencia de Materiales de Aragón (ICMA), CSIC-Universidad de Zaragoza, E-50009 Zaragoza, Spain*
[4]*Condensed Matter Theory Group, The Blackett Laboratory, Imperial College, London SW7 2BW, United Kingdom*
(Received 23 December 2008; revised manuscript received 18 March 2009; published 23 April 2009)

Possible superlensing effects in holey metal films are theoretically analyzed using the multiple-scattering formalism. We show that within the effective-medium limit and at some resonant frequencies, holey perfect conductor films make perfect endoscopes, i.e., are capable of transforming an image from the input to the output surface of the film with subwavelength resolution. To corroborate our finding in a realistic structure, a full numerical calculation including diffraction and losses is presented for a one-dimensional perforated metal film in the terahertz regime.

DOI: 10.1103/PhysRevB.79.153407 PACS number(s): 42.30.Wb, 41.20.Jb, 78.20.Ci

The idea of subwavelength imaging using a slab of an artificially engineered metamaterial (superlensing) was proposed some years ago.[1] It was proved that a thin slab of material with a refractive index of −1 yields a lens with almost unlimited resolution. The challenge is now to engineer a metamaterial with the desired optical properties. In the electrostatic limit, near-field superlensing can be obtained with a thin metal slab.[1–3] Examples of metamaterials that have been recently investigated for subwavelength imaging are layered metal-dielectric structures,[4–9] metallic wire media,[10–13] and electromagnetic (EM) or photonic crystals.[14–17]

The key to perfect lensing appearing in a homogeneous metal slab is the amplification of evanescent waves by means of resonantly excited surface plasmon polaritons (SPPs). More specifically, this phenomenon is linked to the existence of a flat region in the dispersion relation of SPPs for large parallel momenta at optical frequencies.[1] In this Brief Report we analyze whether this superlensing effect can be extended to lower frequencies by taking advantage of the so-called *spoof* SPPs.[18,19] These surface EM modes emerge when a perfect conductor film is perforated with a periodic array of apertures (see Fig. 1) and have similar characteristics to canonical SPPs. Here we will demonstrate that, contrary to the aforementioned expectations, superlensing effects do not appear in holey metal films. Instead, these structures can operate as perfect endoscopes, i.e., transmit all incident plane waves (propagating and evanescent) with unit efficiency at some resonant wavelengths.

Holey metal films have been extensively studied in recent years mainly in connection with the emergence of the phenomenon of extraordinary optical transmission.[20] In our theoretical analysis we first assume that all metal regions behave as perfect conductors, which is a good approximation in a wide range of frequencies, from dc up to terahertz frequencies. The effect of the finite absorption present in a real metal will be checked at a second stage.

An incident plane wave will excite several waveguide modes (TE and TM) within the holes but, in the very subwavelength regime, the fundamental mode dominates the transmission process because all higher-order modes are strongly evanescent. It is therefore a very good approximation in that limit to consider only the fundamental waveguide mode.[21] We also assume that the two surrounding dielectric media (1 and 3 in Fig. 1) and the medium within the apertures are the same. Within the single-mode approximation, the transmission coefficient of a holey metal film associated with the nth diffraction order can be written as a sum of all the multiple-scattering events,

$$t^{(n)} = \tau_{12}\tau_{23}^{(n)} \exp(iq_z h) + \tau_{12}\tau_{23}^{(n)}\rho^2 \exp(3iq_z h) + \tau_{12}\tau_{23}^{(n)}\rho^4 \exp(5iq_z h) + \cdots = \frac{\tau_{12}\tau_{23}^{(n)} \exp(iq_z h)}{1-\rho^2 \exp(2iq_z h)}, \quad (1)$$

where τ_{12}, $\tau_{23}^{(n)}$, and ρ are the different two-media scattering coefficients for a single interface and q_z is the propagation constant of the fundamental waveguide mode. τ_{12} is the transmission amplitude by which an incident plane wave in medium 1 is transmitted into medium 2, ρ is the reflection amplitude of the waveguide mode when it scatters from either interface 2-1 or 2-3, and $\tau_{23}^{(n)}$ is the transmission ampli-

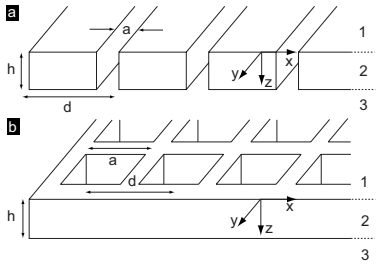

FIG. 1. Two examples of holey metal films. (a) One-dimensional metal film periodically perforated with subwavelength slits of width a and lattice constant d. (b) Two-dimensional metal film perforated with $a \times a$ square holes in a $d \times d$ lattice. The thickness of both films is h and extents along the z axis.

tude by which the waveguide mode, traveling towards the interface 2-3, transmits into a plane wave of diffraction order n that propagates away from the interface in medium 3. To simplify the notation, index n should be regarded as an index that comprises both polarizations and diffraction orders. The different two-media scattering coefficients can be determined by a proper matching of the parallel components of the EM field at the interfaces. After matching and substituting into Eq. (1) we obtain for $t^{(n)}$,

$$t^{(n)} = \frac{4Y_{\text{hole}}Y_0 S^{(0)*}S^{(n)} \exp(iq_z h)}{[Y_{\text{hole}}+G]^2 - [Y_{\text{hole}}-G]^2 \exp(2iq_z h)}, \tag{2}$$

where Y_{hole} is the admittance of the waveguide mode within the holes ($Y_{\text{hole}}=q_z/k_0$ if the fundamental mode is TE or $Y_{\text{hole}}=k_0/q_z$ for a TM mode) and $S^{(n)}$ is the overlap integral between an nth diffraction order and the fundamental waveguide mode. The term G contains a sum over diffracted modes, $G=\Sigma_{n=-\infty}^{\infty} Y_n |S^{(n)}|^2$, where Y_n is the admittance that relates the electric and the magnetic components of the plane waves in regions 1 and 3: $Y_n=k_0/k_z^{(n)}$ for p polarization and $Y_n=k_z^{(n)}/k_0$ for s polarization, with $k_z^{(n)}$ being the component of the wave vector along the z axis. The wave number in free space is $k_0=\omega/c$, where ω is the frequency and c the speed of light.

In the extreme subwavelength regime ($\lambda \gg d > a$), Eq. (2) can be further simplified if all diffraction effects are neglected. In this way, $t \equiv t^{(0)}$ becomes the only nonzero transmission coefficient,

$$t = \frac{4Y_{\text{hole}}Y_0 |S^{(0)}|^2 \exp(iq_z h)}{[Y_{\text{hole}}+Y_0|S^{(0)}|^2]^2 - [Y_{\text{hole}}-Y_0|S^{(0)}|^2]^2 \exp(2iq_z h)}. \tag{3}$$

Equation (3) is valid for both s and p polarizations, and the difference in the transmission enters via the admittances and the overlap integral $S^{(0)}$. In particular, for a p-polarized incident field, we obtain

$$t = \frac{4k_z q_z \varepsilon \exp(iq_z h)}{(q_z+\varepsilon k_z)^2 - (\varepsilon k_z - q_z)^2 \exp(2iq_z h)}, \tag{4}$$

where $k_z^{(0)}$ has been replaced with k_z and ε is given as

$$\varepsilon = \frac{q_z^2}{|S^{(0)}|^2 k_0^2}. \tag{5}$$

Equation (4) is exactly the transmission coefficient of p-polarized light through a homogeneous slab of thickness h characterized by a dielectric constant ε. Additionally, as the propagation constant inside the effective medium is q_z, the effective magnetic permeability is $\mu=|S^{(0)}|^2$. More precisely, in the two-dimensional (2D) case and for a square periodic array, the electric permittivity is a diagonal second-rank tensor with $\varepsilon_x=\varepsilon_y=\varepsilon$ and $\varepsilon_z=\infty$. In this case, $q_z=\sqrt{k_0^2-\pi^2/a^2}$ and $S^0=2\sqrt{2}a/(\pi d)$ and the permittivity shows a Drude-type behavior in which the cutoff frequency of the hole waveguide acts as an effective plasma frequency [see Eq. (5)]. The effective permeability takes a constant value $\mu_x=\mu_y=8a^2/(\pi^2 d^2)$. Interestingly, the same expressions for the electric permittivity and magnetic permeability were obtained when the concept of spoof SPP was first introduced,[18] although in that case the analysis was done for a semi-infinite slab, and not for a film of finite thickness. For the one-dimensional (1D) case, however, $\varepsilon_x=\varepsilon$ and $\varepsilon_y=\varepsilon_z=\infty$ with $q_z=k_0$ and $S^0=\sqrt{a/d}$. Thus, the 1D structure resembles an anisotropic dielectric medium with $\varepsilon_x=d/a$, $\mu_x=1$, and $\mu_y=\mu_z=a/d$.[19]

It is interesting to notice that Eq. (4) is equivalent to the expression that was used to demonstrate perfect lensing.[1] In the electrostatic limit, perfect lensing in an uncorrugated film is achieved when $\varepsilon \to -1$ because then $q_z=k_z$ for all parallel momenta $k_\parallel=\sqrt{k_x^2+k_y^2}$. For this condition, Eq. (4) reduces to $t=\exp(-ik_z h)$ for all $k_\parallel$, which shows how evanescent waves are amplified. For a holey metal film, however, q_z is fixed by the fundamental waveguide mode and it is not equal to $k_z=\sqrt{k_0^2-k_\parallel^2}$. Thus, we conclude that perfect lensing with holey metal films [requiring $t=\exp(-ik_z h)$ for all $k_\parallel$] cannot be realized. However, one may realize that at the Fabry-Pérot resonance condition ($q_z h=m\pi, m\geq 0$), Eq. (4) simplifies significantly to

$$t = e^{im\pi} = (-1)^m \; \forall \; k_\parallel. \tag{6}$$

At the Fabry-Pérot resonance condition, all incident plane waves (both propagating and evanescent) are perfectly transmitted through a holey perfect conductor film. This resonant regime where all incoming plane waves are transmitted with unit efficiency has been recognized before for metallic wire media.[10–13] Notice that the condition for excitation of spoof SPPs at large parallel momenta reads $q_z=0$, which fulfills the Fabry-Pérot resonance condition for $m=0$. Therefore, within the effective-medium limit ($\lambda \gg d > a$) and at the Fabry-Pérot resonances, Eq. (4) predicts that a holey perfect conductor film makes a perfect endoscope capable of transforming an image at the input surface with subwavelength resolution to the output surface of the film. This is the main conclusion of this Brief Report.

For proof-of-principle purposes, here in this Brief Report we analyze the simplest holey metal film: an infinite slit array [Fig. 1(a)]. The Fabry-Pérot resonance condition in this case is $\lambda=2h/m$ with $m\geq 1$. Given the input surface being at a distance z_1 from the incident field, we calculate the image at a distance z_2 from the output surface. The incident field is p polarized with its electric field directed along the x axis and consists of two spikes of height E_0, width w, and separation l. This field is expanded in terms of p-polarized plane waves characterized by parallel momentum $k_x^{(0)}$. From the knowledge of the different transmission coefficients $t^{(n)}$ [Eq. (2)] and by taking into account diffraction effects, it is straightforward to calculate the electric field at the image plane.

In order to approach the effective-medium limit where Eq. (4) is valid and where diffraction can be safely neglected, $t^{(0)} \gg t^{(n)}$ for $n \neq 0$ should be satisfied. For a slit array, $k_x^{(n)}=k_x^{(0)}+n\frac{2\pi}{d}$ and $k_z^{(n)}=i\sqrt{k_x^{(n)2}-k_0^2}$. If we choose parameters such that $\lambda \gg w \gg d$, it is obvious that the evanescent decay of all the diffracted waves for $n \neq 0$ is dominated by the term π/d, whereas the dominant $k_x^{(0)}$'s are on the order of π/w. Hence, in the extreme near field of the output surface (z_2

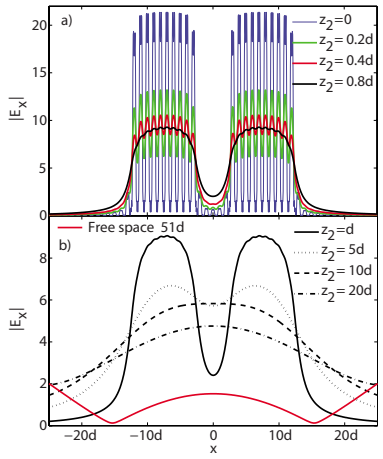

FIG. 2. (Color online) $|E_x(x)|$ for different distances z_2. The distance z_1 is chosen to be 0. d is used as the unit length of the structure and the resonant wavelength is $\lambda=2h=100d$. The width of the slits is $a=0.5d$ and the thickness of the film is $h=50d$. The parameters of the incident field are $E_0=10$, $l=15d$, and $w=10d$. In panel (b), it is also shown the image of the E field after free-space propagation through a $h+d$ distance (the curve with label free space $51d$).

≈ 0), higher-order diffracted waves will distort the perfect image that only can be obtained if diffraction can be completely neglected. However, one may realize that the higher-order diffracted waves will die much faster than the zero-order diffracted waves as $w \gg d$. Thus, if the distance from the output surface to the image plane z_2 is increased, the higher-order diffracted waves will disappear from the image. To illustrate this, we have calculated the image for different distances z_2 from the slit array [Fig. 2]. For details of the slit array, incident field, and wavelength, see caption of Fig. 2. It is clear that there are two near-field zones: one for $z_2 \ll d$, where the higher-order diffracted modes from the array distort the image [Fig. 2(a)] and the other one emerges at $d < z_2 < w$ where the image of the two spikes is recovered [Fig. 2(b)] with subwavelength resolution. Notice how the field for $z_2=d$ is nicely reconstructed in a subwavelength image of the source. In the absence of the holey metal film, most information of the source would be lost at this plane after free-space propagation [see the curve with label free space $51d$ in Fig. 2(b)]. This is also the case if the image plane is located at $z_2 \gg d$. As seen in Fig. 2(b), for $z_2 = 10d, 20d$ it is no longer possible to distinguish the two spikes of the incident field.

By reducing the width of the spikes and its separation (results not shown here), we have found that the ultimate resolution of the endoscope is d, which is the period of the array. This is similar to what occurs in the perfect lens in the optical regime,[1] in which the ultimate resolution would be the interatomic distance if the absorption in the metal film could be ignored.[22] We have also checked that almost identical images are obtained for film thicknesses $h_m = m\lambda/2$ ($m \geq 1$) that fulfill the Fabry-Pérot resonance condition at that particular wavelength. In this way, the thickness of the endoscope could be much larger than the operating wavelength.

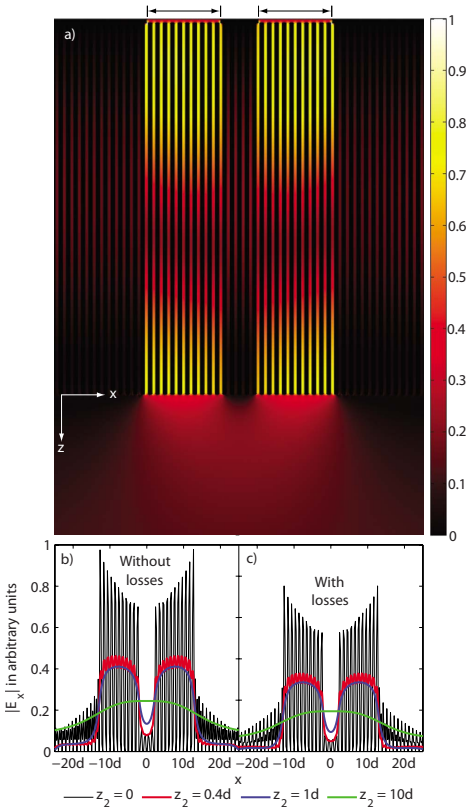

FIG. 3. (Color online) (a) E-field amplitude ($|E_x(x,z)|$) evaluated at the first Fabry-Pérot resonance. The incoming p-polarized field is impinging from above into an opaque screen in which two subwavelength apertures have been perforated (marked with arrows in the figure). The opaque screen is placed just in front of the input surface of the structure. The output surface of the slit array is marked by the x axis in the figure. (b) Calculation of $|E_x(x)|$ at different distances z_2 from the slit array in which Ohmic losses in the metal have not been included. (c) $|E_x(x)|$ at several z_2's that correspond to different cuts in the figure of panel (a).

To test the effect of the absorption in the metal and the accuracy of the single-mode approximation, we have carried out numerical calculations using the commercial finite element solver provided by COMSOL MULTIPHYSICS [Fig. 3]. We have considered a 1D slit array where the period is $d=1$ μm and the relation to all the other parameters of the film and source are the same as before (see caption of Fig. 2). This yields the first Fabry-Pérot resonance frequency at ν_0

=3 THz. Losses of the metal regions are included through the Drude model $\varepsilon_m = 1 - \omega_p^2/[\omega(\omega + i\Gamma)]$, where $\omega_p = 13.8 \times 10^{15}$ s^{-1} is the plasma frequency, $\Gamma = 1.075 \times 10^{14}$ s^{-1} is the damping constant, and the values are for gold and taken from Ref. 23. The 2D field distribution of $|E_x(x,z)|$ including losses is presented [Fig. 3(a)] and the image of the source for different distances z_2 is shown for both the cases without and with absorption [Figs. 3(b) and 3(c), respectively]. It is seen that the endoscope effect in holey metal films is not very sensitive to losses; the only difference when losses are included is a small damping of the field when compared to the lossless case.

In conclusion, we have shown how holey metal films can behave as perfect endoscopes at some resonant frequencies, i.e., they transmit light with unity efficiency for both propagating and evanescent incoming plane waves. In the terahertz regime, we have exemplified our ideas by means of a full numerical calculation on a 1D slit array where both diffraction effects and losses were included. Our findings suggest that holey metal films may find useful applications for subwavelength imaging.

We acknowledge Alexandre Mary for valuable discussions and financial support from the Spanish Ministry of Science under Project No. CSD2007-046-NanoLight.es and from a NABIIT project supported by the Danish Research Agency (Contract No. 2106-05-033).

*fj.garcia@uam.es

[1] J. B. Pendry, Phys. Rev. Lett. **85**, 3966 (2000).
[2] D. O. S. Melville and R. J. Blaikie, Opt. Express **13**, 2127 (2005).
[3] N. Fang, H. Lee, C. Sun, and X. Zhang, Science **308**, 534 (2005).
[4] S. A. Ramakrishna, J. B. Pendry, M. C. K. Wiltshire, and W. J. Stewart, J. Mod. Opt. **50**, 1419 (2003).
[5] P. A. Belov and Y. Hao, Phys. Rev. B **73**, 113110 (2006).
[6] B. Wood, J. B. Pendry, and D. P. Tsai, Phys. Rev. B **74**, 115116 (2006).
[7] Y. Xiong, Z. Liu, and X. Zhang, Appl. Phys. Lett. **93**, 111116 (2008).
[8] Z. Liu, H. Lee, Y. Xiong, Ch. Sun, and X. Zhang, Science **315**, 1686 (2007).
[9] I. I. Smolyaninov, Y.-J. Hung, and C. C. Davis, Science **315**, 1699 (2007).
[10] P. A. Belov, Y. Hao, and S. Sudhakaran, Phys. Rev. B **73**, 033108 (2006).
[11] G. Shvets, S. Trendafilov, J. B. Pendry, and A. Sarychev, Phys. Rev. Lett. **99**, 053903 (2007).
[12] S. Kawata, A. Ono, and P. Verma, Nat. Photonics **2**, 438 (2008).
[13] P. A. Belov, Y. Zhao, S. Tse, P. Ikonen, M. G. Silveirinha, C. R. Simovski, S. Tretyakov, Y. Hao, and C. Parini, Phys. Rev. B **77**, 193108 (2008).
[14] P. A. Belov, C. R. Simovski, and P. Ikonen, Phys. Rev. B **71**, 193105 (2005).
[15] P. Ikonen, P. Belov, C. Simovski, and S. Maslovski, Phys. Rev. B **73**, 073102 (2006).
[16] C. Luo, S. G. Johnson, J. D. Joannopoulos, and J. B. Pendry, Phys. Rev. B **65**, 201104(R) (2002).
[17] P. V. Parimi, W. T. Lu, P. Vodo, and S. Sridhar, Nature (London) **426**, 404 (2003).
[18] J. B. Pendry, L. Martin-Moreno, and F. J. Garcia-Vidal, Science **305**, 847 (2004).
[19] F. J. Garcia-Vidal, L. Martin-Moreno, and J. B. Pendry, J. Opt. A, Pure Appl. Opt. **7**, S97 (2005).
[20] T. W. Ebbesen, H. J. Lezec, H. F. Ghaemi, T. Thio, and P. A. Wolff, Nature (London) **391**, 667 (1998).
[21] L. Martin-Moreno, F. J. Garcia-Vidal, H. J. Lezec, K. M. Pellerin, T. Thio, J. B. Pendry, and T. W. Ebbesen, Phys. Rev. Lett. **86**, 1114 (2001).
[22] F. D. M. Haldane, arXiv:cond-mat/0206420 (unpublished).
[23] L. Novotny and B. Hecht, *Principles of Nanooptics* (Cambridge University Press, Cambridge, England, 2006).

Appendix G

Submitted to New J. Phys. (2009)

Light transmission properties of holey metal films in the metamaterial limit:
effective medium theory and superlensing effects
by
Jesper Jung, Luis Martin-Moreno, and Francisco J. Garcia-Vidal

This page is intentionally left blank

Light transmission properties of holey metal films in the metamaterial limit: effective medium theory and superlensing effects

J Jung[1,2], L Martín-Moreno[3] and F J García-Vidal[2]

[1] Department of Physics and Nanotechnology, Aalborg University, Skjernvej 4A, DK-9220 Aalborg Øst, Denmark

[2] Departamento de Física Teórica de la Materia Condensada, Universidad Autónoma de Madrid, E-28049 Madrid, Spain

[3] Instituto de Ciencia de Materiales de Aragón (ICMA) and Departamento de Física de la Materia Condensada, CSIC-Universidad de Zaragoza, E-50009 Zaragoza, Spain

E-mail: fj.garcia@uam.es

Abstract. Light transmission properties of holey metal films in the metamaterial limit, where the unit length of the periodic structures is much smaller than the operating wavelength, are analyzed theoretically utilizing the modal expansion formalism. A detailed derivation of the transmission coefficients of both one-dimensional slit and two-dimensional hole arrays is presented. We demonstrate how such films effectively can be mapped into homogenous anisotropic films with optical properties controlled by the geometrical parameters of the holes. We also show that holey metal films can, for *p*-polarized light, operate as endoscopes with superlensing properties, i.e., they are capable of transforming an image with subwavelength resolution from the input to the output surface of the film.

PACS numbers: 42.30.-d,78.20.+Ci,41.20.Jb,42.30.Wb

1. Introduction

The pioneering work of Ebbesen *et al.* on extraordinary optical transmission (EOT) through an optically thick metal film perforated with subwavelength holes [1] has opened a new avenue of research within electromagnetism. This scientific avenue was first dedicated to reveal the physics of the EOT phenomenon [2, 3, 4] and later to study light transmission through various holey metal films [5, 6, 7] and single subwavelength holes [8, 9, 10, 11, 12, 13, 14].

Ebbesen and co-workers discovered that holey metal films can exhibit transmission resonances with efficiencies that are orders of magnitude larger than predicted by standard aperture theory [15], and also pointed out that there is a link between EOT resonances and excitation of surface plasmon polaritons (SPPs) in the film. A few years later, this connection was substantiated with a theoretical explanation of the EOT phenomenon [4]. Using the multiple scattering formalism, this full three-dimensional theoretical study of EOT revealed that the enhancement of the optical transmission is due to photon tunnelling through SPPs formed on the individual metal-dielectric interfaces of the film. Surprisingly, the theory also predicted that EOT through holey metal films exists even when the metal is treated as a perfect electrical conductor (PEC). In the beginning this was considered strange because a flat PEC surface does not support SPPs. However, it was also known that corrugated PEC surfaces indeed support bound surface modes, and that the corrugations strongly compress the electromagnetic (EM) field of the surface modes in the material above the surface active medium [16, 17]. More recently, it was discovered that if a PEC structure is perforated by an array of subwavelength holes, it behaves as an effective medium where the EM waves are governed by an effective dielectric constant which is form invariant with the dielectric constant of a simple plasma ($\varepsilon = 1 - \omega_p^2/\omega^2$) [18, 19]. In the case of a holey PEC surface, the plasma frequency ω_p is not an intrinsic material property, but it is given by the cutoff frequency of the hole waveguides [18, 19]. This result has two important implications. First, as the dielectric constant is reduced to the simple plasma form, it means that a holey PEC surface can support bound surface EM modes whose properties mimic those of canonical SPPs. This is because the interface between e.g. air and a medium described by a dielectric constant of the simple plasma form fulfill the criteria for the existence of bound surface modes [20, 21, 22]. However, as these geometrically-induced SPPs (i.e. *spoof* SPPs) have a completely different origin than canonical SPPs, spoof SPPs are supported for frequencies below ω_p and not $\omega_p/\sqrt{2}$ as canonical SPPs [18]. This is due to the anisotropy in the optical response of the structure. Second, as the plasma frequency is given by the cutoff frequency of the hole waveguides, which is strongly dependent on the size of the waveguide, this *plasma frequency* can be tailored by means of the size of the holes. Recently, the existence of spoof SPPs governed by the cutoff frequency of the hole waveguide has been experimentally verified in the microwave regime [23]. Nowadays it is generally accepted, that EOT through holey metal films is attributed to photon tunnelling though SPPs formed on the two surfaces of the film,

where the SPPs can be either spoof or a mixture of spoof and canonical SPPs depending on the conductivity of the metal. Even more generally, extraordinary transmission of waves (matter and acoustic waves, for example) can be expected whenever the surface of the structure supports surface modes [24, 25, 26].

Another important discovery within electromagnetism that also relies on excitation of SPPs is superlensing. Less than ten years ago, Pendry proved that a planar film with a refractive index of -1 can be used as an almost perfect lens that not only cancels the phase delay of the propagating waves both also is capable of compensating the exponential decay of the evanescent ones [27]. In this seminal work, Pendry showed that, in the electrostatic limit where the two polarizations become decoupled, near-field superlensing can be achieved with a thin metal slab. This has later been verified with experiments [28, 29]. The physical mechanism behind electrostatic superlensing is enhancement of evanescent waves by means of resonantly excited SPPs [27]. At the spectral location where the permittivity of the metal ε_m fulfills $-\varepsilon_m \sim \varepsilon$, ε being the permittivity of the dielectric that surrounds the metal, the SPP dispersion relation becomes virtually flat for large parallel momenta, meaning that the band of parallel momentum where it is possible to excite SPPs becomes very broad, which results in the superlensing effect [28].

In reference [30] we presented a theoretical analysis of holey metal films based on the multiple scattering formalism. The original idea was to take advantage of the spoof SPP concept in holey metal films in order to transfer Pendry's idea of superlensing in the optical regime to lower frequencies. We found that spoof SPPs on holey metal films are not able to amplify the EM field associated with the incident evanescent waves as canonical SPPs do in an un-corrugated metal film. Instead, our theoretical analysis demonstrated that in the metamaterial limit ($\lambda >> d$, where d is the unit cell size of the holey metal film), where diffraction effects can be neglected, and at some resonant Fabry-Perot frequencies, all incident plane waves (both propagating and evanescent) are transmitted with unit efficiency, meaning that a holey metal film can act as a perfect endoscope, where an image is transferred from the input surface to the output surface with subwavelength resolution. As a difference, in the EOT regime ($\lambda \sim d$), where diffraction effects are important, spoof SPPs help to enhance the incident propagating plane waves, but their spectral location is very sensitive to the parallel momentum, i.e., angle of incidence.

Other examples of metamaterials that have been investigated for superlensing are layered metal-dielectric media [31, 32, 33, 34, 35], metallic wire media [36, 37, 38, 39], and photonic crystals [40, 41, 42, 43]. Some of these, e.g. metallic wire media, can also work as superlenses at terahertz frequencies, where they are capable of transforming all incoming plane waves with unit efficiency through the medium. Thus, as holey metal films, a lens based on a metallic wire medium can transform an image with subwavelength details across the lens. However, unlike metal wire media, holey metal films are readily implemented and therefore much more attractive from an application point of view. With the nanofabrication tools available today, it is considered an easy

task to make holes in metal films even on a scale of sub-optical wavelengths. It is also important to notice that Babinet's principle is not applicable for screens of finite width, so there is no obvious relation between holey metal films and metallic wire media. Hence, the previous work on metallic wire media [36, 37, 38, 39] can not be used to explain the optical transmission properties of holey metal films analyzed in this work.

This paper is a follow up on our short paper [30], where some of our work on holey metal films were presented on a superior level. In this work, we present in detail the derivation of the transmission coefficients for light transmission through holey metal films using the modal expansion formalism. We also analyze the effective optical properties of holey metal films and derive how holey metal films can be mapped into anisotropic homogenous media, with optical properties determined by the geometrical parameters of the holes in the film. Lastly, we present the superlensing effect in holey metal films and the analysis of an endoscope consisting of a PEC film perforated with an arrangement of periodic cut-through one-dimensional (1D) slits. Important issues, as the ultimate resolution and optimal configuration of the holes, are also analyzed and discussed.

The paper is organized as follows. Section 2 is devoted to set up and study the transmission coefficients of holey metal films. 1D slit and two-dimensional (2D) hole arrays are analyzed in individual subsections (section 2.1 and section 2.2, respectively). In section 3 the effective optical properties of holey metal films are analyzed and section 4 presents the superlensing effect. In section 5 we deliver our conclusions.

2. Light transmission through holey metal films in the metamaterial limit

The transmission coefficients of holey metal films are derived using the quasianalytical modal expansion formalism. The idea of the formalism is to expand the EM field in terms of plane wave eigenmodes outside the film and in waveguide eigenmodes inside the holes of the film. We assume that the metals of the films are PECs and the fields in the metal regions are therefore zero. The PEC assumption is valid for zero frequency and all the way up up to terahertz frequencies. We also assume that the media outside the film and within the holes are the same, described by a dielectric constant $\epsilon = 1$. We consider an incident p-polarized plane wave with parallel momentum described by k_x (thus $k_y = 0$). Inside the holes several waveguide modes will be excited by the incident field but, in the metamaterial limit, only the fundamental waveguide mode will be important for the transmission properties, as all higher order modes are strongly evanescent [4]. By matching the EM fields at the input and output surfaces a self consistent set of linear equations is obtained.

2.1. 1D slit array

First we analyze an array of 1D apertures (slits) drilled in a PEC film of thickness h. The width of the slits is a and the size of the unit cell is d. The coordinate system is

chosen such that the z axis is perpendicular to the film plane, and $z = 0$ and $z = h$ are the positions of the input and output surfaces of the film, respectively [figure 1].

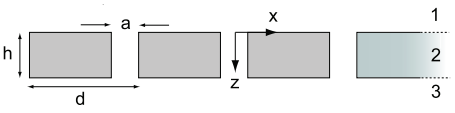

Figure 1. 1D film perforated with subwavelength slits. The film thickness is h, the width of the slits is a, and the size of the unit cell is d. The film is illuminated from region 1 by a p-polarized incident field characterized by the parallel momentum $k_{\parallel} = k_x$.

We consider the case where the film is illuminated by a p-polarized plane wave, which only has parallel momentum along the x axis ($k_{\parallel} = k_x$). The EM field associated with the incident field at point $\vec{r} = (x, z)$ is given as

$$\mathbf{E}_i(\vec{r}) = \frac{1}{\sqrt{d}} e^{ik_x x} e^{ik_z z} \left(\hat{x} - \frac{k_x}{k_z} \hat{z} \right); \quad \mathbf{H}_i(\vec{r}) = \frac{Y}{\sqrt{d}} e^{ik_x x} e^{ik_z z} \hat{y}\,, \tag{1}$$

where $Y = k_0/k_z$ is the admittance, $k_z = \sqrt{k_0^2 - k_x^2}$, $k_0 = \omega/c$, ω is the angular frequency and c is the speed of light in vacuum. The refracted and transmitted plane waves associated with the nth-order of diffraction can be written as

$$\begin{aligned} \mathbf{E}^{(n)}(\vec{r}) &= \frac{1}{\sqrt{d}} e^{ik_x^{(n)} x} e^{\pm ik_z^{(n)} z} \left(\hat{x} - \frac{k_x^{(n)}}{k_z^{(n)}} \hat{z} \right) \\ \mathbf{H}^{(n)}(\vec{r}) &= \frac{\pm Y^{(n)}}{\sqrt{d}} e^{ik_x^{(n)} x} e^{\pm ik_z^{(n)} z} \hat{y} \end{aligned}, \tag{2}$$

where + is used for the transmitted plane waves in region 3 and - is used for reflected plane waves in region 1 [see figure 1], $k_x^{(n)} = k_x + n2\pi/d$, $k_z^{(n)} = \sqrt{k_0^2 - k_x^{(n)2}}$ and $Y^{(n)} = k_0/k_z^{(n)}$. The EM field associated with the fundamental TEM waveguide mode inside the slits, α, can be written as

$$\mathbf{E}_\alpha(\vec{r}) = \frac{1}{\sqrt{a}} e^{\pm ik_0 z} \hat{x}; \quad \mathbf{H}_\alpha(\vec{r}) = \frac{\pm Y_\alpha}{\sqrt{a}} e^{\pm ik_0 z} \hat{y}, \tag{3}$$

where - is used in the case of backward propagating TEM waveguides modes and the admittance is $Y_\alpha = k_0/k_0 = 1$. The x component of the electric field E_x, that must be continuous at every point within the unit cell, can be expanded in terms of the eigenmodes in the three different regions (before, in, and after the film) as

$$\begin{aligned} |E_x^1\rangle &= |k_x\rangle e^{ik_z z} + \sum_{n=-\infty}^{\infty} \rho^{(n)} |k_x^{(n)}\rangle e^{-ik_z^{(n)} z} \\ |E_x^2\rangle &= |\alpha\rangle \left(A e^{ik_0 z} + B e^{-ik_0 z} \right) \\ |E_x^3\rangle &= \sum_{n=-\infty}^{\infty} t^{(n)} |k_x^{(n)}\rangle e^{ik_z^{(n)} (z-h)} \end{aligned}, \tag{4}$$

where we have introduced the Dirac notation as

$$\langle \mathbf{r}|k_x^{(n)}\rangle = \frac{e^{ik_x^{(n)}x}}{\sqrt{d}}, \quad \langle \mathbf{r}|\alpha\rangle = \frac{1}{\sqrt{a}}, \quad \text{and} \quad \langle \mathbf{r}|\vec{E}\rangle \equiv \vec{E}(\vec{r}), \tag{5}$$

$\rho^{(n)}$ and $t^{(n)}$ are the nth-order reflection and transmission coefficients, respectively, and A and B are the constants of the linear combination of the forward and backward propagating TEM waveguide modes within the holes. The magnetic field $\mathbf{H} = H_y\hat{y}$ which must be continuous only across the holes, can be related to E_x as $-\mu_z \times \mathbf{H} = \pm Y^{(n)}E_x\hat{x}$ using the Maxwell equations, where μ_z is a unit vector along the z direction. Thus, in the three regions

$$\begin{aligned} -\mu_z \times |\mathbf{H}^1\rangle &= Y|k_x\rangle e^{ik_z z} - \sum_{n=-\infty}^{\infty} \rho^{(n)}Y^{(n)}|k_x^{(n)}\rangle e^{-ik_z^{(n)}z} \\ -\mu_z \times |\mathbf{H}^2\rangle &= |\alpha\rangle\left(Ae^{ik_0 z} - Be^{-ik_0 z}\right) \\ -\mu_z \times |\mathbf{H}^3\rangle &= \sum_{n=-\infty}^{\infty} t^{(n)}Y^{(n)}|k_x^{(n)}\rangle e^{ik_z^{(n)}(z-h)} \end{aligned}, \tag{6}$$

must be continuous only over the holes. By matching parallel components of the electric field in equation (4) using standard boundary conditions at $z = 0$ and $z = h$ and then projecting the equations into the set $\langle k_x^{(n)}|$ one readily obtains

$$t^{(n)} = -S^{(n)}E'; \quad \rho^{(n)} = -\delta_{0,n} + S^{(n)}E, \tag{7}$$

where δ is the Kronecker delta function, $E = A + B$, $E' = -(Ae^{ik_0 h} + Be^{-ik_0 h})$ and $S^{(n)} = \langle \alpha|k_x^{(n)}\rangle$ is the overlap integral between an nth-order plane wave and the TEM waveguide mode given as

$$S^{(n)} = \frac{1}{\sqrt{ad}}\int_{-a/2}^{a/2} e^{-ik_x^{(n)}x}\mathrm{d}x = \sqrt{\frac{a}{d}}\mathrm{sinc}\left(\frac{k_x^{(n)}a}{2}\right). \tag{8}$$

By matching equation (6) at $z = 0$ and $z = h$, projecting the equations into the set $\langle \alpha|$, and substituting with equation (7) one obtains after some algebra a self consistent set of linear equations in E and E'

$$\begin{aligned} (G - \Sigma)E - E'G^V &= I_0 \\ (G - \Sigma)E' - EG^V &= 0, \end{aligned} \tag{9}$$

where $I_0 = 2iY^{(0)}S^{(0)*}$, $G = i\sum_{n=-\infty}^{\infty} Y^{(n)}|S^{(n)}|^2$, $\Sigma = 1/\tan(k_0 h)$, and $G^V = 1/\sin(k_0 h)$. Solving for E' in equation (9) and substituting into equation (7) yields an expression for the transmission coefficients

$$t^{(n)} = \frac{-S^{(n)}I_0 G^V}{(G - \Sigma)^2 - G^{V2}}. \tag{10}$$

By substituting for I_0, G^V and Σ this can, after some algebra, be rewritten as

$$t^{(n)} = \frac{4Y^{(0)}S^{(0)*}S^{(n)}e^{ik_0 h}}{e^{2ik_0 h}(G - i)^2 - (G + i)^2}. \tag{11}$$

In the metamaterial limit all diffraction effects can be neglected, and the transmission coefficient $t \equiv t^{(0)}$ can be reduced to

$$t = \frac{4Y^{(0)}|S^{(0)}|^2 e^{ik_0 h}}{\left[1 + Y^{(0)}|S^{(0)}|^2\right]^2 - \left[1 - Y^{(0)}|S^{(0)}|^2\right]^2 e^{2ik_0 h}}. \tag{12}$$

Equation (12) coincides with the general expression stated in reference [30] for the case of a 1D slit array. As a difference, in reference [30] the multiple scattering formalism was used in the derivation of t.

2.2. 2D hole array

Now we consider PEC films perforated with a periodic 2D array of square holes. The hole area size is $a \times a$, the unit cell size of the lattice is $d \times d$, and the thickness of the film is h. The coordinate system is chosen such that the z axis is perpendicular to the film plane and $z = 0$ and $z = h$ are located at the input and output surfaces of the film, respectively [figure 2]. Again we consider the case where the film is illuminated by a p

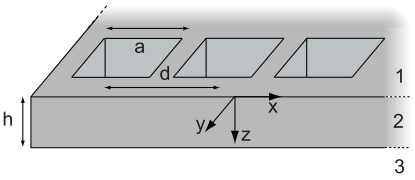

Figure 2. 2D perfect conductor film perforated by $a \times a$ square subwavelength holes in a $d \times d$ lattice. The film thickness is h, and the film is illuminated from region 1 by a p polarized plane wave with parallel momentum k_x.

polarized plane wave ($k_\parallel = k_x$). The EM field associated with the incident field may be written as

$$\mathbf{E}_i(\vec{r}) = \frac{1}{d} e^{ik_x x} e^{ik_z z} \left(\hat{x} - \frac{k_x}{k_z}\hat{z}\right); \quad \mathbf{H}_i(\vec{r}) = \frac{Y}{d} e^{ik_x x} e^{ik_z z} \hat{y}, \tag{13}$$

where $Y = k_0/k_z$ is the admittance. The EM field outside the metal film is expanded in p- and s-polarized plane wave eigenmodes. The EM field associated with an n, m order

diffracted eigenmode may be expressed as

$$\begin{aligned}
\mathbf{E}_p^{(n,m)}(\vec{r}) &= \frac{1}{d} e^{ik_x^{(n)}x} e^{ik_y^{(m)}y} e^{\pm ik_z^{(n,m)}z} \left(\frac{k_x^{(n)}}{k_\parallel^{(n,m)}}\hat{x} + \frac{k_y^{(m)}}{k_\parallel^{(n,m)}}\hat{y} - \frac{k_\parallel^{(n,m)}}{k_z^{(n,m)}}\hat{z} \right) \\
\mathbf{E}_s^{(n,m)}(\vec{r}) &= \frac{1}{d} e^{ik_x^{(n)}x} e^{ik_y^{(m)}y} e^{\pm ik_z^{(n,m)}z} \left(\frac{-k_y^{(n)}}{k_\parallel^{(n,m)}}\hat{x} + \frac{k_x^{(m)}}{k_\parallel^{(n,m)}}\hat{y} \right) \\
\mathbf{H}_p^{(n,m)}(\vec{r}) &= \frac{\pm Y_p^{(n,m)}}{d} e^{ik_x^{(n)}x} e^{ik_y^{(m)}y} e^{\pm ik_z^{(n,m)}z} \left(\frac{-k_y^{(n)}}{k_\parallel^{(n,m)}}\hat{x} + \frac{k_x^{(m)}}{k_\parallel^{(n,m)}}\hat{y} \right) \\
\mathbf{H}_s^{(n,m)}(\vec{r}) &= \frac{\pm Y_s^{(n,m)}}{d} e^{ik_x^{(n)}x} e^{ik_y^{(m)}y} e^{\pm ik_z^{(n,m)}z} \left(\frac{-k_x^{(n)}}{k_\parallel^{(n,m)}}\hat{x} + \frac{-k_y^{(m)}}{k_\parallel^{(n,m)}}\hat{y} + \frac{k_\parallel^{(n,m)}}{k_z^{(n,m)}}\hat{z} \right)
\end{aligned} \tag{14}$$

where the subscripts p and s refer to p and s polarization, $+$ is used for the transmitted eigenwaves in region 3, - is used for reflected eigenwaves in region 1, $k_x^{(x)} = k_x + 2\pi n/d$, $k_y^{(m)} = 2\pi m/d$, $k_z^{(n,m)} = \sqrt{k_0^2 - k_x^{(n)2} - k_y^{(m)2}}$, $k_\parallel^{(n,m)} = \sqrt{k_x^{(n)2} + k_y^{(m)2}}$, and the admittances are $Y_p^{(n,m)} = k_0/k_z^{(n,m)}$ and $Y_s^{(n,m)} = k_z^{(n,m)}/k_0$. As the EM boundary conditions only require continuity of the parallel components (x and y) of $\mathbf{E}$ and $\mathbf{H}$, we disregard the z component and introduce bivectors in order to apply matching conditions at $z = 0$ and $z = h$. The bivectors for p and s polarization are given as

$$\begin{aligned}
\langle \mathbf{r}|\mathbf{k}^{(n,m)}p\rangle &= \frac{e^{ik_x^{(n)}x} e^{ik_y^{(m)}y}}{dk_\parallel^{(n,m)}} \left(k_x^{(n)}\hat{x} + k_y^{(m)}\hat{y} \right) \\
\langle \mathbf{r}|\mathbf{k}^{(n,m)}s\rangle &= \frac{e^{ik_x^{(n)}x} e^{ik_y^{(m)}y}}{dk_\parallel^{(n,m)}} \left(-k_y^{(m)}\hat{x} + k_x^{(n)}\hat{y} \right)
\end{aligned} \tag{15}$$

respectively. By means of Eq. (15), we can express the parallel components of the eigenmodes outside the film as

$$\begin{aligned}
|\mathbf{E}_\sigma^{(n,m)}\rangle &= |\mathbf{k}^{(n,m)}\sigma\rangle e^{\pm ik_z^{(n,m)}z} \\
-\mu_z \times |\mathbf{H}_\sigma^{(n,m)}\rangle &= \pm Y_\sigma^{(n,m)} |\mathbf{k}^{(n,m)}\sigma\rangle e^{\pm ik_z^{(n,m)}z}
\end{aligned} \tag{16}$$

where σ is the polarization (either p or s). The EM field of the fundamental TE_{01} waveguide mode within the holes α can be written as

$$\begin{aligned}
\mathbf{E}_\alpha(\vec{r}) &= \frac{\sqrt{2}}{a} \sin(k'_y y + \frac{\pi}{2}) e^{\pm ik'_z z}\hat{x} \\
-\mu_z \times \mathbf{H}_\alpha(\vec{r}) &= \frac{\pm Y_\alpha \sqrt{2}}{a} \sin(k'_y y + \frac{\pi}{2}) e^{\pm ik'_z z}\hat{x}
\end{aligned} \tag{17}$$

where $-$ is used for backward propagating TE_{01} waveguide modes, $k'_y = \pi/a$, $k'_z = \sqrt{k_0^2 - (\pi/a)^2}$, and the admittance of the hole waveguide mode is given as $Y_\alpha = k'_z/k_0$. Note, that primed wave vectors are used inside the holes. As in the 1D case the parallel components of the field in the three regions [Fig. 2] can be expanded in terms of the

eigenmodes

$$
\begin{aligned}
|\mathbf{E}^1\rangle &= |\mathbf{k}^{(0,0)}p\rangle e^{ik_z^{(0,0)}z} + \sum_\sigma \sum_{n,m=-\infty}^{\infty} \rho_\sigma^{(n,m)} |\mathbf{k}^{(n,m)}\sigma\rangle e^{-ik_z^{(n,m)}z} \\
|\mathbf{E}^2\rangle &= |\alpha\rangle \left[Ae^{ik'_z z} + Be^{-ik'_z z} \right] \\
|\mathbf{E}^3\rangle &= \sum_\sigma \sum_{n,m=-\infty}^{\infty} t_\sigma^{(n,m)} |\mathbf{k}^{(n,m)}\sigma\rangle e^{ik_z^{(n,m)}(z-h)} \\
-\mu_z \times |\mathbf{H}^1\rangle &= Y_p^{(0,0)} |\mathbf{k}^{(0,0)}p\rangle e^{ik_z^{(0,0)}z} - \sum_\sigma \sum_{n,m=-\infty}^{\infty} Y_\sigma^{(n,m)} \rho_\sigma^{(n,m)} |\mathbf{k}^{(n,m)}\sigma\rangle e^{-ik_z^{(n,m)}z} \\
-\mu_z \times |\mathbf{H}^2\rangle &= Y_\alpha |\alpha\rangle \left[Ae^{ik'_z z} - Be^{-ik'_z z} \right] \\
-\mu_z \times |\mathbf{H}^3\rangle &= \sum_\sigma \sum_{n,m=-\infty}^{\infty} t_\sigma^{(n,m)} Y_\sigma^{(n,m)} |\mathbf{k}^{(n,m)}\sigma\rangle e^{ik_z^{(n,m)}(z-h)}
\end{aligned}
\tag{18}
$$

By applying a scheme similar to the 1D case, we obtain equations for the reflection and transmission coefficients as

$$
\rho_\sigma^{(n,m)} = -\delta_{n,0}\delta_{m,0}\delta_{\sigma,p} + S_\sigma^{(n,m)} E; \quad t_\sigma^{(n,m)} = -S_\sigma^{(n,m)} E', \tag{19}
$$

and a set of linear equations in $E = A + B$ and $E' = -(Ae^{ik'_z h} + Be^{-ik'_z h})$ which is form invariant with equation (9). For 2D hole arrays $I_0 = i2Y_p^{(0,0)} S_p^{(0,0)*}$, $G = i\sum_\sigma \sum_{n,m=-\infty}^{\infty} Y_\sigma^{(n,m)} |S_\sigma^{(n,m)}|^2$, $\Sigma = Y_\alpha / \tan(k'_z h)$, $G^V = Y_\alpha / \sin(k'_z h)$, and $S_\sigma^{(n,m)}$ is the overlap integral between an eigenmode (of diffraction order n, m and polarization σ) and the fundamental TE_{01} waveguide mode. The overlap between the p polarized incident field and the waveguide mode is given as

$$
\begin{aligned}
S_p^{(0,0)} &= \frac{\sqrt{2}}{ad} \int_{-a/2}^{a/2} \int_{-a/2}^{a/2} e^{ik_x x} \sin\left(\frac{\pi}{a}y + \frac{\pi}{2}\right) \mathrm{d}x\mathrm{d}y \\
&= \frac{2\sqrt{2}a}{d\pi} \mathrm{sinc}(k_x a/2),
\end{aligned}
\tag{20}
$$

and in general the overlap integral for p polarization yields

$$
\begin{aligned}
S_p^{(n,m)} &= \frac{\sqrt{2}k_x^{(n)}}{a d k_\parallel^{(n,m)}} \int_{-a/2}^{a/2} \int_{-a/2}^{a/2} e^{ik_x^{(n)}} e^{ik_y^{(m)}y} \sin\left(\frac{\pi}{a}y + \frac{\pi}{2}\right) \mathrm{d}x\mathrm{d}y \\
&= \frac{-2\pi\sqrt{2}k_x^{(n)} a \mathrm{sinc}(k_x^{(n)}a/2) \cos(k_y^{(m)}a/2)}{d k_\parallel^{(n,m)} (k_y^{(m)}a + \pi)(k_y^{(m)}a - \pi)}.
\end{aligned}
\tag{21}
$$

For s-polarization, the general overlap integral can be readily found as $S_s^{(n,m)} = -k_y^{(m)} S_p^{(n,m)} / k_x^{(n)}$. By solving for E' in equation (9), substituting into equation (19), and using the analytical expressions for G^V, Σ and I_0, one obtains after some algebra a final result for the transmission coefficients of 2D hole arrays

$$
t_\sigma^{(n,m)} = \frac{4Y_\alpha Y_p^{(0,0)} S_p^{(0,0)*} S_\sigma^{(n,m)} e^{ik'_z h}}{e^{2ik'_z h}(G - iY_\alpha)^2 - (G + iY_\alpha)^2}. \tag{22}
$$

In the metamaterial limit, where all diffraction effects can be neglected, the only non-zero transmission coefficient $t \equiv t_p^{(0,0)}$ [$S \equiv S_p^{(0,0)}$ and $Y \equiv Y_p^{(0,0)}$] reduces to

$$t = \frac{4Y_\alpha Y|S|^2 e^{ik'_z h}}{\left[Y_\alpha + Y|S|^2\right]^2 - \left[Y_\alpha - Y|S|^2\right]^2 e^{2ik'_z h}}, \tag{23}$$

which coincides with the general expression stated in reference [30] for the case of a 2D hole array.

3. Effective medium theory of holey metal films in the metamaterial limit

In this section we present a scheme for deriving effective optical parameters of holey metal films. Using these, holey metal films can effectively be mapped into anisotropic homogenous media. The method is to set up expressions for the transmission coefficients of anisotropic homogenous films, compare them with the metamaterial limit transmission coefficients of holey metal films [equation (12) for 1D slit arrays and equation (23) for 2D hole arrays] and, from the comparison, extract the effective optical parameters of the holey metal films. We present the full scheme for 2D hole arrays. For 1D slit arrays we only present the starting point and the final results. In the case of a 1D slit array, the starting point is that a corresponding anisotropic homogenous film would have permittivity and permeability tensors on the form [19]

$$\bar{\varepsilon}_{1D}^{-1} = \begin{bmatrix} \varepsilon_x^{-1} & 0 & 0 \\ 0 & 0 & 0 \\ 0 & 0 & 0 \end{bmatrix}; \quad \bar{\mu}_{1D}^{-1} = \begin{bmatrix} 1 & 0 & 0 \\ 0 & \mu_y^{-1} & 0 \\ 0 & 0 & \mu_z^{-1} \end{bmatrix}. \tag{24}$$

In the case of a 2D hole array with square holes in a square lattice, symmetry requires that the response tensors have diagonal elements on the form $\varepsilon_x = \varepsilon_y = \varepsilon_\parallel$ and $\mu_x = \mu_y = \mu_\parallel$. Furthermore as the fundamental waveguide mode within the holes shows no dispersion with the parallel momentum a further requirement is $\varepsilon_z = \mu_z = \infty$ [18, 19]. The relative permittivity and permeability tensors of a corresponding anisotropic homogenous film therefore take the form

$$\bar{\varepsilon}_{2D}^{-1} = \begin{bmatrix} \varepsilon_\parallel^{-1} & 0 & 0 \\ 0 & \varepsilon_\parallel^{-1} & 0 \\ 0 & 0 & 0 \end{bmatrix}; \quad \bar{\mu}_{2D}^{-1} = \begin{bmatrix} \mu_\parallel^{-1} & 0 & 0 \\ 0 & \mu_\parallel^{-1} & 0 \\ 0 & 0 & 0 \end{bmatrix}. \tag{25}$$

We now start the derivation for 2D hole arrays. The first step is to set up the transmission coefficient for light through an anisotropic homogenous film of thickness h using the response tensors of equation (25) [figure 3]. We consider monochromatic plane waves, where $\nabla\times \rightarrow i\mathbf{k}\times$ and $\partial/\partial t \rightarrow -i\omega$. Starting from the Maxwell curl equations in $\mathbf{k}$ and ω space, the wave equation of the electric displacement $\mathbf{D}$ within the film can be written as

$$k_0^2\mathbf{D} = -\mathbf{k}' \times \bar{\mu}_{2D}^{-1}\mathbf{k}' \times \bar{\varepsilon}_{2D}^{-1}\mathbf{D} = -\varepsilon_\parallel^{-1}\mu_\parallel^{-1} \begin{bmatrix} -k_z'^2 & 0 & 0 \\ 0 & -k_z'^2 & 0 \\ k'_x k'_z & k'_y k'_z & 0 \end{bmatrix} \mathbf{D}, \tag{26}$$

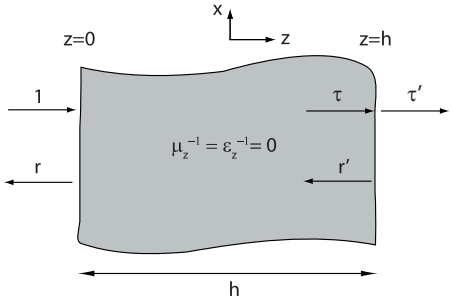

Figure 3. Light transmission through an anisotropic film of thickness h.

Note again, that primed wave vectors are used inside the film. Equation (26) has two degenerate non-trivial solutions, where for p polarization the important is

$$\mathbf{D} = k'_x\hat{x} + k'_y\hat{y} - \frac{k'^2_x + k'^2_y}{k'_z}\hat{z}, \quad \text{with} \quad k'^2_z = k_0^2\varepsilon_\parallel\mu_\parallel. \tag{27}$$

For a p polarized incident field the wave vector in vacuum outside the film is given as $\mathbf{k}_i = k_x\hat{x} + k_z\hat{z}$. This leads to a solution of the wave equation of the electric displacement in vacuum as

$$\mathbf{D}_i = k_z\hat{x} - k_x\hat{z}, \quad \text{with} \quad k_0^2 = k_x^2 + k_z^2. \tag{28}$$

The EM boundary conditions are that E_x and D_z must be continuous across the interface. Matching E_x and D_z at both $z = 0$ and $z = h$ [figure 3] yields two-media transmission and reflection coefficients as

$$\tau = \frac{2\varepsilon_\parallel k'_z k_z}{(\varepsilon_\parallel k_z + k'_z)k_x}; \quad \tau' = \frac{2k_x}{\varepsilon_\parallel k_z + k'_z}; \quad r = r' = \frac{\varepsilon_\parallel k_z - k'_z}{\varepsilon_\parallel k_z + k'_z}. \tag{29}$$

The transmission through the entire film is given by summing all the multiple scattering events, which yields

$$t = \frac{\tau\tau' e^{ik'_z h}}{1 - r'^2 e^{2ik'_z h}} = \frac{4\varepsilon_\parallel k'_z k_z e^{ik'_z h}}{(\varepsilon_\parallel k_z + k'_z)^2 - (\varepsilon_\parallel k_z - k'_z)^2 e^{2ik'_z h}}. \tag{30}$$

By comparing equation (30) with equation (23) (the metamaterial limit transmission coefficient of 2D hole arrays) an expression for $\varepsilon_\parallel$ can be extracted. First we substitute for $Y = k_0/k_z$ and $Y_\alpha = k'_z/k_0$ in equation (23) and rearrange, this yields

$$t = \frac{4\frac{k'^2_z}{|S|^2k_0^2}k'_z k_z e^{ik'_z h}}{(\frac{k'^2_z}{|S|^2k_0^2}k_z + k'_z)^2 - (\frac{k'^2_z}{|S|^2k_0^2}k_z - k'_z)^2 e^{2ik'_z h}}, \tag{31}$$

which after comparison with equation (30) yields

$$\varepsilon_\parallel = \frac{k'^2_z}{|S|^2k_0^2} = \frac{d^2\pi^2}{8a^2\mathrm{sinc}^2(k_x a/2)}\left(1 - \frac{\pi^2c^2}{a^2\omega^2}\right), \tag{32}$$

where equation (20), $k_z' = \sqrt{k_0^2 - (\pi/a)^2}$, and $k_0 = \omega/c$ have been used. In the metamaterial limit, where λ is large, $k_x a$ is small, and $\varepsilon_\parallel$ can be approximated as

$$\varepsilon_\parallel = \frac{d^2\pi^2}{8a^2}\left(1 - \frac{\omega_p^2}{\omega^2}\right), \tag{33}$$

where $\omega_p = \pi c/a$. As $k_z'^2 = k_0^2 \varepsilon_\parallel \mu_\parallel$, we immediately see from equation (32) that in the long wavelength limit [$\mathrm{sinc}(k_x a/2) \approx 1$]

$$\mu_\parallel = |S|^2 = \frac{8a^2}{d^2\pi^2}. \tag{34}$$

Equations (25), (33), and (34) present the effective EM response of a 2D holey metal film in the metamaterial limit. From equations (34) and (33) it is seen that the corresponding anisotropic homogenous film is described by a constant effective permeability and an effective permittivity on the canonical plasma form, where the cutoff frequency of the hole waveguide [$\pi c/a$] plays the role of an effective plasma frequency. The same expressions where obtained when spoof SPPs were first predicted [18], although in that work the analysis was based on an infinite thick surface perforated with subwavelength holes and not on a film of finite thickness h.

In the 1D case the effective optical parameters become

$$\varepsilon_x = \frac{d}{a\ \mathrm{sinc}^2(k_x a/2)} \approx \frac{d}{a}; \quad \mu_y = \mu_z = \frac{a\ \mathrm{sinc}^2(k_x a/2)}{d} \approx \frac{a}{d} \quad \mu_x = 1 \tag{35}$$

which together with equation (24) present the effective optical parameters of a 1D slit array in the metamaterial limit [19].

Our analysis show how holey metal films effectively can be mapped into homogenous media with optical properties predominantly controlled by the geometrical parameters of the holes (d and a). This is important because optical material properties normally is regarded as an intrinsic property which is related to the underlying electronic states and therefore is difficult to change or control [44].

4. Superlensing effects in holey metal films

Now we consider superlensing effects in holey metal films. By superlensing we mean lensing capable of producing an image with details on a deep subwavelength scale. In Ref. [27] Pendry showed that a thin homogenous isotropic metal slab can be used as an electrostatic near-field superlens for p-polarization. By using two-media Fresnel reflection and transmission coefficients and by summing all multiple scattering events Pendry derived the transmission coefficient for p polarization as

$$t = \frac{4\varepsilon k_z' k_z e^{ik_z' h}}{(\varepsilon k_z + k_z')^2 - (\varepsilon k_z - k_z')^2 e^{2ik_z' h}} \tag{36}$$

where ε is the dielectric constant of the homogenous isotropic slab, $k_z' = i\sqrt{k_x^2 + k_y^2 - \varepsilon\mu k_0^2}$ is the z component of the wavevector inside the slab, $k_z = i\sqrt{k_x^2 + k_y^2 - k_0^2}$ is the z component of the wave vector in vacuum outside the slab, and h is the thickness of the

slab [27]. In the electrostatic limit where $k_0 \ll \sqrt{k_x^2 + k_y^2}$ the two z components of the wave vectors become identical $k_z' = k_z$ [27]. With this in mind, it is easy to see from equation (36) that the dependence of μ completely disappears for p-polarization in the electrostatic limit. If we take the limit of the SPP resonance frequency $\varepsilon = -1$, the transmission coefficient of p-polarization in the electrostatic limit simplifies as

$$t = e^{-ik_z h},\ \forall\ \sqrt{k_x^2 + k_y^2}, \tag{37}$$

It is important to notice that equation (37) is truly independent of the parallel momentum, which means that not only the phase of propagating waves is corrected, but also evanescent waves are exponentially amplified across the lens. Thus, the proper alignment of the source, the lens, and the image plane enables near-field perfect lensing where both propagating and evanescent waves contribute to the reconstruction of the image.

In the previous section we derived the effective optical parameters of 2D hole arrays by requiring that the transmission coefficients of equation (30) and equation (31) must be identical. By comparing these two equations with the transmission coefficient derived by Pendry [equation (36)] it can be seen that they all three are form invariant. This is also the case for the transmission coefficient of slit arrays [equation (12)], if it is properly rewritten. Thus, in the metamaterial limit, transmission coefficients of both 1D and 2D holey metal films can be rewritten such that they are form invariant with the expression that Pendry used to demonstrate near-field perfect lensing. Even though that this is indeed true, it can readily be shown that perfect lensing is *not* possible utilizing holey metal films. Pendry's perfect lens relies of the fact that the z components of the wave vectors inside and outside the lens become identical for all parallel momentums. This can be achieve for a homogenous isotropic film either with a negative refractive index of $n = -1$, where perfect lensing can be realized for both polarizations, or in the electrostatic limit where k_z' becomes identical to k_z, as shown above. In the electrostatic limit the two polarizations simply become decoupled and for p-polarization perfect lensing can be realized with only $\varepsilon = -1$. Likewise, for s polarization electrostatic perfect lensing can be achieved with only $\mu = -1$. For holey metal films, however, the condition $k_z' = k_z$ for all parallel momenta, cannot be met. As a difference to a homogenous isotropic film, the z component of the wave vector inside holey metal films is not a function of the parallel momentum; instead it is constant and fixed by the fundamental waveguide mode. As the z component of the wave vector outside the film is always a strong function of the parallel momentum, we can therefore conclude that perfect lensing, as suggested by Pendry in reference [27] for isotropic homogenous films, cannot be realized with holey metal films.

A second difference between holey metal films and a homogenous metal film is related to the difference between canonical SPPs and spoof SPPs. In the electrostatic limit perfect lensing for a homogenous metal film is achieved at the SPP resonance frequency where $\varepsilon = -1$. The resonance frequency of spoof SPPs of holey metal films, on the other hand, is not at $\varepsilon_\parallel = -1$, but $\varepsilon_\parallel = 0$ [18]. Thus, in the limit $\varepsilon_\parallel = -1$,

where the transmission coefficient would simplify to equation (37) if $k'_z = k_z$ were true for all $k_\parallel$, there is no well defined resonantly excited spoof SPPs, and hence no physical mechanism behind a possible exponential enhancement of evanescent waves across the lens. This again prevents perfect lensing by means of holey metal films.

However, as k'_z is fixed by the fundamental waveguide mode (independently of the parallel momentum), another interesting phenomenon which can be used for superlensing exists in holey metal films. If the fixed k'_z fulfill the condition $k'_z h = m\pi$, the transmission coefficient of holey metal film simplifies significantly

$$t = (-1)^m \forall\ k_x, \tag{38}$$

which can be seen by substituting $k'_z h = m\pi$ into equation (30). $k'_z h = m\pi$ is the well known Fabry-Perot resonance condition. Equation (38) tells us that at some resonance wavelengths, a holey metal film can work as a perfect endoscope that is capable of transforming all waves independent of the parallel momentum from the input to the output side of the film. This means that holey metal films can transform an image with subwavelength details across the film and therefore work as a superlens. In contrary to the perfect lens where evanescent waves are amplified across the lens, holey metal films do not amplify the evanescent waves and therefore can not cancel the evanescent decay of evanescent waves outside the film. Previous work on wire media also discovered a resonant regime where all incoming plane waves are transmitted with unit efficiency through the structure; this regime was named the *canalization* regime [42]. For 1D slit and 2D square hole arrays k'_z is k_0 and $\sqrt{k_0^2 - (\pi/a)^2}$, respectively. This yields resonance wavelengths for 1D slit and 2D square hole arrays as

$$\lambda_m = \frac{2h}{m} \text{ for } m \geq 1; \quad \lambda_m = \frac{2}{\sqrt{\left(\frac{m}{h}\right)^2 + \left(\frac{1}{a}\right)^2}} \text{ for m} \geq 0, \tag{39}$$

respectively. In the metamaterial limit, where $\lambda >> d > a$, k'_z for 2D square hole arrays becomes imaginary and it is seen that the resonance condition $k'_z h = m\pi$ can not be fulfilled. However, there are two ways to fix this problem. The holes can either be filled with a material with a large dielectric constant ε_h or the holes can be made rectangular with $a_y >> a_x$. In the first case k'_z will be $\sqrt{\varepsilon_h k_0^2 - (\pi/a)^2}$, which is a real number for large ε_h, and in the second case k'_z will be $\sqrt{k_0^2 - (\pi/a_y)^2}$, which is real if a_y is in the order of the wavelength.

In order to proof that holey metal films can work as endoscopes, and to support our ideas, we investigate what happens when diffraction effects are included. Using the modal expansion formalism, we present numerical calculations including all diffraction modes needed to achieve convergence, and study in detail the imaging properties of the simplest holey metal film: a 1D slit array.

4.1. Imaging properties of slit arrays

Starting with an incident EM field at a source plane on one side of the slit array, we calculate the field at an image plane on the other side. The distance between the source

plane and the slit array is denoted by z_1 and the distance between the slit array and image plane is z_2 [figure 4]. We choose a p polarized ($\mathbf{E}^i = E_x^i$) incident field which

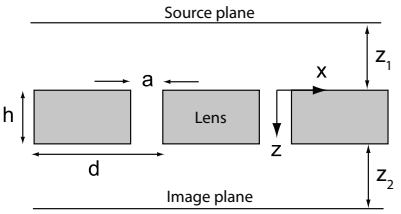

Figure 4. An incident field at a source plane in a distance z_1 from the lens is propagated through the lens and to an image plan in a distance z_2 from the lens.

consists of two subwavelength w wide spikes separated by a subwavelength center-to-center gap distance l

$$E_x^i(x) = \begin{cases} E_0 & \text{for } \frac{-l-w}{2} < x < \frac{-l+w}{2} \text{ and } \frac{l-w}{2} < x < \frac{l+w}{2} \\ 0 & \text{otherwise} \end{cases}. \quad (40)$$

A schematic of the incident field at the source plane can be seen in the inset of figure 5 b). Its Fourier space representation $E_x^i(k_x)$ is given as

$$E_x^i(k_x) = 2E_0 w \cos(k_x l/2)\text{sinc}(k_x w/2), \quad (41)$$

and the field at the image plane is calculated as

$$E_x(x) = \frac{1}{2\pi}\int_{-\infty}^{\infty} E_x^i(k_x) E_x^o(k_x) e^{ik_z z_1} \mathrm{d}k_x, \quad (42)$$

where $E_x^o(k_x)$ is the Fourier space representation of the field at the output side of the slit array, given as a sum over all the diffracted plane waves

$$E_x^o(k_x) = \sum_{n=-\infty}^{\infty} t^{(n)} e^{ik_x^{(n)} x} e^{ik_z^{(n)} z_2}, \quad (43)$$

where $t^{(n)}$ is the transmission coefficients specified in equation (11).

We start the analysis of the slit array endoscope by introducing a configuration of parameters that specifies what we will refer to as the standard configuration of the endoscope. Investigations on how the various parameters of the endoscope affects the imaging properties of the system will be performed within the standard configuration for comparison purposes. To study subwavelength imaging the wavelength must be chosen larger than the parameters specifying the source $\lambda >> w, l$, and to enter the into metamaterial limit, the unit cell size of the slit array must be chosen smaller than the operating wavelength $\lambda >> d$. As we are working in the PEC limit, where all results are scalable, all length parameters of the standard configuration are specified with respect to the unit length of the slit array, d. The standard parameters of the endoscope are presented in table 1. First we will investigate the evolution of the image as the distance between the lens and the image plane z_2 is increased [figure 5]. In a) the image of the

Table 1. Parameters of the standard configuration of the slit array endoscope. Notice, that $\lambda = 2h$ is chosen as the operating wavelength. This is the first Fabry-Perot resonance with $m = 1$.

Symbol	Description	Value
a	width of the slits	$0.5d$
h	thickness of the slit array	$50d$
λ	wavelength	$100d$
l	center-to-center distance between spikes	$15d$
w	width of the spikes	$5d$
E_0	strength of the spikes	10
z_1	distance between lens and image plane	0
z_2	distance between source plane and lens	d

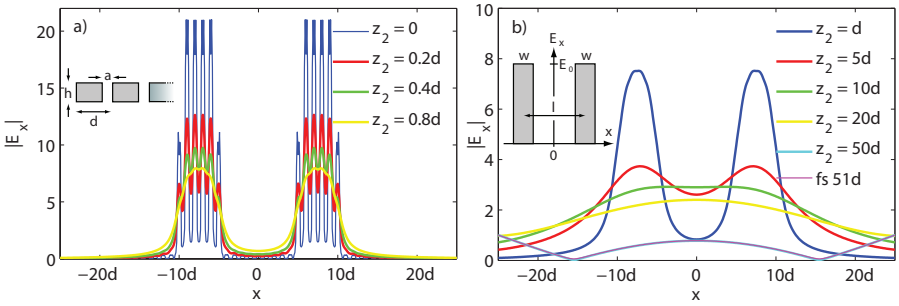

Figure 5. (Color online) $|E_x(x)|$ at the image plane for different distances z_2. All other parameters are specified by the standard configuration, see table 1.

source is calculated for different z_2's, all smaller than the period of the slit array. It is seen that when z_2 is small compared to d the image of the source is distorted by the higher order diffracted waves. This is because, close to the lens, the strongly evanescent higher order diffracted waves are present and will distort the perfect image that only could be obtained if all diffraction effects could be completely neglected, as they were in the derivation of equation (38). However, as the higher order diffracted waves are more strongly evanescent than the zero order diffracted waves, they can be excluded from the image if the distance z_2 is increased. This is presented in figure 5 b), where z_2 is equal to or larger than the period of the array d. Notice how the image of the subwavelength incident field is nicely reconstructed in an image with subwavelength resolution for $z_2 = d$ (blue curve). Also shown in b) is the image after free space propagation through a distance $h + d$ (the curve with legend fs $51d$). To illustrate the effect of the slit array this free space propagation image must be compared to the image at $z_2 = d$. It is seen that in the absence of the lens most information of the source is lost at this plane, whereas if the lens is present a nice subwavelength image of the source is revealed. At distances $z_2 = 10d, 20d, 50d$ it is seen that it is no longer possible to

distinguish the two spikes of the incident field. At the distance $z_2 = 50d$ the image is almost identical to the image of the free space propagation of $51d$, which indicates that the incident field is almost perfectly transmitted from the input to the output side of the slit array.

To illustrate that the endoscope effect in holey metal films is a resonant phenomenon, we next investigate how the image change if the wavelength is varied. The image is calculated for wavelength at and between the first and second order Fabry-Perot resonances ($\lambda = 2h = 100d$ and $\lambda = h = 50d$, respectively) [figure 6]. At the two

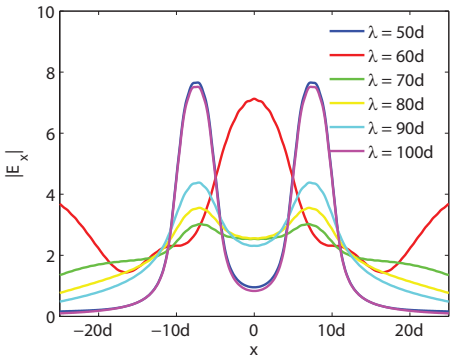

Figure 6. (Color online) $|E_x(x)|$ at the image plane for different wavelengths. All other parameters are specified by the standard configuration, see table 1.

Fabry-Perot resonances almost identical images are obtained, whereas the image can be heavily distorted if the wavelength is off-resonance. The calculations show that the two Fabry-Perot resonances are approached in a different manner. For a wavelength close to the first Fabry-Perot resonance some features of the incident field can be recognized in the image, whereas for wavelength close to the second Fabry-Perot resonance the field is strongly oscillating and it is impossible to see features of the incident field at the image plane.

In order to show that the thickness of the slit array can be much larger than the operating wavelength, we have calculated the image for a series of thicknesses, all of them fulfilling the Fabry-Perot resonance condition $h_m = m\lambda/2(m \geq 1)$ [figure 7 a)]. The same result is obtained for all three different thicknesses, even for the thickness h_{20}, where the slit array endoscope is 10 times thicker than the operating wavelength. This indicates that, as long as the thickness of the endoscope match the Fabry-Perot resonance condition for a given wavelength, the slit array endoscope can be made almost arbitrary thick.

In reference [30] we presented a full numerical calculation including both diffraction effects and losses, where the result showed that losses in the metal (at least in the terahertz-regime) do hardly have any effect of the imaging properties of the slit array

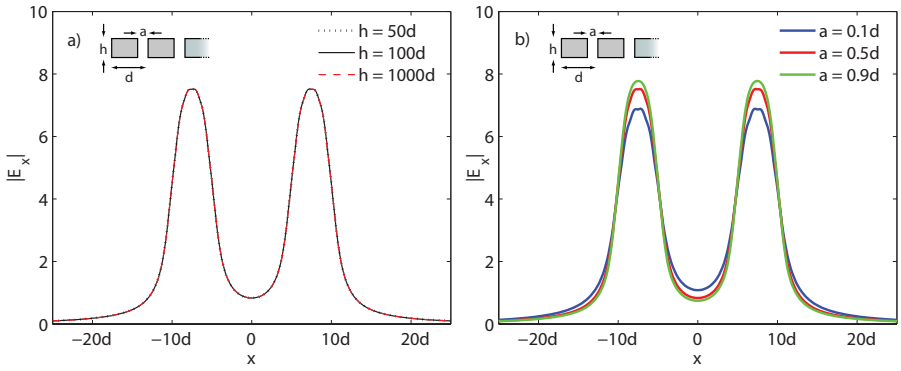

Figure 7. (Color online) a) $|E_x(x)|$ at the image plane for different thicknesses of the slit array. b) $|E_x(x)|$ at the image plane for different hole sizes a. All other parameters are specified by the standard configuration, see table 1.

endoscope. The effect of including losses in the metal was a small overall damping of the field at the image plane. Thus, even in the terahertz regime, a slit array superlens can be made very thick and is therefore capable of transforming an image with subwavelength resolution over several wavelengths (into the far-field zone of the source). The possibility of a large z-shift of a subwavelength image is very attractive from a technological point of view, where superlenses based on holey metal films may find many useful applications. One example could be in a scanning near-field optical microscope, where holey metal film superlenses could enable near-field optical probing in a situation where the probe is in the far-field zone of the sample.

In figure 7 b) we investigate how the image change when we vary the width of the slits. The results show a tendency of a slightly better image when the slits are large compared to the metal regions between them. However, the image is only marginally modified when a is varied, even if the change in a is large, as e.g from $a = 0.1d$ to $a = 0.9d$ (blue and green curve, respectively).

In order to clarify how well can the slit array endoscope resolve an image, we have made calculations where starting from the standard configuration and reducing in steps the center-to-center distance between the two spikes of the incident field, l, until the gap between them closes [figure 8]. The results show how the dip between the two spikes disappears as the two spikes approach each other. However, even for a gap size of only d (the dashed green curve for $l = 6d$) the two spikes of the source field can still be distinguished in the image. To further investigate the ultimate resolution of the slit array endoscope we have made calculations where the width of the two spikes in the incident field is varied [figure 9 a)], showing how the strength of the field is damped as the width of the two spikes is reduced. For a width of only d the lens is still capable of producing an image where the main features of the source still easily can be recognized.

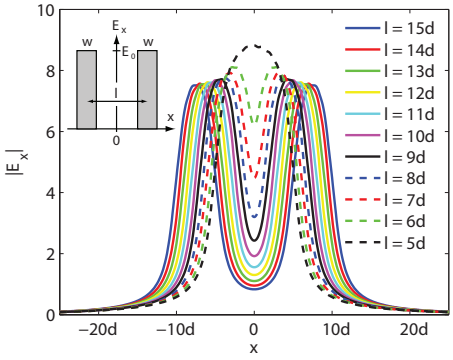

Figure 8. (Color online) The gap between the spikes in the incident field is in steps reduced to zero. All other parameters are specified by the standard configuration, see table 1.

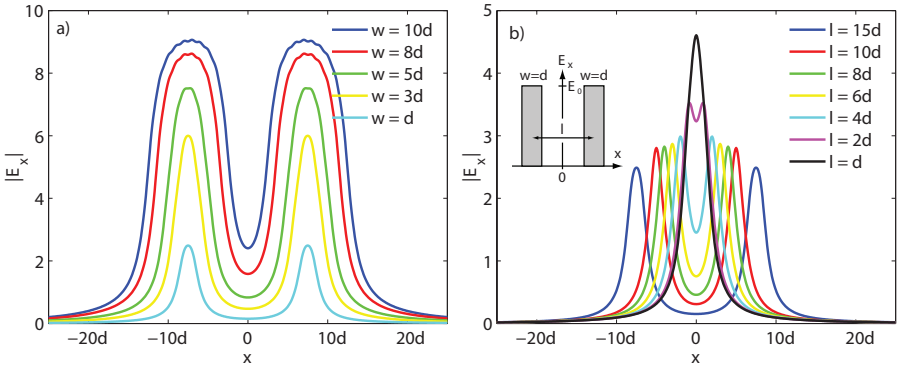

Figure 9. (Color online) a) $|E_x(x)|$ at the image plane for different widths of the spikes in the incident field. b) The width of the spikes in the incident field is reduced to d and the gap between the spikes is in steps reduced to zero. All other parameters are specified by the standard configuration, see table 1.

In the ultimate test of the resolution of the slit array endoscope, the distance between two spikes of width d is reduced in steps to zero [figure 9 b)]. Here it is seen that, even when two spikes of width d are separated by only a gap size of d, the dip in the field between the two spikes can be distinguished in the image produced by the slit array endoscope. We therefore conclude that the ultimate resolution of the slit array endoscope is in the range of the period of the slit array d. This is similar to the perfect lens in the optical regime suggested by Pendry [27], where the ultimate resolution would be the inter-atomic distance between the atoms in the lattice if absorption in the metal could be ignored [45].

5. Conclusion

Light transmission properties of holey metal films in the metamaterial limit, where the operating wavelength is much larger than the unit length of the holey metal films, have been analyzed with focus on effective medium theory and superlensing effects. Transmission coefficients of both 1D slit and 2D hole arrays have been derived in the perfect conductor approximation using the modal expansion formalism. We have presented the effective medium theory of holey metal films, which shows how such films can effectively be mapped into anisotropic homogenous film with optical properties dictated by the geometrical parameters of the holes, e.g. in the case of a 2D hole array, the x and y components of the diagonal relative permittivity tensor shows a Drude-like behavior, where the cut-off wavelength of the hole waveguide $\lambda = 2a$ plays the role of an effective plasma frequency. We have showed that holey metal films in the metamaterial limit have superlensing properties and can work as endoscopes capable of transforming a subwavelength image from the input to the output surface of the film. If the operating wavelength matches the Fabry-Perot resonance condition of the structure, the metamaterial limit transmission coefficient for p-polarization simplifies significantly and becomes unity independent of the parallel momentum, meaning that all EM waves, both propagating and evanescent, are perfectly transmitted though the film. Using the derived modal expansion transmission coefficients, the imaging properties of a 1D slit array endoscope have been analyzed. The analysis shows that the ultimate resolution of an endoscope, based on a 1D perfect conductor film periodically perforated with subwavelength apertures is of the order of the unit cell size and that such an endoscope is capable of transforming an image with subwavelength resolution into the far-field zone of the source. All these properties of holey metal films make them attractive from a technological point of view and we are confident that they will find many useful applications within near-field imaging.

Acknowledgments

We acknowledge Alexandre Mary for valuable discussions and financial support from the Spanish Ministry of Science under projects No. CSD2007-046-NanoLight.es and MAT2008-06609-C02 and from a NABIIT project supported by the Danish Research Agency (contract No. 2106-05-033).

References

[1] T. W. Ebbesen, H. J. Lezec, H. F. Ghaemi, T. Thio, and P. A. Wolff. *Nature*, 391:667, 1998.
[2] U. Schröter and D. Heitmann. *Phys. Rev. B*, 58:15419, 1998.
[3] J. A. Porto, F. J. Garcia-Vidal, and J. B. Pendry. *Phys. Rev. Lett.*, 83:2845, 1999.
[4] L. Martin-Moreno, F. J. Garcia-Vidal, H. J. Lezec, K. M. pellerin, T. Thio, J. B. Pendry, and T. W. Ebbesen. *Phys. Rev. Lett.*, 86:1114, 2001.
[5] J. Bravo-Abad, F. J. Garcia-Vidal, and L. Martin-Moreno. *Phys. Rev. Lett.*, 93:227401, 2004.

[6] K. L. van der Molen, K. J. K. Koerkamp, S. Enoch, F. B. Segerink, N. F. van Hulst, and L. Kuipers. *Phys. Rev. B*, 72:045421, 2005.
[7] A. Mary, S. G. Rodrigo, F. J. Garcia-Vidal, and L. Martin-Moreno. *Phys. Rev. Lett.*, 101:103902, 2008.
[8] D. E. Grupp, H. J. Lezec, T. Thio, and T. W. Ebbesen. *Adv. Mater.*, 11:860, 1999.
[9] F. J. Garcia de Abajo. *Opt. Express*, 10:1475, 2002.
[10] H. J. Lezec, A. Degiron, E. Devaux, R. A. Linke, L. Martin-Moreno, F. J. Garcia-Vidal, and T. W. Ebbesen. *Science*, 297:820, 2002.
[11] A. Degiron, H. J. Lezec, N. Yamamoto, and T. W. Ebbesen. *Opt. Commun.*, 239:61, 2004.
[12] J. A. Matteo, D. P. Fromm, Y. Yuen, P. J. Schuck, W. E. Moerner, and L. Hesselink. *Appl. Phys. Lett.*, 85:648, 2004.
[13] M. J. Lockyear, A. P. Hibbins, J. R. Sambles, and C. R. Lawrence. *Phys. Rev. Lett.*, 94:193902, 2005.
[14] F. J. Garcia-Vidal, E. Moreno, J. A. Porto, and L. Martin-Moreno. *Phys. Rev. Lett.*, 95:103901, 2005.
[15] H. A. Bethe. *Phys. Rev.*, 66:163, 1944.
[16] G. Goubau. *J. Appl. Phys.*, 21:1119–1128, 1950.
[17] D. L. Mills and A. A. Maradudin. *Phys. Rev. B*, 39:1569, 1989.
[18] J. B. Pendry, L. Martin-Moreno, and F. J. Garcia-Vidal. *Science*, 305:847, 2004.
[19] F. J. Garcia-Vidal, L. Martin-Moreno, and J. B. Pendry. *J. Opt. A: Pure Appl. Opt.*, 7:S97, 2005.
[20] D. L. Mills and E. Burstein. *Rep. Prog. Phys.*, 37:817–926, 1974.
[21] V. M. Agranovich and A. A. Maradudin. *Surface Polaritons - Electromagnetic Waves at Surfaces and Interfaces*. North-Holland, 1st edition, 1982. ISBN 0-444-86165-3.
[22] L. Novotny and B. Hecht. *Principles of Nanooptics*. Cambridge University Press, 1st edition, 2006. ISBN 0-521-53988-9.
[23] A. P. Hibbins, B. J. Evans, and J. R. Sambles. *Science*, 308:670, 2005.
[24] E. Moreno, A. I. Fernandez-Dominguez, J. I. Cirac, F. J. Garcia-Vidal, and L. Martin-Moreno. *Phys. Rev. Lett.*, 95:170406, 2005.
[25] J. Christensen, L. Martin-Moreno, and F. J. Garcia-Vidal. *Phys. Rev. Lett.*, 101:014301, 2008.
[26] H. Estrada, P. Candelas, A. Uris, F. Belmar, F. Meseguer, and F. J. G. de Abajo. *Appl. Phys. Lett.*, 93:011907, 2008.
[27] J. B. Pendry. *Phys. Rev. Lett.*, 85:3966, 2000.
[28] N. Fang, H. Lee, C. Sun, and X. Zhang. *Science*, 308:534, 2005.
[29] D. O. S. Melville and R. J. Blaikie. *Opt. Express*, 13:2127, 2005.
[30] J. Jung, F. J. Garcia-Vidal, L. Martin-Moreno, and J. B. Pendry. *Phys. Rev. B*, 79:153407, 2009.
[31] S. A. Ramakrishna, J. B. Pendry, M. C. K. Wiltshire, and W. J. Stewart. *J. Mod. Opt.*, 50:1419, 2003.
[32] P. A. Belov and Y. Hao. *Phys. Rev. B*, 73:113110, 2006.
[33] Z. Liu, H. Lee, Y. Xiong, C. Sun, and X. Zhang. *Science*, 315:1686, 2007.
[34] I. I. Smolyaninov, Y. J. Hung, and C. C. Davis. *Science*, 315:1699, 2007.
[35] Y. Xiong, Z. Liu, and X. Zhang. *Appl. Phys. Lett.*, 93:111116, 2008.
[36] P. A. Belov, Y. Hao, and S. Sudhakaran. *Phys. Rev. B*, 73:033108, 2006.
[37] G. Shvets, S. Trendafilov, J. B. Pendry, and A. Sarychev. *Phys. Rev. Lett.*, 99:053903, 2007.
[38] S. Kawata, A. Ono, and P. Verma. *Nat. Photonics*, 2:438, 2008.
[39] P. A. Belov, Y. Zhao, S. Tse, P. Ikonen, M. G. Silveirinha, C. R. Simovski, S. Tretyakov, Y. Hao, and C. Parini. *Phys. Rev. B*, 77:193108, 2008.
[40] C. Lou, S. G. Johnson, J. D. Joannopoulos, and J. B. Pendry. *Phys. Rev. B*, 65:201104(R), 2002.
[41] P. V. Parimi, W. T. Lu, P. Vodo, and S. Sridhar. *Nature*, 426:404, 2003.
[42] P. A. Belov, C. R. Simovski, and P. Ikonen. *Phys. Rev. B*, 71:193105, 2005.
[43] P. Ikonen, P. Belov, C. Simovski, and S. Maslovski. *Phys. Rev. B*, 73:073102, 2006.
[44] J. T. Shen, P. B. catrysse, and S. Fan. *Phys. Rev. Lett.*, 94:197401, 2005.

[45] F. D. M. Haldane. *cond-mat/0206420*, 2002.